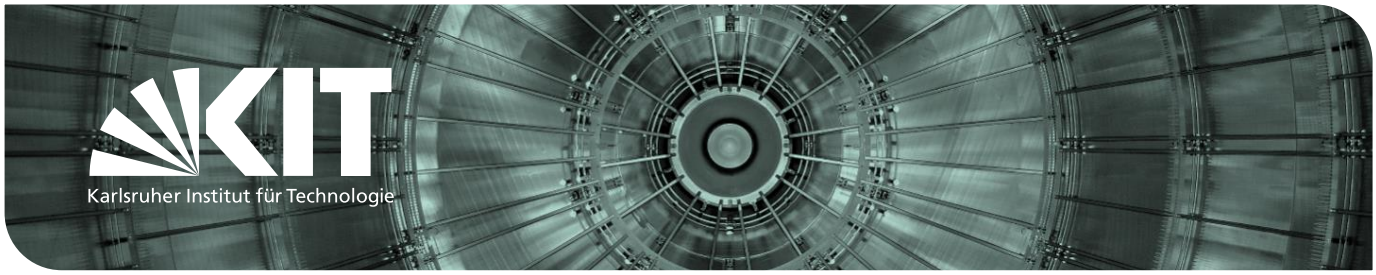

Background systematics and extensions to the KATRIN background model

zur Erlangung des akademischen Grades eines

Doktors der Naturwissenschaften (Dr. rer. nat.)

von der KIT-Fakultät für Physik
des Karlsruher Instituts für Technologie (KIT)

angenommene

Dissertation

von

M. Sc. Dominic Fabian Hinz

aus Baden-Baden

Referent:	Prof. Dr. Guido Drexlin Institut für Experimentelle Teilchenphysik (ETP), KIT
Korreferent:	Prof. Dr. Ralph Engel Institut für Experimentelle Teilchenphysik (ETP), KIT

Tag der mündlichen Prüfung: 29. Juli 2022

Declaration of Authorship

Herewith I affirm that I wrote the current thesis on my own and without the usage of any other sources or tools than the cited ones and that this thesis has not been handed neither in this nor in equal form at any other official commission.

Erklärung der Selbstständigkeit

Hiermit versichere ich, die vorliegende Arbeit selbstständig angefertigt zu haben und keine Hilfsmittel jenseits der kenntlich gemachten verwendet zu haben. Weiterhin habe ich weder diese noch eine äquivalente Version dieser Arbeit bei einer anderen Prüfungskommission vorgelegt.

Karlsruhe, den .....

Dominic Fabian Hinz

Introduction

Neutrino physics evolved to a vital field of research over the last decades since the postulation of neutrinos by W. Pauli 1930 [1]. The discovery of neutrino oscillation caused particular attention, as this requires neutrinos to have mass. This observation, leading to the Nobel Prize in 2015 was in contradiction to the successful Standard Model of Particle Physics (SM), in which neutrinos are assumed to be massless particles [2]. Hence, various experiments focus on the investigation of the neutrino properties and how they are incorporated into the Standard Model. The neutral charged neutrinos oscillate between their associated flavour states of slightly different masses where the key parameters mass splitting Δm^2_{ik} and mixing angles θ_{ik} describe the oscillation. They only interact via the weak interaction which requires a high particle flux for reasonable direct detection. However, their mass scale is many times smaller than that of charged leptons such as electrons, so new theories had to be developed about how neutrinos obtain their mass, although their absolute mass is undetermined and only upper limits have been given.

World-leading sensitivity on the experimental determination of the effective electron neutrino mass is achieved with the KATRIN experiment [3] which provides the most stringent limit of

$$m_\nu < 0.8\,\mathrm{eV/c^2} \text{ at } 90\,\% \text{ C.L.} \tag{1}$$

from direct neutrino mass measurements using precision spectroscopy of β-electrons from tritium beta decays [4]. Besides direct methods to determine the neutrino mass by spectroscopy of electrons from tritium beta decays and electron capture processes of holmium [5], indirect model-dependent methods exist, deriving the neutrino mass scale by cosmological observations or the search for neutrinoless double beta decay to limits below $0.2\,\mathrm{eV/c^2}$ [6, 7]. To reach the final neutrino mass sensitivity of $0.2\,\mathrm{eV/c^2}$ (90 % C.L.) with KATRIN, steady improvements on the statistical and systematic uncertainties are required. In particular, optimisation of the measurement configuration regarding the background level and corresponding uncertainties which arise in the main spectrometer volume is particularly relevant as this currently limits the final sensitivity. Background-related systematic errors dominated the systematic budget of the first measurement campaigns KNM1 and KNM2, from which the current upper limit is derived. Therefore, knowledge of the mechanism of background generation in the KATRIN main spectrometer is imperative in order to take appropriate countermeasures.

Current assumptions about the mechanism of background electron generation in the main spectrometer include two relevant background sources. On the one hand, the radioactive noble gas radon emanates from the inner surface and the getter pump material, decays emitting electrons with energies up to several keV. Such electrons are likely trapped in the magnetic bottle of the main spectrometer flux tube, ionising residual gas atoms and thus generating background electrons. On the other hand, a major part of the background,

emerging in the main spectrometer, is assumed to arise from the ionisation of highly excited hydrogen atoms (Rydberg atoms) by black-body-radiation (BBR), which is called the Rydberg background model [8, 9]. Excited atoms originate from the inner main spectrometer surface and the electrodes due to an intrinsic contamination of the stainless steel surfaces by radioactive ^{210}Pb. The decay produces a high-energy recoil ion that knocks on atoms in the stainless steel, atomising surface-adsorbed hydrogen atoms, some of which may be excited. Due to the low energy of the BBR photons, very high excitations are necessary which lead to electron energies on the order of meV after ionisation.

In this thesis the analysis and improvements on background-related systematics at KATRIN Neutrino Mass (KNM) measurements are presented. By changing the measurement configuration from a centered to a shifted analysing plane towards the detector, the background rate is significantly reduced. Furthermore, background systematics which arise from residual radon decays were eliminated. Additionally, the analysis and interpretation of a dedicated background study, using a passive transverse energy filter (pTEF) is shown. With this filter, which serves as a geometric boundary for background electrons with high transverse energy, the Rydberg background model was investigated with regard to the initial kinetic energy spectrum of the background electrons. The pTEF is a micro-structured gold plate, placed in front of the detector and equipped with hexagonal channels on the micrometer scale. Since the electrons are adiabatically guided in strong magnetic fields, they perform cyclotron motion of defined radial extent, corresponding to their Larmor radius which is energy-dependent. If the Larmor radius exceeds the channel dimensions, the filter hinders the number of electrons counted at the detector. The final electron energy and the polar angle with respect to the detector magnetic field lines is directly related to the initial kinetic energy within the electromagnetic field inside the main spectrometer, through which the background electron energy scale can be derived by the rate reduction behind the pTEF.

Outline

In chapter 1 and 2, an overview on neutrino physics in the Standard Model and beyond is given with description of neutrino oscillation, theoretical mass generation, and current experimental limits on the neutrino mass. In chapter 3, an overview of the design of the KATRIN experiment with the individual components, and the neutrino mass measurement campaigns configurations is given. Furthermore in chapter 4, an extended description of various background processes, observed from the main spectrometer is given, supplemented with latest data and analysis, and the current Rydberg background model. In chapter 5, analysis of the three spectrometer background systematics during the KNM measurements (KNM1-KNM5) is shown, and the influence on the neutrino mass sensitivity is presented. In chapter 6, the properties of the Rydberg background electrons and the working principle of the transverse energy filters are presented, supported by simulations. Thereafter, the analysis and results of the pTEF measurement campaign with derivation of the initial transverse energy scale under consideration of systematic effects is presented and an outlook to further research on active transverse energy filters is shown. The results do not represent the expectations of the current Rydberg background

model, thus extensions on the background generation mechanisms were made in chapter 7. Finally, a summary of the outcome of the background investigations at KNM and pTEF measurements is given. Extensions on the Rydberg background model and an outlook of near-future investigation are also presented.

Contents

Introduction . . . . . **iii**

I. Standard Model neutrino physics and beyond

1. Standard Model neutrinos **3**
1.1. History of discovering neutrinos 3
1.2. Treatment in the Standard Model of physics 5

2. Massive Neutrinos **9**
2.1. Neutrino oscillation and mass generation 9
2.2. Measurements of the neutrino mass 15
2.2.1. Model-dependent limits from cosmology and experiments 15
2.2.2. Direct neutrino mass determination 17

II. The Karlsruhe Tritium Neutrino Experiment

3. Design and operation **23**
3.1. Main components of the KATRIN experiment 23
3.1.1. Windowless gaseous tritium source 24
3.1.2. Differential and cryogenic pumping section 25
3.1.3. Monitoring Devices 26
3.1.4. The KATRIN spectrometers and detector 27
3.2. Measuring the effective neutrino mass 31
3.2.1. Electromagnetic field setting 31
3.2.2. Measurement time distribution 34
3.2.3. Systematic budget 35

4. Background processes in the KATRIN experiment **37**
4.1. Emission of secondary electrons from surfaces 38
4.2. Intrinsic detector background 39
4.3. Penning traps 41
4.4. Radon-induced main spectrometer background 42
4.5. The Rydberg background model 44
4.5.1. Parameter dependencies on the background level 45
4.5.2. Identification and contamination of ^{210}Pb 47
4.5.3. Generation and ionisation of Rydberg atoms by BBR at KATRIN . 53

III. Analysis and simulation of background

5. Background systematics for neutrino mass measurements . . . 61
5.1. Distribution broadening by non-Poisson effects . . . 61
5.1.1. Description of the non-Poisson fraction Σ_{np} . . . 61
5.1.2. Temporal changes of the background rate . . . 63
5.1.3. Radon proportion in the comparison of NAP and SAP . . . 66
5.2. High-voltage-dependent background slope . . . 67
5.3. Effect of the inter-spectrometer Penning trap . . . 69
5.4. Neutrino mass sensitivities . . . 72

6. Minimising the background level with micro-structured filters . . . 75
6.1. Characteristics of Rydberg background electrons . . . 75
6.2. Basic principle of transverse energy filters . . . 78
6.3. Parameter studies on micro-structured honeycombs . . . 80
6.4. Dedicated background measurements with a passive filter . . . 82
6.4.1. Passive transverse energy filter (pTEF) . . . 82
6.4.2. Measurement configurations and complementary simulations . . . 85
6.4.3. Analysis of the transverse energy scale . . . 90
6.5. Research on active transverse energy filters . . . 99

7. Developments on the Rydberg background model . . . 103

8. Conclusion and outlook . . . 111

Bibliography . . . 115

List of Figures . . . 129

List of Tables . . . 133

Appendix . . . 135

Acknowledgment . . . 157

Part I.

Standard Model neutrino physics and beyond

1. Standard Model neutrinos

1.1. History of discovering neutrinos

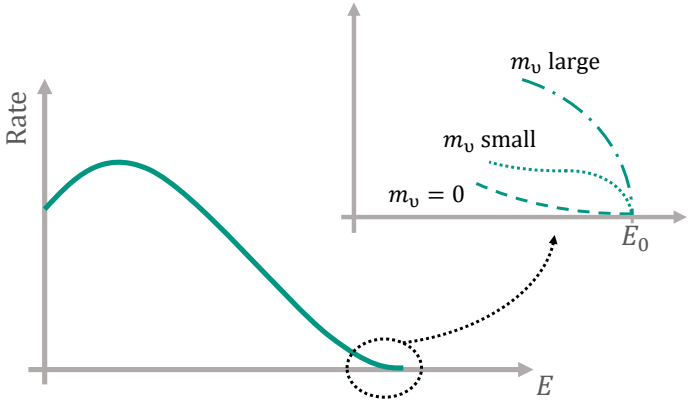

Figure 1.1.: Outline of a continuous energy spectrum of β-electrons. A zoom on the endpoint E_0 region with the spectral shape for different cases of neutrino masses (adapted from [10]). The larger the neutrino mass m_ν the larger the shape distortion with sharper truncation of the spectrum at E_0. Generously, the endpoint E_0 of the beta spectrum changes for different neutrino masses, it is shifted to lower values the higher the neutrino mass is.

Historically, postulation, ideas and investigations regarding neutrinos already began more than 100 years ago. James Chadwick measured beta spectra of radioactive radium and observed continuous spectra of the beta particles in 1914 [11]. The continuity of the beta particle spectra, as shown in fig. 1.1, was additionally proven by Ellis and Wooster 1927 [12]. At that time, this observation was shocking since a continuous spectrum would have violated energy conservation for radioactive decays into two particles (daughter nucleus and electron) - mono-energetic spectra were expected. The consequence was the postulation of an additional involved particle that was not measured or even understood. The existence of neutrinos, or at least one, was postulated by W. Pauli 1930 with his famous letter to the 'Liebe Radioaktive Damen und Herren' [1], originally named 'neutron'. The mass of the particle had to be small, similar to that of electrons or even smaller, and its spin had to be 1/2. A few years later, in 1934, E. Fermi developed a theoretical description of beta decay that resolved the observed beta spectra [10]. In the meantime, the neutron was discovered as the second neutral component of atomic nuclei, which is why Fermi gave the additional particle the name 'neutrino'. He discovered that the imprint of the

neutrino mass is most pronounced at the endpoint region (E_0) of the beta spectrum, as shown in fig. 1.1. From the comparison with the available data, he also concluded that the neutrino mass must be either very small or zero. Beta decay is described by a three-body decay

$$\mathrm{M}(A, Z) \rightarrow \mathrm{D}(A, Z+1) + \mathrm{e}^- + \overline{\nu}_\mathrm{e} \tag{1.1}$$

with the initial particle M (mother) and the final particle D (daughter), electron e^-, and electron antineutrino $\overline{\nu}_\mathrm{e}$. The initial and final particles M and D are defined by their nucleon number A and proton number Z. In β^--decays neutrons are transformed into protons under emission of electrons and electron antineutrinos.

However, the experimental discovery of a neutrino succeeded in 1953 by F. Reines and C. Cowan as part of the 'Poltergeist' project [13]. Using a liquid scintillator loaded with cadmium (Cd), coincident photon (γ) signals were measured. The experiment was carried out near a nuclear reactor that delivered a high neutrino flux of electron antineutrinos. Thus, the reaction of inverse beta decay

$$\overline{\nu}_\mathrm{e} + \mathrm{p} \rightarrow \mathrm{n} + \mathrm{e}^+ \,, \tag{1.2}$$

releasing a neutron and a positron within the liquid scintillator was measured. The observed γs are produced by electron-positron annihilation and neutron capture by the Cd atoms.

Experimental investigations with μ mesons gave rise to the theory of additional neutrino flavours. The expectation was that μ mesons decay into an electron and one pair of neutrino and antineutrino which would annihilate into a photon. This decay could never been experimentally proven. In 1962, L. Ledermann, M. Schwartz, and J. Steinberger studied the interactions of muon-like neutrinos [14]. At the Alternating Gradient Synchrotron (AGS) at the Brookhaven National Laboratory a muon neutrino flux was generated by high energy protons hitting a beryllium target producing pions and kaons which further decay into muons (μ) and muon neutrinos (ν_μ). For the general reaction

$$\nu_\ell + X \rightarrow \ell + Y \tag{1.3}$$

with the charged lepton ℓ and its associated neutrino ν_ℓ. Differences on the final particles can be investigated. They measured a significantly higher ratio of muon-like events ($\ell = \mu$ in eq. 1.3) than electron-like events, confirming the presence of ν_μ [14]. This discovery was granted with the Nobel Prize in 1988. Measurements of the invisible width of the Z^0 boson at electron positron collisions at the Large Electron Positron Collider (LEP), where the reaction $\mathrm{e}^+\mathrm{e}^- \rightarrow \nu\overline{\nu}\gamma$ is observed, can be used to derive the total number of neutrino flavour to $N_\nu = 2.92 \pm 0.05$ [15]. In 2001, the third neutrino associated to the τ-lepton ν_τ was experimentally detected by the DONUT collaboration [16]. A 800 GeV proton beam hitting on a tungsten target, producing D_S mesons which decay into τ and $\overline{\tau}$ with small branching ratios. The interaction of ν_τ results in a short-living τ which can be identified by a kink in the direction of reconstructed tracks of the decay products.

1.2. Treatment in the Standard Model of physics

The Standard Model of Particle Physics (SM) [18] is the theoretical description of the fundamental forces electromagnetic, weak, and strong. Gravitation could not yet be included in a unified theory of all four (known) fundamental forces. In the SM, all known elementary particles are categorised into twelve elementary fermions: six quarks u, d, c, s, t, b, three charged leptons e, μ, τ, three neutral neutrinos ν_e, ν_μ, ν_τ, and five elementary bosons: $\gamma, W^\pm, Z^0, g, H$, see fig. 1.2. The fermions (quarks and leptons) also exists as antiparticle. Quarks are further split into three colours by their colour charge, resulting in six states of each quark. Gluons are described by 8 independent combinations of colour and anticolour which mediate the strong interaction. Mediators of the weak interaction are the W and Z bosons. The W boson is a doublet of two charged variations W^+ and W^-, the Z boson is electrically neutral. In combination with the photon (γ), which mediates the electromagnetic force, the electroweak interaction is the unified description of these two fundamental interactions. No lepton participates in the strong interaction. Since neutrinos are electrically neutral, they can only interact via the weak interaction. A feature of weak interaction is parity violation. Parity transformation is the operation of mirroring $x \longrightarrow -x$. That weak interaction is not parity conserving was discovered by Wu et. al in 1957 [19]. This is connected to the helicity $H = \frac{\vec{S}\vec{p}}{|\vec{S}||\vec{p}|}$ the projection of the spin vector to the momentum of neutrinos which can be expressed as a chirality. Neutrinos only exist left-handed ($H = -1$) [20], hence antineutrinos are right-handed ($H = 1$). Since in the initial Standard Model neutrinos are massless, they propagate with the speed of light, therefore, no reference frame exists in which neutrinos are right-handed [18]. This implies that helicity is not conserved for massive particles.

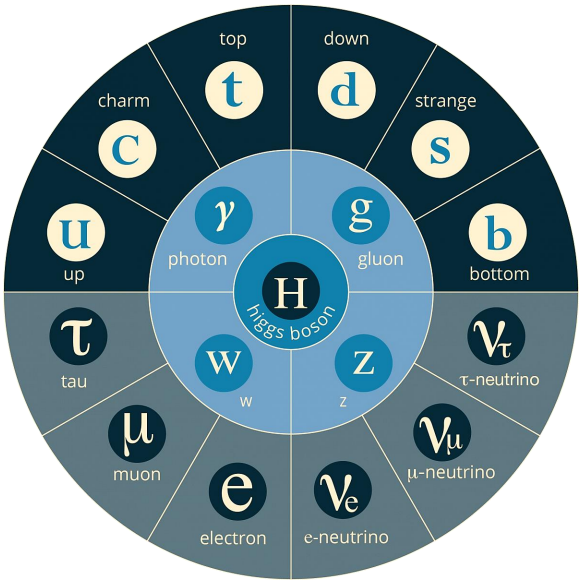

Figure 1.2.: The Standard model of particle physics, consisting of quarks (upper outer semicircle), leptons (lower outer semi circle), gauge bosons (inner circle) and the Higgs boson (center) [17].

To construct the standard model Lagrangian one takes four different sectors into account: the quantum chromodynamics (QCD) sector which describes interactions between quarks and gluons - a Yang-Mills gauge theory with $SU(3)$ symmetry, the electroweak sector - a Yang-Mills theory with symmetry group $U(1)\times SU(2)_L$ - the unification of electromagnetic and weak interactions, the Higgs sector with the complex scalar Higgs field of the group $SU(2)_L$, and the Yukawa sector which is used the describe coupling by Yukawa's interaction between the Higgs field and massless fundamental fermions (quarks and leptons) [21–23]. The masses of these fermions are generated by the spontaneous symmetry breaking of the Higgs field.

Considering a scalar complex field $\phi(x)$ one can assume the Lagrangian of the field to be given by

$$\mathcal{L} = \partial_\alpha \phi^\dagger \partial^\alpha \phi - V(\phi^\dagger \phi) \tag{1.4}$$

with the potential

$$V(\phi^\dagger \phi) = -\mu^2 \phi^\dagger \phi + \lambda(\phi^\dagger \phi)^2 = \lambda \left(\phi^\dagger \phi - \frac{\mu^2}{2\lambda}\right)^2 - \frac{\mu^4}{4\lambda}\,, \tag{1.5}$$

where μ^2 and λ are positive constants. Hence, the minimum of that potential $V_0 = -\mu^4/4\lambda$ is reached at the value of the field, when

$$\phi_0^\dagger \phi_0 = \frac{\mu^2}{2\lambda}\,. \tag{1.6}$$

Therefore, the potential minimum is attained at

$$\phi = \phi_0 = \frac{v}{\sqrt{2}} e^{i\alpha} = \text{const. with } v^2 = \frac{\mu^2}{\lambda}\,. \tag{1.7}$$

The Hamlitonian of this system is given by

$$\mathcal{H} = \partial_0 \phi^\dagger \partial_0 \phi + \sum_{i=1}^{3} \partial_i \phi^\dagger \partial_i \phi + V(\phi^\dagger \phi)\,. \tag{1.8}$$

The energy of the system is minimal for $\phi = \phi_0$ at a value different from zero. Additionally, the minimum is reached at an infinite number of vacuum values by eq. 1.7 which results into the vacuum expectation value (vev) of the field

$$\phi_0 = \frac{v}{\sqrt{2}}\,, \tag{1.9}$$

by choosing $\alpha = 0$ in eq. 1.7. Such a symmetry violation of the Lagrangian is called spontaneous. By introducing two real fields χ_1 and χ_2 with vacuum expectation values of zero, connected to the field $\phi(x)$ by

$$\phi(x) = \frac{v}{\sqrt{2}} + \frac{\chi_1 + i\chi_2}{\sqrt{2}}\,, \tag{1.10}$$

one obtains the following expression for the Lagrangian of the system

$$\begin{aligned}\mathcal{L} &= \frac{1}{2}\sum_i \partial_\alpha \chi_i \partial^\alpha \chi_i - \frac{\lambda}{4}\left((v+\chi_i)^2 + \chi_2^2 - v^2\right)^2 \\ &= \frac{1}{2}\sum_i \partial_\alpha \chi_i \partial^\alpha \chi_i - \mu^2\chi_1^2 - \lambda v \chi_1(\chi_1^2+\chi_2^2) - \frac{\lambda}{4}(\chi_1^2+\chi_2^2)^2 \end{aligned} \tag{1.11}$$

of the two interacting real fields χ_1 and χ_2. The second term in eq. 1.11 represents the mass term of the field χ_1, while χ_2 has no mass term. Hence, the quanta of the fields χ_1 are neutral particles with mass $m_{\chi_1} = \sqrt{2}\mu$ and neutral massless particles ($m_{\chi_2} = 0$) of the field χ_2. These neutral massless particles are called Goldstone bosons [24], whose appearance is a consequence of the spontaneous violation of a continuous symmetry. This is problematic for the Standard Model theory since no massless scalar bosons were observed in experiments.[22]

However, Higgs [25] developed a method in which no Goldstone scalar boson appears in a theory of local gauge invariance and the gauge bosons are massive. Therefore, consider the scalar complex field $\phi(x)$ and the real vector gauge field $A_\alpha(x)$ with the Lagrangian of the system to be

$$\mathcal{L} = ((\partial_\alpha + igA_\alpha)\phi)^\dagger((\partial^\alpha + igA^\alpha)) - V(\phi^\dagger\phi) - \frac{1}{4}F_{\alpha\beta}F^{\alpha\beta}\,, \tag{1.12}$$

where

$$F_{\alpha\beta}(x) = \partial_\alpha A_\beta(x) - \partial_\beta A_\alpha(x)\,, \tag{1.13}$$

with the potential $V(\phi^\dagger\phi)$ given as in eq. 1.5 and the real dimensionless constant g. The field $\phi(x)$ and the potential holds the same condition of its minimum as in eq. 1.7 with its vacuum expectation value eq. 1.9, which will violate the symmetry spontaneously. Thus, the complex field $\phi(x)$ can be expressed as follows

$$\phi(x) = \frac{v+\chi(x)}{\sqrt{2}}e^{i\theta(x)} \xrightarrow{\Lambda(x)} \frac{v+\chi(x)}{\sqrt{2}} \tag{1.14}$$

with the real functions $\chi(x)$ and $\theta(x)$ whose vacuum values are equal to zero and a local gauge transformation by $\Lambda(x)$

$$\phi'(x) = e^{i\Lambda(x)}\phi(x), \quad A'_\alpha(x) = A_\alpha(x) - \frac{1}{g}\partial_\alpha\Lambda(x)\,, \tag{1.15}$$

through which the phase $\theta(x)$ becomes obsolete. Now, the Lagrangian of the real scalar field $\chi(x)$ and the real vector gauge field $A_\alpha(x)$ is given by

$$\begin{aligned}\mathcal{L} &= \frac{1}{2}\partial_\alpha\chi\partial^\alpha\chi + \frac{1}{2}g^2v^2A_\alpha A^\alpha - \mu^2\chi^2 \\ &\quad + \frac{1}{2}g^2(2v\chi+\chi^2)A_\alpha A^\alpha - \frac{\lambda}{4}(4v\chi^3+\chi^4) - \frac{1}{4}F_{\alpha\beta}F^{\alpha\beta}\,. \end{aligned} \tag{1.16}$$

Here, the first and last term can be recognized as the kinetic terms of the scalar and vector fields, the fourth and fifth terms are related to interactions of the fields, while the second

and third term express the mass terms of the vector and scalar fields. Those result from spontaneous symmetry breaking as well as from the covariant derivative and the potential. Because of this, the masses of the vector and scalar particles of the fields $A_\alpha(x)$ and $\chi(x)$ are given by

$$m_A = gv \quad \text{and} \quad m_\chi = \sqrt{2}\mu \,. \tag{1.17}$$

This mechanism that generates the mass of the vector field is called *Higgs mechanism* with the Higgs field $\phi(x)$.[22]

2. Massive Neutrinos

2.1. Neutrino oscillation and mass generation

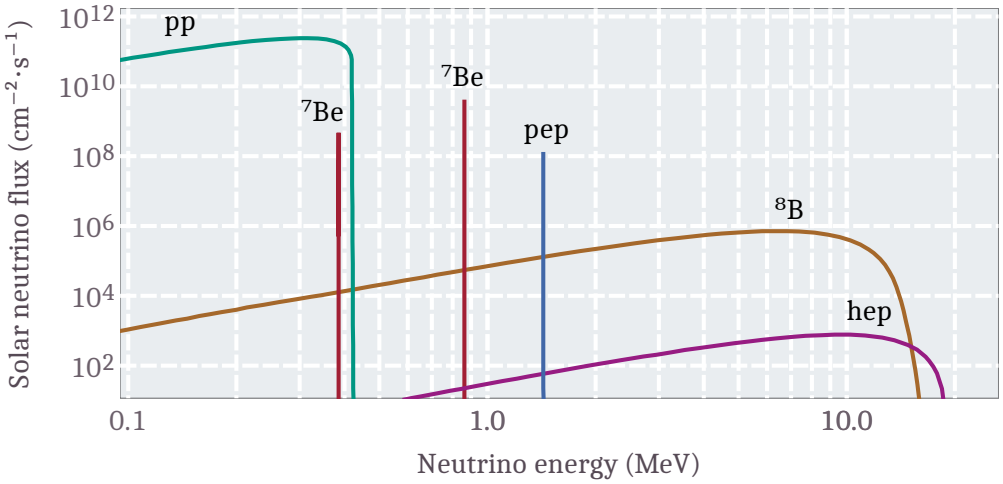

Figure 2.1.: Solar neutrino spectrum of pp-chain neutrinos. Flux is given in units of $\mathrm{cm}^{-2}\,\mathrm{s}^{-1}$ for the mono-energetic sources ^{7}Be and pep and in $\mathrm{cm}^{-2}\,\mathrm{s}^{-1}\,\mathrm{MeV}^{-1}$ for the continuum sources (pp, ^{8}B, hep), according to [26].

Solar neutrino problem

Due to the very small cross section of weak interactions of neutrinos, neutrinos are optimally suited for astronomical investigations, since they can not be electromagnetically deflected and thus pointing to their source. So are neutrinos from the sun. During fusion processes in the solar core, different reactions take place, releasing electron neutrinos. The reactions of the *pp cycle*

$$\begin{aligned}
\text{pp}: &\quad \mathrm{p} + \mathrm{p} &&\rightarrow \mathrm{D} + \mathrm{e}^+ + \nu_\mathrm{e} \\
\text{pep}: &\quad \mathrm{p} + \mathrm{e}^- + \mathrm{p} &&\rightarrow \mathrm{D} + \nu_\mathrm{e} \\
^7\text{Be}: &\quad ^7\mathrm{Be} + \mathrm{e}^- &&\rightarrow ^7\mathrm{Li} + \nu_\mathrm{e} \\
^8\text{B}: &\quad ^8\mathrm{B} &&\rightarrow ^8\mathrm{Be}^* + \mathrm{e}^+ + \nu_\mathrm{e} \\
\text{hep}: &\quad ^3\mathrm{He} + \mathrm{p} &&\rightarrow ^4\mathrm{He} + \mathrm{e}^+ + \nu_\mathrm{e}
\end{aligned} \tag{2.1}$$

lead to the neutrino energy spectrum displayed in fig. 2.1, where D is deuterium. Additionally, there exists a second chain which releases electron neutrinos in the sun - the

CNO cycle, whose contribution is estimated about 1%. Here, larger atoms such as carbon, nitrogen, and oxygen are involved in the fusion reactions.[22]

Although the SM theoretically describes interactions of all known particles very successfully, there was an unforeseen problem. During the time when the theory was established, the neutrino oscillation conjecture was made. Solar neutrino experiments measured a lower than expected electron neutrino flux from the sun by the pp-Chain and CNO cycle. First observed at the Homestake experiment [27] but consistent with other solar neutrino experiments such as Kamiokande-II [28]. Later, the discrepancy of the observed electron neutrino flux from the sun was confirmed by other experiments such as Super-Kamiokande [29] and the Sudbury Neutrino Observatory (SNO) [30]. Even before that, a deficit of atmospheric muon neutrinos was measured at Super-K [31], indicating the first observation of neutrino oscillation. Both Super-K and SNO use the same experimental principle by measuring Cherenkov radiation, which can be produced when neutrinos interact with matter such as in eq. 1.3 or by elastic scattering. High energy neutrinos result in high energy leptons within the detector material. Once these leptons are faster than the speed of light in the material, Cherenkov light is emitted. Super-K consists of a large water tank surrounded by photomultipliers for the light detection, while SNO uses heavy water (D_2O). The advantages of using heavy water are the observable reactions of neutrinos with heavy water

$$\begin{aligned} \text{CC}: &\quad \nu_e + D &&\rightarrow e^- + p + p - 1.44\ \text{MeV} \\ \text{NC}: &\quad \nu_\ell + D &&\rightarrow \nu_\ell + p + n - 2.23\ \text{MeV} \\ \text{ES}: &\quad \nu_\ell + e^- &&\rightarrow \nu_\ell + e^- \end{aligned} \tag{2.2}$$

where subscript ℓ represents any neutrino flavour $\ell = e, \mu, \tau$, see [32]. At Super-K only elastic scattering (ES) of neutrino on electrons was measured by Cherenkov light due to the recoil electron. Since the effective cross section for this reaction for ν_μ and ν_τ is significantly smaller than for ν_e, mainly the electron neutrino flux from the sun was measured [22, 29]. At SNO, charge current (CC) and neutral current (NC) reactions could additionally be resolved, whose energy thresholds are given in eq. 2.2. Therefore, all flavours were measured in their entirety and the electron neutrino reactions were measured on their own. Consequently, the total flux of all solar neutrinos was measured, which agreed with the expected total rate, in addition to confirming the absence of electron neutrinos.

In combination of the results of SNO and Super-K, the neutrino oscillation was discovered which was awarded with the Nobel Prize in 2015 [2]. From this it can be deduced that neutrinos have mass and are not massless, as originally assumed in the Standard Model. Extensions have to be made that include physics beyond the Standard Model.

Neutrino oscillation

Neutrino oscillation describes the probability that one neutrino flavour eigenstate $|\nu_\ell\rangle$ with $\ell = e, \mu, \tau$ can change its state to one of the remaining ones. This is only possible, if the flavour eigenstates $|\nu_\ell\rangle$ are connected to mass eigenstates $|\nu_i\rangle$ with $i = 1, 2, 3$ according to

$$|\nu_\ell\rangle = \sum_{i=1}^{3} U^*_{\ell i} |\nu_i\rangle = U^*_{\ell 1} |\nu_1\rangle + U^*_{\ell 2} |\nu_2\rangle + U^*_{\ell 3} |\nu_3\rangle \ . \tag{2.3}$$

U is the Pontecorvo-Maki-Nakagawa-Sakata (PMNS) [33] matrix which describes the mixing between the states.

$$
\begin{aligned}
U &= \begin{pmatrix} U_{e1} & U_{e2} & U_{e3} \\ U_{\mu 1} & U_{\mu 2} & U_{\mu 3} \\ U_{\tau 1} & U_{\tau 2} & U_{\tau 3} \end{pmatrix} \\
&= \begin{pmatrix} 1 & 0 & 0 \\ 0 & c_{23} & s_{23} \\ 0 & -s_{23} & c_{23} \end{pmatrix} \begin{pmatrix} c_{13} & 0 & s_{13}e^{-i\delta} \\ 0 & 1 & 0 \\ -s_{13}e^{i\delta} & 0 & c_{13} \end{pmatrix} \begin{pmatrix} c_{12} & s_{12} & 0 \\ -s_{12} & c_{12} & 0 \\ 0 & 0 & 1 \end{pmatrix} \begin{pmatrix} e^{\frac{i\alpha_1}{2}} & 0 & 0 \\ 0 & e^{\frac{i\alpha_2}{2}} & 0 \\ 0 & 0 & 1 \end{pmatrix},
\end{aligned} \tag{2.4}
$$

with $c_{ik} = \cos(\theta_{ik})$ and $s_{ik} = \sin(\theta_{ik})$. The parameters of the state mixing are the mixing angles θ_{12}, θ_{13}, and θ_{23}. Ancillary parameters which occur in the mixing matrix are the phases $\alpha_{1,2}$ and δ. The phase factors $\alpha_{1,2}$ demonstrate the possibility that neutrinos may be their own antiparticles. So the field $|\nu_\ell\rangle = \nu_\ell(x)$ can be either a Dirac field of neutrinos and antineutrinos or a Majorana field of neutrinos. The phase factor δ has a non-zero value if neutrino oscillation violates CP-symmetry.[22, 32]

The evolution in time of a neutrino flavour state $|\nu_\ell\rangle$ for $t \geq 0$ is given by

$$
|\nu_\ell\rangle_t = e^{-iHt} |\nu_\ell\rangle = \sum_{i=1}^{3} e^{-iE_i t} U^*_{\ell i} |\nu_i\rangle \ . \tag{2.5}
$$

In general the neutrino Energies E_i are different but in relation to the mass splitting of the mass eigenstates $|\nu_i\rangle$. Assume a mixed neutrino state, characterised by momentum $\vec{p}$ and masses m_i. This leads to $m_i^2/p^2 << 1$ and therefore,

$$
E_i \simeq p + \frac{m_i^2}{2p}, \ \text{ and } \ E_i - E_k \simeq \frac{\Delta m_{ik}^2}{2E} \ \text{ with } \ \Delta m_{ik}^2 = m_i^2 - m_k^2 \,, \tag{2.6}
$$

where $E \simeq p$ is the neutrino energy. For relativistic neutrinos, the time difference t between production and detection in eq. 2.5 can be approximated by $t \simeq L$, where L is the distance between production and detection. Hence, the transition probability can be expressed by the following

$$
P(\nu_{\alpha \to \beta}) = \sum_{i,k} U_{\beta i} U^*_{\beta k} U^*_{\alpha i} U_{\alpha k} e^{-i \frac{\Delta m_{ki}^2}{2E} L} \ . \tag{2.7}
$$

The appearance probability $1 - P(\nu_{\alpha \to \beta})$ of an travelling electron neutrino with energy $E_\nu = 18.6\,\text{keV}$ is shown in fig. 2.2. Here, the first minimum (circle) is directly related to the mixing parameters θ_{13} and Δm_{13}^2. The position of the minimum with respect to the travel distance is related to the mass splitting $\Delta m_{13}^2/E$, while the depth of the minimum depends on the mixing angle $\sin(2\theta_{13})$. Similarly, the position of the global minimum (square) depends on $\Delta m_{12}^2/E$, while the depth depends on $\sin(2\theta_{12})$. [22, 32]

Several experiments aim for measuring the mixing parameters which are either solar neutrino, atmospheric, reactor or accelerator-based neutrino experiments. The mixing can be investigated by appearance or disappearance of specific neutrino flavours depending on the distance to the source and the energy at the origin of the neutrinos as shown in eq. 2.7

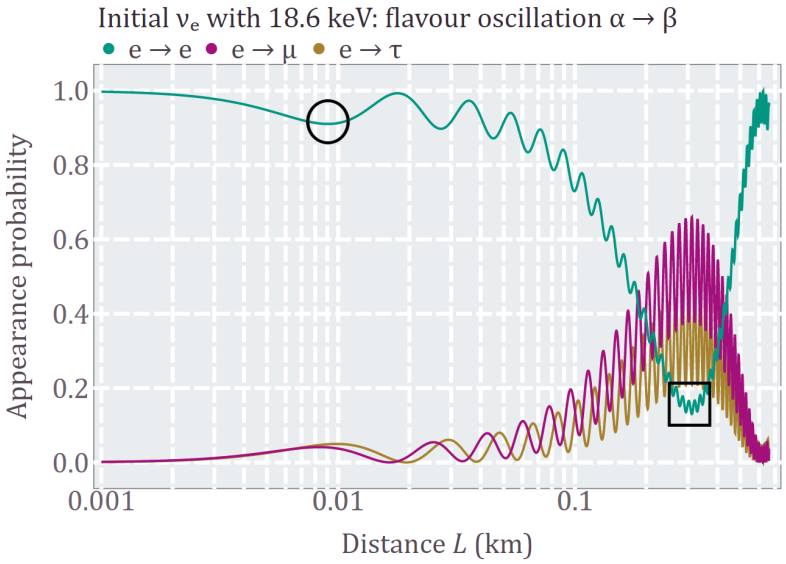

Figure 2.2.: Probability of appearance of an oscillating electron neutrino with energy $E_\nu = 18.6\,\text{keV}$. Two essential sections are shown: ◯: position and depth of the first local minimum and □: position and depth of the global minimum, which depend on the mixing parameters θ_{13}, Δm^2_{13}, θ_{23}, and Δm^2_{23} in the case of an initial electron neutrino. The values for normal ordering (NO) are used which are given in eq. 2.8.

and fig. 2.2. To be mentioned here are the experiments T2K [34], Daya-Bay [35], RENO [36], Double-Chooz [37], KamLAND [38], NOvA [39], SNO [40], and Super-Kamiokande [41] which significantly contribute to the current values and limits on the mixing parameters. The NuFit group [42] takes the available data into account to perform global fits on all mixing parameters, their results [43] are the following

$$
\begin{aligned}
\sin^2(\theta_{12}) &= 0.304^{+0.012}_{-0.012} && \text{(NO \& IO)} \\
\sin^2(\theta_{23}) &= 0.450^{+0.019}_{-0.016} && \text{(NO)} \\
\sin^2(\theta_{23}) &= 0.570^{+0.016}_{-0.022} && \text{(IO)} \\
\sin^2(\theta_{13}) &= 2.246^{+0.062}_{-0.062} \cdot 10^{-2} && \text{(NO)} \\
\sin^2(\theta_{13}) &= 2.241^{+0.074}_{-0.062} \cdot 10^{-2} && \text{(IO)} \\
\delta_{\text{CP}} &= 230^{+36\,\circ}_{-25} = 1.28^{+0.20}_{-0.14} \cdot \pi && \text{(NO)} \\
\delta_{\text{CP}} &= 278^{+22\,\circ}_{-30} = 1.54^{+0.12}_{-0.17} \cdot \pi && \text{(IO)} \\
\Delta m^2_{21} &= 7.42^{+0.21}_{-0.20} \cdot 10^{-5}\ \text{eV}^2 && \text{(NO \& IO)} \\
\Delta m^2_{3l} &= +2.510^{+0.027}_{-0.027} \cdot 10^{-3}\ \text{eV}^2 && \text{(NO)} \\
\Delta m^2_{3l} &= -2.490^{+0.026}_{-0.028} \cdot 10^{-3}\ \text{eV}^2 && \text{(IO)}
\end{aligned}
\tag{2.8}
$$

where NO denotes normal mass ordering and IO the inverted ordering. Here, $\Delta m^2_{3l} = \Delta m^2_{31} > 0$ for NO and $\Delta m^2_{3l} = \Delta m^2_{32} < 0$ for IO. Since only the difference on squared masses

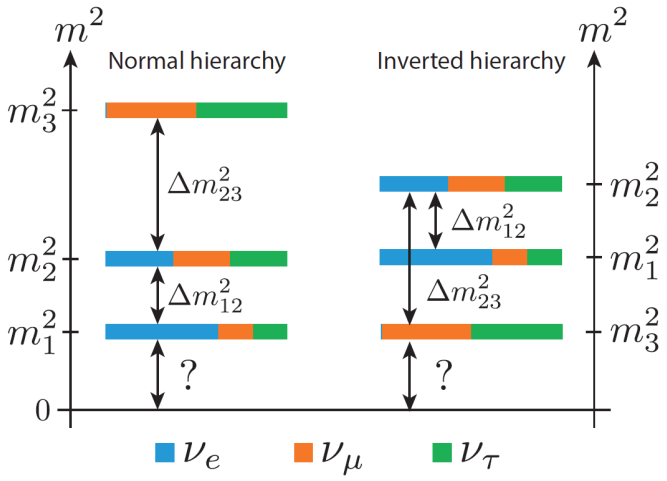

Figure 2.3.: Mass ordering of the neutrino masses m_i^2 for the normal and inverted ordering. **Normal ordering (NO):** $m_1 < m_2 << m_3$, so that ν_1 is the lightest mass eigenstate, while it is ν_3 for the **Inverted ordering (IO):** $m_3 << m1 < m2$. Moreover, the global mass scale of the neutrinos is not known; only upper limits can be determined. The three colours of the individual mass eigenstates indicate their flavour content [45].

can be observed in experiments, the hierarchy of the mass eigenstates is not definite. Merely the sign of Δm_{21}^2 could be measured for solar neutrinos due to the MSW effect [44], an effect that changes the oscillation condition for neutrinos within dense matter such as the solar core. Therefore, different order of the masses are possible, as shown in fig. 2.3. The global fit of the NuFit group [42] favours normal mass ordering, but inverted ordering is only disfavoured on a low significance level, leaving the neutrino mass order question open [43].

Neutrino mass generation

It is now clear that neutrinos have mass, which is why the generation of these masses must be defined within the framework of the Standard Model of particle physics. Originally, only massless right-handed (left-handed) neutrinos (antineutrinos) were described as discussed in section 1.2. Two possibilities arise for the generation of the masses of neutrinos: on the one hand, an inclusion of right-handed neutrinos (left-handed antineutrinos) as analogy to the other fermions. This allows to derive a Dirac neutrino mass term with Yukawa coupling to the Higgs field. However, the large mass differences between neutrinos and charged leptons must be explained by a very weak Yukawa coupling to the Higgs field, which is not preferred. Therefore, the second formulation on the other hand, deals with considering neutrinos as Majorana particles, i.e. neutrinos are their own antiparticle. Additionally, the generalised approach here is the combination of Dirac and Majorana mass terms, which will be outlined in the following, based on the references [22, 32].

The standard Dirac mass term of Dirac particles of the Lagrangian reads

$$\mathcal{L}_M = m_D \bar{\psi} \psi \ . \tag{2.9}$$

Here, ψ is a four-component Dirac spinor, which can be also expressed using two-components Weyl spinors ψ_L and ψ_R

$$\mathcal{L}_M = m_D(\bar{\psi}_L\psi_R + \bar{\psi}_R\psi_L)\,, \tag{2.10}$$

where m_D is the Dirac mass of the particle, L and R denotes the chirality. In special relativity, the four-component Dirac spinor field ψ in a Lagrangian $\mathcal{L}$ must be Lorentz-invariant and Hermitian, which is fullfilled for the most general case of

$$2\mathcal{L} = m_D(\bar{\psi}_L\psi_R + \bar{\psi}^c_L\psi^c_R) + m_L\bar{\psi}_L\psi^c_R + m_R\bar{\psi}^c_L\psi_R + h.c.\,, \tag{2.11}$$

where, $\bar{\psi} = \psi^\dagger\gamma_0$ the Dirac adjoint of the spinor ψ and ψ^c the charge conjugate of ψ. This can be simplified to

$$2\mathcal{L} = (\bar{\psi}_L, \psi^c_R)\cdot\underbrace{\begin{pmatrix} m_L & m_D \\ m_D & m_R \end{pmatrix}}_{M}\cdot\begin{pmatrix}\psi^c_R \\ \psi_R\end{pmatrix} + h.c.\,. \tag{2.12}$$

By introduction of an arbitrary mixing angle ϑ defined by

$$\tan(2\vartheta) = \frac{2m_D}{m_R - m_L}\,, \tag{2.13}$$

two independent Majorana fields $\chi_{1,2}$ can be formulated

$$\chi_1 = \cos\vartheta\cdot(\psi_L + \varepsilon_1\psi^c_R) - \sin\vartheta\cdot(\psi^c_L + \varepsilon_1\psi_R) \tag{2.14}$$

$$\chi_2 = \sin\vartheta\cdot(\psi_L + \varepsilon_2\psi^c_R) + \cos\vartheta\cdot(\psi^c_L + \varepsilon_2\psi_R)\,, \tag{2.15}$$

with $\varepsilon_i = \pm 1$, corresponding to the CP-eigenvalue of the Majorana field χ_i with $\chi^c_i = \varepsilon_i\chi_i$. The Lagrangian becomes

$$2\mathcal{L} = m_1\bar{\chi}_1\chi_1 + m_2\bar{\chi}_2\chi_2\,, \tag{2.16}$$

where the diagonalised matrix of M of eq. 2.12 was used with its eigenvalues

$$m_i = \frac{1}{2\varepsilon_i}\left[(m_L + m_R) \pm \sqrt{(m_L - m_R)^2 + 4m_D^2}\right]\,, \tag{2.17}$$

so that $m_i \geq 0$ by choosing ε_i accordingly [8]. From this general formulation the pure Dirac case with $m_L = m_R = 0$ can be derived as well as a pure Majorana case for $m_D = 0$ as well as the combined case, which is known as the See-saw case [46, 47]. The See-saw mechanism gives neutrinos their mass by the small mixing to the large Majorana mass which is related to a right-handed neutrino which does not interact due to its chirality - the sterile neutrino. In this model the left-handed Majorana mass $m_L = 0$ so that

$$M = \begin{pmatrix} 0 & m_D \\ m_D & m_R \end{pmatrix}\,, \tag{2.18}$$

which results to the individual masses with $m_R >> m_D$ to

$$m_1 = \frac{m_D^2}{m_R} \quad\text{and}\quad m_2 = m_R\left(1 + \frac{m_D^2}{m_R^2}\right) \approx m_R\,. \tag{2.19}$$

In this scenario, χ_1 can be interpreted as the light active neutrino mass eigenstate with ψ_L and ψ_R^c, which interacts via weak interaction. Whereas χ_2 represents a heavy sterile neutrino, which does not interact with gauge bosons of the SM. The large mass differences of neutrinos with respect to the other charged leptons arises from the small coupling with $\vartheta \approx 0°$ to the large Majorana mass m_R which can be on the order of GeV. [22, 32]

2.2. Measurements of the neutrino mass

2.2.1. Model-dependent limits from cosmology and experiments

Cosmological limits on the neutrino mass

Cosmological observations and their embedding in a model have been the subject of current research for many decades. With these high-precision data, strong limits can also be set for the neutrino masses. These bounds on cosmological data as well as other experimental approaches, regarding the neutrino mass which base either on model assumptions for the measurement, or on model assumptions on the underlying physics, are model-dependent. The extracted neutrino masses are not necessarily correct if the model is missing information. Nevertheless, many investigations in agreement with the Standard Model of Cosmology (ΛCDM) lead to certain small neutrino masses, which are compatible with the later described results of model-independent measurements. Within the ΛCDM model, our universe consists of dark energy, cold dark matter (CDM) and (baryonic) matter, to which neutrinos contribute because they have mass. Neutrinos are called hot dark matter because their weak interaction properties make them almost invisible, but hot because they travel almost at the speed of light. Noteworthy investigations of our universe are the measurements regarding the cosmic microwave background (CMB) - an omnipresent photon signal that pervades the entire universe in most abundance. The latest data were taken with the Planck space telescope from 2009 to 2013 [48]. In combination with the full-shape data of the Baryonic Oscillation Spectroscopic Survey (BOSS) a limit on the total neutrino mass (at 95% C.L.) to

$$\begin{aligned} M_{\text{tot}} &< 0.18\,\text{eV/c}^2 && \text{(NO)} \\ M_{\text{tot}} &< 0.21\,\text{eV/c}^2 && \text{(IO)}\,, \end{aligned} \tag{2.20}$$

is derived for the two cases of inverted and normal ordering as described beforehand [6]. Additionally, other experiments or observation can be taken into account, such as data from the Hubble space telescope [49], the WiggleZ Dark energy survey [50] which lead to neutrino mass bounds in the same region below 200 meV/c^2 [51]. A stand-alone method to extract upper bounds on neutrino masses was made by the detection of the time-of-flight of supernova neutrinos from the famous supernova SN1987A which were observed by different underground detectors, e.g. Kamiokande-II [52]. From these data, an upper bound of $m_\nu < 5.7\,\text{eV/c}^2$ was derived by Lamb & Loredo using Bayesian analysis techniques [53]. However, many model assumptions had to be made about individual processes that take place when supernovae explode.

Neutrinoless double beta decay

Double beta decay is the simultaneous β-decay of two nucleons within one atomic nucleus, according

$$2\nu\beta^+\beta^+ : \ {}^{A}_{Z}X \rightarrow {}^{A}_{Z-2}Y + 2e^+ + 2\nu_e$$
$$2\nu\beta^-\beta^- : \ {}^{A}_{Z}X \rightarrow {}^{A}_{Z+2}Y + 2e^- + 2\overline{\nu}_e \, ,$$

with Z the proton number and A the nucleon number. The first discovery was made with the isotope ^{82}Se as $2\nu\beta^-\beta^-$-decay [54]. There exist 35 naturally occurring isotopes that decay via double beta decay [55], while eleven have been observed in experiments [15]. Additionally, another second order decay process is double electron capture ($\epsilon\epsilon$) which was found for three isotopes, latest for ^{124}Xe at the XENON1T experiment [56]. Such processes are rare since double beta decay is a second-order process that leads to very long half-lives on the order of 10^{23} years, although it is energetically favourable for atoms to decay by double beta decay, as shown in fig. 2.4a.

However, a special case of double beta decay is the neutrinoless double beta decay ($0\nu\beta\beta$), where no neutrino is generated, see fig. 2.4b. This occurs if neutrinos are their own antiparticle, i.e. Majorana particles, as described in section 2.1. Here, the Majorana neutrino is a mediator particle that is emitted and absorbed within the nucleus. Therefore,

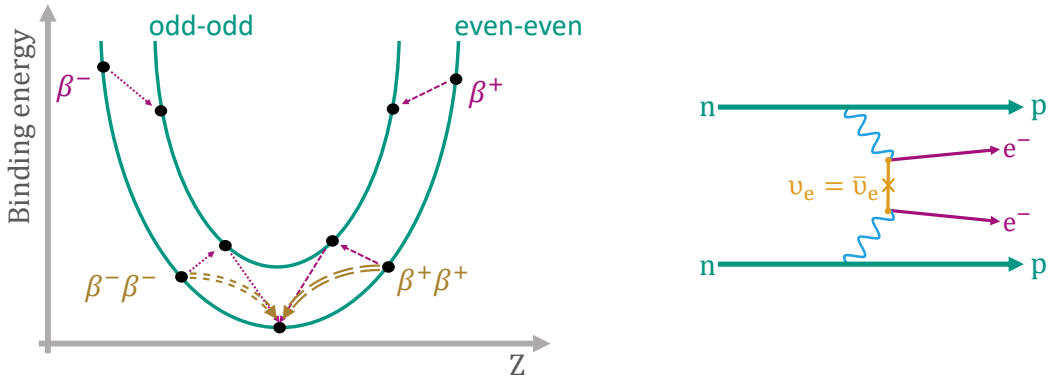

(a) Binding energy diagram. **(b)** Feynman diagram of $0\nu\beta\beta$ decay.

Figure 2.4.: (a): Outline of the binding energy (mass) diagram of atoms as a function of their proton number Z, using the Bethe-Weizsäcker formula. Dotted arrows indicate β^--decay, dashed arrow β^+-decay and doubled arrows double beta decays. Upward pointing arrows indicate forbidden decays. Only energetically more favourable decay channels are allowed - decreasing binding energy. Odd-odd and even-even is related to the proton and nucleon numbers A and Z, which are either both odd or even numbers. **(b):** Feynman diagram of the $0\nu\beta^-\beta^-$-decay. If neutrinos are Majorana particles the interacting neutrinos ν_i are their own antiparticle and therefore act as mediator particle in this process.

the emitted electrons (positrons) for a $0\nu\beta^-\beta^-$ ($0\nu\beta^+\beta^+$) decay share the full energy of the decay which leads to a peak in the beta electrons spectrum above the continuous $2\nu\beta\beta$-spectrum. Hence the measurement of $0\nu\beta\beta$-spectra allows the determination of the effective Majorana neutrino mass

$$|m_{\beta\beta}| = \frac{m_e^2}{G^{0\nu\beta\beta}\left|\mathcal{M}^{0\nu\beta\beta}\right|^2 T_{1/2}^{0\nu\beta\beta}} = \left|\sum_{i=1}^{3} U_{ei}^2 m_i\right| . \tag{2.21}$$

The observable depends on the phase space factor $G^{0\nu\beta\beta}$, the nuclear transition matrix element $\mathcal{M}^{0\nu\beta\beta}$ as a function of the half-life of the decay. It represents the coherent sum of the mass eigenstates. Search for neutrinoless double beta decay evolved to a large field of research in neutrino physics. Since many atoms are favoured to investigate, many experiments exist. Best limits are achieved at searches with ^{76}Ge [7, 57], ^{136}Xe [58, 59] and ^{100}Mo [60]. While the best limits of combined analysis on the Majorana neutrino mass of their data is achieved by GERDA [7] and KamLAND-Zen [59]

$$\text{GERDA}: \quad |m_{\beta\beta}| < 70\,\text{meV/c}^2 \text{ to } 160\,\text{meV/c}^2 \quad (^{76}\text{Ge}) \tag{2.22}$$

$$\text{KamLAND}-\text{Zen}: \quad |m_{\beta\beta}| < 61\,\text{meV/c}^2 \text{ to } 165\,\text{meV/c}^2 \quad (^{136}\text{Xe})\ . \tag{2.23}$$

As introduced in section 2.1 eq. 2.4 the mixing matrix U holds two additional phases in the case of Majorana neutrinos. As a result, the contributions from the mass eigenstates m_i can cancel out, reducing or even vanishing the effective Majorana neutrino mass $|m_{\beta\beta}|$. Consequently, only direct measurements are feasible for measurements of the neutrino mass since the observable at $0\nu\beta\beta$-decays is not directly comparable to the absolute neutrino mass. Model assumptions have to be made for the additional phases as well as the nuclear matrix element $\mathcal{M}$.

2.2.2. Direct neutrino mass determination

Model-independent approaches, i.e. direct neutrino mass measurements, focus on the evaluation of the kinetic energy spectrum of electrons that result from β^--decays. The endpoints E_0 of β^--decay spectra are the maximal kinetic energy an emitted electron can have. This is directly related to the decay energy Q which corresponds to the mass difference between the mother and daughter atom, see eq. 1.1. For massive neutrinos, $E_0 < Q$ applies, since the rest mass of the neutrino can not be transferred as kinetic energy to the electron. The shape of the differential β-spectrum

$$\frac{d\Gamma}{dE} = \frac{G_F^2 \cos^2(\theta_C)}{2\pi^3} |\mathcal{M}|^2 F(Z,E) p(E+m_e) \cdot \sum_{i=1}^{3} |U_{ei}|^2 \epsilon \sqrt{\epsilon^2 - m_i^2}\,\Theta(\epsilon - m_i) \tag{2.24}$$

is based on Fermi's golden rule. It contains the Fermi function $F(Z,E)$, the Fermi coupling constant G_F, the Cabbibo angle θ_C that describes the coupling of u and d quarks, the nuclear transition matrix element $\mathcal{M}$, and $\epsilon = E_0 - E$ the difference between the endpoint and the kinetic energy E. Energy conservation is full-filled through the Heaviside step

function Θ. Assuming quasi-degenerate neutrino masses, the measurement observable from β-decay experiments is the incoherent sum of the mass eigenstates

$$m_\nu^2 = \sum_{i=1}^{3} |U_{ei}|^2 \, m_i^2 \,, \tag{2.25}$$

which is the squared effective electron neutrino mass. [61]

For experimental reasons, it is mandatory to use β-emitters that have low endpoints. On the one hand, high endpoints lead to an even lower count rate in the sensitive endpoint region where the neutrino mass imprint is greatest. On the other hand, low endpoints lead to less energetic electrons that can be measured spectroscopically. In addition, their half-life must be short and their availability high enough that significant count rates can be achieved. Most suitable candidates are the elements tritium, rhenium and holmium, which are used in recent experiments. Holmium (^{163}Ho) and rhenium (^{187}Re) have the lowest endpoints, while holmium decays not by β-decay but by electron capture (ϵ). Their decay scheme reads as the following

$$\mathrm{e}^- + {}^{163}\mathrm{Ho} \rightarrow {}^{163}\mathrm{Dy} + \nu_\mathrm{e} \,, \qquad Q = 2.83\ \mathrm{keV} \tag{2.26}$$

$$ {}^{187}\mathrm{Re} \rightarrow {}^{187}\mathrm{Os} + \mathrm{e}^- + \overline{\nu}_\mathrm{e} \,, \qquad Q = 2.47\ \mathrm{keV} \ . \tag{2.27}$$

Holmium is used at the ECHo [62] and Holmes [63] experiments, which were not able to set a competitive limit on the neutrino mass. However, an upper limit on the neutrino mass of $m_\nu < 15\,\mathrm{eV/c^2}$ (90% C.L.) was achieved at the MIBETA experiment [64] by measuring the β-spectrum of rhenium with cryogenic microcalorimeters [65]. Both elements hold the disadvantage of very long half-lives of $4570(25)\ y$ for ^{163}Ho [5] and $4.12(11) \times 10^{10}\ y$ for ^{187}Re [66]. Therefore, large amounts of these rare elements are required.

The best limits for neutrino mass are obtained by spectroscopic measurement of the beta electrons produced at decays of tritium (^{3}H or T)

$${}^3\mathrm{H} \rightarrow {}^3\mathrm{He}^+ + \mathrm{e}^- + \overline{\nu}_\mathrm{e} \,. \tag{2.28}$$

The current upper limit on the effective neutrino mass is

$$m_\nu < 0.8\,\mathrm{eV/c^2}\ (90\%\ \mathrm{C.L.}) \,, \tag{2.29}$$

achieved at the KATRIN experiment, using a gaseous source of molecular tritium (T_2) [4]. Using tritium is beneficial for several reasons: Tritium has a medium half-life of $12.32(2)\ y$ [67] and a low endpoint of $E_0 = 18.57\,\mathrm{keV}$ [4]. Since tritium is a hydrogen-like atom, only one outer electron is present which vanishes Coulomb interaction within the atomic hull and additionally inelastic scattering of the beta electrons with source gas is diminished. Beta decay of tritium eq. 2.28 is a super-allowed decay with the transition $J = 1/2 \rightarrow J = 1/2$ through which the nuclear transition matrix element $\mathcal{M}$ (see. eq. 2.24) becomes energy-independent. In general, using gases as source eliminates energy losses due to solid-state effects.

However, a molecular source leads to systematics of the final states of the residual molecule, e.g. electronic or rotational excitation in the eV-range. To achieve ultimate

sensitivity on the effective neutrino mass using tritium, an atomic source is needed to avoid molecular systematic effects in future experiments. One way of using atomic tritium in cold traps as a source is currently being developed as part of Project 8, which aims to measure the energy of electrons by cyclotron radiation emission spectroscopy - a novel spectroscopy technique. In the scope of the experiment a neutrino mass sensitivity down to 40 meV/c^2 can be achieved. [68]

Part II.

The Karlsruhe Tritium Neutrino Experiment

3. Design and operation

3.1. Main components of the KATRIN experiment

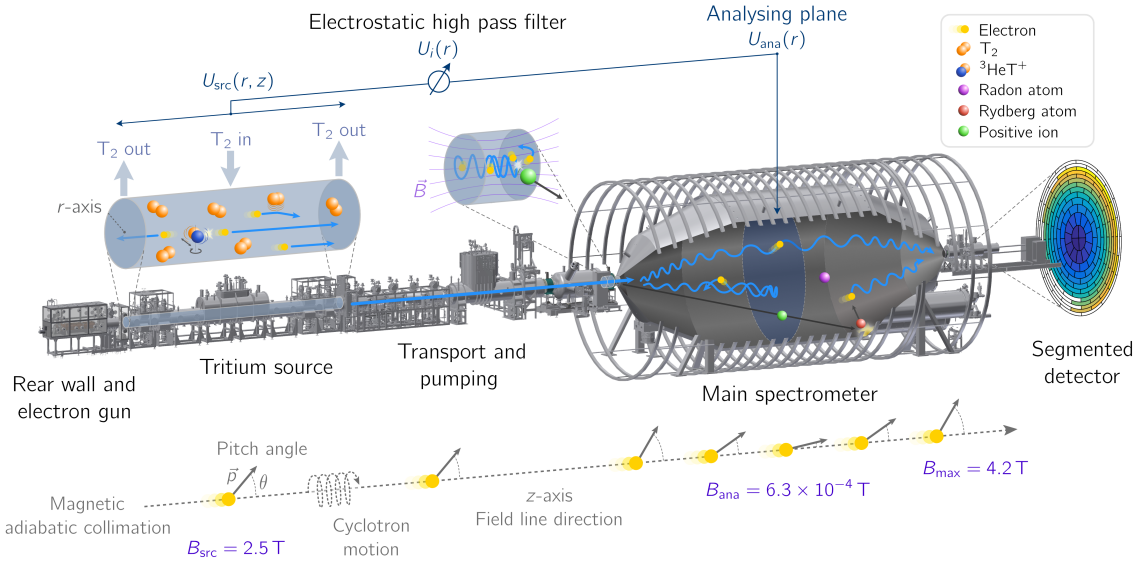

Figure 3.1.: Overview of the KATRIN beamline which consists of five main sections: the rear wall with electron gun, the tritium source, the transport and pumping section, the pre- and main spectrometer, and the detector. Figure kindly provided by L. Köllenberger.

The following sub-chapters of the technical description of the KATRIN experiment are based on the updated technical design report from 2021, which is the as-built documentation, see ref. [3], if not referred differently. The description contains the individual main components of the KATRIN beamline (see fig. 3.1), starting with the Windowless Gaseous Tritium Source (WGTS), followed by transport and pumping section composed of the Differential Pumping (DPS) and Cryogenic Pumping Section (CPS). Further on with monitoring devices such as the rear wall, e-gun and additional systems which observe the tritium source. Subsequently, the description of the spectrometers, which act as a high-pass filter for electrons after the MAC-E (Magnetic Adiabatic Collimation with Electrostatic) filter principle and the segmented Focal Plane Detector (FPD). Beta electrons generated within the source are guided magnetically by superconducting magnets into the main spectrometer, where their energy is resolved by a counteracting electric potential. If the energy of an electron exceeds the potential, the electron is transmitted to the detector. The application of this technique leads to the measurement of the integrative beta spectrum of tritium beta electrons.

3.1.1. Windowless gaseous tritium source

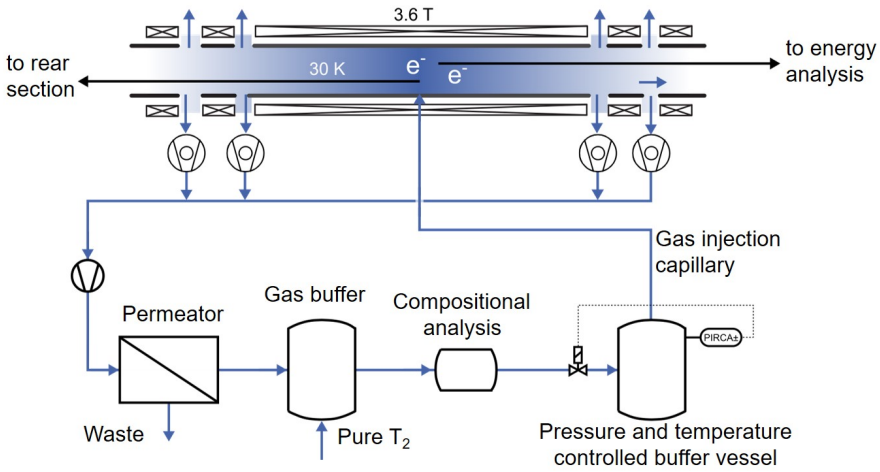

Figure 3.2.: Schematic of the inner loop of tritium gas circulation at the WGTS. Tritium is continuously injected at the center and pumped at both ends. The blue shading outlines the gas density profile within the 10 m long beamline with an diameter of 9 cm [3].

In the KATRIN experiment a gaseous tritium source is used with an activity of up to 10^{11} Bq. This gas is introduced into the beamline at the center of the windowless gaseous tritium source (WGTS). Pumps on both ends reduce the gas density so that electrons can pass to the rear section or the spectrometer, where their energy is analysed. The pumped gas will be cleaned at the permeator to guarantee that tritium (T_2) of high purity can be re-injected. In the Tritium Laboratory Karlsruhe (TLK), there are further loop systems in which the analysis of the gas composition and the purification of the circulating gas takes place so the purity of tritium is kept above 95 %. The relative concentration of individual gas species, such as T_2, DT, and HT, is monitored by Laser-Raman-Spectroscopy (LARA) before the injection capillary (D = deuterium and H = hydrogen). The tritium throughput through the WGTS and inner loops is about 40 g/day during measurement phases. The beamline is surrounded by superconducting magnets with maximum field strengths of 3.6 T. In addition, the beamline is kept at cold temperatures of 30 K to obtain stable measurement conditions in terms of pressure stability with a high number of molecules in the source and of high tritium purity. This is also advantageous for minimising Doppler broadening if the decaying molecules are slow [69]. The amount of molecules to provide the high activity of beta decays is described by the integrated particle density $\rho_0 d = 5 \times 10^{17} \mathrm{cm}^{-2}$ along the WGTS beam tube of length d, which is called column density. The stability of the source is crucial for reaching the sensitivity goal of KATRIN which is required to be less than $0.1\%/\mathrm{h}$. The latest results were achieved with a column density of $(4.23 \pm 0.01) \times 10^{17} \mathrm{cm}^{-2}$ at a very stable temperature of 30.065 ± 0.001 K, while the tritium (T_2) concentration was kept high at $97.3 \pm 0.5\%$ which results in an activity of 9.5×10^{10} Bq [4].

3.1.2. Differential and cryogenic pumping section

On their way to the detector, the electrons are guided through the DPS (fig. 3.3a) and CPS (fig.3.3b). Both make use of the charge of the electrons as they can be magnetically guided through these two chicanes. This improves the pumping efficiency at the bend points to further reduce the residual gas density. No tritiated molecules should enter the spectrometers, as they would cause background events there after decay and violate the radiation protection requirements. Since ions that are constantly generated by beta decays are guided as well, three electric dipole coils are installed to block and remove these low energetic positive ions in electrostatic traps via $E \times B$ drifts. The reduction factor of residual gas in the DPS is about 4×10^3 measured with 1% DT in D_2. Combination of the pumping efficiency of the DPS with the WGTS leads to a reduction of pure tritium by a factor of $(9.6 \pm 1.0) \times 10^7$ at nominal column density. Additional seven orders of magnitude reduction of flow rate have to be achieved at the CPS which cannot be further reduced by TMPs due to back-diffusion.

The main part of the gold-plated CPS beam tube acts as a cold trap that is operated at a temperature of 3 K. This low temperature is obtained by a large liquid helium (LHe) reservoir vessel at 4.5 K and the smaller 3-K vessel which is pumped to a pressure of 0.3 bar to establish the low temperature of 3 K inside. To fulfill the reduction requirements a cryo-sorption pump is the method of choice. The pumping medium is a layer of condensed argon gas on the surface of the cold beam tube which is further enlarged by fins, see fig. 3.3b. This argon frost layer provides a large absorption ability and therefore pumping capacity. As the condensed argon provides a large cold area, tritium molecules stick to

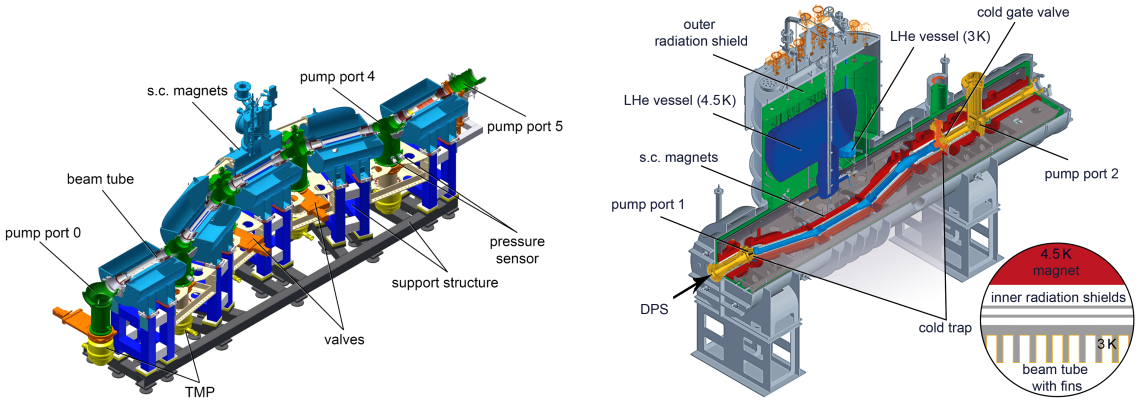

(a) DPS. **(b)** CPS.

Figure 3.3.: (a): The Differential Pumping Section (DPS) is located next to the WGTS downstream to the spectrometer. It consists of five superconducting magnets (light blue) arranged in a chicane and six pump ports, where turbo-molecular pumps (TMPs) (yellow) are located. **(b):** The Cryogenic Pumping Section (CPS) is also a chicane with superconducting magnets (red) but with additionally cooling down to 3 K which act as a cold trap (light blue) for residual tritiated molecules. The magnets as well as the cold trap are supplied with LHe from a large vessel (dark blue) [3].

it with an estimated sticking coefficient of $\alpha = 0.7$ that provides the necessary pumping efficiency. Subsequent desorption after adsorption of the tritium molecules is temperature-dependent for which reason the beam tube is kept at 3 K so the mean sojourn time is as large as possible. Flow simulations and measurements revealed that the reduction factor of the CPS is four orders of magnitude higher than its requirement, wherefore the total reduction of the tritium flow rate from the WGTS to the spectrometers is larger than 2×10^{19}, well above the design demands [69, 70].

3.1.3. Monitoring Devices

In the KATRIN experiment, numerous monitoring devices are in operation, some of which will be explained in more detail below. Starting at the rear section, where the Rear Wall (RW) is located. As tritium decays (see eq. 2.28) ions as well as electrons are produced. Furthermore, electrons can scatter with the source gas, producing additional ions. Thus, in the WGTS of the KATRIN experiment, a plasma is created that can be described by an effective potential. This plasma potential is monitored and influenced by the large gold-coated stainless steel plate - the Rear Wall. By application of a bias voltage to the RW, the plasma potential can be directly influenced and the voltage of best coupling extracted which is needed for understanding the resulting beta spectrum since the plasma potential influences the final kinetic energy of beta electrons and therefore the neutrino mass signal. Behind the RW an electron gun is mounted which can be used to measure the column density. It provides high electron rates with a narrow energy width and fine pitch angle selectivity. The e-gun is coupled to the main spectrometer high voltage and produced electrons can be generated with different surplus energies to overcome the retarding

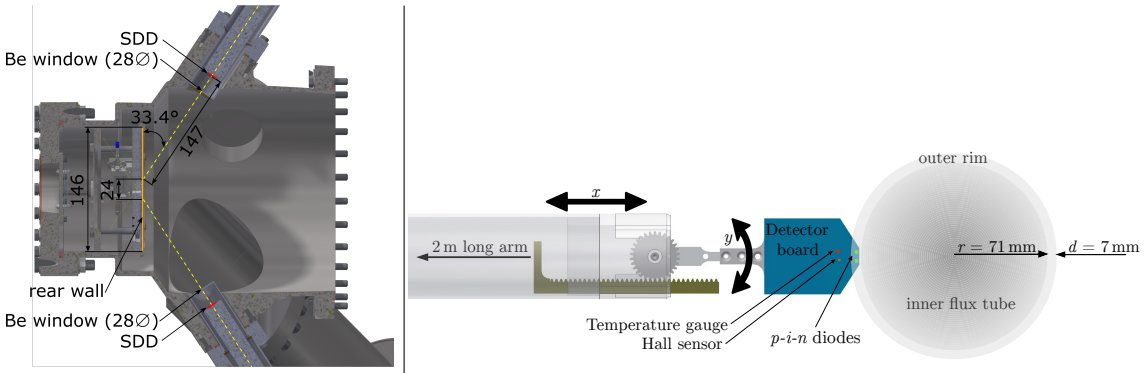

(a) BIXS. **(b)** FBM.

Figure 3.4.: (a): β-Induced X-ray Spectroscopy (BIXS) system at the RW chamber. The silicon drift detector (SDDs) have a direct line of sight onto the RW surface, where X-ray emission takes place for adsorption on β-electrons in gold. The detectors are shielded by beryllium (Be) window to prevent tritium contamination of the detectors. **(b):** The Forward Beam Monitor (FBM) is located at pump port 2 at the CPS, compare fig. 3.3b. It continuously measures the relative intensity of the β-electron flux towards the main spectrometer on the outer edge of the flux tube [3].

potential. Investigations regarding angular selective dependencies of electrons within the KATRIN beamline can be performed as well as scattering through the source gas and transmission conditions which are of high relevance for the analysis [71].

Two detector systems are installed. At the RW two silicon drift detectors are mounted to monitor the source activity in the WGTS by measuring X-ray radiation, produced at absorption processes of β-electrons in the gold coating of the RW. This is system is called BIXS (β-Induced X-ray Spectroscopy). The detectors are shielded from the source by beryllium windows, so no tritium contamination can take place, which can be seen in fig. 3.4a. The second detector system is located in the CPS beamtube. The Forward Beam Monitor (FBM), which is also a silicon drift detector, is used to monitor the relative intensity of the electron flux towards the main spectrometer and detector. It is possible to move the FBM across the whole flux tube within the beam tube to measure the spatial distribution of resulting β-electrons before energy selection takes place at the main spectrometer. During neutrino mass measurements, it is located at the outer edge of the sensitive flux tube so as not to shadow relevant pixels on the focal plane detector and still monitor the relevant quantity, as shown in fig. 3.4b.

Also ions which are guided magnetically to the spectrometer are monitored. Resulting positive ions are guided to the spectrometers which are measured at the pre-spectrometer. Inside the pre-spectrometer large cone electrodes are installed for fine-tune the electric field inside. To decelerate electrons negative potentials are necessary which act attractive to positive ions. These ions will hit the downstream cone electrode and produce electrons so a current can be measured with an ammeter. There are safety triggers used if the measured current exceeds a certain value of 5 pA, which corresponds to a rate of $3 \times 10^7 \,\mathrm{ions/s}$, the connection between the source section and the spectrometers is then closed due to possible tritium contamination [72].

In addition to these source-related monitors many others are installed such as pressure sensors, magnetometers which are distributed over the entire beamline, especially surrounding the main spectrometer. The retarding potential at the main spectrometer is determined, using unique high-voltage-dividers of ppm-precision with 8.5-digit precision digital voltmeters. The stability and reproducibility of the high-voltage system is of key importance, as this quantity determines the absolute energy with which the electrons are filtered.

3.1.4. The KATRIN spectrometers and detector

There are two spectrometers at KATRIN: the pre-spectrometer (PS) and the main spectrometer (MS). These are essential for resolving the kinetic energy of the beta electrons that arrive at the detector and used as MAC-E filters (magnetic adiabatic collimation with electrostatic). The basic principle of MAC-E filters is shown in fig. 3.5. A key feature is the adiabatic electron transport with full energy conservation. The momenta of beta electrons generated in the source are isotropically distributed, which is unfavourable for an energy measurement. Thus, the magnetic gradient force can be used to transform their transverse

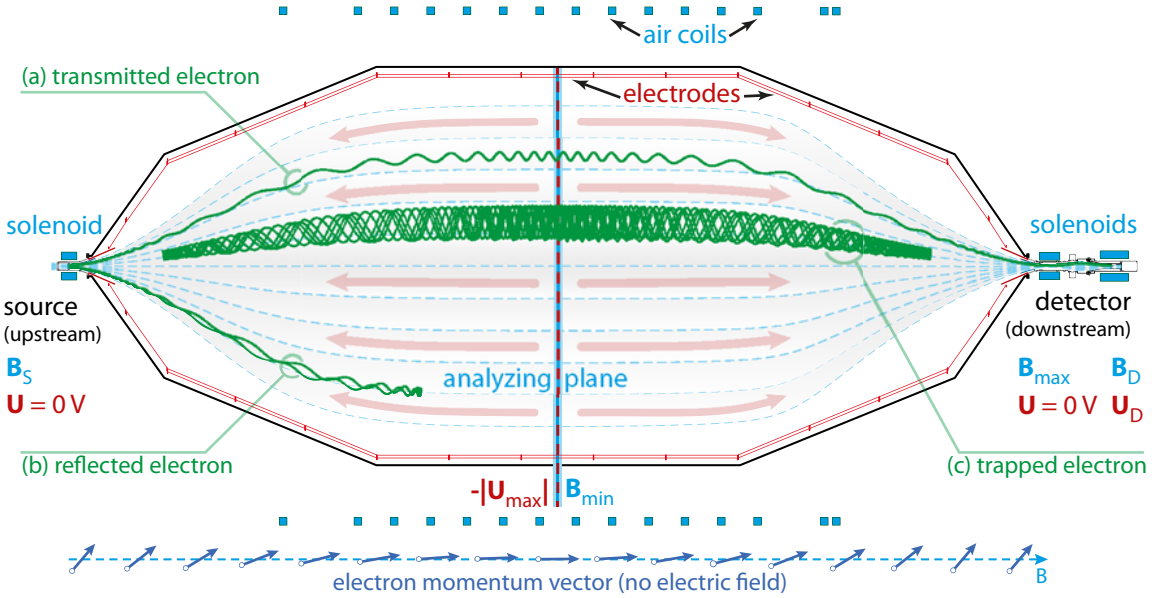

Figure 3.5.: The MAC-E filter principle at the main spectrometer. Electrons arriving from the source are either transmitted (a) if their energy is high enough to overcome the retarding potential $U_{\mathrm{ret}} = qU_{\mathrm{max}}$, or (b) electrostatically reflected back to the RW if their energy is not sufficient. Electrons which are generated within the main spectrometer volume may are magnetically trapped (c) within the strong fields provided by superconducting magnets on both ends. According to adiabatic particle transport, the magnetic moment of the electrons (see eq. 3.1) remains constant so transverse momentum is transformed to longitudinal momentum by lowering the magnetic field to the centered analysing plane (AP), where the absolute high voltage is maximal [3].

energy into longitudinal energy since the magnetic moment of the electrons cyclotron motion around a magnetic field line is conserved, it follows

$$\mu = |\vec{\mu}| = \frac{\mathrm{e}}{2m_{\mathrm{e}}}|\vec{l}| = \frac{E_{\perp}}{B} = \text{const.}\,, \tag{3.1}$$

with the transverse energy $E_{\perp} = E \cdot \sin^2(\theta)$ and magnetic field B. Here, θ denotes the angle between momentum $\vec{p}$ and magnetic field $\vec{B}$. Such spectrometers have excellent energy resolution when the magnetic field drops by several orders of magnitude towards the center of the main spectrometer which localises the analysing plane. Here, the transverse energy of the electrons reaches its minimum. While combining the magnetic field minimum and the retarding potential maximum $|U_{\mathrm{max}}|$, only electrons with longitudinal energies larger than the filter energy $E_{\parallel} = E \cdot \cos^2(\theta) > qU_{\mathrm{max}}$ are transmitted. The energy resolution is given by

$$\Delta E = \frac{B_{\mathrm{min}}}{B_{\mathrm{max}}} \cdot E\,, \tag{3.2}$$

which is about 1 eV at the KATRIN experiment for standard values of $E = 18.6\,\mathrm{keV}$, $B_{\mathrm{min}} = 0.3\,\mathrm{mT}$ and $B_{\mathrm{max}} = 6\,\mathrm{T}$ at the pinch magnet. This can be interpreted as the

remaining transverse energy of electrons at the analysing plane. Another quantity that depends on the magnetic fields is the acceptance angle

$$\theta_{\max} = \arcsin\left(\sqrt{\frac{B_S}{B_{\max}}}\right) \tag{3.3}$$

of beta electrons that start in the source (B_S) which is about 51° for the nominal fields at KATRIN. The design is not completely flawless as the superconducting magnets on both ends provide a magnetic bottle wherein electrons are able to be trapped, see fig. 3.5(c), if their initial polar angle and/or kinetic energy is large. As these electrons are adiabatically transported, eq. 3.1 is valid which can be used to compare initial (i) and final (f) states of inside-generated electrons. It reads

$$\begin{aligned} \mu_i &= \frac{E_{\perp,i}}{B_i} = \frac{E_{\perp,f}}{B_f} = \mu_f \\ \frac{E_i \sin^2(\theta_i)}{B_i} &= \frac{E_f \sin^2(\theta_f)}{B_f} \rightarrow E_i = \underbrace{E_f \cdot \frac{B_i}{B_f}}_{\approx \Delta E} \cdot \frac{\sin^2(\theta_f)}{\sin^2(\theta_i)} , \end{aligned} \tag{3.4}$$

where the first part of eq. 3.4 can be approximated by the energy resolution ΔE if the initial state is somewhere in the low magnetic field region ($\approx B_{\min}$) within the spectrometer whereas the final state is located at the exit after acceleration due to the retarding potential $|U_{\max}| \approx E_f$ within the strong magnetic field of the superconducting magnet $B_{\max}$. The second part of the equation is given by the squared sine functions which individually are smaller or equal to one but positive. Therefore, the trapping condition for inside-generated electrons reads

$$E_i < E_f \cdot \frac{B_i}{B_f} \cdot \frac{1}{\sin^2(\theta_i)} \approx \frac{\Delta E}{\sin^2(\theta_i)} , \tag{3.5}$$

which results for an polar angle of $\theta_f < 90°$ at the maximum magnetic field. From this follows that already electrons with few eV energy can be trapped, if their initial polar angle with respect to the magnetic field is large enough. On the other hand, higher energetic electrons can still be transmitted if their initial momentum is nearly parallel to the magnetic field lines. It is crucial that such electrons should be avoided to be produced as well as positive ions which are electrostatically trapped within the main spectrometer fields as they serve as a background source. Many background sources related to the spectrometers will be discussed in sec. 4. The spectrometers are operated under ultra-high-vacuum (UHV) conditions at a pressure on the order of 10^{-11} mbar. Thus, the scattering of electrons by residual gas on their way through the spectrometers is strongly suppressed.

The detector system at the KATRIN experiment is composed of a silicon multi-pixel *p-i-n*-diode array with custom electronics and ultra-high-vacuum as well as a high-vacuum system, and superconducting magnets, see fig. 3.6a. The wafer is divided into 148 pixel, which are arranged in 12 rings, with 12 pixels each, and the bulls-eye of 4 pixels. Each pixel holds the same surface area of 44 mm^2 and a design capacitance of 8.2 pF. Combinations of the pixels within one ring are used for radial effects of the detector system, the source,

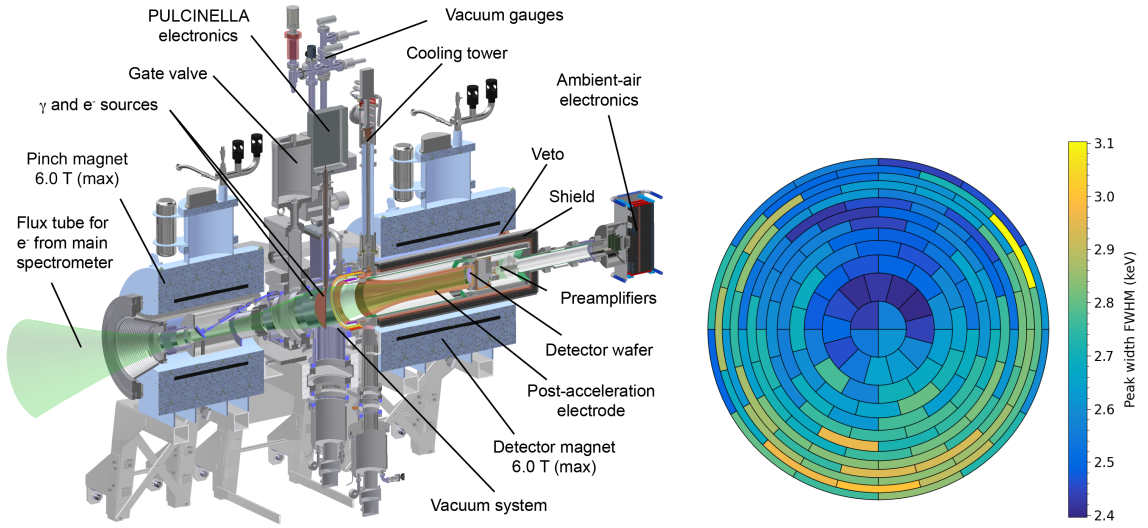

(a) FPD system. **(b)** Energy resolution pixel map.

Figure 3.6.: (a): Overview of the KATRIN detector system and its components [73]. **(b):** Pixel map of calibration data: Data taken with an ^{241}Am source in 2022. A fit of the γ energy at 59.54 keV is performed to determine the energy resolution at full width at half maximum (FWHM). The mean value of the distribution is 2.648 keV with a standard deviation of 0.145 keV.

or background electrons. Additionally, calibration and monitoring devices are installed between pinch and detector magnet. As γ calibration source an ^{241}Am source is used while electrons can be produced at various energies from a titanium plate which is operated with high-voltage by photo-electron emission, using UV-light (PULCINELLA). The detector wafer sits within the detector magnet at a nominal field of 2.5 T surrounded by a lead shield and a scintillating veto to discriminate signal electrons to background events of cosmic muons [73]. To reduce backscattering effects from the FPD wafer a post-acceleration-electrode (PAE) is installed which is nominally operated at 10 kV, so arriving electrons are accelerated longitudinally by 10 kV. Additionally, this reduces the intrinsic detector background in the signal energy region as it is slightly energy-dependent and lower for higher electron energies. Backscattering of electron from silicon is an important quantity for the analysis and will be discussed in more detail in sec. 6.4 in the scope of the pTEF analysis.

Recent calibration measurement with the ^{241}Am source are used to determine the energy resolution of the FPD wafer, see fig. 3.6b. Here, the most frequent γ-ray at 59.54 keV [74] is measured and analysed in terms of the peak width. The energy resolution of the wafers at KATRIN are between 2 and 3 keV which is not of concern since the energy measurement of the electrons is made via the retarding potential in the main spectrometer, the detector is utilised to count the transmitted electrons.

3.2. Measuring the effective neutrino mass

In this section the technical operation of the KATRIN experiment during neutrino mass measurements is described. Measurement campaigns are numbered consecutively, starting with the first official neutrino mass run KNM1 in spring 2019. So far, six measurement campaigns have been completed, with campaigns KNM1-KNM5 being of relevance in the context of this thesis.

3.2.1. Electromagnetic field setting

3.2.1.1. Nominal analysing plane (NAP)

The nominal analysing plane (NAP) configuration of the main spectrometer MAC-E filter is the standard configuration. The magnetic field is reduced by about 4 orders of magnitude from the outer superconducting magnets to the center of the main spectrometer vessel,

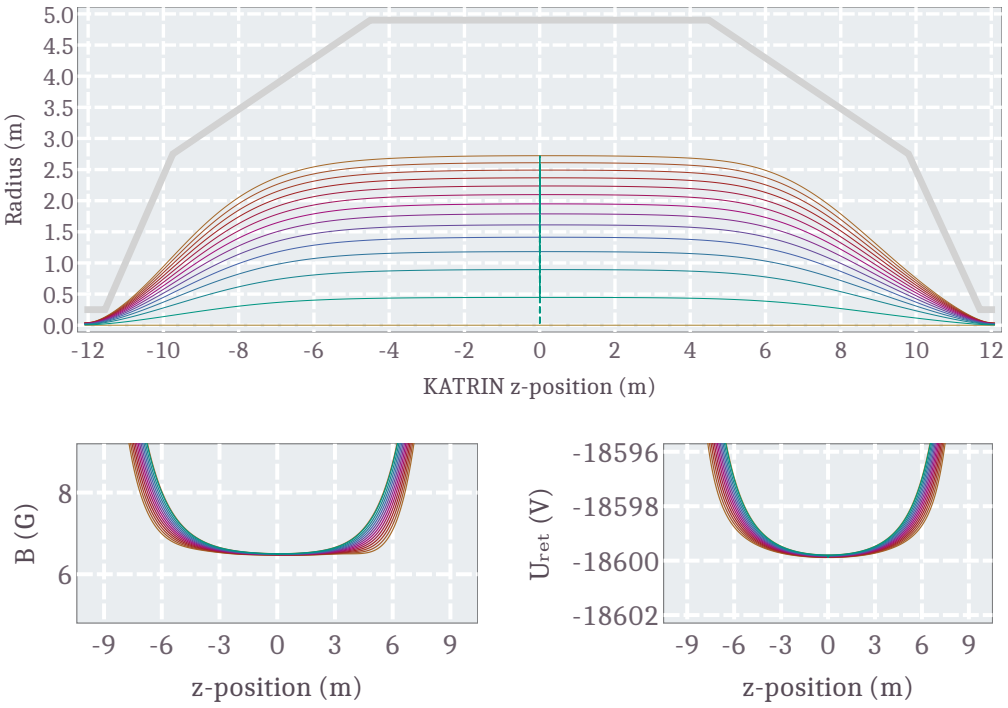

Figure 3.7.: Top: Magnetic flux tube as a function of the position along the beam line axis (z). As the system is axial symmetric only the radial component is shown. The individual lines are mapped between the detector rings so each line represents the enveloping of ring-by-ring volumes. The vertical green line at the center denotes the analysing plane (AP), where the absolute high voltage is maximal. The solid grey line represents the main spectrometer vessel wall. **Bottom:** Magnetic field B (left) and retarding voltage U_{ret} (right) in the center region of the main spectrometer for the NAP configuration. Magnetic fields in the AP are often written in cgs units: $1\,\mathrm{G} = 1{\times}10^{-4}\,\mathrm{T}$.

while the retarding potential is maximal as well there. The mapping of the magnetic field flux tube on to detector can be seen in fig. 3.7. Each line belongs to the track of magnetically guided electrons, arriving between pixels of neighbouring rings on the FPD, simulated with Kassiopeia [75] - an electromagnetic particle tracking framework, wherein the global KATRIN beamline is contained. The NAP configuration is characterised by high homogeneity of the magnetic field strength and retarding potential at the analysing plane (AP) which leads to an unitary spectrometer resolution (eq. 3.2) over the whole flux tube. This setting was used for the first two neutrino mass runs KNM1 and KNM2 with an average magnetic field at the analysing plane of $B_{\mathrm{ana}} = 6.308{\times}10^{-4}\,\mathrm{T}$ which results into a spectrometer resolution of $\Delta E = 2.76\,\mathrm{eV}$ for electron energies of $E = 18\,575\,\mathrm{eV}$ and the maximal magnetic field at the pinch magnet of $B_{\mathrm{max}} = 4.239\,\mathrm{T}$ [4].

The total flux tube volume between the superconducting magnets at the main spectrometer is about $365\,\mathrm{m}^3$, where the sensitive flux tube volume is defined as the volume downstream of the analysing plane of $177\,\mathrm{m}^3$, the ring resolved values can be found in the appendix A.1. The mean background rate of this configuration at the mentioned measurement campaigns was about 0.25 counts per second (cps), or 250 mcps respectively. This exceeds the initially assumed design background value of 10 mcps [69] by a factor of 25 and therefore significantly limits the neutrino mass sensitivity. Ways to reduce the background level were taken into account and it turned out that reducing the downstream flux tube volume is a favourable way to do so, leading to the shifted analysing plane configuration [76] which will be explained in the following.

3.2.1.2. Shifted analysing plane

As the background level is much higher than anticipated the shifted analysing plane (SAP) configuration was developed [77]. In comparison to the NAP configuration the background level could be lowered by a factor of 2 which is why this is used for current neutrino mass runs since KNM3 as standard measurement configuration [76]. In fig. 3.8, the magnetic flux tube, the minimal magnetic field, and the minimal retarding voltage for the SAP configuration of the main spectrometer is shown. In contrast to the NAP configuration, the magnetic flux tube is no longer mirror-symmetrical about $z = 0\,\mathrm{m}$. The largest extension of the flux is shifted downstream, where the magnetic field and retarding voltage minima come to terms, so the analysing plane is shifted towards the detector. Thus, the sensitive flux tube volume is reduced to about $60\,\mathrm{m}^3$.

Additionally, this leads to inhomogeneities in both the magnetic field and the retarding potential. Due to the geometry of the main spectrometer vessel and its electrodes, potential depression occurs so that the foreseen field value of $-18\,600\,\mathrm{V}$ cannot be reached at the analysis plane, even though this voltage is set at the inner electrodes, wherein the potential also decreases from the outer to the inner volumes that are mapped on the detector. This manifests as a maximal retarding potential difference between the innermost and outermost pixel rings of 3.6 eV. Similarly, the magnetic field strength is also inhomogeneous in the AP, higher in the center of the flux tube and decreasing to larger radii. The total difference is about 1.8 G but maintaining the energy resolution of the NAP configuration at the innermost pixels, wherefore the resolution improves on the outer radii, since the minimal

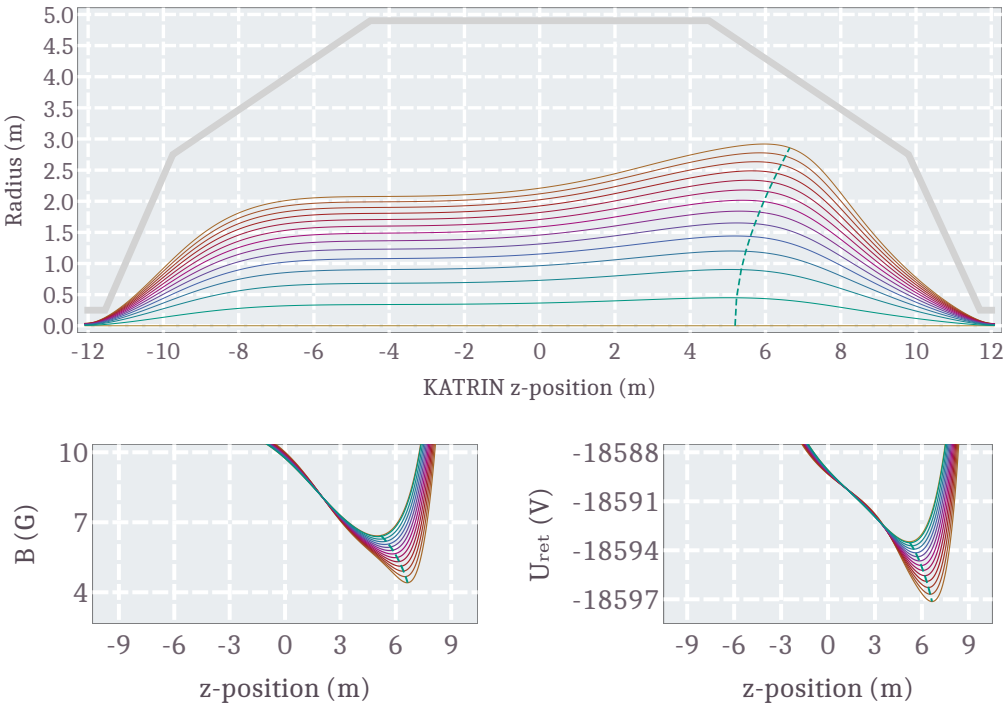

Figure 3.8.: Top: Magnetic flux tube as a function of the position along the beam line axis (z). As the system is axial symmetric only the radial component is shown. The individual lines are mapped between the detector rings so each line represents the enveloping of ring-by-ring volumes. The dashed green line denotes the shifted analysing plane, defined by the maximal absolute high voltage value and the solid grey line represents the main spectrometer vessel wall. **Bottom:** Magnetic field B (left) and retarding voltage U_{ret} (right) in the center region of the main spectrometer for the SAP configuration with its strongly pronounced minima shifted downstream to $5 < z < 7$ m.

magnetic field B_{min} of eq. 3.2 decreases. Ring resolved values of the volumes, magnetic field, retarding voltages, and energy resolution can be found in app. 8.

The inhomogeneities of the electromagnetic fields influences the neutrino mass measurements. In the analysis, the radial and azimuthal pixelation of the detector becomes more important as every pixel gains a slightly different transmission function, defined by the individual potential. Nevertheless, pixels can be grouped into patches instead of rings, to take the inhomogeneities, as well as misalignment into account, so that the electric potential ($\delta qU \leq 0.25$ eV) and magnetic field variations ($\delta B \leq 0.014$ mT) over one patch are small. A precise calibration measurement of the pixel-wise field parameter was performed with ^{83m}Kr, in addition to measurements with mono-energetic electrons from an angular-selective photo-electron source (e-gun). [76]

It reveals that the systematic contribution of the SAP fields to the KATRIN sensitivity on m_ν^2 is $\Delta m^2_{\nu,sys} \approx 3\times10^{-3}$ eV^2 [78] which fulfills the maximal systematic contribution of 7.5×10^{-3} eV^2 [69]. As other systematic contributions are currently significantly higher

(see [4] Table 2), it turned out that using the SAP configuration is beneficial in terms of background reduction and hence statistical uncertainty. Furthermore, the systematic contribution by non-Poisson background is highly diminished, which leads to an improved neutrino mass sensitivity.[76]

3.2.2. Measurement time distribution

The measurement time distribution (MTD) is of central importance because it directly influences the observable neutrino mass signal. The choice of unfavourable steps, values and time intervals on the retarding potential leads to worse neutrino mass sensitivity and thus to unsatisfactory neutrino mass results. An exemplary MTD is shown in fig. 3.9

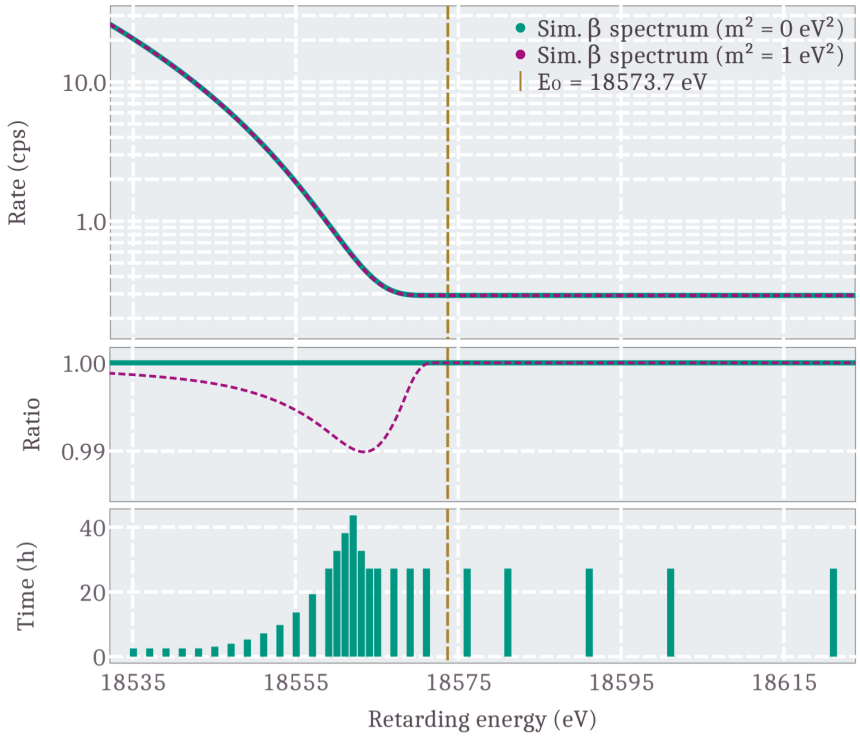

Figure 3.9.: General view on the neutrino mass measurements. **Top:** Integrated model spectra of continuous β-spectra obtained with a MAC-E filter. The electron rate is plotted as a function of the retarding energy for two different cases of neutrino masses $m_\nu^2 = 0\,\mathrm{eV}^2$ (green solid line) and $m_\nu^2 = 1\,\mathrm{eV}^2$ (purple dashed line). **Center:** The ratio of the spectra in comparison to the massless neutrino case is shown. The strongest deviation of the spectrum with a massive neutrino is about 10 eV below the endpoint E_0. **Bottom:** The measurement time distribution (MTD) illustrates the amount of time spent at different retarding potentials. It is optimised for a neutrino mass sensitivity of 1 eV while the largest amount of time is attributed to the region of the largest deviation. Regenerated according to ref. [3].

at the bottom which is optimised for observations of spectrum distortion by a neutrino mass of $m_\nu = 1\,\mathrm{eV}$ ($c \equiv 1$) and was used at the KNM1 measurement campaign with a total measurement time of 521.7h [79]. The largest deviation of the spectrum in comparison to the β-spectrum for massless neutrinos occurs about 10 eV below the endpoint E_0 which is why most of the scanning time is spent there. The scanning time drops to lower values of the retarding potential as more and more electrons are able to be transmitted through the MAC-E filter so the rate increases significantly, wherefore statistics are not of concern. For background investigations and observations during the neutrino mass runs the retarding potential is set above the endpoint E_0, hence, no tritium beta electrons are transmitted from the source to the detector as their energy is not sufficient to overcome the retarding potential. The background points are distributed equally in time but at various retarding potentials to measure potentially systematics by a potential-dependent background component. This will be described in more detail in chapter 5 in addition to other systematics evoked by the background.

Data are not taken at once for each individual retarding potential for the given time of the MTD. During a campaign many runs (scans) are recorded with run lengths of 1-3 hours which contain the MTD relatively. The data recorded for individual retarding potential set points are called subruns. At the final analysis, the subruns of each scan are combined to one final spectrum which will be fit [79].

3.2.3. Systematic budget

The systematic budget at KATRIN neutrino mass measurement campaigns consists of various contributions which are shown in fig. 3.10. Largest contribution over the last five measurement campaigns is made by systematics related to background. In particular, the contributions are made by non-Poisson distributed background electrons Bg-nP, Penning background Bg-Penn., and the background slope over retarding potential Bg-slope. Since their contribution is large, their study is of great importance, as the ubiquitous goal of KATRIN is to improve the sensitivity on the neutrino mass, which is why these background related systematics will be described in more detail in chapter 5. The global background rate becomes part of the statistical error that is increased due to increased rate.

Further systematics with less effect on the neutrino mass sensitivity arise from the source and the magnetic fields. The electrons and ions generated in the WGTS form a plasma that influences the starting potential of the electrons, whereby their energy is affected on the meV scale [80]. The potential energy is a minor problem compared to the longitudinal asymmetry along the WGTS beamline [81]. Variations on the tritium column density ρ are taken into account by a combination of the integral column density along the beamline of the WGTS ρd times the scattering probability σ as this quantity is part of the response function which is needed to model the rate of arriving electrons on the detector [78].

Systematic contribution on the neutrino mass sensitivity by magnetic fields are described by uncertainties on the global values of the analysing plane magnetic field (AP), the source magnetic field B-src and the pinch magnetic field B-pch. The latter two are essential to describe the transmission of electrons through the MAC-E filter, according to eq. 3.3,

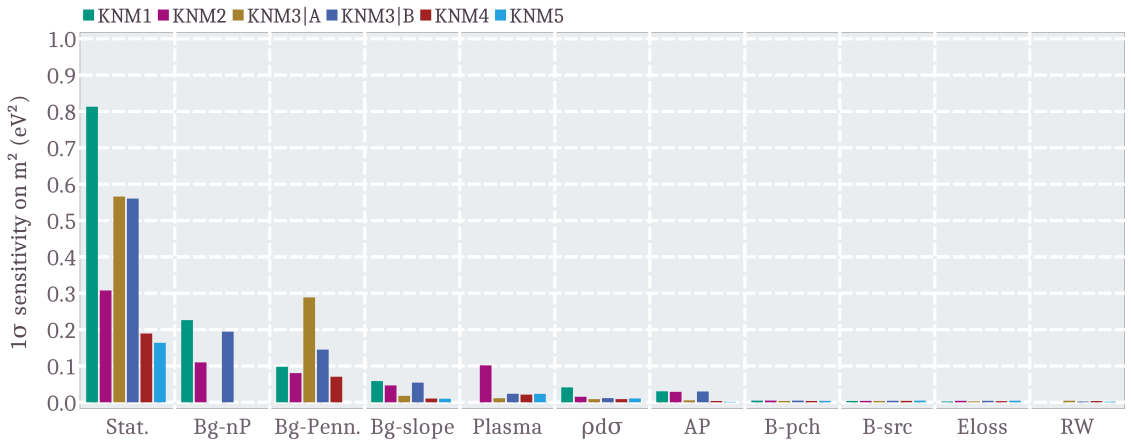

Figure 3.10.: Systematic breakdowns on the individual neutrino mass campaigns KNM1 - KNM5 on Monte Carlo data.

whereas AP includes in addition to the magnetic field the retarding potential variations which occur by measurements in the SAP configuration [76, 78].

The remaining systematics are beta electrons background of residual tritium which accumulated on the rear wall surface (RW) and the energy loss (Eloss) of electrons when scattering inelastically with the WGTS source gas [45].

Over the course of the first five neutrino mass measurement campaigns performed, statistical and systematic error contributions could have been steadily improved. The current neutrino mass limit was obtained at analysis of the first two measurement campaigns KNM1 and KNM2 with both dominated by contributions of the background related systematics. As of now, in KNM5 the background related systematics were highly reduced in addition to enhanced statistics which results in a statistical uncertainty below $0.2\,\mathrm{eV}^2$.

4. Background processes in the KATRIN experiment

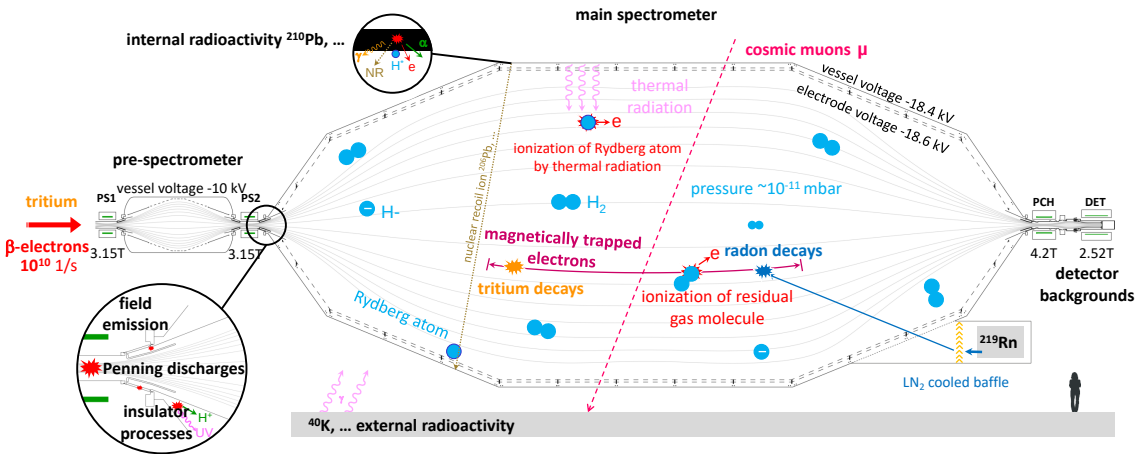

Figure 4.1.: Overview of various background processes at the KATRIN spectrometers. Passing cosmic muons, Penning discharges, detector backgrounds, and contributions by external or internal radioactivity, e.g. radon or tritium decays and ionisation of highly excited atoms by black-body-radiation (BBR) [82].

As the background level is significantly enlarged, compared to the design value of 10 mcps [69] by a factor of 25 for the 6.3 G NAP configuration [4]. Many investigations concerning the origin of the observed background electrons as well as their signature on the detector were performed. In fig. 4.1, an overview of the various processes that generate background electrons at the spectrometers are shown. Penetrating cosmic muons interact with the stainless steel of the main spectrometer vessel and produces electrons of various energies. Although the sea-level muon flux is high, cosmic muons can not explain the observed background rate [8, 83], which will be described in sec. 4.1.

Larger background contribution was found to arise from the detector itself. This intrinsic detector background already exceeds the design value slightly but is smaller than 30 mcps and additionally depending on the energy region of interest (ROI), see sec. 4.2. Operating both spectrometers with high voltage leads to an electrostatic trap (Penning trap) within the superconducting magnet PS2. This allows low-energy electrons to be trapped, producing secondary electrons and ions that fill this trap and eventually ignite, releasing several hundred electrons at once, which is called Penning discharge [83].

Furthermore, radioactivity plays a major role for the description of the background at KATRIN. On the one hand, emanating radon from the getter pump material (NEG) as well

as the stainless steel vessel generates high energetic electrons within the spectrometer volume which are most likely being magnetically trapped [84]. Due to the long storage times in the UHV-conditioned spectrometer, several ionisations of the residual gas take place, resulting in observable background electrons on the detector. Likewise, tritium contamination of the spectrometer section would lead to similar background. On the other hand, an intrinsic radioactive contamination of the stainless steel vessel surface by ^{210}Pb was encountered [8]. In the decay chain of ^{210}Pb, alpha decay of ^{210}Po occur, where the resulting high energetic recoil ion $^{206}Pb^{X+}$ is able to sputter of atoms from the surface. Some of which are excited to states of high principle quantum number n, which are able to get ionised by black-body-radiation (BBR) [8, 9, 85]. The so-called Rydberg background will be extensively be described in sec. 4.5, as it accounts for the largest contribution of the current background level. The investigation of the external radioactivity showed that it is not relevant with the standard measurement configuration of the main spectrometer [83].

4.1. Emission of secondary electrons from surfaces

As the muon flux through the main spectrometer is approximately $10^5 s^{-1}$, large background contribution by secondary electron emission by muons can be expected. The inside stainless steel vessel surface is about 690 m^2 with additional surface area due to the inner electrode (IE) system and its peripherals of 532 m^2 [3]. Interacting muons (μ) or gammas (γ) within the stainless steel mainly generate low energy electrons of energies below 50 eV [86]. Such low energetic electrons are efficiently shielded by the electromagnetic field design inside the main spectrometer, as shown in fig. 4.2. Two shielding mechanism emerge. On the one hand, electrostatic shielding of electrons which leave the spectrometer surface as the absolute inner electrode voltage U_{IE} is higher than the vessel voltage U_{vessel} by 200 V in standard configurations. On the other hand, electrons that escape from the IE surfaces

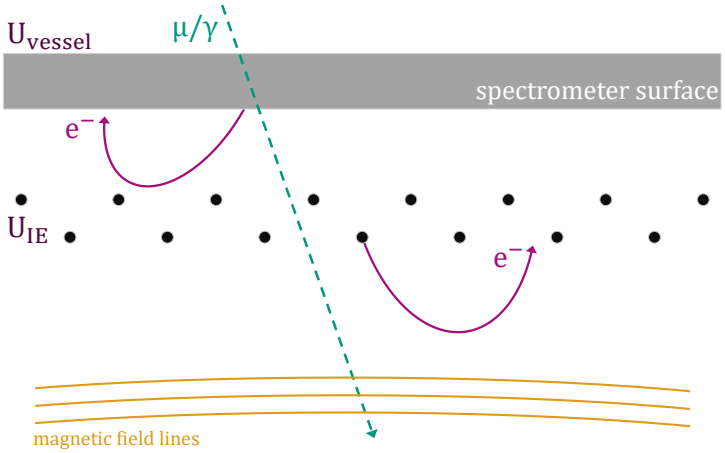

Figure 4.2.: Electric and magnetic shielding of low energy electrons from the vessel ($U_{vessel} < -18\,000$ V) and inner electrode ($U_{IE} = U_{vessel} - 200$ V) surface. Passing muons (μ) or gammas (γ) produce low energy electrons that are either electrostatically or magnetically be reflected.

are magnetically reflected by the Lorentz force as the magnetic field lines are parallel to the spectrometer surface to the first order. However, electrons with higher energy and specific starting angles to the magnetic field are able to arrive within the sensitive flux tube volume. However, detection at the FPD is possible but very improbable, depending on their energy and flight direction.It is on the order of 0.2×10^{-3} % for isotropically started electrons from the IE surface with energies between 5 and 30 keV [8].

Dedicated measurements investigating the secondary electron emission from the main spectrometer surfaces by changing the magnetic guiding field in a way that the surface is mapped onto the detector enables the observation of the muon-induced electrons directly. Supplementary muon detector panels were installed, surrounding the main spectrometer vessel, so the muon flux could be measured and modelled. Correlation analysis of the muon and the electron rate on the FPD resulted in a muon-induced background fraction of only 13.6(8) % from the inner spectrometer surfaces [8].

This result was puzzling since a large amount of about 86 % of the measured electrons from the inner surface had to have a different origin than cosmic muons, whereas contributions by external radioactivity, e.g. γ particles, were already excluded. Nevertheless, in a standard symmetric magnetic field configuration, higher energetic electrons from the inner surfaces are barely able to reach the sensitive flux tube volume. Here, residual gas ionisation with the generation of trapped electrons is possible and the detection at the FPD but this tiny fraction cannot be considered as the dominant background source. [8]

4.2. Intrinsic detector background

The FPD is designed for high efficiency counting of electrons while maintaining a low intrinsic background contribution within the region-of-interest (ROI) for the neutrino mass measurements. The design value made 10% of the total background level and was planned to be less than 1 mcps [69]. The muon-veto-system which is additionally installed within the bore hole of the detector magnet can be used to actively tag events at the FPD induced by through-passing cosmic muons [73]. A coincidence of signals from the muon-veto and the detector within 1 µs triggers the veto, while the detector signal is removed from the analysis which reduces the intrinsic detector background by about 40 %, see fig. 4.3 and 4.4a. The detector background is slightly energy-dependent in the standard ROIs of 14-32 keV (KNM1,KNM2) and 22-34 keV (KNM3 and following), see fig. 4.3-Right. As the post-acceleration-voltage (PAE) is standard operated at 10 kV the endpoint of the tritium spectrum is at about 28.6 keV on the detector. The intrinsic detector background rate at these energy ranges for the current wafer is extracted

$$\begin{aligned} \mathrm{ROI}: 14-32\,\mathrm{keV}: \; r_{\mathrm{BG,Det}} &= 21.2 \pm 0.2\ \mathrm{mcps}\,, \\ \mathrm{ROI}: 22-34\,\mathrm{keV}: \; r_{\mathrm{BG,Det}} &= 13.0 \pm 0.2\ \mathrm{mcps}\,, \end{aligned} \tag{4.1}$$

using the exponential fit (black dashed line) in fig. 4.3-Right. The shown data were taken in February 2021. This wafer was installed before the KNM3 measurement campaign in spring 2020, due to slightly worse energy resolution compared to the formerly used wafer, a more narrow ROI is beneficial with respect to the background rate.

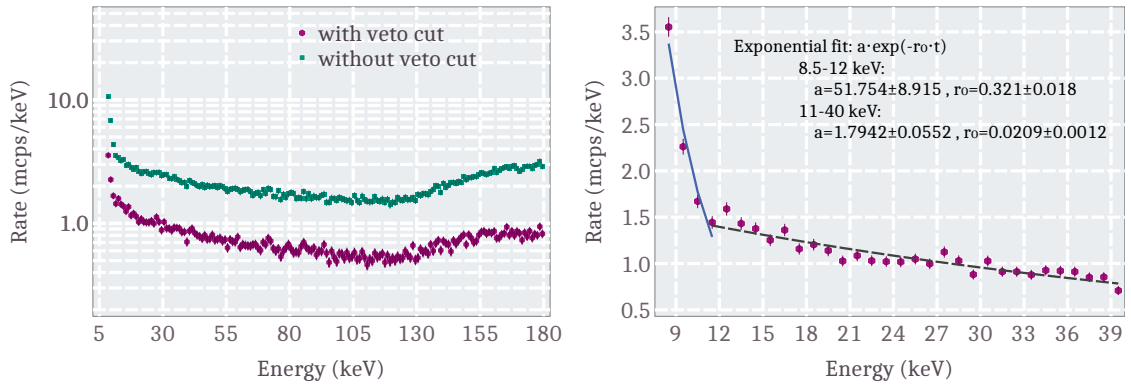

Figure 4.3.: Intrinsic detector background as a function of the measured energy. **Left:** Energy range of 7 to 180 keV. Rate is shown for the whole detector (148 pixel) with and without application of the muon veto-cut. At $E < 11\,\text{keV}$ the electronic noise is visible. $E > 120\,\text{keV}$ is related to charged ionising particles which pass through the FPD wafer. Their energy-loss follows a Landau-distribution. **Right:** Detailed view on the intrinsic detector background in the energy range from 8 to 40 keV which is of interest for standard measurements such as neutrino mass runs. Two exponential fits are made: on the noise part (solid blue line) for $8.5\,\text{keV} \leq E \leq 12\,\text{keV}$ and on the relevant energy part (dashed black line) for $11\,\text{keV} \leq E \leq 40\,\text{keV}$.

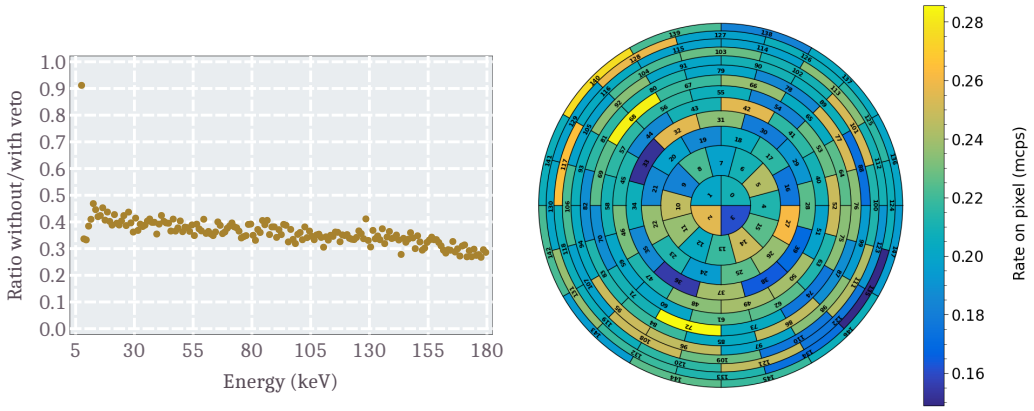

(a) Veto-cut background ratio.

(b) FPD pixel background rate distribution.

Figure 4.4.: **(a):** Ratio of the detector background rate for $7 \leq E \leq 180\,\text{keV}$. Shown is the ratio of the rate with application of the veto cut of 1 µs divided by the rate without the cut for energy bins of 1 keV width. The uncertainty of each data point is about 8.5% but not plotted for better readability. **(b):** FPD pixel map distribution of the intrinsic detector background given for an energy range of 11 to 40 keV. The mean background rate on a pixel is $r_{\text{BG,Det,pixel}} = 0.214(25)\,\text{mcps}$, resulting in a total background rate of 31.6(3) mcps for the whole detector and this energy range.

4.3. Penning traps

Another known background contributor are Penning discharges, as shown in fig. 4.1 on the left. Firstly observed at stand-alone investigations at the pre-spectrometer between the ground and cone electrodes [87], see fig. 4.5. In KATRIN, both spectrometers are used in tandem operation. Such as the main spectrometer, also the pre-spectrometer can be set on high voltage. Initially, the basic plan was to pre-filter electrons before entering the main spectrometer by a lower counteracting potential. If less beta electrons are able to enter the spectrometer, less scattering on residual gas and therefore, less secondary electrons are produced, which reduces background events. However, the operation of both spectrometers on high voltage forms an electrostatic trap between them in the high magnetic field of the superconducting magnet PS2, where the beam tube is on ground potential. Low energetic electrons that are generated near the ground potential inter-spectrometer region can therefore are electrostatically as well as magnetically being trapped. These trapped electrons scatter on residual gas, producing secondary electrons and positive ions, so the trap gets filled with electrons. Once, the amount of electrons is too high to be blocked by the counteracting high voltage potential, a Penning discharge occurs, releasing enormous numbers of electrons into the spectrometers. This effect strongly depends on the pressure and the applied high voltages. [83]

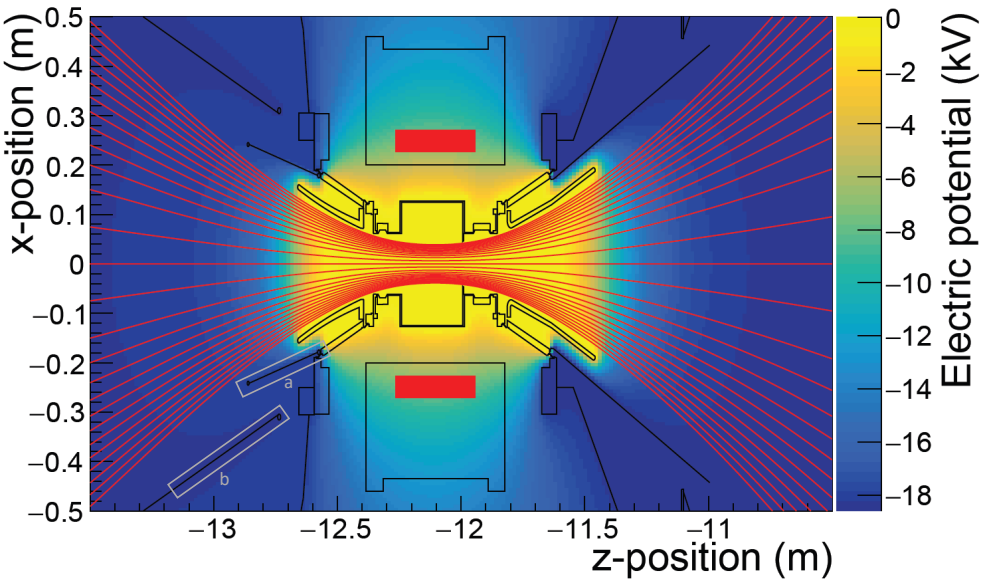

Figure 4.5.: Electromagnetic field condition in the inter-spectrometer region. The colour scale denotes the electric potential in kV, only valid inside the beam tube. Red lines mark the magnetic field lines depicted on the FPD, while their constriction is a measure of the magnetic field strength. The coils position of the superconducting magnet PS2 is marked as red rectangles. Grey borders show the ground electrode at 0 V (a) and the cone electrode at −18.3 kV (b) in the pre-spectrometer. Figure from [83] with highlights a and b according to [87].

To counteract against the inter-spectrometer Penning trap as a background source a movable wire was introduced into the valve, sitting inside the PS2 magnet. This device is called Penning wiper and is used to clear the trap from electrons as it moves through the magnetic flux tube. Any electron that hits the Penning wiper is caught and removed from the trap, effectively preventing Penning discharges. [3, 88]

Although the induced background rate by the Penning trap and discharges is small due to regular wiper operations and the UHV condition at $p \approx 4{\times}10^{-11}$ mbar, it results in a large systematic in neutrino mass measurements, as can be seen in fig. 3.10. Description of this systematic on the data is made in section 5.3.

4.4. Radon-induced main spectrometer background

Background electrons produced by radioactive decays of radon atoms, mainly ^{219}Rn, within the main spectrometer volume lead to high-energy electrons that are magnetically trapped in the magnetic bottle and produce several secondary electrons.

Radon as a naturally occurring radioactive noble gas is present in the ambient air. Its most common isotope is ^{222}Rn, which accounts for up to 90% of the total prevalence. Other isotopes include ^{220}Rn (9%) and ^{219}Rn (1%), among others in trace amounts. At KATRIN, the isotope abundance differs from natural occurrence in ambient air as the isotopes have different half-lives which is related to their relevance in the experiment.

- ^{220}Rn as part of the ^{228}Th decay chain has a half-life of $T_{1/2} = 55.8(3)$ s [89]. Since radon emanates from any stainless steel surface, it is also present within the main spectrometer volume, therefore potentially generating background electrons.
- ^{219}Rn is short-living with a half-life of $T_{1/2} = 3.98(3)$ s [90]. Thus, if such an atom is present in the main spectrometer volume, background contribution is highly favoured as it cannot be pumped before decay. It arises from the non-evaporable getter (NEG) pump material, established to maintain the UHV condition at a pressure on the order of 10^{-11} mbar. Therefore, a direct background source is installed as it emanates ^{219}Rn in large amounts which makes it the most challenging contribution.
- ^{222}Rn is not of concern in the KATRIN experiment due to its long live-time of 3.82 d [91] as the mean pump-out time is about $\tau_{\mathrm{MS}} \approx 360$ s [8]. However, ^{222}Rn becomes of relevance in section 4.5 as its decay products evolved to the strongest source of background within the main spectrometer.

Collectively, radon-induced background is made of emanating ^{220}Rn from the inside main spectrometer surfaces and ^{219}Rn from the NEG material. However, the radon contribution within the sensitive main spectrometer volume could be efficiently reduced by installing a liquid-nitrogen-cooled copper baffle [92], whose location is shown in fig. 4.1 on the bottom right side next to the NEG pump material within the pump ports. The baffle system covers the direct line-of-sight from the getter pump into the main spectrometer volume. Due to its low temperature, released radon atoms of thermal velocity have a certain probability to stick on the cold surface, long enough to decay there [93]. In fig. 4.6a the measured cluster rate with an artificial ^{220}Rn source, installed behind the baffle is shown as a function of

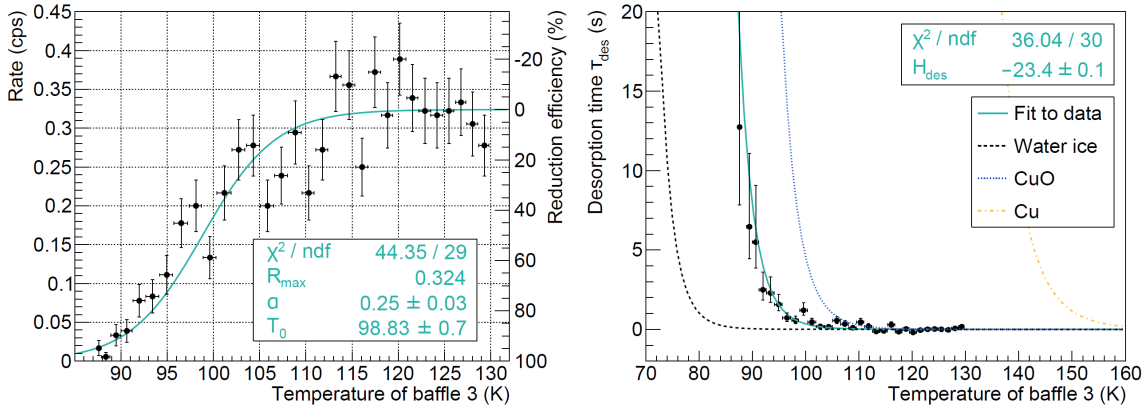

(a) Background rate. **(b)** Desorption time.

Figure 4.6.: (a) Background rate and **(b)** desorption time of ^{219}Rn as a function of the baffle temperature, provided by J. Wolf according to [93].

the temperature. Cooling down to 90 K leads to a radon-induced background reduction of about 95% [8, 93]. The desorption time, shown in fig. 4.6b, is a result of the comparison of molecular-flow simulations and measurement. The surface desorption time of radon atoms on cold surfaces rises significantly with decreasing temperatures up to a level of several half-lives of the short-living isotope ^{219}Rn so that its background contribution is significantly reduced. The baffle efficiency will decrease over time as water molecule adhere to the cold surface which reduces the ability of radon atoms being desorbed. To further increase the efficiency of the baffle system on long operation periods, a pre-cooling stage of the LN2 was installed. Before being transported to the baffles, liquid nitrogen gets pumped to a pressure of about 250 mbar further reducing its temperature, hence, enhancing the desorption time since temperatures down to 77 K are achievable. The global effect of further radon-induced background reduction was small but investigated after a preceding bake-out of the main spectrometer and baffle system, whereby no water could accumulate on the cold surfaces over time [94].

When radon decays in the main spectrometer volume up to 20 electrons can be released with various energies such as inner-shell shake-off ($E \approx 1$ keV), conversion ($E \approx 100$ keV), relaxation ($E \approx 1$ keV), or shell-reorganisation ($E \approx 10$ eV) electrons [8, 84, 95]. Since most of these electrons do not fulfil the transmission condition eq. 3.5 because their energy is large, these electrons are magnetically trapped or can leave the flux tube by non-adiabatic motion. An exemplary path of a trapped high-energy electrons in the magnetic bottle of the main spectrometer is shown in fig. 4.7. The magnetron motion creates a ring-shaped imprint on the FPD, as secondary electrons are generated by residual gas ionisation along the path of the primary trapped electron.

Since scattering on residual gas is a non-random process which depends on the electron energy, the pressure, and the temperature inside the main spectrometer, the signature of radon-induced background can be derived from the inter-arrival time spectrum of a measurement. The inter-arrival time is the time-span between two consecutive electron arrivals on the detector. The distribution of these times follows an exponential distribution if the measured electrons are generated completely randomly which arise from Poisson

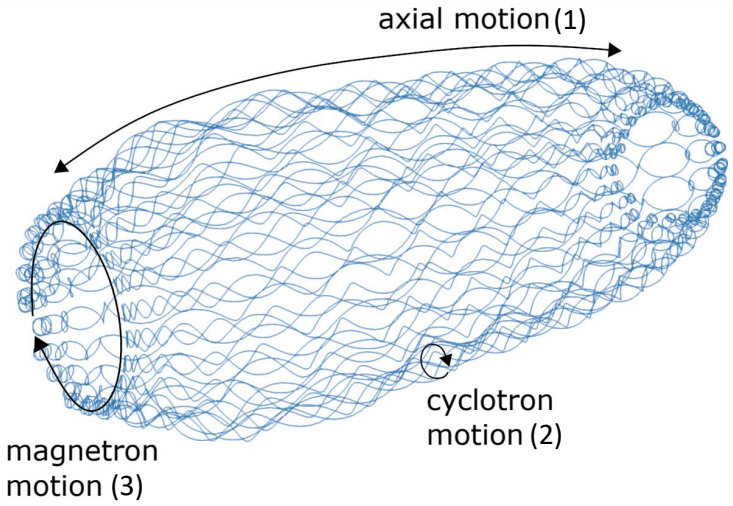

Figure 4.7.: Motion of magnetically trapped electron in the main spectrometer field. The motion of trapped particles consists of three components: (1) axial motion along the magnetic field lines, (2) cyclotron motion around the magnetic field lines and (3) a magnetron drift around the symmetry axis due to field inhomogeneities [96].

statistics. Furthermore, the number of electrons within a certain period of time follows the Poisson distribution for random generation. Deviations from this also indicate non-Poisson events, which are presumably induced by radon. Analysis of data on these cases are given in section 5.1.3.

4.5. The Rydberg background model

This section describes the largest contribution to the current background level which is also related to radioactivity. Background electrons due to the ionisation of highly excited Rydberg atoms released from the vessel surface by radioactive contamination with ^{210}Pb, a daughter of ^{222}Rn, which is called Rydberg background model.

The Rydberg background model [8, 9, 85, 97, 98] is the description of the main contribution to the current background level at the KATRIN experiment. It arises from many investigations concerning the background with respect to dependencies on the pressure, the magnetic field, the high voltage potential, and the inner electrode offset voltages. Of main importance are the dependencies on the magnetic field flux tube which can be used to investigate the background rate per sensitive flux tube volume as well as the radial background distribution on the detector [8], and on the inner electrode potential [9]. The following section is divided into three parts, starting with the different dependencies on the background level, followed by the description of the radioactive long-living ^{210}Pb contamination of the main spectrometer and conclusively, the background electron generation mechanism within the sensitive main spectrometer flux tube volume by ionisation of sputtered highly excited Rydberg atoms by black-body-radiation (BBR).

4.5.1. Parameter dependencies on the background level

The radial background profile within the sensitive flux tube volume can be investigated by means of the pixelised detector wafer. In fig. 4.8a the pixel-wise background distribution during the KNM3|B measurement campaign is shown. The data were taken in the nominal analysing plane (NAP) as formerly used during the measurement campaigns KNM1 and KNM2, which is described in section 3.2.1.1. The combination of the pixels within one ring leads to the radial background profile shown in fig. 4.8b. The increase of the first data point arise from misalignment of the magnetic flux tube, which can also be seen in fig. 4.8a as the minimum rate is slightly shifted downwards. However, the radial distribution mapped on the flux tube radius of the sensitive volume within the main spectrometer points shows a radially increasing background rate from inner to outer radii which corresponds to less distance to the spectrometer vessel wall. In combination with former measurements of slightly different electromagnetic field settings, a two-component background can be extracted, shown in fig. A.1. A homogeneous background contribution that serves the entire volume and a radially increasing component, related to the inner spectrometer surface.

The main spectrometer is equipped with an inner wire electrode system (IE) to fine-tune the electric potential within. It is divided into 11 individual operable sectors [3]. The nominal potential offset of the inner electrodes is $U_{\mathrm{IE}} = -200\,\mathrm{V}$, whereas in NAP configuration only the outer parts at the ends of the main spectrometer are supplied with an additional positive offset voltage for better transmission conditions. In SAP, the individuality of the system is used to tune the electric potential maximum downstream to the detector. The background dependence on this inner electrode potential offset is of main importance as no effect on the background level within the sensitive flux tube

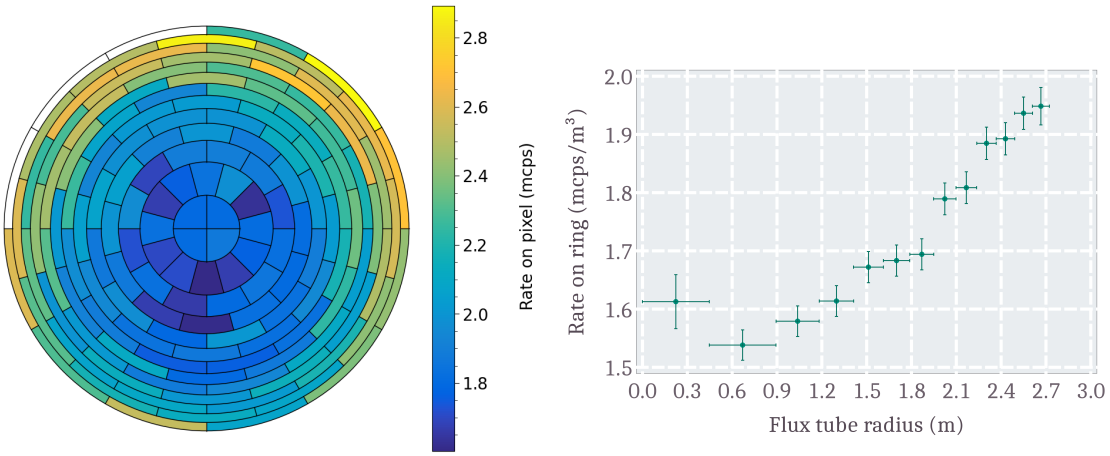

(a) FPD pixel map of background rate.

(b) Ring-wise background rate representation.

Figure 4.8.: **(a):** pixel-wise background rate of the KNM3|B neutrino mass measurement campaign. Three pixels on the top left side are excluded due to misalignment. **(b):** Ring-wise representation of the background rate mapped to the radius of the magnetic flux tube in the analysing plane at the center of the main spectrometer.

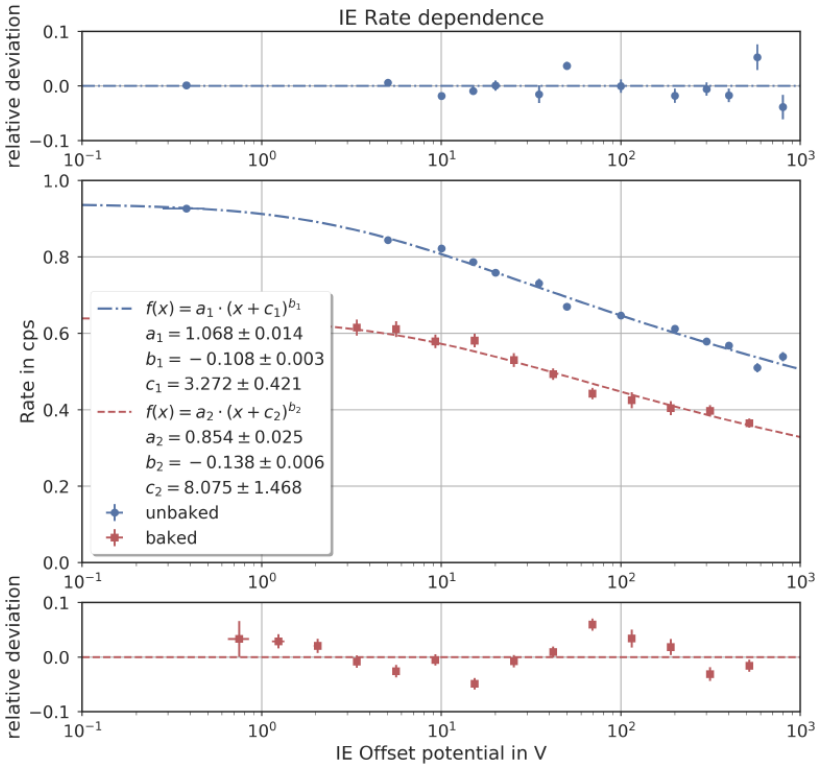

Figure 4.9.: Background rate as a function of the inner electrode potential offset U_{IE} for the cases of a baked and unbaked main spectrometer. Both are fit with a broken power law $f(x) = a_1 \cdot (x + c_1)^{b_1}$ and its relative deviations are shown at the top (unbaked) and the bottom (baked) [9].

volume was expected. Low energetic electrons are electrically reflected due to the electric field and higher energetic ones are magnetically reflected by the magnetic field.

The measurements, performed by N. Trost demonstrate a decreasing background level by increasing the offset potential, which is shown in fig. 4.9. Surprisingly, the total background is decreasing homogeneously over the entire flux tube [9], which points towards a background source in the sensitive volume, driven by mechanisms occurring at the inner spectrometer surface. Additionally, the effect of the main spectrometer baking can be seen. Baking of the main spectrometer is made to improve the UHV conditions as residual gas molecules can adsorb on inner surfaces and the baffle surfaces [3]. Of main relevance is water (H_2O) that adsorbs on surfaces. Baking has a strong effect on the background level of the main spectrometer of approximately 40 % at $|U_{\mathrm{IE}}| =$ 200 V, derived with the given fit function in fig. 4.9, through which surface adsorbed molecules efficiently are removed. This observation supplements the surface relation of the background generation within the main spectrometer sensitive flux tube volume. Dedicated investigations regarding the correlation of electrons originating from the volume and the inner surface have been made, using a short-living radioactive source. An intrinsic radioactive contamination of the inner main spectrometer surface was performed. By changing the magnetic field configuration the contributions from the surface and inside

were measured and a correlation of 99.9 % was found with additional confirmation on the inner electrode potential offset with an artificial ^{226}Ra background source [96, 99].

Changes on the inner electrode potential correspond to changes of the electric field between the spectrometer surface and the wire electrode. As the background rate is influenced within the spectrometer volume several meters apart from the area of this electric field, a mediator particle which carries electrons from the surface into the volume is necessary to explain these observations.

4.5.2. Identification and contamination of ^{210}Pb

Identification

At further investigations regarding the background electron generation several long-term measurements in a 3.8 G symmetric magnetic field configuration revealed the presence of high energy electrons at the detector well above the nominal signal electrons [8] which could be associated with conversion electrons at the decay of long-living ^{210}Pb into ^{210}Bi, as shown in fig. 4.10a. These conversion electrons of ^{210}Bi occur with sharp energies at 30.152 keV (58%), 42.540 keV (13.7%) and 45.601 keV (3.5%) from the L, M and N shell, respectively [91], which are shown in tab. A.3. The energy spectrum of resulting electrons after ^{210}Pb decays is shown in fig. 4.10b that composes of two individual β-decays of maximum energies of 17.0 keV and 63.5 keV with probabilities of 80 % and 20 %, respectively. Additionally to the conversion electrons, Auger as well as shell reorganisation electrons can be released with energies up to 17 keV.

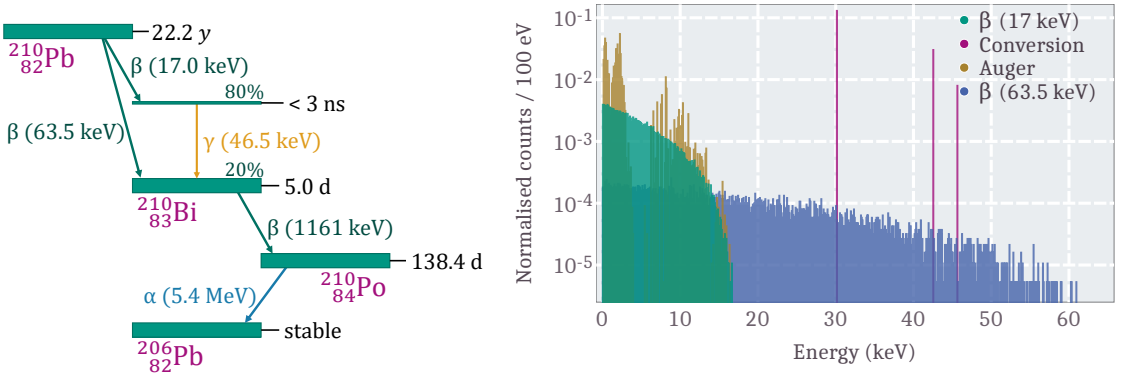

(a) Decay chain of ^{210}Pb

(b) Electron energy distribution

Figure 4.10.: (a): Decay scheme of long-living ^{210}Pb. Two transition to ^{210}Bi are possible via β decay of either 17 keV (80%) or 63.5 keV (20%). Decay chain ends at stable ^{206}Pb. **(b):** Simulated electron energy spectrum of 10^6 decays with Kassiopeia [75], resulting in 1867360 electrons. The continuous β-spectra (green and blue), induced Auger electrons (yellow) and the three conversion electrons (purple) are represented. Transition probabilities and energy data according to [91].

Simulations on the arrival probability of 30 keV electrons that start on the inner spectrometer surface or the inner electrodes lead to a nearly vanishing detection probability of these electrons on the order of 10^{-6}. The rate in the region of interest of the 30-keV conversion-electron was 2.2(2) mcps which lead to an estimated ^{210}Pb activity within the spectrometer of 1 kBq [8].

Since these measurements had been performed, the standard measurement configuration changed from the 3.8 G symmetric magnetic field (see fig. A.1) to the SAP configuration which is discussed in section 3.2.1.2. The radial expansion of the flux tube is smaller and the magnetic field strength increased accordingly. However, the high-energy conversion electrons in ^{210}Pb decays are only slightly affected by the magnetic field configuration,

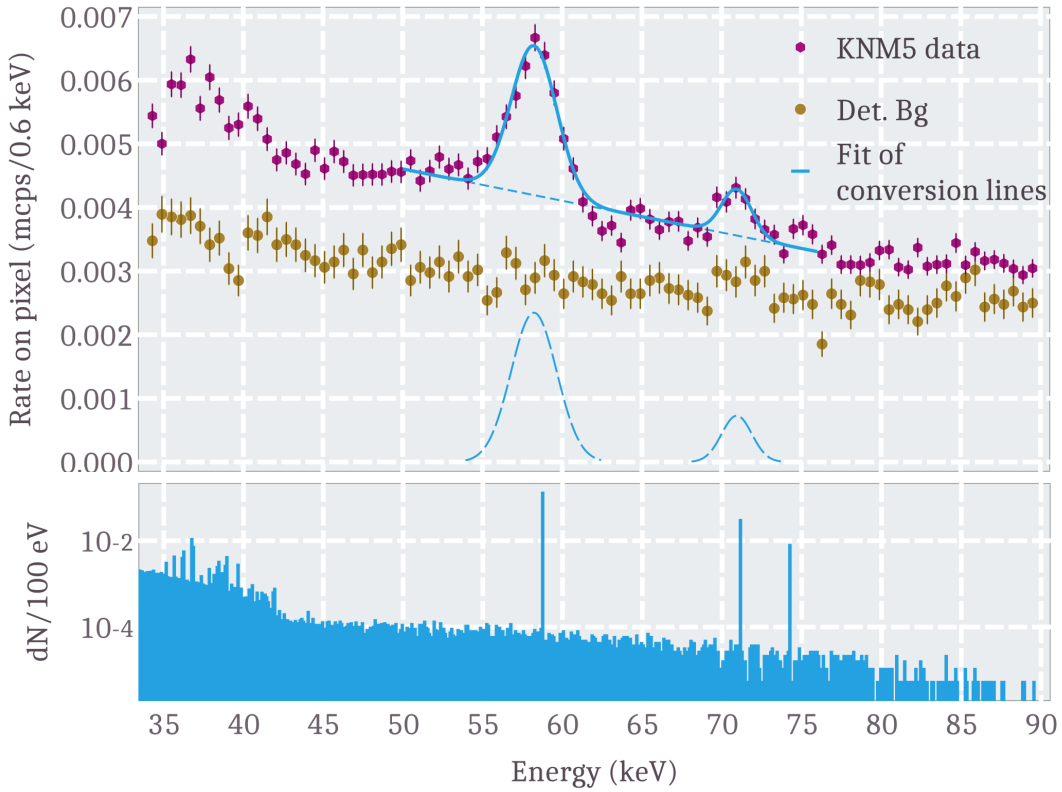

Figure 4.11.: Top: Background electron rate distribution in the energy region of the expected conversion electron signal per pixel and energy bin size of 600 eV. KNM5 data (purple), detector background (yellow) and a fit on the two predominant conversion electron energies (blue) with the standalone Gaussian distributions of the individual fits (blue dashed). The fit conversion electron energies are $E_L = 58.26(9)$ keV and $E_M = 70.94(23)$ keV for the transitions out of the L and M-shell, respectively. **Bottom:** Energy spectrum of generated electrons after ^{210}Pb decays, as shown in fig. 4.10b but shifted to higher energies according to the time-weighted mean of the electric potential $|U_{\mathrm{ret,mean}}| = 18\,602.47$ V and the post-acceleration-voltage of $U_{\mathrm{PAE}} = 10$ kV used at this measurement.

Table 4.1.: Expected and fit energies E_T of the conversion electrons at ^{210}Pb decays and the fit peak width σ_T in KNM5 data.

Transition	position	fit position E_T	fit peak width σ_T
L-shell	58.75 keV	58.26 ± 0.09 keV	1.42 ± 0.10 keV
M-shell	71.14 keV	70.94 ± 0.23 keV	0.96 ± 0.25 keV

since their excess energy above the spectrometer potential leads to a non-adiabatic motion, which is why the arrival probability on the detector can be assumed to be constant for different magnetic field configurations. Hence, the analysis of recent data with respect to these high energy conversion electrons is of interest. In the data taken during KNM5 in SAP configuration a significant amount of electrons in the region of interest of the conversion electrons is found. An extended background region for retarding potentials of $|U_{\mathrm{ret}}| > 18\,577$ V was taken into account which amounts into a total measurement time of 340.35 h for this investigation.

The expected line positions are calculated from the literature values [91] with an additional offset, arising from the time-weighted mean of the retarding potential $|U_{\mathrm{ret,mean}}| = 18\,602.47$ V and the post-acceleration voltage $U_{\mathrm{PAE}} = 10$ kV, which increase the electron energy at the detector. The theoretical and measured values of the conversion electrons are given in table 4.1. The positions are slightly shifted to lower values which can arise from the energy resolution of the FPD but more probable due to the fact, that these electrons originally get produced within the stainless steel of the spectrometer surface and therefore loose energy before leaving the surface [8]. A combination of two Gaussian distributions are fit along the data, convoluted with a common linear function as background, whereas the highest conversion electron energy is not taken into account, as its occurrence probability is much smaller compared to the remaining ones, although its imprint in the data can be suspected at around 75 keV. With the individual Gaussian distribution (see fig. 4.11 dashed blue lines), the rate of these conversion electrons can be derived to

$$r_{\mathrm{L}} = 1.75 \pm 0.11 \text{ mcps}$$
$$r_{\mathrm{M}} = 0.36 \pm 0.08 \text{ mcps}\,,$$

above other contributions which matches previous investigations within uncertainties. The total rate of the KNM5 data around the peak position ($E_L \pm 5 \cdot \sigma_L$) is 14.2(1) mcps,whereas the detector background amounts to 10.46(3) mcps but its long-term stability is not guaranteed within this energy region. Hence, the rate difference between the detector background and the KNM5 data which are not related to conversion electrons can arise from other background events, especially the high energy β-electrons from the ^{210}Pb decay, but also from an elevated intrinsic detector background which is not falsifiable.

Contamination

Naturally, ^{210}Pb arises within the decay chain of ^{238}U (see fig. A.3) that involves the intermediate daughter atom ^{222}Rn. ^{222}Rn, as noble gas, emanates from the soil and is

present in the ambient air. The local outdoor radon concentration is about $10\,\mathrm{Bq\,m^{-3}}$ [100]. During the construction of the inner electrode system in the main spectrometer, the volume was supplied with ambient air over a long time of about 5 years. Technically, there was a re-circulation pump which exchanged the air inside ($1240\,\mathrm{m^3}$) up to 3-4 times during one hour, equipped with HEPA filters [8]. As radon is a noble gas, filtering is not efficient and a radon activity within the spectrometer over the course of construction can be assumed. The main spectrometer is made out of stainless steel of the type EN 10028-7 - 1.4429 (AISI 316 LN, X2CrNiMoN17-13-3). It was selected due to its specification of thermal expansion, UHV suitability and radioactivity [101]. Since the intrinsic radioactivity of the steel is low, the observed radioactive contamination had to occur after its completion and during the construction works of the inner electrode system on site. The total activity of ^{210}Pb was calculated from the simulated arrival probability of the L-shell conversion electron with an energy of 30.152 keV on the FPD and the observed rate r_L. It is deduced to be about 1 kBq. [8]

Contamination is caused by surface implantation, as radon decays via α decay into polonium, which penetrates the steel when the decay occurs close to the surface. The primary decay reads

$$^{222}_{86}\mathrm{Rn} \rightarrow \underbrace{^{4}_{2}\mathrm{He}^{2+}}_{\alpha} + {}^{218}_{84}\mathrm{Po}^{X+} + X\mathrm{e}^{-} + Q(5.59\,\mathrm{MeV}),\ (X < 20), \tag{4.2}$$

with the α-particle, a doubly-ionised helium atom, the daughter atom polonium, which can be ionised after emission of X electrons, and the decay energy of 5.59 MeV. Up to 20 electrons can be released when the remaining polonium atom is emitted in an excited state [102].

The implantation of the polonium daughter atom can be simulated, using the SRIM code [103]. With this software, *The Stopping and Range of Ions in Matter* (SRIM) of chosen ions in individually composition of materials can be investigated. The collisions are based on the binary-collision-approximation (BCA), a classical description of atomic interactions. Each primary particle knocks on atoms (PKA), leading to secondary atoms (SKA) that propagate through the material. These are tracked until they fall below a certain energy threshold or leave the target [104]. Such simulations were already performed in previous works of collaborators [8, 9, 85, 105]. However, the true composition of the inner main spectrometer surface remains unknown but can be modelled, using the technical description of the

Table 4.2.: Chemical composition of the stainless steel and its passive layer for the simulation with SRIM, given in %. Compounds that are only present in traces or that do not characterise the steel properties are neglected.

	depth (Å)	Fe	Cr	Ni	Mo	Mn	O	H	C	density ($\mathrm{g\,cm^{-3}}$)
Water layer	3	0	0	0	0	0	33	66	0	0.523
Carbon layer	5	11	15	4	0	0	45	0	25	3.506
Passive layer	30	16	23	8	0	0	50	0	3	4.407
Vessel	bulk	66	18	13	3	2	0	0	0	7.935

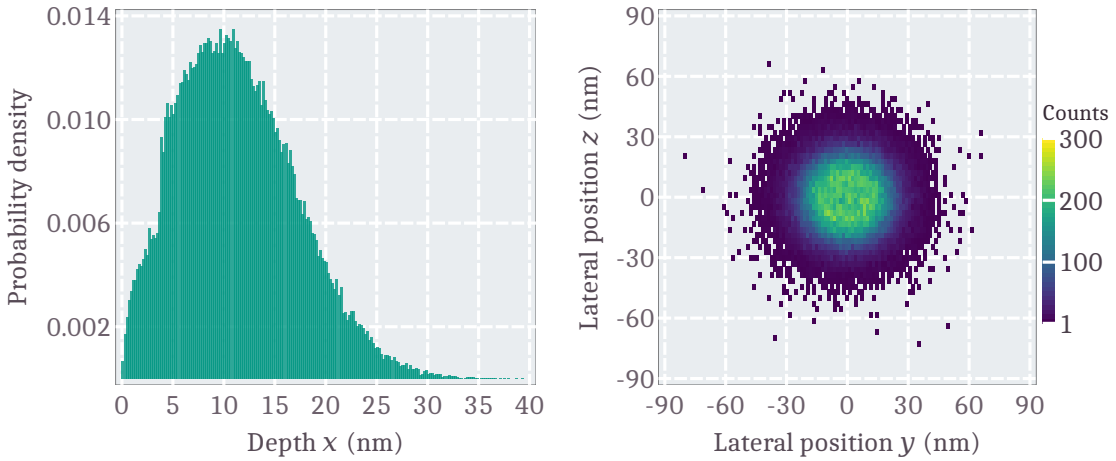

(a) Implantation depth.

(b) Lateral positions.

Figure 4.12.: (a): Implantation depth probability distribution of ^{218}Po ions, released at ^{222}Rn decays with a bin size of 0.2 nm. **(b):** 2D histogram of the final lateral positions. The surface is defined to be in the yz-plane and the depth into the material along the x axis.

electro-polishing procedure, RGA measurements [98] and the literature [106–109]. The deduced surface composition is shown in tab. 4.2, whereas the chemical composition of the main spectrometer stainless steel is given in app. A.5. Due to the electro-polishing, a passive layer that mainly consists of chromium oxide is formed [106] in addition to a thin layer with large amounts of carbon [109]. Surface-adsorbed water has to be taken into account naturally as adsorption of water within the main spectrometer is known from the LN2-cooled copper baffle.

At the decay, given in eq. 4.2, the polonium ion gains energy according to the energy and momentum conservation, whereas its kinetic energy can be calculated by the mass differences of the products of such decays

$$E_{\text{kin,daughter}} \simeq \frac{m_\alpha}{m_{\text{mother}}} \cdot Q \longrightarrow E_{\text{kin},^{218}\text{Po}} = \frac{4u}{222u} \cdot 5.59\,\text{MeV} = 100.7\,\text{keV}, \tag{4.3}$$

with the atomic mass unit u, neglecting the mass of the electron. Thus, the implantation simulation of ^{218}Po can be performed. The radon is assumed to decay directly at the surface of the inner main spectrometer, releasing the daughter atoms into the steel, whose directions are uniformly distributed on a hemisphere projecting into the material. A total number of 99989 initial decays of ^{222}Rn have been simulated. In fig. 4.12 the implantation depth and lateral position distribution is shown. The mean implantation depth is 11.36 nm with a pronounced edge at $x = 3.8$ nm due to changing material densities of the different surface layers. The lateral positions distribution is circular as expected with the maximum in the center at the decay position $r_0 = (0, 0, 0)$.

A fraction of 11.40(11) % of the simulated ^{218}Po ions was not implanted but back-scattered. However, as further α-decays occur in the decay-chain of ^{222}Rn the implantation profile in fig. 4.12a cannot represent reality of the present ^{210}Pb contamination depth

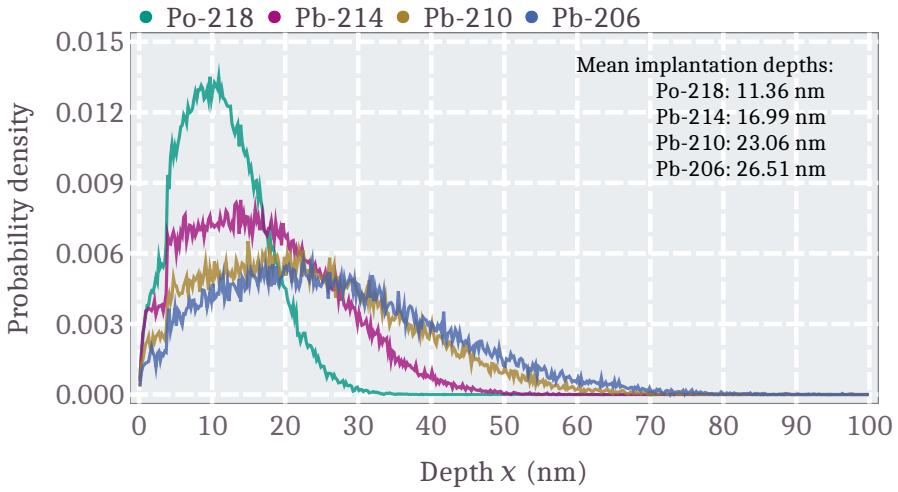

Figure 4.13.: Evolution of the implantation depth of consecutive α-decays of ^{222}Rn. The implantation depth profile is shown for the individual products ^{218}Po, ^{214}Pb, ^{210}Pb, and stable ^{206}Pb as probability density with bin sizes of 0.2 nm. With each iteration the mean implantation depth increases.

profile. The final positions of the implanted ions is used for affiliating simulations of the following decay products, according to the decay chain (fig. A.3). The processes of relevance with the corresponding recoil energies are

$$\begin{aligned}
&\text{a)}\ {}^{218}_{84}\mathrm{Po} \longrightarrow \alpha + {}^{214}_{82}\mathrm{Pb} + Q(6.12\,\mathrm{MeV}) \mapsto E_{^{214}\mathrm{Pb}} = 112.2\,\mathrm{keV}\\
&\text{b)}\ {}^{214}_{84}\mathrm{Po} \longrightarrow \alpha + {}^{210}_{82}\mathrm{Pb} + Q(7.83\,\mathrm{MeV}) \mapsto E_{^{210}\mathrm{Pb}} = 146.4\,\mathrm{keV}\\
&\text{c)}\ {}^{210}_{84}\mathrm{Po} \longrightarrow \alpha + {}^{206}_{82}\mathrm{Pb} + Q(5.41\,\mathrm{MeV}) \mapsto E_{^{206}\mathrm{Pb}} = 103.0\,\mathrm{keV}
\end{aligned} \tag{4.4}$$

where the kinetic energy of the resulting daughter atoms are calculated via eq. 4.3 and the decay energies are taken from [91]. Between the processes a)-b) and b)-c) two β^--decays take place which do not change the position of the implanted radioactive elements as their energy transfer to the recoiling atoms is small. Overview on the individual decays and the energies of recoils can be found in tab. A.4.

Each simulation delivers the final position of the primary ions that are used to be the start position of the following simulation iteration. According to the recoil ions and their energy, given in eq. 4.4, the evolution of the contamination implantation depth profile is given in fig. 4.13. A fraction of 52.3(2) % of the total number of primarily simulated radon decays lead to the implantation of ^{210}Pb, while the implantation depth flattens and the mean increases to 23.06 nm with a maximum depth of about 90 nm.

4.5.3. Generation and ionisation of Rydberg atoms by BBR at KATRIN

Sputtering of (excited) atoms

Rydberg atoms are assumed to act as the mediator particle of electrons from the inside main spectrometer surfaces. As ^{210}Pb decays after two β^--decays into ^{210}Po and finally via α-decay into stable ^{206}Pb, the resulting recoil is propagating through the stainless steel and knocks on atoms. Thus, sputtering of atoms is possible. Sputtering describes the vaporisation of atoms from surfaces by particle bombardment with energies from eV to MeV [110]. Many secondary effects occur in sputtering processes, such as excitation, neutralisation, or ionisation of the atomic species involved [110–112]. The amount of sputtered atoms of solid surfaces is part of research over many decades and many models about the sputtering yields depending on the incident particles, their energy and angle have been developed [110, 113–115]. Of special interest at KATRIN is the sputtering of excited atoms of the main spectrometer surface which is possible to take place due to resonant neutralisation when ionised atoms are close to a surface [112, 116–120]. The sputtering yield Y, which is simply the fraction of sputtered atoms divided by the number of incident particles, can also be derived from the simulations performed with SRIM [103] for the main spectrometer surface model, given in tab. 4.2. The final α-decay of ^{210}Po is illustrated in fig. 4.14, whereas the resulting ^{206}Pb-ion propagates through the stainless steel and sputters atoms from the surface. Any atom comprised at the surface is able

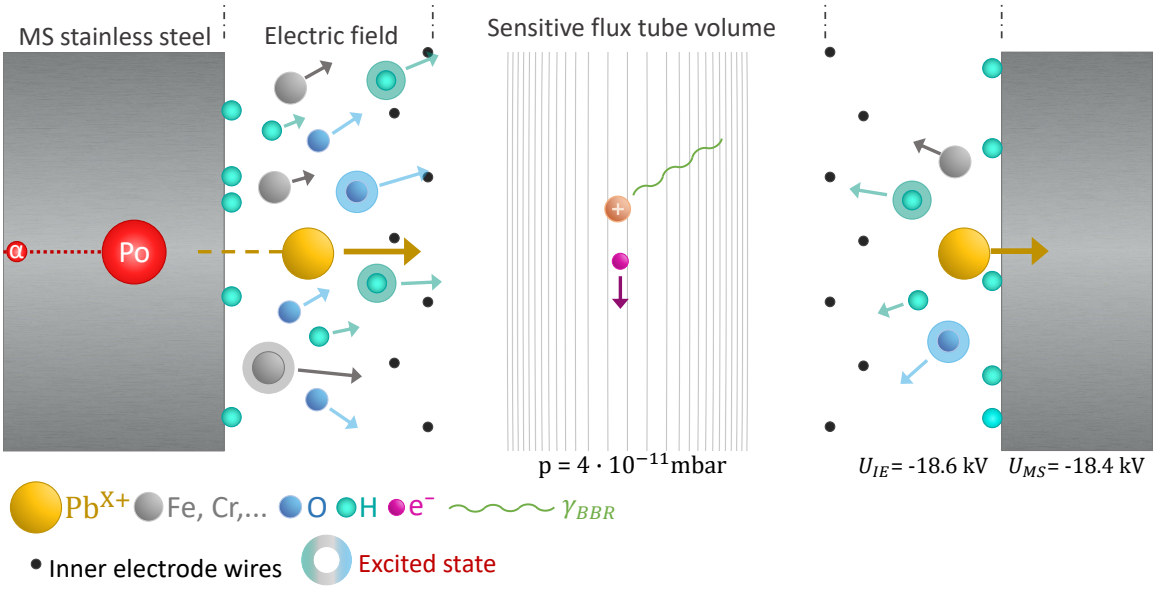

Figure 4.14.: Illustration of sputtering from the inner main spectrometer surface by ^{210}Po decays. The inner electrodes are represented as black dots near the surface, providing the electric field between. In the center, the sensitive flux tube is represented by guiding magnetic field lines onto the detector. Interaction of a BBR photon with an excited atom leads to ionisation, hence, an ion and an electron within the sensitive flux tube volume.

to being sputtered, some of which in excited states. Since hydrogen is adsorbed on the surface only with a low surface binding energy, it is preferentially released again from the surface [8, 9].

First models that describe the sputtering yield Y have been developed by Thompson [121–123] and Sigmund [113]. These lead to the relation of the energy differential sputtering yield

$$\frac{dY}{dE} \propto \frac{E}{(E+U)^{3-2m}} \tag{4.5}$$

on the surface binding energy U and the parameter m which corresponds to the model interaction potential $V(r) \propto r^{-1/m}$ [113, 124]. The atomically resolved sputtering yield of the final α-decay of ^{210}Po is shown in fig. 4.15.

Oxygen, as the most abundant atomic species in the surface composition (tab. 4.2), especially in the passive layer, has the highest sputtering yield. Although hydrogen is only present in the thin water layer of 3 Å thickness, it is also efficiently sputtered which is related to the smaller surface binding energies. The individual sputtering yields, most frequent energies, velocities and the theoretical surface binding energy of the atoms are given in tab. 4.3, whereas the total sputtering yield is

$$Y = 15.546 \pm 0.017 \ \frac{\text{atoms}}{\text{ion}} \ . \tag{4.6}$$

This yield is composed of two effects: First, the decay of ^{210}Po and the resulting sputtering by recoil ^{206}Pb and second, the sputtering of transmitted recoils. In 11.41 % of the simulated decays, the recoil particle has left the material and is therefore able to additionally sputter atoms from the surface when it hits the opposite side of the main spectrometer. The sputtering yield without secondary sputtering by transmitted recoils is 14 $^{\text{atoms}}/_{\text{ion}}$. Not every decay leads to the sputtering of atoms, only 23.6(2) % of the recoils have sputtered atoms from the surface. Additionally to the energy-dependent sputtering yields in fig. 4.15, the velocity distributions are shown in fig. A.4 which belong to the values of the mode velocity in tab. 4.3. Another quantity of interest is the multiplicity of the sputtered

Table 4.3.: Sputtering yields Y, mode energy E_{mode}, mode velocity v_{mode} and surface binding energies E_{bind} of the sputtered atoms from the inner main spectrometer surface. 52275 ^{210}Po decays have been simulated, accordingly the fraction of 52.3 % of initial radon decays. Manganese and molybdenum are not shown as their sputtering yield is smaller than 10^{-2}.

Atom	Y (atoms/ion)	E_{mode} (eV)	v_{mode} (km/s)	E_{bind} (eV)
H	4.0419(88)	4.95	30.55	2.0
C	0.6323(35)	23.71	14.96	7.41
O	8.293(13)	4.32	7.50	2.0
Cr	1.2200(48)	19.28	8.22	4.12
Fe	0.9844(43)	15.67	7.67	4.34
Ni	0.3644(26)	10.59	5.96	4.46

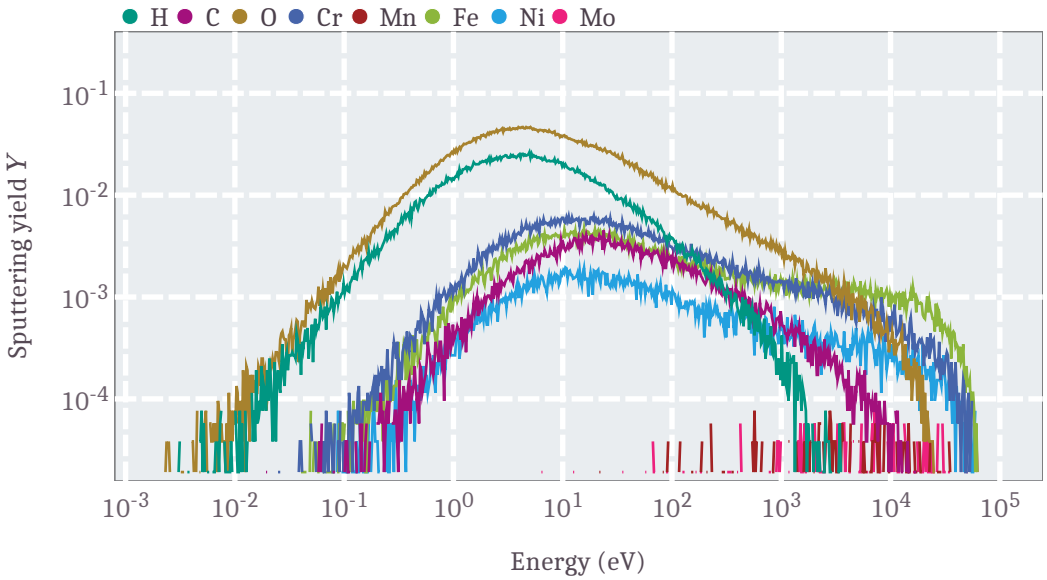

Figure 4.15.: Energy-dependent sputter yield of ^{210}Po decay inside the main spectrometer vessel surface. Each line represents a different atomic species. Oxygen amounts to the most abundant sputtered atom for the chosen surface composition.

atoms, shown in fig. 4.16. Oxygen and hydrogen as the most frequent sputtered atoms also provide large multiplicities up to 200 atoms for one single ^{210}Po decay, which is in agreement with observations of up to 30 electrons from the inner main spectrometer surface [8] if some of the sputtered atoms are ionised on short time scales of $\delta t < 200\,\mu s$, e.g. via Penning ionisation [125].

Some of these sputtered atoms leave the surface in electronically excited states, which has already been observed several times in the past [111, 114, 116, 119, 126, 127]. As the high energetic recoil transfers energy to surrounding atoms, ionisation and excitation occur frequently, which also results in sputtered excited atoms and ions. The SRIM software is not capable of the electronic processes on the atoms while simulating the collision cascades which makes another model necessary to describe the process of the excitations. The excitation process is mainly due to resonant neutralisation when ions are close to surfaces of bulk material, such as stainless steel [112, 128, 129]. When the ion is close above the surface, the potential well of the ion and the valence band of the steel are close enough to each other to allow tunnelling of electrons from the band into the potential well of the ion, through which the ion gets neutralised. This neutralisation may results in an excited state of the neutralised atom, as the excitation scales with the binding energy of the electron. Additionally, further effects among the sputtered atoms can results in the vicinity of the surface to excitations and ionisations [118, 130]. Thus, the presence of excited atoms leaving the inner main spectrometer surface is assumed in the scope of the Rydberg model [8, 9, 85].

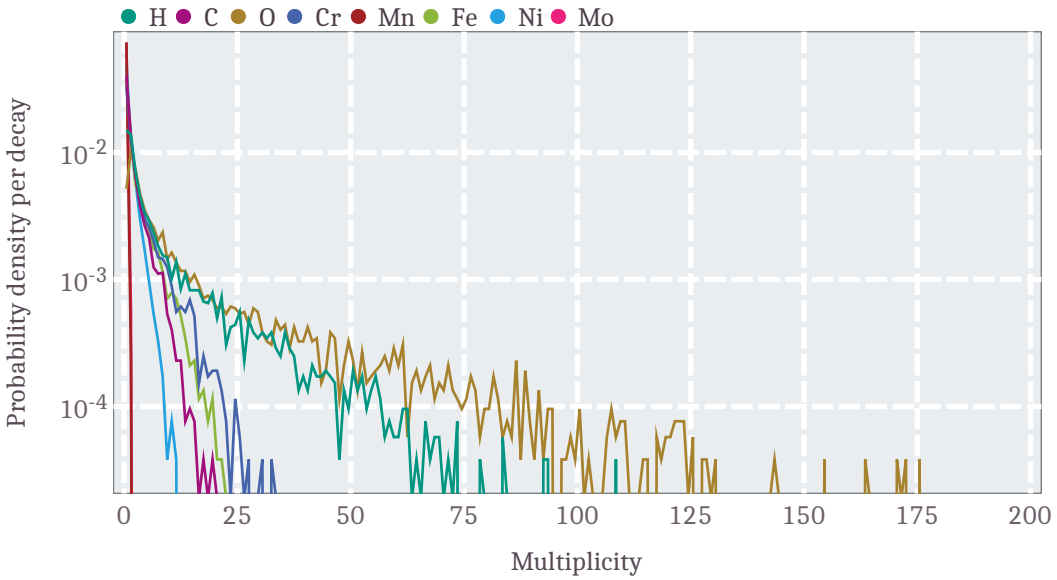

Figure 4.16.: Multiplicity spectra of the sputtered atoms, resolved for the individual atoms that are sputtered. 12360 recoils produce 812649 sputtered atoms, whereas about 76 % of the simulated decays ($N = 52275$) do not contribute.

Ionisation of Rydberg atoms

The current Rydberg background model only takes excited hydrogen and hydrogen-like atoms into account being ionised by black-body-radiation [8, 9, 96, 97]. The consideration of other atomic species was previously made in [85] and was further developed which will be discussed in sec. 7, including additional ionisation mechanisms. In the scope of this section, only excited hydrogen atoms are discussed as the electron mediator from the surface into the sensitive flux tube volume that leads to background electron generation by ionisation of excited states by black-body-radiation.

Rydberg atoms are highly excited atoms with their outer electron excited to a state of principle quantum number $n > 7$ [131]. Classical theories are capable to describe some properties of Rydberg atoms such as their size and the electron binding energy. The orbital radius

$$r_n = \frac{4\pi\epsilon_0 n^2\hbar^2}{Z m_e e^2} = a_0 \frac{n^2}{Z} \,, \tag{4.7}$$

according to the Bohr model [132], is expressed by the principal quantum number n, the reduced planck constant $\hbar$, the vacuum permittivity ϵ_0, the elementary charge e, the electron mass m_e, and the atomic number Z. For a hydrogen atom in its ground state ($Z = 1, n = 1$) this radius is called Bohr radius with $a_0 = 0.529\,\text{Å}$. The binding energy of hydrogen-like atoms can be expressed, using the Rydberg formula [131] which is given by

$$E_n = -\frac{Z^2 Ry}{n^2} = -\frac{Z^2}{n^2} \cdot 13.606\,\text{eV} \,, \tag{4.8}$$

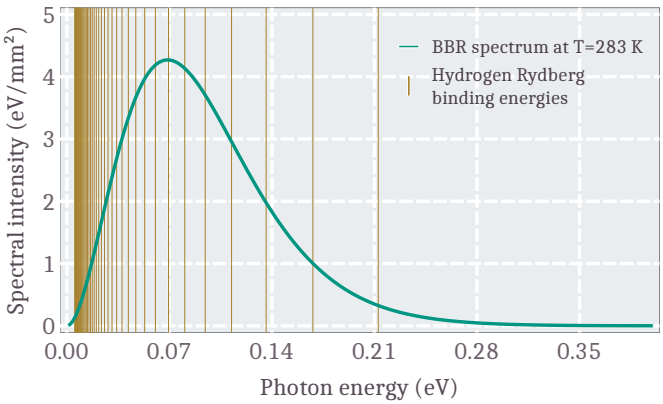

Figure 4.17.: Continuous spectral intensity spectrum of the black-body-radiation photons at $T = 283\,\mathrm{K}$ (green), according to Planck's law [134]. Absolute hydrogen Rydberg atom electron binding energies E_n from eq. 4.8 for principal quantum numbers $n = 8 - 50$.

with the approximate Rydberg constant in units of energy $Ry = 13.606\,\mathrm{eV}$. As atoms, other than hydrogen, are highly excited to states with additional large angular momentum quantum numbers l, these can be treated like heavy hydrogen atoms, as the outer electron is only affected by the cumulative charge of the remaining ion. However, the effect of multi-electron atoms on the binding energy of the outer electron can be described by

$$E_{nl} = -\frac{Z_c^2 Ry}{(n-\delta_l)^2} = \frac{Z_c^2 Ry}{(n^*)^2}\,, \tag{4.9}$$

with the quantum defect δ_l which accounts for core penetration (low-l states) and core polarisation (high-l states), and the charge of the core Z_c which alters the binding energy [133].

The BBR spectrum is given by Planck's law [134] which can be expressed in terms of the photon energy to

$$B(E,T) = \frac{E^3}{4\pi^3 \cdot (\hbar c)^2} \cdot \frac{1}{e^{E/k_B T} - 1}\,. \tag{4.10}$$

The spectral intensity of the BBR spectrum is given in fig. 4.17. It contains a maximum at about 0.07 eV photon energy which matches the binding energy E_{14}. Photo-ionisation by BBR photons of excited hydrogen atoms

$$\mathrm{H}^* + \gamma_{\mathrm{BBR}} \longrightarrow \mathrm{H}^+ + \mathrm{e}^- \tag{4.11}$$

occurs, when the photon energy E_{BBR} exceeds the ionisation threshold of the excited atom. The system of interacting Rydberg atoms with black-body-radiation do not only consist of ionisation. Every excited atom is able to decay radiative to a lower-lying state spontaneously and the BBR photons can tune stimulated emission of photons and absorption that leads to higher-lying states of the atom [135].

These transitions were embedded into a background model developed by N. Trost [9] that leads to the ejected electron spectra in fig. 4.18. Most of the BBR photons have

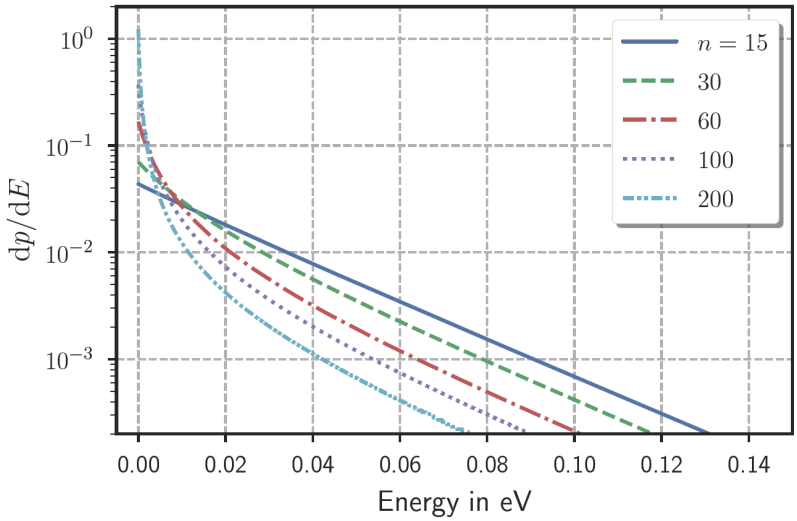

Figure 4.18.: Electron energy spectrum by BBR photo-ionisation of Rydberg atoms. The energy spectra are obtained for different principal quantum numbers n at $l = 1$ and $T = 293\,\mathrm{K}$ [9].

energies below 150 meV, which means that the ejected electrons also have low energies. These kinetic energies of the electrons are well below the spectrometer resolution eq. 3.2 while they have no trapping probability and are thus transferred to the detector or the source side, indistinguishable from beta electrons.

Observations regarding the background rate dependence on the inner electrode potential difference fig. 4.9 and the temperature were resolved in the model [9].

However, measurements of special electromagnetic field settings predict the existence of higher energetic electrons up to the order of eV and several hundreds of meV [77, 96]. These results are strongly influenced by the underlying background model and electromagnetic field calculations which are used to analyse the data. Since the background origin must be modelled in 3D within the main spectrometer, the results can be distorted. Energies on the eV-scale are in conservative contradiction to performed electron trapping measurement with very good spectrometer resolutions at low retarding potentials [97], also here the electromagnetic field calculations are essential but independent on the entire volume background distribution. The electrons with energies on the order of eV can be assumed to arise from residual contribution of radon decays [96], but the origin of background electrons with energies which are not achievable via BBR-induced photo-ionisation of Rydberg atoms remain unresolved.

Further investigations regarding the energy spectrum of the background electrons, originating inside the main spectrometer at KATRIN will be discussed in sec. 6.4.

Part III.

Analysis and simulation of background

5. Background systematics for neutrino mass measurements

In this section the main parameters regarding the background at KATRIN neutrino mass (KNM) measurements KNM2-KNM5 are discussed, as the description of the KNM1 data was made in [96]. The veto cut of 1 µs coincidence interval was applied to all data of the background points above the endpoint of the tritium beta spectrum E_0 presented here. Firstly, time-variations during the campaigns and the effect of non-Poisson events which broaden the events per subrun distribution are discussed. This leads to a systematic effect as the uncertainty on the background becomes larger which further had to be taken into account in the final neutrino mass analysis. Event distribution broadening due to non-Poisson events is presented in more detail with respect to the contribution by residual radon and in comparison of the NAP to the SAP configuration in section 5.1.3. The non-Poisson broadening is the largest systematic in the recent neutrino mass analysis of the combined data KNM1 and KNM2, where an upper limit on the effective neutrino mass of $m_\nu < 0.8\,\mathrm{eV}(c = 1)$ was derived [4]. Thirdly, the background level variations as a function of the applied retarding potential qU also impacts the neutrino mass sensitivity. Subsequent, the most recent detected background systematic which arise by the inter-spectrometer penning trap, leading to a scan-step-duration-dependent background, will be described. The section is concluded with the background systematic evolution over these campaigns and the projection for the final neutrino mass sensitivity based on the presented systematic inputs.

5.1. Distribution broadening by non-Poisson effects

5.1.1. Description of the non-Poisson fraction Σ_{np}

The non-Poisson fraction, or broadening, Σ_{np} describes a quantitative value of the electron counts distribution within the time length of one subrun. The current KATRIN background consists of mainly three contributions: detector background, residual radon background, and Rydberg-induced background that have been described in section 4. The detector and the Rydberg-induced background manifest itself as a stochastic processes that can be described by Poisson statistics. The Poisson distribution and its standard deviation

$$P_\lambda(k) = \frac{\lambda^k e^{-\lambda}}{k!} \approx \frac{e^{k(1+\ln(\lambda/k))} - \lambda}{\sqrt{2\pi(k+1/6)}} \quad \text{with} \quad \sigma_\lambda = \sqrt{\lambda}\,, \tag{5.1}$$

are used to model random processes. The distribution with the number of occurrences k and the mean value λ, which is equal to the variance by definition, can be approximated

with Stirling's formula. The standard deviation is given by the square-root of the mean λ. For large mean values λ, the Poisson distribution can be approximated by a Gauss distribution with $\mu = \lambda$ and $\sigma_\mu = \sigma_\lambda$ which is shown in fig. A.6. This will be utilised to describe the non-Poisson broadening. The mean μ and standard deviation σ_μ of a given data set $E = e_1, ..., e_k$ with entries k can be calculated according

$$\mu = \frac{1}{k}\sum_{i=1}^{k} e_i \equiv \lambda \quad \text{and} \quad \sigma_\mu = \sqrt{\frac{1}{k}\sum_{i=1}^{k}(e_i - \mu)^2}\,. \tag{5.2}$$

The fraction of the individual determined uncertainties describes the broadening of the background event distribution

$$\Sigma_{\text{np}} = \left(1 - \frac{\sigma_\lambda}{\sigma_\mu}\right) \cdot 100\,\%\,. \tag{5.3}$$

The distribution becomes broader than expected from a Poisson distribution if additional processes contribute which affect the measured counts within one subrun, whereat $\sigma_\mu > \sigma_\lambda$ holds.

An exemplary Monte Carlo data set is shown in fig. 5.1 of a typical background electron counts distribution. The rate, going into the MC, is $r = 200$ mcps within time intervals of $t = 360$ s and a total measurement time of $T = 300$ h. The expected mean number of electrons λ for the simulation is simply given by the product of the rate and the time interval $\lambda = r \cdot t = 72$. When simulating background events, and assuming a Gauss distribution, the mean again is given by $\mu = \lambda$. In the case of this data set, the standard deviation is $\sigma_\mu = 1.11\sigma_\lambda$. This is an equivalent to an overdispersion of 11 %. For this trial campaign, the distribution broadening could be reproduced with a value of $\Sigma_{\text{np}} = 11.3\,\%$

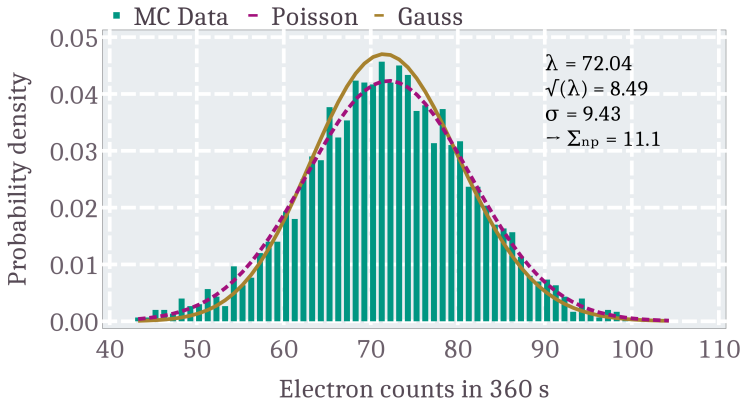

Figure 5.1.: Monte Carlo data set E of a broadened electron counts distribution. The input parameters are a rate of $r = 200$ mcps, time intervals of virtual subruns of $t = 360$ s, and a total measurement time of $T = 300$ h. This results in 3000 entries and a non-Poisson broadening of 11 %.

and a slightly enlarged mean value of $\lambda = 72.18$ counts. However, the uncertainty on Σ_{np} strongly depends on the measurement time. 300 h of background measurement time within campaigns are usually not achieved, as can be seen in tab. 5.1. Therefore, a Monte Carlo simulation with respect to the uncertainty of the observed non-Poisson fraction is performed and shown in fig. A.7. For truly small values of Σ_{np}, there remains some probability that the data fit negative values of the broadening that originate from less statistics. For these cases, the non-Poisson fraction assumed to be zero.

5.1.2. Temporal changes of the background rate

Fluctuations of the background level during a campaign are indirectly taken into account as systematics of the neutrino mass measurements by the non-Poisson broadening. In previous works, the correlation of background electrons within the main spectrometer volume with processes on the surface was investigated [96, 99, 136, 137]. It has been shown that the inner surface and its properties influence the background level. Over time, the amount of atoms adsorbed on the surface can change and thus influence the background level.

An overview on the individual parameters of KNM background data, including the linear fit over time for different campaigns is summarised in tab. 5.1. As different parameters were sometimes changed during a campaign, the data sets were split, e.g. during KNM4 different MTDs were tested. According the underlying MTD, every background point during one scan is measured for a certain amount of time, the subrun length T_{subrun}. The amount of background points times the individual subrun length results in the total background measurement time T_{meas}. The variations on the fit slopes from the different campaigns are large, especially also negative slopes were fit, with partly large uncertainties due to small

Table 5.1.: Parameters extracted from KNM measurement campaigns KNM2-KNM5. T_{meas} is the total time of the campaign spent in the background region above E_0, whereas T_{subrun} describes the mean time spent per individual retarding potential in the background region within one scan. The data are fit with a linear function $f(x) = a \cdot t + b$ with slope a and constant b. Here, t_0 is set to the begin of the individual campaigns. Furthermore, the non-Poisson fraction Σ_{np} is given.

Campaign	T_{meas} (h)	T_{subrun} (s)	slope ($^{\mathrm{mcps}}/_{\mathrm{day}}$)	const. (mcps)	Σ_{np} (%)
KNM2	178.73	357.46	0.359(39)	194.90(102)	12.9
KNM3|A	45.35	286.45	−0.047(201)	112.83(164)	−3.8
KNM3|B	57.62	357.64	0.561(279)	213.68(206)	12.5
KNM4|A	38.47	285.51	0.254(307)	122.40(189)	6.5
KNM4|B	103.23	429.65	−0.188(75)	127.75(117)	0.4
KNM4|C	29.84	429.62	−0.282(356)	126.60(238)	−4.4
KNM4|D	60.24	97.69	0.098(98)	116.28(138)	−0.5
KNM4|E	21.16	97.77	−1.568(656)	120.64(244)	−1.9
KNM5	255.96	429.58	0.020(13)	132.40(67)	0.1

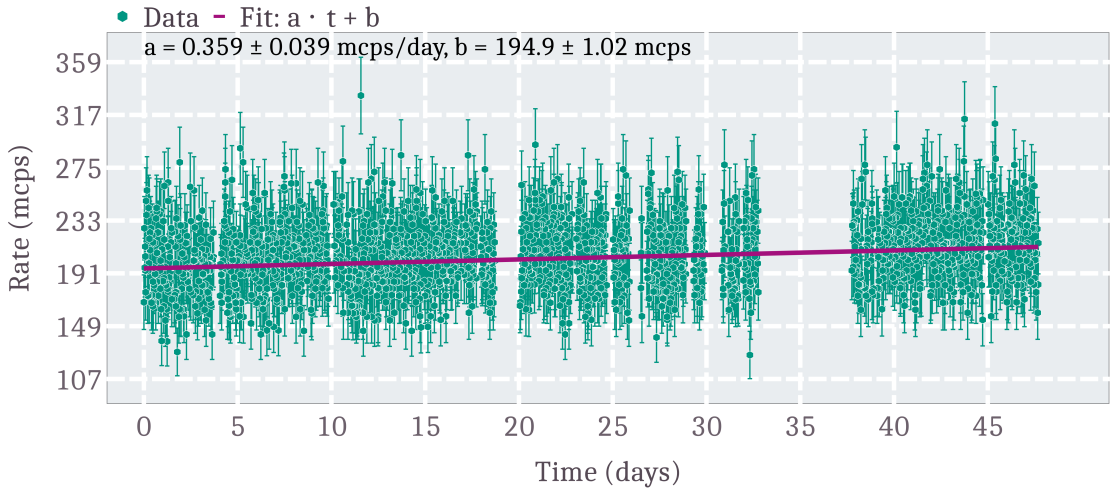

Figure 5.2.: Background rate evolution of KNM2 background data with $|U| > 18\,576\,\mathrm{V}$. Each data point represents the rate of one subrun with a mean length of $T_{\mathrm{subrun}} = 357.46\,\mathrm{s}$. Purple line: linear fit of the background rate with the slope $a = 0.359(39)\,\mathrm{mcps/day}$ and constant offset $b = 194.90(102)\,\mathrm{mcps}$ at $t_0 = 0$.

statistics. However, further effects can affect the background level in time, such as the vessel temperature or the pressure if not kept on a stable level. Additionally, changes on the surface properties over time can not be excluded so a slowly increasing background level is the consequence. This is more pronounced in measurements performed in the NAP configuration. During KNM2 and KNM3|B where the background rate is higher due to the larger flux tube volume, also a positive slope and increased non-Poisson broadening is observed. The non-Poisson broadening Σ_{np} describes the additional uncertainty on the measured background rate from the comparison of Gauss and Poisson distribution on the event counts during one subrun. Therefore, a time-dependent background level acts as a non-Poisson contribution.

In fig. 5.2, the background rate evolution over time during the KNM2 campaign is shown. Each data point corresponds to a rate observed for one subrun of different retarding potential values. The background region $qU > E_0$ is defined as $|U| > 18\,576\,\mathrm{V}$ which is above the tritium endpoint. In general, five different background points are chosen which contribute equally, when no retarding potential slope is present. This will be further discussed in section 5.2. The histogram of the electron counts within the subruns is shown in fig. 5.3a. This representation is used to estimate the non-Poisson broadening Σ_{np} which amounts to 12.9 % with application of the veto-cut (see sec. 4.2). Such a broadening is partially the result of a time-dependent background, as shown for the KNM2 data in fig. 5.2 with a non-vanishing slope over the duration of the campaign of $0.359(39)\,\mathrm{mcps/day}$. To investigate the effect of rising background on the event distribution in particular on the non-Poisson fraction Σ_{np}, a Monte Carlo simulation has been performed.

Parameter inputs to the simulation are a vanishing non-Poisson fraction $\Sigma_{\mathrm{MC}} = 0$, the relative subrun time stamps of the background data taking t_i, the fit slope a and its offset

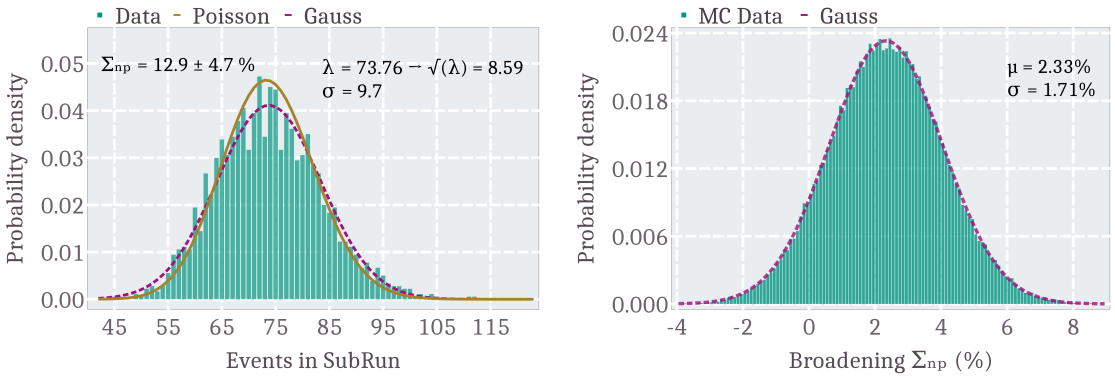

(a) KNM2 background data.

(b) Slope impact MC.

Figure 5.3.: (a): Subrun-wise event distribution of the KNM2 background data. A Poisson (gold, solid) and Gauss (purple, dashed) distribution are included, as well as the non-Poisson fraction $\Sigma_{\mathrm{np}} = 12.9(47)\,\%$. The here shown error on Σ_{np} is only qualitatively estimated from the standard errors on the individual standard deviations. **(b):** Monte Carlo (MC) simulation of the non-Poisson broadening due to a rising background level as obtained for the KNM2 campaign. 10^5 samples were generated for the KNM2 subrun timestamps were used with a vanishing non-Poisson broadening input.

b, and the mean subrun length T_{subrun}. For each background point in the timeline of the KNM2 data set, the number of events of each subrun is sampled according a Poisson distribution with mean $\lambda_i = (a \cdot t_i + b) \cdot T_{\mathrm{subrun}}$ which is done 10^5 times. For each iteration the non-Poisson broadening Σ_{np} is calculated and shown in fig. 5.3b. The mean of the broadening distribution is 2.34 % with a standard deviation of 1.71 %. The time-rising background level leads to a non-Poisson broadening of the background rate distribution, which directly affects the statistical uncertainty on the individual data points during KNM measurements as the mean background rate has larger uncertainty than assumed from the Poisson statistics.

However, as can be seen in fig. 5.3a, the non-Poisson broadening systematic in the KNM2 campaign is even larger and amounts to 12.9 % which cannot only be explained by a time-dependent background rate. In addition for the KNM3|B campaign, a similar broadening is found, which are assumed to arise from residual radon decays within the main spectrometer (sec. 5.1.3). These two campaigns were performed in the former standard NAP configuration (sec. 3.2.1.1) while the remaining have been performed in the SAP configuration (sec. 3.2.1.2) which can also be seen in the reduced constant offsets of the linear fits as the background level is reduced. To reduce the non-Poisson background rate overdispersion is of major relevance as it accounts for the largest systematic on the current upper limit on the neutrino mass [4]. This was successfully reached by changing from the NAP to the SAP configuration as the non-Poisson fractions Σ_{np} are strongly reduced or negative and consistent with zero, while negative values occur at campaign parts of short measurement time.

5.1.3. Radon proportion in the comparison of NAP and SAP

As the observed non-Poisson broadening Σ_{np} at the KNM2 and KNM3|B measurements in the NAP configuration cannot arise from large time-dependent background fluctuations, they are assumed to result from residual radon decays within the main spectrometer. When radon decays, several electrons with up to keV energy are generated which are likely to be magnetically trapped (see sec. 4.4). While trapped, secondary electrons are generated due to scattering and ionisation of residual gas. As this process is not random, as it depends on the energy of the electrons and the pressure within the main spectrometer, a non-Poisson broadening of the event distribution emerges.

Derivation of the total amount of Radon-induced events during KNM measurements is not possible, as the only imprint is done by the broadening of the electron counts distribution (fig. 5.3a) at the UHV condition of $p \simeq 4{\times}10^{-11}$ mbar. High energetic electrons at such low pressures are trapped over several minutes up to hours so the correlation of secondary electrons that arise from the same primary electron cannot be backtracked as the inter-arrival time between these largely exceeds the subrun length and the run lengths to some extend. The inter-arrival time of Radon-induced secondary electrons on the FPD can be simulated using Kassiopeia, which can be seen in fig. A.8. Simulations of Radon-induced electrons have been performed for the NAP and SAP electromagnetic field configuration. The gathered inter-arrival data of Radon-induced electrons at the FPD can then be used to model the background rate with the nominal Poisson-behaving background time structure and the additional times, induced by radon decays, with a total rate

$$R_{\mathrm{BG}} = A \cdot R_{\mathrm{Poisson}} + B \cdot R_{\mathrm{Radon-induced}}\,, \tag{5.4}$$

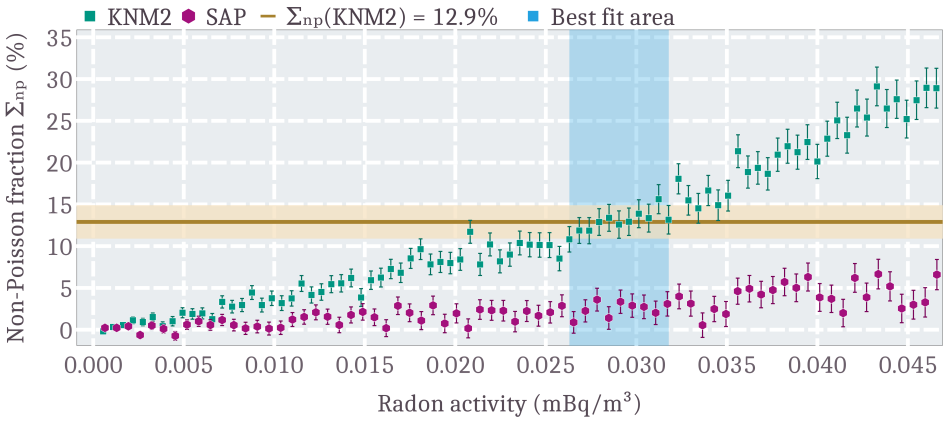

Figure 5.4.: Estimate on the non-Poisson broadening for SAP (purple) and NAP (green) configuration by different modelled Radon activities per cubic meter. The horizontal line represents the non-Poisson fraction as measured for the KNM2 campaign of 12.9(20) % and the blue shaded area denotes the best fit area on Σ_{np}(KNM2) with respect to the radon activity per cubic meter. The individual total flux tube volumes are $V_{\mathrm{NAP}} = 365\,\mathrm{m}^3$ and $V_{\mathrm{SAP}} = 309\,\mathrm{m}^3$.

through which the individual contributions of Radon- and Rydberg-induced background can be modelled to compare it with the measurements. In the scope of this observation, both the KNM2 background data and background data recorded after this measurement campaign in the SAP configuration are used. The model rates are $R_{\mathrm{BG,KNM2}} = 200\,\mathrm{mcps}$ and $R_{\mathrm{BG,SAP}} = 120\,\mathrm{mcps}$ and comparable with the measurement observations. From the radon decay simulations the fraction of electron arrivals per decay (cluster size) can be derived which are shown in fig. A.9.

Hereby, the consecutive occurrence in time of either Rydberg- or Radon-induced background electrons is diced from an exponential distribution, according Poisson statistics with the individual rates according eq. 5.4. The parameter B is changed by varying the decay rate of radon from 0.2 mBq to 18 mBq. For each decay, the inter-arrival times are collected in accordance with the diced amount of electrons from the cluster size distribution for this particular decay. In that sense, a list of events is filled with electron events distributed in time which correspond to a background rate $R_{\mathrm{Radon-induced}}$. Subsequently, the Rydberg, Poisson-behaving, background rate R_{Poisson} is derived to calculate the parameter A so that the model background rates $R_{\mathrm{BG,KNM2}}$ and $R_{\mathrm{BG,SAP}}$ are recovered.

The result of this simulation is shown in fig. 5.4 with the estimates on the non-Poisson fraction Σ_{np} as a function of the radon activity within the individual total flux tube volumes. The strong reduction for the SAP configuration arise from two effects: on the one hand the reduced electron arrival probability of electrons which are generated within the total SAP flux tube volume as the sensitive volume is reduced to 19.5 % of the total volume. The sensitive flux tube volume for the NAP configuration amounts to 48.6 % of the total flux tube volume, through which the Radon-induced background electron arrival probability becomes larger. On the other hand, the cluster size (electron arrivals on the FPD per radon decay) is also suppressed due to the downstream shifted sensitive flux tube. In average, 3 times more electrons arrive at the detector for the NAP configuration that was used during the KNM2 and KNM3|B campaigns, leading to non-Poisson fractions on the order of 10 %. The best fit area, shown in fig. 5.4, corresponds to a value of the simulated broadenings of $\Sigma_{\mathrm{np,NAP}} = 12.9(5)\,\%$ for the KNM2-like data and $\Sigma_{\mathrm{np,SAP}} = 3.2(5)\,\%$ for the SAP which is caused by a mean radon activity of $29.04(17)\,\mu\mathrm{Bq\,m^{-3}}$. Meanwhile, the LN2 pre-cooling (see sec.4.4) was installed before KNM3, so that the residual amount of radon could be further reduced that matches the results of the observed non-Poisson fractions, which are compatible with a vanishing broadening (see tab. 5.1) in line with statistics.

Eliminating the non-Poisson fraction systematic by measuring the tritium beta spectrum in the SAP configuration results in an enhanced neutrino mass sensitivity at the KATRIN experiment. For that reason, the SAP configuration evolved to the standard measurement configuration for neutrino mass measurement since KNM4.

5.2. High-voltage-dependent background slope

Another systematic effect on the neutrino mass originates from a potentially varying background with the applied retarding voltage $|U_{\mathrm{ret}}|$ on the main spectrometer. It accounts for the third largest background-related systematic with $0.06\,\mathrm{eV}^2$ on the squared neutrino mass m_ν^2 at the KNM1-KNM2 combined analysis [4]. That the background rate as a

Table 5.2.: Retarding potential slopes fit parameters from KNM measurement campaigns KNM2-KNM5. A linear fit is performed providing a slope over retarding potential a and a rate offset b and the corresponding uncertainties $\sigma_{a,b}$. ΔU denotes the potential range of which the background data are taken and fitted.

Campaign	a (mcps/kV)	σ_a (mcps/kV)	b (mcps)	σ_b (mcps)	ΔU (V)
KNM2	16.05	11.40	205.7	0.7	135
KNM3|A	4.99	16.86	115.6	1.1	135
KNM3|B	−28.70	20.60	222.0	1.3	135
KNM4|A	15.31	45.05	127.2	1.7	60
KNM4|B	1.98	27.64	127.6	1.0	60
KNM4|C	−12.56	51.30	127.4	1.9	60
KNM4|D	16.94	36.34	128.3	1.3	60
KNM4|E	−42.10	60.87	127.6	2.2	60
KNM4 comb.	2.48	17.65	127.7	0.7	60
KNM5	−1.41	18.08	135.7	0.7	60

function of the high voltage is not stable is known from former background measurements [8, 9] especially at low retarding potentials $|U_{\mathrm{ret}}| < 10\,\mathrm{kV}$. It is recognised to level out at higher potentials [9], but a residual slope due to decays of residual radon atoms or other effects cannot be excluded with confidence on the small values of these slopes within the potential range used at beta scans. Radon-induced electrons of high energy possess different surplus energies above the retarding potential, which potentially affects the trapping conditions and therefore the background rate. According the MTD at KNM measurements, the background points are distributed over a potential range ΔU, which is shown in tab. 5.2, to reasonably monitor the qU-dependent background slope. In table 5.2, the fitted slope and offset parameters with their uncertainties for the individual campaigns are shown. Hereby,the background subrun data of a particular high voltage set point are stacked to receive the background rate at this set point. So, a linear model as a function of the applied retarding potential can be fit to the data. Since the uncertainty of the individual background rates is rarely less than 1 mcps, the uncertainty of the slopes are always large and less significant. For this reason, stand-alone measurements of the background slope had to be carried out in order to obtain more reliable values for the background slopes for NAP and SAP, which will be included in the systematic budget.

At measurements in NAP configuration (KNM1,2,3|B) a conservative slope value was used as systematic input that was achieved from measurements taken in 2018. Adjustments regarding the region of interest and the pixel selection due to a different wafer and pixel-cuts, lead to an uncertainty of the slope of 4.74 mcps/kV that matches a vanishing slope as the central value is smaller than its uncertainty [4]. As the majority of beta scans up to now were taken in SAP configuration, a dedicated measurement in this configuration was performed in 2020 of about 200 h measurement time. With application of the veto-cut, the current pixel, and ROI selection, valid for KNM3 and afterwards, a background retarding potential slope of $a = 2.1 \pm 1.2\,\mathrm{mcps/kV}$ was derived. The data were taken in a

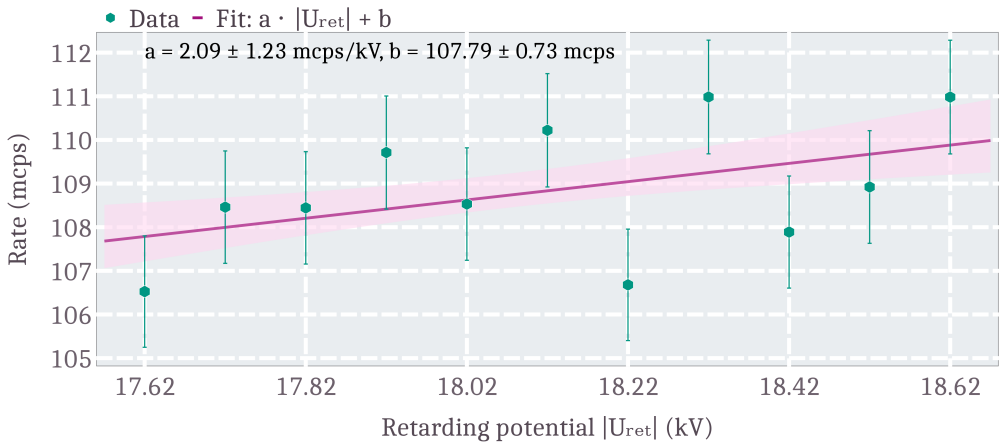

Figure 5.5.: Dedicated background slope measurement in the SAP configuration. A slope of $a = 2.09\,^{\text{mcps}}/_{\text{kV}}$ with an uncertainty of $\sigma_a = 1.23\,^{\text{mcps}}/_{\text{kV}}$ was fitted to the data with the retarding potential ranging from 17 620 V to 18 620 V. The same ROI (22-34 keV) and pixel-cut (app. 8) is applied, as for the KNM measurements in SAP configuration KNM3|A, KNM4, and KNM5.

broad retarding potential range of ΔU = 1 kV ranging from 17.62 kV to 18.62 kV which is shown in fig. 5.5. Such a broad potential range is beneficial to constrain the background slope from data points with less statistics in particular in SAP configuration as the mean background rate is on the order of 130 mcps. Although a combination of the KNM4 and KNM5 campaigns would be feasible, since the measurement configurations are the same with respect to the background, only a non-significant background slope with an even larger uncertainty of $\sigma_a = 12.7\,^{\text{mcps}}/_{\text{kV}}$ within the 60 V wide potential range, but a total background measurement time of 509 h, can be achieved. No correct way of deriving the background slope and its uncertainty from measurements exists. Also for this SAP slope measurement a different potential range consideration can be applied, so that the slope is different. Exemplary, the potential range of ΔU = 0.7 kV, ranging from 17.92 kV to 18.62 kV results to a slope of $a_{0.7} = 1.0 \pm 2.0\,^{\text{mcps}}/_{\text{kV}}$. However, the correct consideration in the final analysis is most important, where a wrong slope value would cause neutrino mass bias, while a large uncertainty turns out as large systematic uncertainty on the neutrino mass result. Only additional background measurements, for which a large amount of time has to be spent, can further improve the background slope constraint and thus reduce the systematic budget for this background feature.

5.3. Effect of the inter-spectrometer Penning trap

As introduced, the recent discovered background systematic arise by the inter-spectrometer Penning trap. The Penning trap background is described in sec. 4.3 and reasonable background rate occurs when both spectrometers are operated with high voltage and the pressure is putatively larger than $1{\times}10^{-10}$ mbar with no Penning-wiper operation [3, 83,

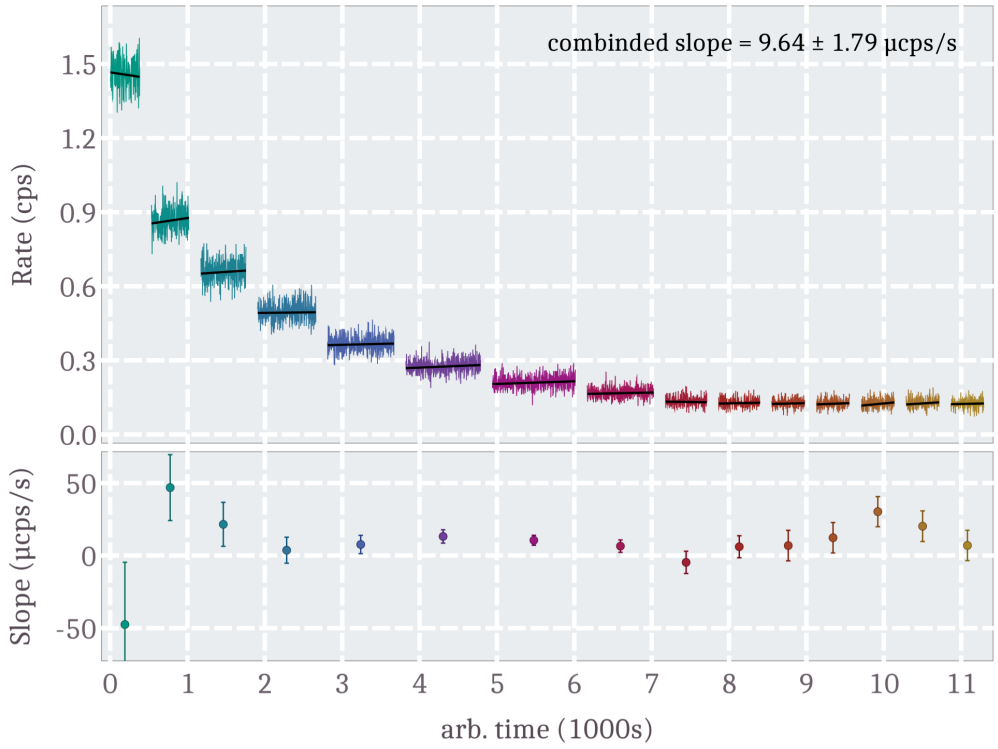

(a) Subrun-wise background rate.

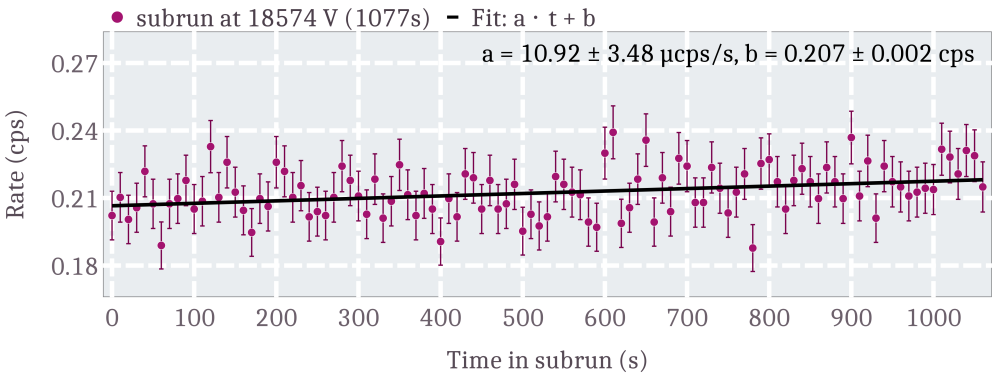

(b) Background rate at 18 574 V.

Figure 5.6.: (a): Investigation on the scan-step-duration-dependent background during KNM4|B. Data are stacked for different high voltage set points that represent the longest subruns at the endpoint and background region of the MTD, denoted by their colour. The potential ranges from 18 567 eV to 18 641 eV divided into 15 subruns of highest retarding potential which are taken into account. Each subrun is fit individually and the slope parameters are combined to a common slope value of $a = 9.64 \pm 1.79$ µcps/s. **(b):** Background rate as a function of time for the longest subrun at 18 574 V with a duration of $T_{\text{subrun}} = 1077$ s. A linear slope of $a_{\text{long}} = 10.92 \pm 3.48$ µcps/s was fitted for the binned rates of 10 s intervals.

88]. During KNM measurement the Penning wiper is activated before a subrun starts. Previous measurements showed, that significant background rates due to the Penning trap with current UHV-conditions are not expected [83] and the regular wiper operation remains as a safety element.

It turned out during KNM4|B that this assumption could not be validated, as an adjusted MTD with longer subrun times T_{subrun} was used. In fig. 5.6b the observed rate at 18 574 eV retarding potential is shown, which revealed a time-dependent background slope within the scope of one subrun. Fitting a linear model to the data yields to a sufficiently significant slope of background increase of $a_{\text{long}} = 10.92 \pm 3.48$ µcps/s during this subrun. The systematic input is extracted by the combination of linear models fitted individually to the longest subruns by calculating a combined slope as the weighted mean of the time-dependent background increases during subruns according their subrun length T_{subrun}. On the top of fig. 5.6a, the measured rate as a function of time is shown. The data is sorted according to the applied retarding voltage and an artificial offset of 150 s between the subruns is included for better visibility. The highest rate corresponds to the high voltage set point at 18 567 V and the last subrun to the background point at 18 641 V. The individual slopes of the subruns are shown on the bottom of fig. 5.6a which are used to calculate the combined slope to $a = 9.64 \pm 1.79$ µcps/s which is of high confidence as its uncertainty is comparably small.

The overview of the subrun-duration-dependent background slopes of the campaigns KNM2-KNM5 is shown in tab. 5.3. Positive, non-negligible slopes were determined for the KNM2-KNM4|C measurement campaigns, with KNM4|B showing the effect most reliably. KNM4|D and E have to be excluded because both the maximum subrun times (97 s) and the total measurement times were too short to provide sufficient statistics. Therefore, they are only listed for the sake of completeness. These values, or comparably derived by a global fit of a common slope with different offsets according the distinct subruns, will be input for the upcoming KATRIN neutrino mass publication of the campaigns KNM1-KNM5.

Table 5.3.: Combined scan-step-dependent background slope of the individual campaigns KNM2-KNM5. The derived slope parameter a and its uncertainty σ_a. The total measurement time T_{total} which is used for the analysis and the duration of the longest subrun T_{long} of the dataset is given.

Campaign	a (µcps/s)	σ_a (µcps/s)	T_{long} (s)	T_{total} (h)
KNM2	3.04	2.93	645	630.65
KNM3|A	11.50	3.68	717	194.11
KNM3|B	11.68	5.31	645	197.36
KNM4|A	3.36	4.37	717	165.02
KNM4|B	9.64	1.79	1077	442.35
KNM4|C	4.80	5.70	585	96.34
KNM4|D	77.90	83.34	97	45.18
KNM4|E	−73.76	138.67	97	15.87
KNM5	−0.40	1.11	1256	922.91

Worth highlighting is the combined slope for the KNM5 measurement, resulting in a zero-compatible value of $a = -0.40 \pm 1.11\,\mu\text{cps/s}$. Due to this systematic background effect, which takes up a large part of the systematic budget (see 3.2.3), grounding of the pre-spectrometer was undertaken as a consequence. Therefore, no scan-step-duration-dependent background, generated by the Penning trap can occur, which completely nullifies this systematics on following KNM measurements.

5.4. Neutrino mass sensitivities

At the beginning of neutrino mass measurements at KATRIN the background related sensitivities were dominated by the non-Poisson fraction Σ_{np} which increases the statistical uncertainty of the already large background rate of about 250 mcps in the NAP configuration during the campaigns KNM1, 2, and 3|B. This got vanished by changing to the SAP setting in the campaigns KNM3|A, 4, 5, and following. The Penning-trap-induced background systematic, detected during KNM4, raised to a large systematic contribution in the individual campaigns, especially in KNM3|A as the strongest. Since KNM5, the pre-spectrometer is grounded, through which no Penning-trap-induced background component can arise which leads to disappearance of this systematic. The background slope that depends on the retarding potential remains as the strongest systematic for KNM5 and following, but was the smallest in earlier campaigns. Dedicated background slope measurements in SAP configuration provide a well estimate on its uncertainty, so that this systematic contribution accounts to 0.01 eV^2, while the others got canceled. In first-order, the individual contributions can be summed quadratically to obtain the overall systematics

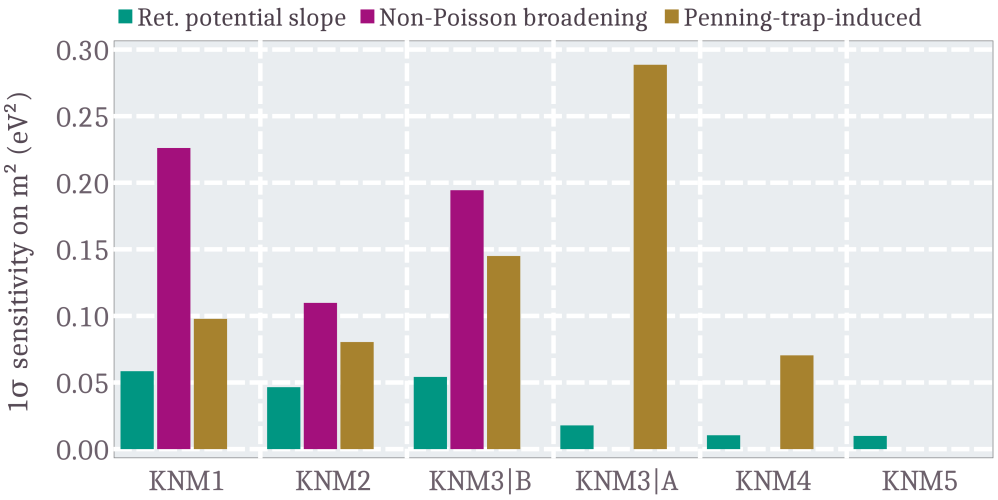

Figure 5.7.: One σ squared neutrino mass sensitivities of the different background related systematics raised by the non-Poisson broadening, the retarding potential slope and the Penning-trap-induced scan-step-duration-dependent background for the individual campaigns KNM1-KNM5.

of each campaign. The total background related systematic in KNM1 was 0.254 eV^2 which evolved to a total background systematic budget of 0.01 eV^2 at KNM5.

Therefore, the final neutrino mass sensitivity is no longer dominated by background systematics as they amount similarly in the budget to other systematics, as shown in sec. 3.2.3. The neutrino mass sensitivity would have been remain poorly if the measurements would have been continued in configurations similar to KNM1. However, the remaining dominant background systematic of the retarding potential slope of 0.01 eV^2 can be further improved with dedicated measurements.

6. Minimising the background level with micro-structured filters

Continued reduction of the background level at KATRIN is an important criteria for achieving the best possible neutrino mass sensitivity. In this section, the basic characteristics of the background electrons according the underlying Rydberg background model are described. In particular with respect to their final polar angle distribution at the detector. Novel concepts of investigations and future detectors regarding the minimisation of background electrons have been developed. These concepts are transverse energy filters whose basic principle will be described. Simulations of transmission properties of electrons through micro-structured honeycombs have been performed which are essential for a dedicated background measurement with a passive transverse energy filter (pTEF). The properties of the pTEF, as well as the measurement configurations, used in the measurement campaign from Dec. 2021 to Jan. 2022, followed by the data analysis and interpretation are described in sec. 6.4 with a verification on the Rydberg background model. Subsequent further research on micro-structured silicon wafers and micro-scaled scintillators as future detectors are discussed.

6.1. Characteristics of Rydberg background electrons

The time-scale in which background electrons had to be generated within the main spectrometer volume by sputtered Rydberg atoms is of interest. For this purpose, the SRIM simulations (sec. 4.5.3) can be used to derive the velocity of the atoms, and simulations with Kassiopeia are performed to calculate the maximal flight path of atoms leaving the inner main spectrometer surface. 10^5 neutral particles were uniformly distributed on the surface of the main spectrometer with initial inclination angles according to fig. A.5 and tracked through the main spectrometer until they hit the opposite surface. By comparing the start and end positions, the path length is determined, shown in fig. 6.1a. A pronounced peak at 9.8 m is visible, which results from the spectrometer diameter.

According the total velocity distribution of the sputtered atomic species (fig. A.4), the time of flight can be calculated. For each of the 10^5 simulated atoms, a velocity from the distribution is diced and the time of flight calculated, presented in fig. 6.1b. The atoms have energies in the eV-range, resulting in velocities on the order of $10\,\mathrm{km\,s^{-1}}$. In combination with the obtained path lengths, the time of flight distribution has a maximum at about 1 ms. This is the time scale on which the background electron generation, and therefore the ionisation of the excited Rydberg atom by black-body-radiation, must take place. As previously discussed (sec. 4.5.1), the background is assumed to consist of two components. A radially homogeneous and a radially increasing component. A radially

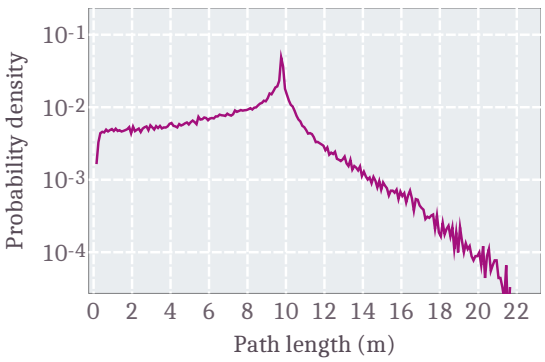

(a) Sputtered atom flight distance.

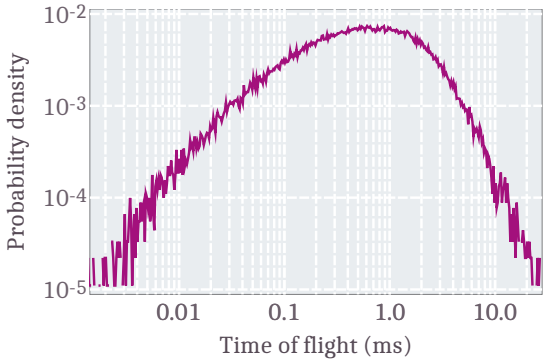

(b) Time of flight.

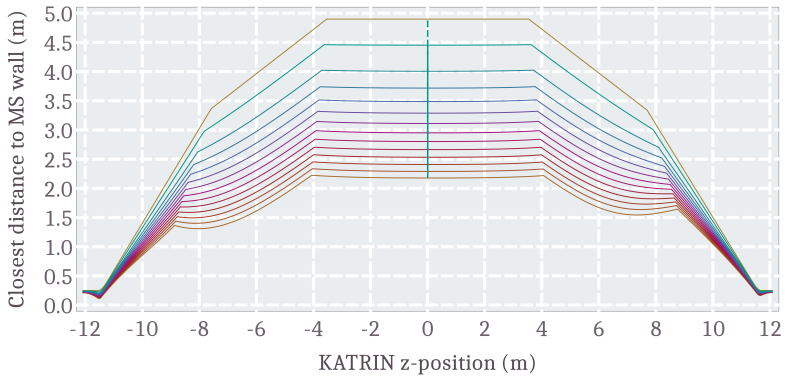

(c) Ring-wise closest distance to MS wall.

Figure 6.1.: (a): Simulated travel distance of sputtered atoms from the MS surface. 10^5 atoms have been simulated, starting uniformly distributed on the inner MS surface with starting pitch angles to the surface normal according the SRIM simulations (fig. A.5). **(b):** Time of flight distribution of sputtered atoms. The sum of the individual velocities (fig. A.4) was used in addition to the travel distance. **(c):** Closest distance to the inner main spectrometer surface along the magnetic field lines, mapped between the individual detector rings, as in fig. 3.7 for the 6.3 G NAP setting, with the analysing plane at the center (green line).

increasing rate results from states with short lifetimes below milliseconds, since these states are ionised before they reach the inner main spectrometer volume. A homogeneously distributed background density is achieved by long-lived states far above the millisecond range, so that they have an almost constant ionisation probability on their way through the main spectrometer volume. Therefore, the background electron generation density can not be constant in the flux tube volume. As can be seen in fig. 6.1c, the mean shortest distance along each magnetic field line of the FPD rings shrinks towards both ends of the main spectrometer. A local minimum is present in the area of the SAP analysis plane ($z \approx 6\,\mathrm{m}$), which is why most of the background is expected there. In the steep cone region ($z \gtrsim 8\,\mathrm{m}$) the magnetic field is dominantly formed by the super conducting pinch magnet

so that differences between the NAP and SAP configuration are minor, nevertheless, in fig. A.10 the closest distance to the main spectrometer vessel wall is shown for the SAP configuration.

On the basis of the electromagnetic field design and the assumption of shorter and longer living atomic states as the source of background electrons, the difference in the radial background profile on the FPD (fig. A.11) in NAP and SAP configuration can be explained. Although the sensitive flux tube in the SAP configuration is smaller by a factor of three (see sec. 3.2.1), the background rate is only halved. In particular, the background density (rate/volume) is increased and less homogeneous in the SAP configuration. It is increased by 50 % in the center of the sensitive flux tube volume and by more than 200 % in the outer flux tube regions, which originates from the shorter distances to the inner main spectrometer surface, where the excited Rydberg states are generated. Excited atoms in the sensitive flux tube of the SAP setting can be influenced by the electric field [9] of the main spectrometer retarding potential as a non-negligible gradient is present in this region, see fig. 3.8, which may lead to field-ionisation of the Rydberg atoms.

As shown in fig. 4.18, the kinetic energy of the background electrons generated from ionisation of Rydberg atoms by black-body-radiation are below approximately 100 meV. With this constraint, the final polar angle at the FPD can be calculated from the adiabatic motion approximation and eq. 3.4, which can be rewritten to

$$\theta_{\text{final}} = \arcsin\left(\sqrt{\frac{E_i}{E_f}\frac{B_f}{B_i}\cdot\sin^2(\theta_i)}\right), \tag{6.1}$$

where i is the initial state and f is the final state of the kinetic energy E, B is the magnetic field, and θ is the polar angle between the momentum and the magnetic field direction. Using this equation, a Monte Carlo simulation of the final polar angular distributions of electrons, generated inside the sensitive flux tube, was performed. The parameters of kinetic energy and magnetic field strengths are individually changed. For the simulation, presented in fig. 6.2, a symmetric magnetic field configuration with a minimum magnetic field of 5 G at the center was chosen. The initial direction of the electrons is isotropically distributed, while the initial kinetic energy is varied. The final magnetic field is fixed at 2.4 T which corresponds to the magnetic field at the FPD position. The initial magnetic field values are achieved by dicing positions randomly within the individual ring-wise sensitive flux tube volumes according the probability density along the z-axis which connects the mapped volume with the mean closest distance to the inside surface. Hereby, for each detector ring volume the same number of electrons are simulated and the normalised probability density distributions are shown in fig. A.12. The final kinetic energy is approximately equal to the applied retarding potential, where $E_f = 18.6\,\text{keV}$ was used.

For energies in the expected regime of the Rydberg background below 100 meV, final polar angles θ_f below 10° are obtained. The final polar angle distributions show pronounced peaks at their ends which correspond to the minimum magnetic field region in the center of the main spectrometer near the analysing plane. The tails to lower polar angles are also connected to the magnetic field as some electrons are generated closer to the pinch magnet within a stronger magnetic field, through which the final polar angle becomes small, according eq. 6.1. As beta electrons are isotropically generated in the WGTS, but in

a higher magnetic field, their minimum kinetic energy in the main spectrometer increases up to the spectrometer resolution (eq. 3.2) on the order of eV. An electron with 2 eV energy in the analysing plane which is transmitted to the detector, has a final polar angle to the magnetic field lines of about 45° at the detector.

6.2. Basic principle of transverse energy filters

The divergence on the final polar angle distribution for background and beta electrons that arise from the different kinetic energy in the main spectrometer flux tube is shown in fig. 6.3. The final polar angle distribution of background electrons with energies below 100 meV, according fig. 4.18, is narrow with angles below 10° compared to the distribution from beta electrons. These started isotropically in the WGTS within a strong magnetic field, however with high energy. The spectrometer resolution (eq. 3.2) and the acceptance angle (eq. 3.3) define their maximal kinetic energy in the main spectrometer analysing plane and therefore their final polar angle, which rises up to $\theta_{\text{max}} = 51°$.

The basic transverse energy filter principle is shown in fig. 6.4. Here, the filter acts as a geometrical boundary to electrons of high θ_f. Therefore, beta electrons will hit the filter and are blocked. Such a filtering device was used in the pTEF measurement campaign, which will be discussed in section 6.4. As the electrons are guided in magnetic fields, they fulfill a cyclotron motion around the guiding magnetic field line. The radius of this motion is given by the Larmor radius

$$r_{\text{Larmor}} = \frac{p_{\text{t}}}{|q|B} = \frac{\gamma m_0 v_{\text{t}}}{|q|B} = \frac{\gamma m_0 \cdot v\sin(\theta)}{|q|B} = \frac{v \cdot \sin(\theta)}{\Omega}\,, \tag{6.2}$$

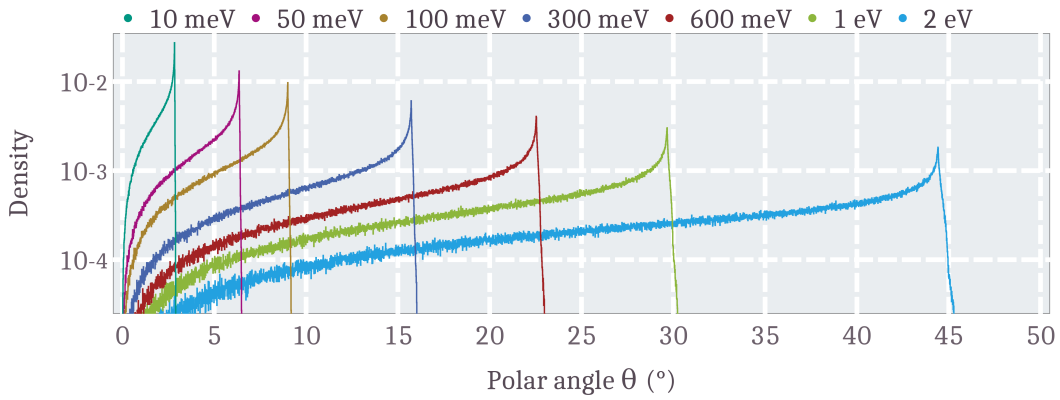

Figure 6.2.: Simulation of final polar angles for different kinetic starting energies in a 5 G symmetric magnetic field configuration. The momenta are distributed isotropically, while the positions are diced within the sensitive flux tube volume, according ring-wise probability distributions along the beamline axis (fig. A.12).

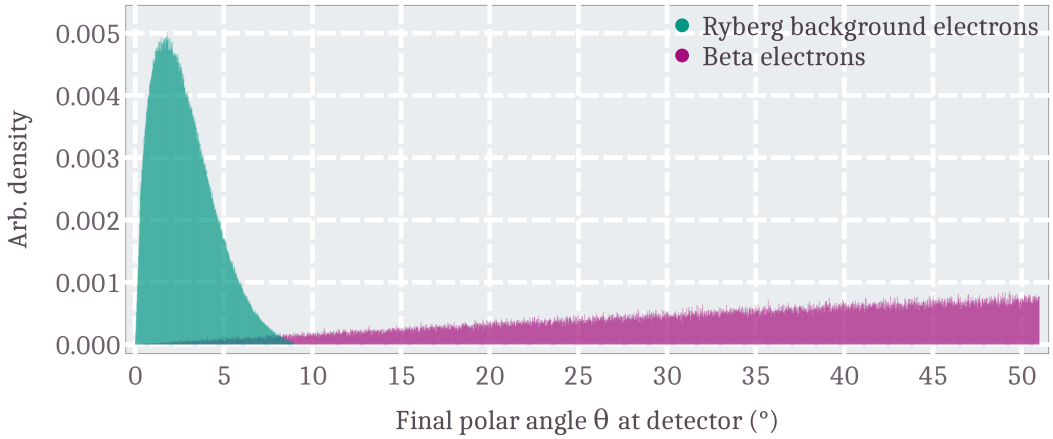

Figure 6.3.: Polar angle distribution of Rydberg background and tritium beta electrons at the detector. The Rydberg background electrons have energies according to [9] (fig. 4.18), and tritium beta electrons started isotropically in the source. The maximal angle of 51° results from the acceptance angle eq. 3.3.

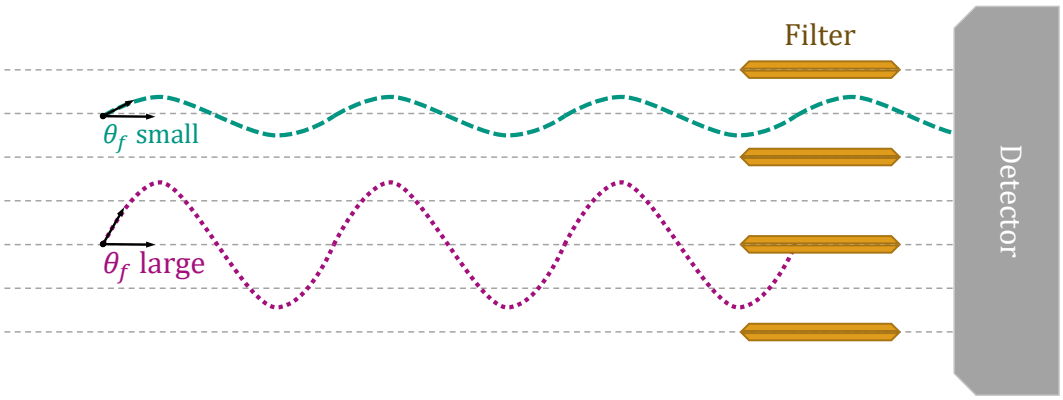

Figure 6.4.: Sketch of transverse energy filter principle. Electrons with small polar angles move on small Larmor radii, whereas electrons with high polar angles have larger Larmor radii. The technique shown here blocks electrons of high polar angles, while those with small angles are transmitted and detected.

and is defined by the transverse momentum with the relativistic angular frequency Ω and the magnetic field B. The Larmor radius increases with the transverse energy E_t which is defined by the transverse part of the velocity $v_t = v \cdot \sin(\theta)$. For example, the Larmor radii for electrons with 18.6 keV at the FPD with polar angles of 10° and 50° are 33.2 µm and 146.3 µm, respectively. It follows, that a micro-scaled device had to be developed, that can distinguish electrons by their transverse energy or by their polar angle related to the circular motion around the magnetic field. For this purpose, a passive micro-structured honey-comb filter was built to investigate the remaining background (sec. 6.4) at KATRIN with respect to their final polar angle distribution.

Future detectors are in development for detecting only electrons with polar angles higher than the remaining Rydberg background. In contrast to fig. 6.4, the detector itself will be the geometric boundary, while electrons with small angles are not detected, therefore a strong background reduction could be feasible. Such devices are described in section 6.5.

6.3. Parameter studies on micro-structured honeycombs

Originating from the first ideas to use commercial micro-channel-plates as a novel detector system, simulations on the geometric properties have been made. Since no device is available that fulfill all of the desired requirements, simulations on every parameter were performed to derive the favourable geometry. The open area ratio (OAR) was a strong requirement, as there should be as little loss as possible, which led to honeycomb structures being considered for their low OAR. The parameters of structures with hexagonal channels are the inner side length a, the wall thickness b between neighbouring channels, and the depth d, as shown in fig. 6.5. The open-area-ratio is given by

$$\frac{\mathrm{OAR}_{\mathrm{hex}}}{100\,\%} = \frac{A_{\mathrm{open}}}{A_{\mathrm{with\ wall}}} = \frac{\frac{3\cdot\sqrt{3}}{2}\cdot a^2}{\frac{3\cdot\sqrt{3}}{2}\cdot\left(a+\frac{b}{\sqrt{3}}\right)^2} = \frac{a^2}{\left(a+\frac{b}{\sqrt{3}}\right)^2}\,, \tag{6.3}$$

where the ratio of open hexagonal area to the hexagonal area with half of the walls between the hexagons is given by a hexagon with side length $a + b/\sqrt{3}$. Therefore, the wall thickness b must be minimal to achieve the best OAR. Investigations on the depth parameter can be achieved by simulations and calculations of the 3D motion of the electrons. The motion can be expressed as

$$\vec{r} = \begin{pmatrix} x \\ y \\ z \end{pmatrix} = \begin{pmatrix} r(\theta)\cdot\cos(\phi(t)) \\ r(\theta)\cdot\sin(\phi(t)) \\ v_{\mathrm{l}}(\theta)\cdot t \end{pmatrix} = \begin{pmatrix} \frac{v\cdot\sin(\theta)}{\Omega}\cdot\cos(\Omega t) \\ \frac{v\cdot\sin(\theta)}{\Omega}\cdot\sin(\Omega t) \\ v\cdot\cos(\theta)\cdot t \end{pmatrix}, \tag{6.4}$$

where $r(\theta)$ is the Larmor radius (eq. 6.2) and v_{l} the longitudinal component of the velocity. From the time of one cyclotron period, $t = 2\pi/\Omega \simeq 15\,\mathrm{ps}$, which is independent of the polar

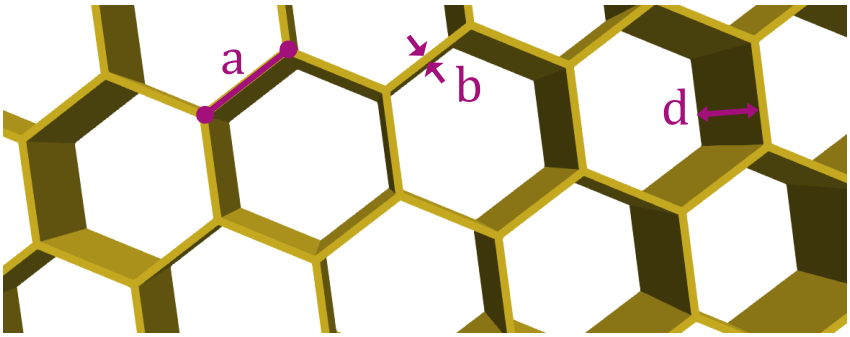

Figure 6.5.: Geometry of micro-structured honeycomb plate, implemented in Kassiopeia. The design is characterised by three parameters: inner side length a, wall thickness b, and depth d.

angle, the path length along the z-axis can be calculated. For an electron with 18.6 keV energy (velocity $v \simeq 0.27c$) the path length Δz for polar angles of 10° and 50° is 1.18 mm and 0.77 mm, respectively. From this it follows that depths of 0.5 − 1.5 mm are preferred, as the best resolution on the angle can be achieved. However, the manufacturing of such a filter plate with micro-scaled hexagonal channels of high OAR and a depth on the order of mm is not feasible. Nevertheless, a micro-scaled structure with honeycombs on the micro-meter scale and limited depth of 250 µm could be provided by Microworks [138] for KATRIN. The limited depth arises from the manufacture procedure of X-ray lithography at KARA (Karlsruhe Research Accelerator) which serves as synchrotron radiation source to expose a photo-mask. With the mask a negative of the final structure is made wherein dissolved gold in a solution precipitates, forming the final micro-structured honeycomb filter.

To finalise the hexagonal side length a, simulations with Kassiopeia were performed. Electrons are started in front of a micro-structured filter within the detector magnet, with varying side length but fixed depth of 250 µm and fixed wall thickness of 8 µm, limited by the manufacturing process. When an electron hits a surface of the structure, its track is terminated, even if the electron was transmitted through the structure. The polar angle is diced from the distributions, given in fig. 6.3, and an efficiency parameter ε for the beta and background electrons is calculated,

$$\varepsilon_{\mathrm{bg}} = f_{\mathrm{trans}} \cdot (1 - f_{\mathrm{front}}) \cdot (1 - f_{\mathrm{inside}}) \tag{6.5}$$

$$\varepsilon_{\beta} = f_{\mathrm{inside}} \cdot (1 - f_{\mathrm{front}}) \cdot (1 - f_{\mathrm{trans}}) \,, \tag{6.6}$$

where f_{trans}, f_{front}, and f_{inside} are the relative parts of the transmission with termination during transmission, at the front, and inside respectively. The best efficiency for beta electrons is given for high inside channel terminations and best background efficiency for high transmission arise from the considerations of an active transverse energy filter

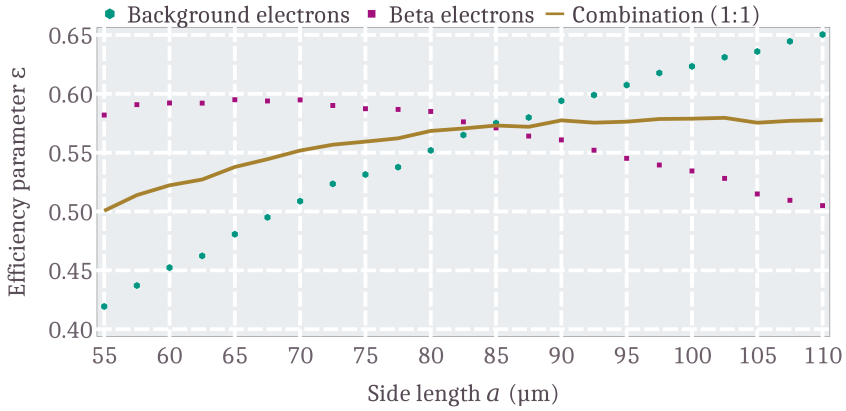

Figure 6.6.: Rydberg background and beta electrons filter efficiency for different side lengths. The efficiency parameter ε is a combination of inner channel termination, transmission and front surface collision. The combination is given in a ratio of 1:1 for beta and background electrons.

detector (sec. 6.5). Terminations on the front, related to the OAR reduce both in the same amount. The individual and combined efficiencies of background and beta electrons can be seen in fig. 6.6. $\varepsilon_{\mathrm{bg}}$ increases with increasing side length, since the open area becomes larger and thus also the transmission. The beta electrons efficiency ε_{β} shows a slight maximum at about 65 µm and decreases with increasing side length, as more electrons are transmitted which is a disadvantage for beta electron detection in such a device. The combined efficiency is stable for side lengths >90 µm for the 1:1 ratio of background to beta electrons.

As it was clear that the pTEF measurement campaign will take place over Christmas, with no tritium operation, the beta electrons efficiency can be neglected. Therefore, the measurements were planned to investigate only the background electrons, therefore the side length was fixed to 100 µm which is comparable to the derived side lengths that could be used for investigations with tritium beta electrons and provides higher efficiency on background electrons.

6.4. Dedicated background measurements with a passive filter

In this chapter the properties of the pTEF and the measurement campaign and configuration is presented. For the analysis of the individual measurement configurations supplementary Monte Carlo simulations are performed and discussed. Subsequently, the analysis of the pTEF measurement data is shown with discussion and consideration of systematic effects, as well as the result of the initial transverse energy scale of the background electrons.

6.4.1. Passive transverse energy filter (pTEF)

The passive transverse energy filter (pTEF) as ordered at Microworks GmbH [138] is made out of gold with geometry parameters

$$a = 100\,\mu\mathrm{m}, \quad b = 8\,\mu\mathrm{m}, \quad d = 250\,\mu\mathrm{m} \quad \rightarrow \quad \mathrm{OAR} = 91.4\,\% \,. \tag{6.7}$$

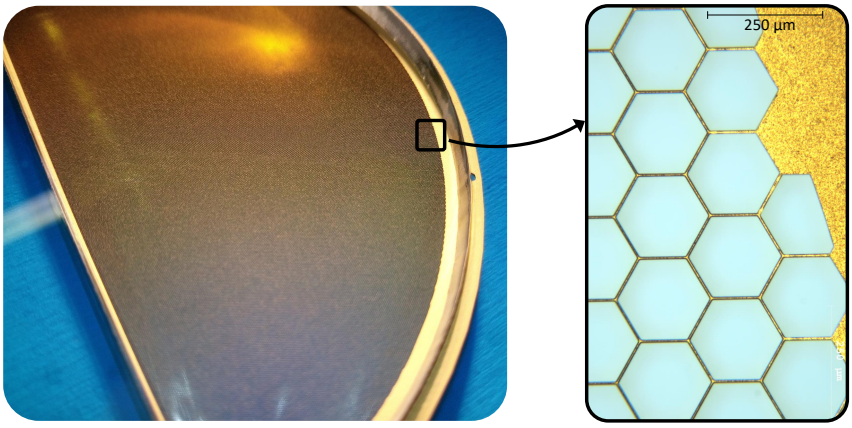

Figure 6.7.: Photo and optical microscope image of the pTEF.

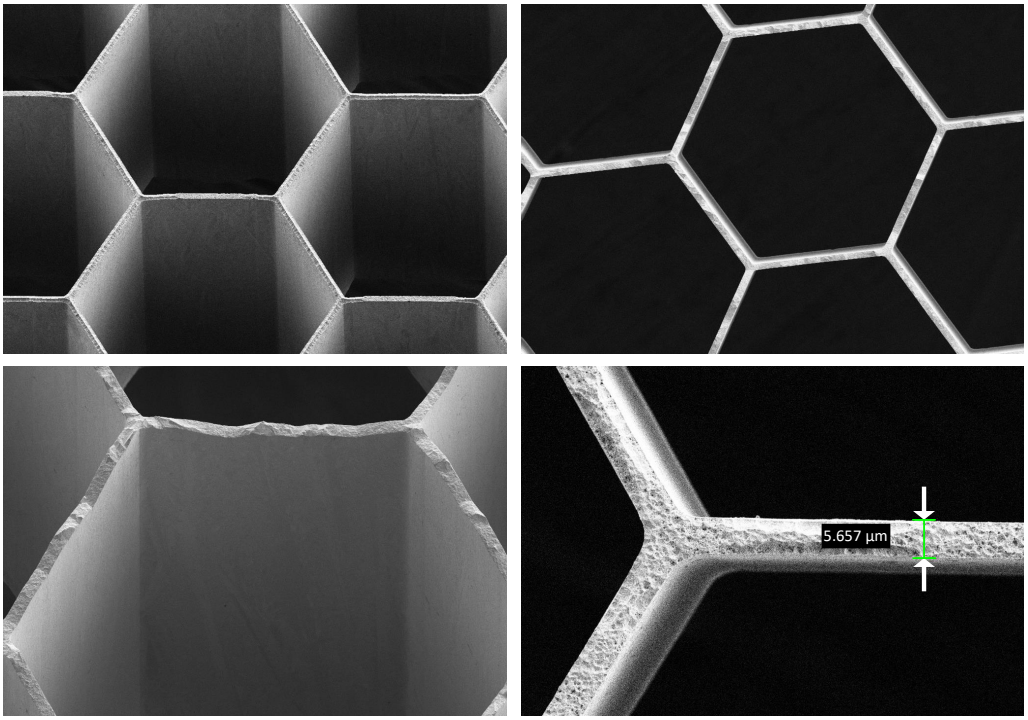

Figure 6.8.: Electron microscope images of the fabricated pTEF. Provided by the manufacture company Microworks [138].

The filter was manufactured as a semi-circle with a 5 cm radius, so that a measurement of the regular background rate and the observation behind the filter can be performed simultaneously, as only half of the FPD is shadowed. The filter was fabricated with sufficient precision of the parameters side length, wall thickness and depth with variations on the micrometer scale. In fig. 6.8 electron microscope images are shown that illustrate the remarkable precision which was achieved on the hexagons and their edges. However, on the bottom left picture variations of the channel depth can be seen which are about 5 µm. In addition, the wall thickness was measured to be smaller than 8 µm. As not every wall could be measured individually, a mean wall thickness of 6 µm is assumed from the pictures taken, which would lead to an enlarged OAR by 2 %. Optical measurements with an electron microscope also show that the channel depth is slightly increased to a mean value of 260 µm with the mentioned variations.

Simulations have been performed with the design parameters (eq. 6.7) before the manufacturing was finished, therefore the presented simulations regarding transmission conditions of electrons through the pTEF are made with the design values. The increased OAR and deeper channels are counteractive effects on the global transmission, it manifests that the transmission for small polar angles ($< 10°$) is increased while it decreases for medium to large angles ($> 25°$) on the scale of less percent.

The transmission probability for electrons of various polar angles is simulated with Kassiopeia. The filter structure is implemented with the design parameters (eq. 6.7) and

placed in the center of the detector magnet. Electrons are generated at the nominal magnetic field strength $B_{\text{det}} = 2.5\,\text{T}$ with an energy of 18.6 keV within a volume immediately in front of the filter, distributed over an area of $3.14\,\text{cm}^2$. Electrons are stopped and counted when transmission, inside wall collision, or front surface collision occurred. Each data point in fig. 6.9 corresponds to 25000 simulated electrons within an uniformly distributed polar angle range of 1°. The transmission is fit according the following function

$$\xi(\theta, c_1, c_2, c_3, c_4) = \begin{cases} 0 & f < 0 \ \vee \ \frac{df}{d\theta} \geq 0 \ \vee \ \theta > 90° \\ f(\theta, c_i) & \text{else} \end{cases} \tag{6.8}$$

$$\text{with} \ \ f(\theta, c_1, c_2, c_3, c_4) = (c_1 \cdot \theta) \cdot \left(1 - \tanh\left(\frac{\theta - c_3}{c_4}\right)\right) + c_2 \quad \theta \in [0, 51]$$

where the fit parameters c_{1-4} are given in tab. A.7. The conditions for vanishing ξ are necessary to maintain physical truth, so no negative probabilities or transmission above $\theta_{\text{trans,max}}$ can occur. The mean uncertainty of the fit on individual data points is about 0.05 % and is thus suitable for describing the electron transmission probability. The fit transmission probability will later be used in the final fit function of the observed transmission probabilities for different magnetic field settings.

Variations on the final kinetic energy E_f, in the electron energy in transmission probability simulations, affects the maximal polar angle $\theta_{\text{trans,max}}$. The higher the electron energy, the smaller $\theta_{\text{trans,max}}$ as the Larmor radius (eq. 6.2) increases accordingly. However, one has to keep in mind, that for different energies the transverse energy component is

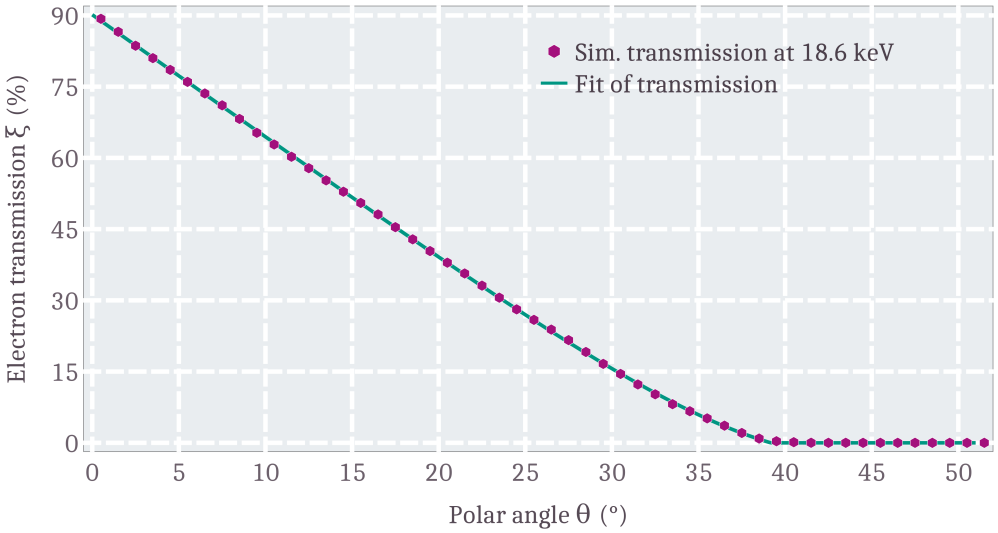

Figure 6.9.: Simulated transmission probability of 18.6 keV electrons through the micro-structured pTEF. For each point, 25000 electrons have been simulated in a uniform polar angle range of 1°, distributed over an area of $3.14\,\text{cm}^2$ in front of the filter. The transmission is fit with the fit functions eq. 6.8 and the corresponding fit parameters are shown in tab. A.7. The maximum polar angle of transmission is $\theta_{\text{trans,max}} \approx 40°$.

different for fixed polar angles. The transverse component of the kinetic energy E is given by

$$E_t = E \cdot \sin^2(\theta) \ . \tag{6.9}$$

The polar angle related expression can be derived by equate two different energy and angle combinations with the same transverse energy, it follows

$$\begin{aligned} E_1 \cdot \sin^2(\theta_1) &= E_2 \cdot \sin^2(\theta_2) \\ \theta_1 &= \arcsin\left(\sqrt{\frac{E_2}{E_1}} \cdot \sin(\theta_2)\right) \ . \end{aligned} \tag{6.10}$$

For example, an electron of 18.6 keV and a polar angle of 10° has the same transverse energy as an electron of 34.1 keV with a polar angle of 7.37°. The effect of different kinetic energies on the transmission probability ξ can be seen in fig. A.14, derived from eq. 6.8 for simulations of different energies.

6.4.2. Measurement configurations and complementary simulations

The pTEF is mounted on a specialised holding structure and directly connected to the FPD wafer flange, as shown in fig. 6.10. Its position is about 11 cm in front of the FPD at the position of maximum and most-homogeneous magnetic field of the flux tube. The radius of the micro-structured semi-circle area is $r_{\mathrm{pTEF}} = 46$ mm which exceeds the flux tube radius $r_{\mathrm{flux}} \lesssim 44$ mm at the pTEF position ($z_{\mathrm{KATRIN}} = 13.783\,75$ m in global KATRIN coordinates) to minimise possible systematic effects due to misalignment of the holding structure. The global flux tube in the detector section and local at the detector and pTEF position is shown

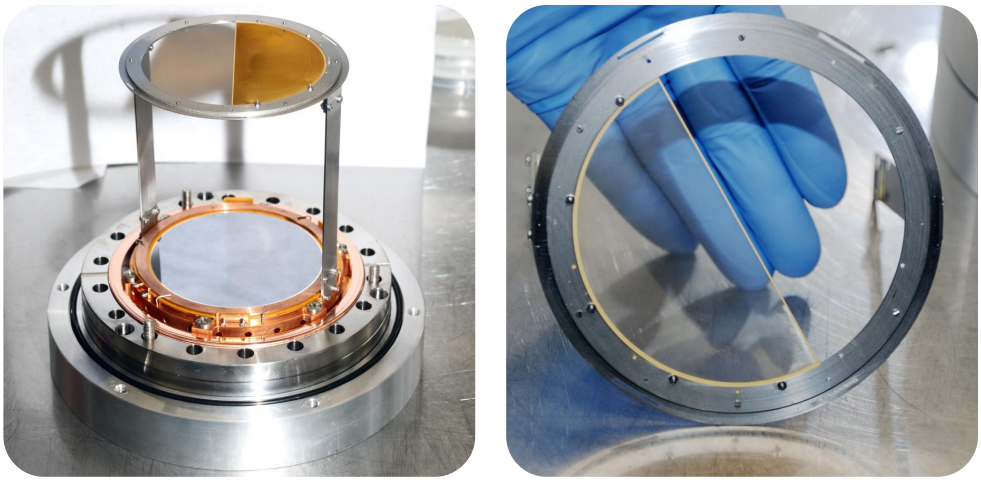

Figure 6.10.: Dedicated holding structure of the pTEF, mounted on FPD wafer flange. The pTEF is located about 11 cm in front of the FPD since the detector itself is not placed in the center of the detector magnet, where the magnetic field is most homogeneous. The micro-structured area exceeds the flux tube dimension, so the outer edges are not of concern.

in fig. A.15. The nominal field of the superconducting magnets, including the field at the detector remains constant as changes on these parameters would lead to uncertain measurement configurations, as no comparable measurements are available.

The underlying theoretic model of eq. 6.1 on the final polar angle

$$\theta_{\text{final}} = \arcsin\left(\sqrt{\frac{E_i}{E_f}\frac{B_f}{B_i}\cdot\sin^2(\theta_i)}\right)$$

contains four parameters of the initial and final electromagnetic field situation. As previously described, the detector magnetic field remains constant at 2.5 T which corresponds to B_f. However, the final kinetic energy E_f and the initial magnetic field B_i can be easily varied by changing the applied high voltage potential and the magnetic field configuration by the eLFCS coils. The initial kinetic energy E_i is the value of interest which combines with the sinus of the initial polar angle in the magnetic flux to the initial transverse energy $E_t = E_i \cdot \sin^2(\theta_i)$.

Variations on the initial magnetic field B_i have been performed by measuring the background rate for different magnetic field settings. The envelopes of the corresponding magnetic field configurations are shown in fig. 6.11. The minimal magnetic field strengths in the center of the main spectrometer, besides the SAP configuration, were changed from 2.7 G to 17 G, using an inversely shifted analysing plane setting. The analysing plane is shifted upstream towards the source side of the experiment. Therefore, the sensitive flux tube volume is increased and higher background rates are achieved to reduce the statistical

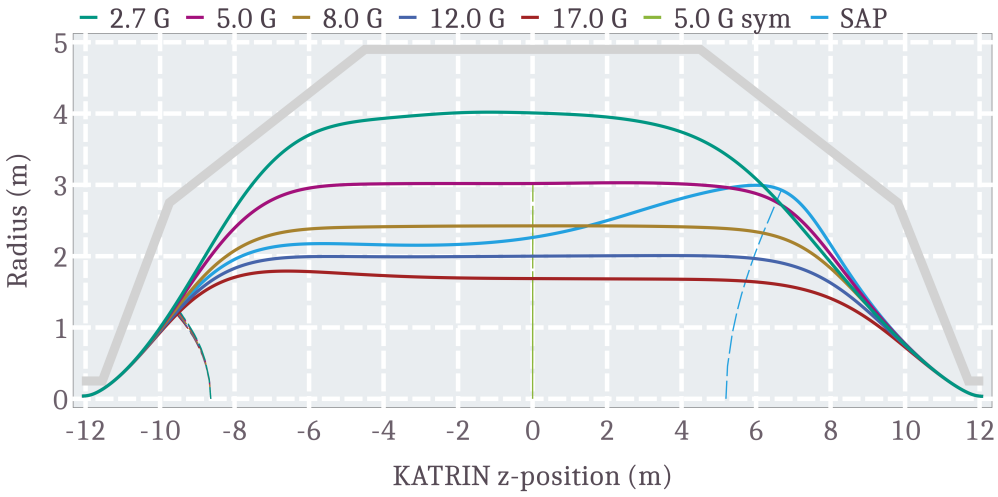

Figure 6.11.: Magnetic flux tube envelopes of the settings used during the pTEF measurement campaign. Six different magnetic field settings have been used. To gain more statistics on the background events, measurements have also been performed in a inversely shifted analysing plane configuration. The analysing planes are shown as dashed lines for the individual configurations.

error. Additionally, measurements with a symmetric retarding potential setting at 5.0 G, as well as measurements in the standard SAP configuration have been performed.

The retarding potential, which influences the final kinetic energy E_f, have been set to three different values: 12.0 keV, 18.6 keV, and 34.1 keV. Measurements have not been performed in every field configuration. For the 12 keV and 34 keV retarding potentials, only the settings at 2.7 G, 5.0 G, and 8.0 G minimum magnetic field, and the SAP configuration, were used. Thus, the entire parameter space of the electromagnetic field configurations is covered at 18.6 keV. The post-acceleration was set to zero, since there should be no bias of the final polar angle by the additional electric field.

For detailed investigations of the measurement data, additional simulations of the expected transmission probability are mandatory. For this purpose, Monte Carlo simulations with electrons were performed that start within the individual ring-wise flux tube volumes. For each electromagnetic field configuration, magnetic tracking simulations with Kassiopeia deliver the ring-wise volumes, and also the retarding potential and magnetic field strengths within the sensitive flux tube volumes. These are used to determine the initial magnetic field strengths at diced positions within the ring-wise flux tube volumes. In addition, the individual probability density along the beamline axis z, as shown in fig. A.13, is used for the electron generation to take the distance to the main spectrometer vessel wall into account. For example, the generated electron starting positions and their initial magnetic field strengths for the SAP configuration are shown in fig. 6.12. The colour of the points denotes the mapping on one of the 13 FPD pixel rings, where the innermost volume corresponds to the bulls-eye with index 1. The main part of the initial magnetic

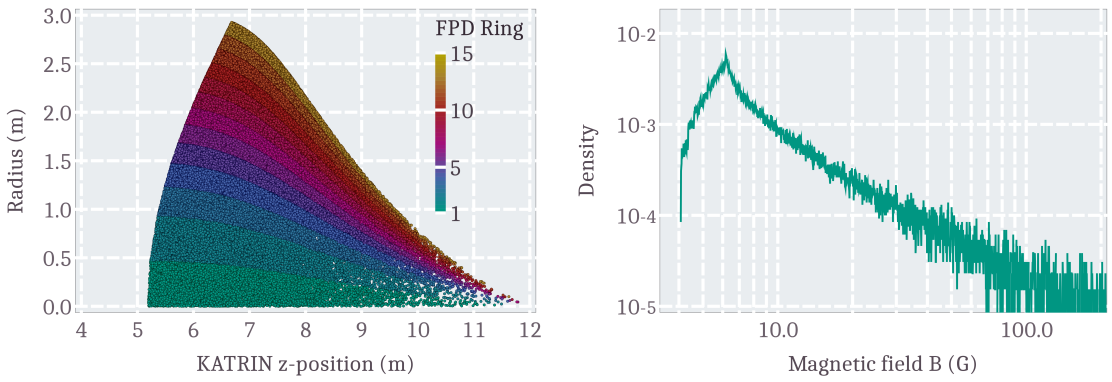

(a) Ring-wise generation positions.

(b) Initial magnetic field.

Figure 6.12.: (a): Ring-wise simulated electron generation positions for the SAP configuration sensitive flux tube volume. Here, 10^4 electrons for each of the 13 rings have been generated. **(b):** Density of the initial magnetic field strength B_i for the simulated electron generations in **(a)**. The increasing part at low magnetic fields arises from the inhomogeneous magnetic field in the SAP analysing plane which rise from 4.6 G to 6.4 G. The decreasing part to high magnetic fields originates from closer positions to the pinch magnet at $z = 12.2$ m.

field strengths B_i is in the range of 4.5 G and 10 G with a peak at about 6 G. However, B_i also rises above 100 G in some cases which strongly influences the final polar angle, according eq. 6.1.

The global simulations for the different magnetic field configurations contain the generation of 10^5 electrons for each FPD ring volume with uniform initial kinetic energies from 0 eV to 1 eV under isotropic emission. From eq. 6.1 and the initial values of the energy and magnetic fields, the final polar angles θ_f at the pTEF position for fixed final magnetic field of $B_f = 2.5\,\mathrm{T}$, and final kinetic energy of $E_f = 18.6\,\mathrm{keV}$ are calculated. Subsequently, the ring-wise transmission probability can be derived from the transmission properties of the pTEF (fig. 6.9 and eq. 6.8) in an energy-dependent way by choosing certain intervals of E_i. In fig. 6.13, the expected observable background fraction Ψ from the simulations for the different magnetic field configurations at $U_{\mathrm{ret}} = 18.6\,\mathrm{keV}$, is shown. The simulation data is divided into parts of 100 meV energy range which corresponds to the mean values according the data which range from 0.1 eV to 0.7 eV. The data points correspond to the individual magnetic field configurations by their geometric mean of the initial magnetic field strengths B_i. The geometric mean of values

$$\bar{X}_{\mathrm{geom}} = \sqrt[n]{\prod_{i=1}^{n} X_i} = \sqrt[n]{X_1 \cdot X_2 \cdots X_n}\,, \tag{6.11}$$

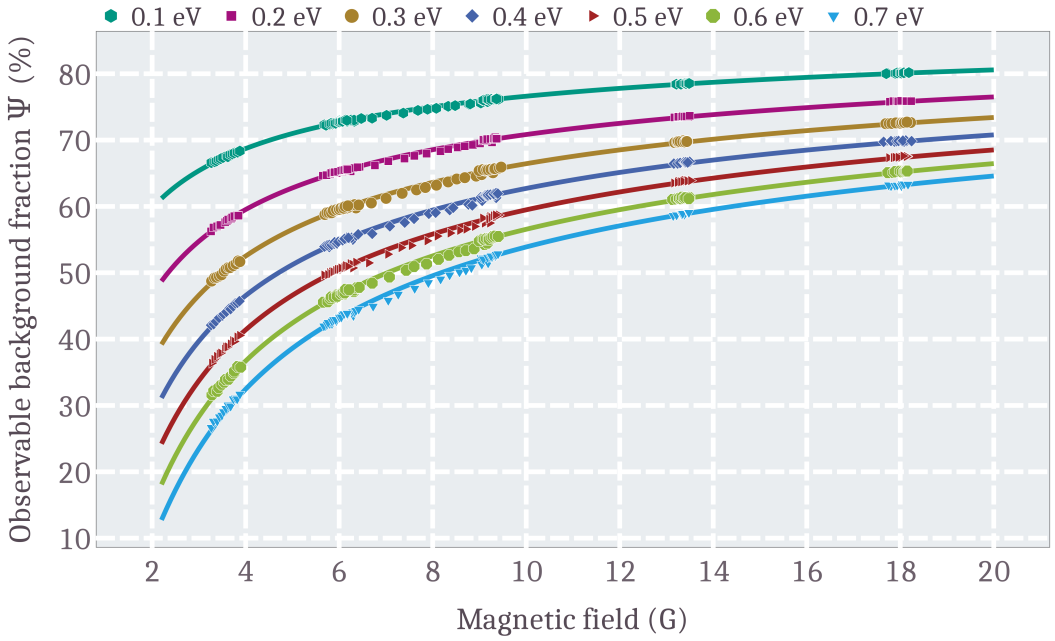

Figure 6.13.: Observable background fraction Ψ of simulated electrons from the individual ring-wise sensitive flux tube volumes for different mean kinetic starting energies E_i from 0.1 eV to 0.7 eV, started isotropically. The geometric means of the ring-wise magnetic field strengths are given in tab. A.8.

Table 6.1.: Result of transverse energy scale fits, according eq. 6.12 for initial energies of 100 meV to 900 meV. The energy range ΔE_i of the initial kinetic electron energy and mean energy $\bar{E}_i$ of the simulation data is given. The fit results e_i, their corresponding uncertainty σ_e, and the derived mean initial kinetic energy $\epsilon_{\text{fit}} = {}^{e_i}/_{0.667}$ from the fit result are shown.

Range ΔE_i (eV)	$\bar{E}_i$ (meV)	e_i (meV)	σ_e (meV)	ϵ_{fit} (meV)	$\sigma_{\epsilon_{\text{fit}}}$ (meV)
0.05-0.15	100.0	62.5	0.7	93.7	1.0
0.15-0.25	200.0	127.0	0.9	190.4	1.4
0.25-0.35	300.1	191.0	1.1	286.4	1.6
0.35-0.45	400.0	255.3	1.2	382.8	1.8
0.45-0.55	500.0	318.4	1.3	477.4	1.9
0.55-0.65	599.9	381.6	1.3	572.1	2.0
0.65-0.75	700.1	443.8	1.4	665.4	2.0
0.75-0.85	799.9	505.4	1.4	757.7	2.1
0.85-0.95	900.1	565.6	1.4	847.9	2.1

is more applicable to describe the distribution of the initial magnetic fields B_i (fig. 6.12b) as it better accounts for the number of small values and is less affected by the rarely occurring field strengths above 100 G, whereby it applies $\bar{x}_{\text{geom}} \leq \bar{x}_{\text{arithm}}$. The individual ring-wise magnetic field strengths are given in tab. A.8 which will be also used for the final analysis of the pTEF measurement data, so that there exists a model-dependence of the result by the electron generation position and the corresponding fields.

The simulation data are fit according a convoluted function of the final polar angle (eq. 6.1) and the simulated polar-angle-dependent transmission probability ξ (eq. 6.8).

$$\Psi(B, e_i) = \xi(\theta_{\text{final}}(e_i, E_f, B, B_f), c_1, c_2, c_3, c_4) \;\text{ with }\; \theta_{\text{final}} = \arcsin\left(\sqrt{\frac{e_i}{E_f}\frac{B_f}{B}}\right), \tag{6.12}$$

is a function of the magnetic field B and the transverse energy scale e_i as a fit parameter, containing the parameters c_i of the transmission probability ξ, whereby B_f and E_f are constant for the specific configurations. This function can only be used to derive the mean transverse energy scale, since the observable transmission only contains information about the mean energy. Results of the fits are given in tab. 6.1.

The mean value for isotropic directions of $\sin^2(\theta_i)$ in eq. 6.9 is $\alpha_{\text{iso}} = \sin^2(\bar{\theta}_{\text{iso}}) \simeq 0.667$. However, the evaluated transverse energy scales of the individual fits does not fully reproduce the initial kinetic energy as the mean ratio of e_i divided by $\bar{E}_i$ is $\alpha_{\text{fit}} = 0.634(1)$. So the initial kinetic energy ϵ_{fit} is underestimated by about 5 % from the combined fit of the simulation data with eq. 6.12. This fact may arise from the approximation of the initial magnetic fields B_i to one value for the description of the ring-wise observable transmission in fig. 6.13. On the other hand, it is not clear whether the isotropic emission of electrons within the main spectrometer volume due to the ionisation of the Rydberg atoms is realistic, since a Doppler-shift due to the Rydberg atoms motion and a aligning torque on the atom, induced by the electromagnetic field, can be present.

6.4.3. Analysis of the transverse energy scale

The analysis on the transverse kinetic energy scale relies on the observed rate behind the pTEF and on the not-shadowed FPD pixels. The observed background fractions for the different electromagnetic field settings is shown in fig. 6.14. It can be easily seen that the background fraction increases for increasing central magnetic field strengths from about 40 % to about 60 %. This is in contradiction to the expected transmitted background fraction from the Rydberg background model, see fig. 6.13, where for 100 meV electrons a transmission probability of $\Psi \geq 70\,\%$ is expected. Such reduced transmission hints to higher electron starting energies of the remaining KATRIN background. Therefore, a closer look into the data selection and analysis regarding systematics will be made.

The data taken during the pTEF measurement campaign are filtered with a pixel selection and an applied region of interest (ROI) cut. The veto system of the FPD was used, as described in sec. 4.2. At measurements of high rate, induced by deliberate ignition of the inter-spectrometer Penning trap, high statistics can be achieved which is useful to perform the pixel selection for the campaign. The pixel selection is shown in fig. 6.15b, where the boundary of the semi-circle can be seen by the green coloured pixels through the center of the FPD. Since no precise calibration could be made, every pixel which was partly shadowed by the pTEF has been rejected. Besides the pixel selection, the region of interest cut was chosen as $U_{\mathrm{ret}} \pm 3\,\mathrm{keV}$. This is narrow compared to the cuts at KNM measurements where the energy ranges from 22 keV to 34 keV for measurements near

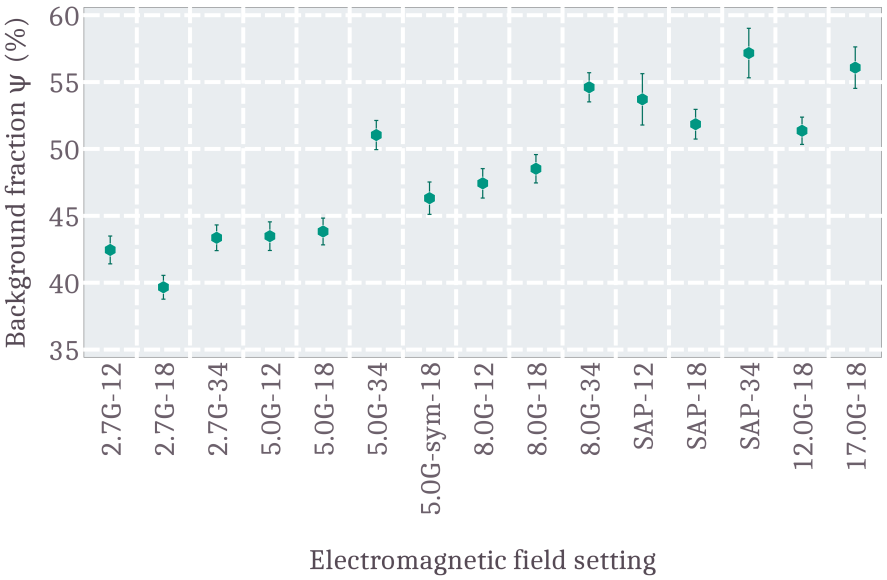

Figure 6.14.: Measured background fractions for various electromagnetic field configurations. The indices 12, 18, 34 correspond to the high voltage set points of 12.0, 18.6, and 34.1 kV. Index sym at the 5.0 G measurements denotes a symmetric potential (NAP) configuration. Other measurements are performed in the inversely shifted SAP for different center magnetic fields or the standard SAP configuration.

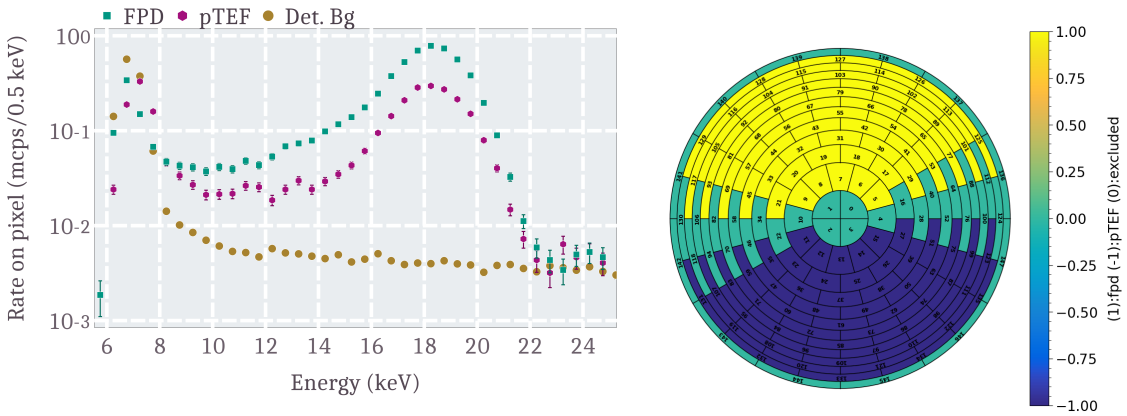

(a) Energy histogram. **(b)** Pixel selection map.

Figure 6.15.: (a): Energy histogram of counts in bins of 0.5 keV width. Green data points on FPD pixel selection, purple data points behind pTEF and light brown data points represent the detector background. **(b):** Map of pixel selection, used at the analysis of the pTEF measurement data. Yellow pixels at the top denote the ones not influenced by the pTEF which are used as reference. Dark blue coloured pixel on the bottom are behind the pTEF while the green coloured ones are rejected from the analysis.

the tritium spectrum endpoint with post-acceleration. The narrow region arises from the fact that diverse potential set points and no PAE was used, so that there is no influence on the polar angle spectrum by the additional electric field. As the lowest high voltage set point was chosen to 12 keV, the region of interest has to be narrow, as the intrinsic detector noise dominates at energies below 8 keV, which can be seen in fig. 6.15a. To maintain comparability between the different measurements the common narrow ROI was selected. As the main peak is investigated in a range larger than the energy resolution, significant differences between a narrow and broad ROI are not present. Additionally, the detector background which was measured in advance (see sec. 4.2) was subtracted from the individual measured rates as it would artificially increase the observed background fraction Ψ.

Further systematic considerations arise from the global misalignment of the FPD and pTEF with respect to the magnetic field, maintained by the super-conducting magnets and the air coil system. As described in sec. 4.5.1, misalignment imprints on the detector pixel map as a lateral shift of the minimum rate of the x and y coordinate. This leads to a sinusoidal variation of the rate over pixel number within one detector ring which must be taken into account at the pTEF campaign since the detector is split by the pixel selection in specific areas, so that no entire detector ring is selected. Hereby, a rate difference on the individual detector sections (yellow and dark blue in fig. 6.15b) is present even when no pTEF is installed. This is shown in fig. 6.16 for background data of the KNM5 measurement campaign. The individual pixel selections for the pTEF and FPD part are highlighted with

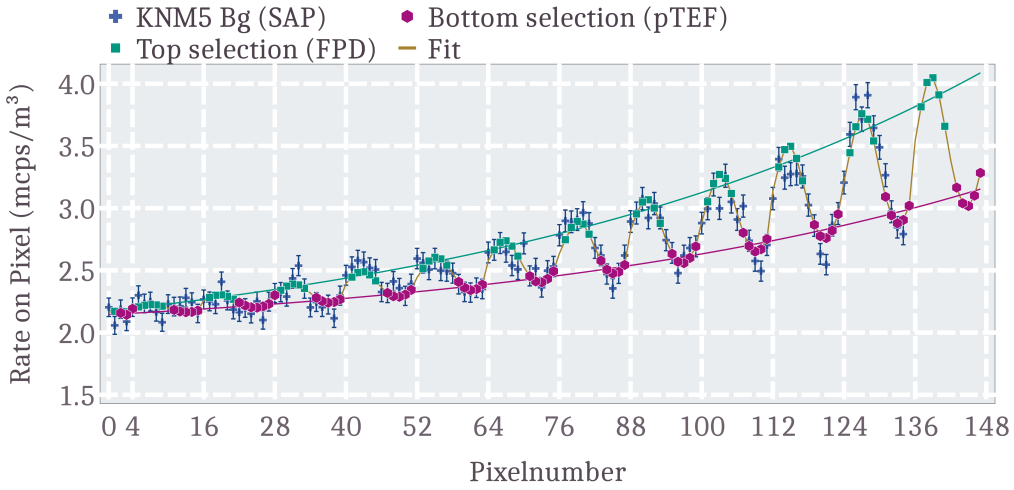

Figure 6.16.: Background rate as a function of pixel number of data taken during KNM5. The FPD (green) and pTEF (purple) pixel selection is highlighted and individually fit with an exponential function. A global fit of the misalignment is made (light brown) which leads to a lateral shift of $(\Delta x, \Delta y) = (2.65(23)\,\text{mm}, -3.61(24)\,\text{mm})$.

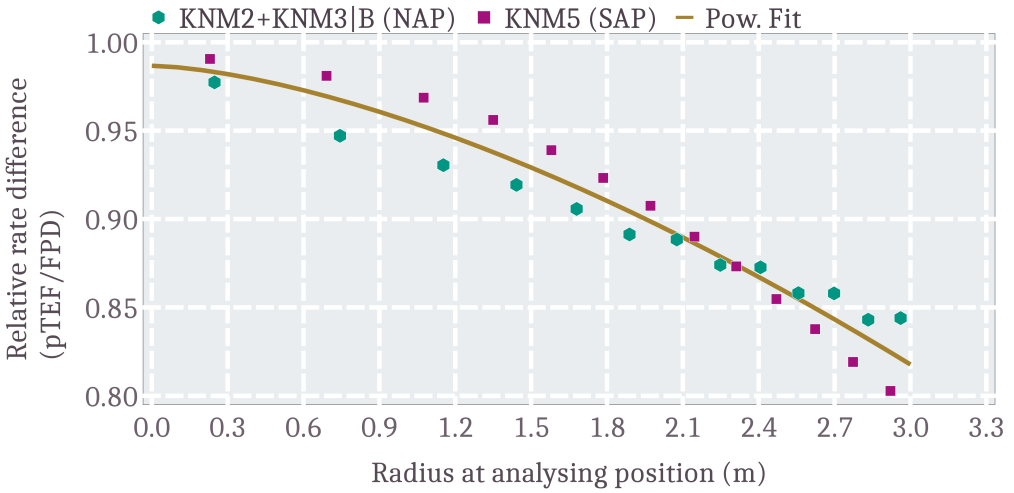

Figure 6.17.: Relative rate difference of the background rate for the pTEF to FPD pixel selection for SAP (KNM5) and NAP (KNM2+KNM3|B) configuration as a function of the analysing plane flux tube radius. The radial differences of both configurations are fit by a power law $p(r) = a + b \cdot r^c$ to describe the rate difference for the pTEF and FPD pixel selection combined. The fit parameters are $a = 0.99(1), b = -0.031(9), c = 1.55(24)$.

purple and green points along the global fit of the effective lateral misalignment along x and y, according

$$B = b_0 - b \cdot \exp^{c \cdot |\vec{r}_p - \vec{r}_0|} , \tag{6.13}$$

whereby a lateral shift by $\vec{r}_0$ with respect to the pixel center positions $\vec{r}_p$ is derived [139]. The fit lateral shift is $\vec{r}_0 = (\Delta x, \Delta y) = (2.65(23)\,\text{mm}, -3.61(24)\,\text{mm})$. Both pixel selections are individually fit with exponential functions which reveal that the rate difference between those significantly increases to outer radii. Since the pixels of the FPD pixel selection have an increased rate, while the rate is low for the pTEF selection, the azimuthal mounting position was a disadvantage and the rate before the pTEF has to be corrected.

The expected rate before the pTEF has to be calculated from the rate observed on the open FPD section by taking the rate difference due to the misalignment into account. The rate difference on the two detector sections is derived by the global misalignment fits, which were performed on data from KNM5 for the SAP configuration and a combination of KNM2 and KNM3|B for the NAP configuration. Therefore, the rate before the pTEF which will be used to derive the observed background fraction consists of the measured rate on the FPD pixel selection multiplied by the relative rate difference, given in fig. 6.17, which is parameterised by a power law, according $p(r) = a + b \cdot r^c$ with the fit parameters $a = 0.99(1), b = -0.031(9)$ and $c = 1.55(24)$.

Another major systematic which has to be considered is backscattering. Backscattering of electrons occurs regularly at the FPD silicon wafer. Depending on the incident polar angle, mean backscattering probabilities of about 20 % are considered [140]. As

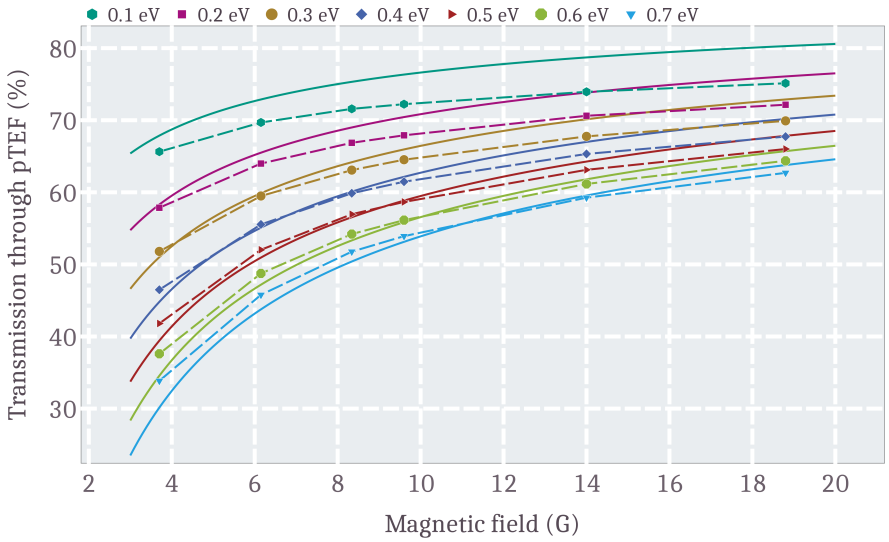

Figure 6.18.: Simulated transmission probability of electrons through pTEF with consideration of backscattering from surfaces. The data points and the dashed lines correspond to the simulations of electrons, started in the main spectrometer volume which are tracked until their energy is below threshold. The solid lines represent the derived simulations outcome, as shown in fig. 6.13.

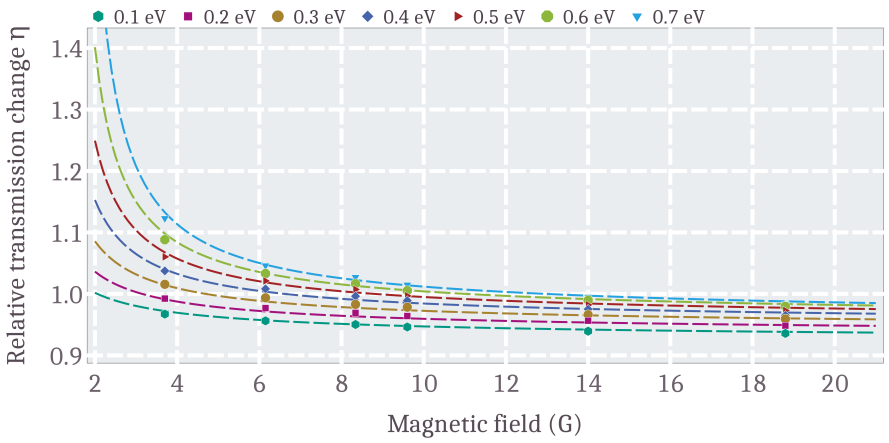

Figure 6.19.: Relative change on the transmission probability from backscattering effects. The points are extracted for simulations at the different magnetic field configurations at −18.6 kV. The effect can be modelled by a combination of eq. 6.12.

electrons backscatter after transmission through the pTEF, their polar angle will change and backwards transmission is not guaranteed, therefore electrons which were transmitted are not detected on the FPD, scatter back, and get lost at the pTEF in the worst case. This would highly reduce the observable background fraction if 20 % of the transmitted electrons were not detected. However, the pTEF itself is made out of gold which provides a higher probability for electrons being scattered from the surface, since the backscattering probability depends on the atomic number Z of the target material [141]. Additionally, the electrons which arrive at the pTEF are assumed to have small polar angles to the magnetic field which is nearly parallel to the hexagonal channels of the filter.

Therefore, the incident electrons which hit inside the pTEF hexagonal channels, arrive under large angles to the surface normal at the inner gold surface, which strongly increases the scattering probability inside the pTEF. The effect of the backscattering from the FPD silicon wafer with the possible loss of electrons, and the scattering of electrons from the golden pTEF which increases the transmission, have been investigated with simulations. To first order it seems that these two effects cancel out and the effect is small. Nevertheless, there exists an initial magnetic field and initial kinetic energy dependence on the final transmission under consideration of scattering from surfaces. In fig. 6.18, the simulation result of the additionally considered backscattering effects is shown. The data points and the dashed lines correspond to the simulation of electrons of various energies in the range from 0.1 eV to 0.7 eV in steps of 0.1 eV, started isotropically in the relevant main spectrometer flux tube volumes for the individual magnetic field configurations, shown in fig. 6.11. The electrons are tracked with scattering of the FPD silicon surface and golden pTEF surface with electrostatic reflection inside the main spectrometer until their energy falls below the detection threshold at the FPD. Subsequently, the derived transmission probability through the pTEF with detection at the FPD can be compared to the formerly

derived transmission in fig. 6.13. It can be seen, that the difference depends on the magnetic field similarly to the initial observable background fraction Ψ but differs especially at low magnetic fields, where the sign inverts for increasing initial kinetic energy, while the effect at high magnetic fields becomes smaller. The relative difference is separately shown in fig. 6.19, supporting this observation. The relative transmission change η can be modelled using a combination of the function, given in eq. 6.12, according to

$$\eta(B, k_1, k_2, k_3) = \frac{k_2 \cdot \Psi(B, k_1)}{\Psi(B, k_3)} \,, \tag{6.14}$$

k_2 is a global reduction parameter on the observable transmission, k_1 is an auxiliary transverse energy scale, and $k_3 = e_i$ from tab. 6.1. The evolution of these parameters, depending on the initial kinetic energy, is given in fig. A.16. The relative transmission change η is most prominent at low magnetic fields and increased initial kinetic energies with effects on the order 10 % at $E_i \approx 600\,\text{meV}$. However, the observable background fraction Ψ in this regime for increased electron energies is already reduced to about 30 % which leads to an absolute effect on the transmission at the percentage level, with a change of sign. On the one hand, transmission is increased at low magnetic fields as the electrons have an higher polar angle, according eq. 6.1, so that scattering through the pTEF is more frequent. On the other hand, the transmission is only slightly reduced at high magnetic fields because the final polar angles are smaller, so the transmission through the pTEF and the backscattering effect from the FPD silicon wafer are almost in equilibrium.

In summary, the considerations at the analysis of the pTEF measurement data are the narrow region of interest (ROI) for inter-comparability of the different high voltage set points, the application of the veto, and the pixel cuts. Furthermore, magnetic field misalignment and the effect of scattering of electrons from either the silicon detector surface or the gold pTEF surface is taken into account and modelled to derive final fit functions for the description of the observed background fractions. The ring-wise mean magnetic field values are extracted from dedicated background simulations which are used to describe the transmission probability ξ. The difference on the used fit function $\Psi(B, E_t)$ in eq. 6.12 is the application of the backscattering effect due to η which leads to

$$\widetilde{\Psi}(B, E_t) = \Psi(B, E_t) \cdot \eta(B, k_i) = \xi(\theta_{\text{final}}(E_t, E_f, B, B_f), c_j) \cdot \eta(B, k_i) \,, \tag{6.15}$$

whereby the parameters c_j are derived from the transmission probability ξ (see fig. 6.9), the parameters k_i are derived according their evolution, given in fig. A.16 and tab. A.9, and the transverse energy scale E_t is fit parameter.

The fit on the measured background fraction, with the mentioned adjustments regarding alignment and detector background, is shown in fig. 6.20. Two different options are taken into account, a global fit of the transverse energy scale E_t, and a modified fit function with an additional pre-factor c, through which possibly unconsidered systematics are taken into account. The regular function eq. 6.15 deviates at small and large magnetic fields from the measured background fraction, which can not be explained by incorrect mean

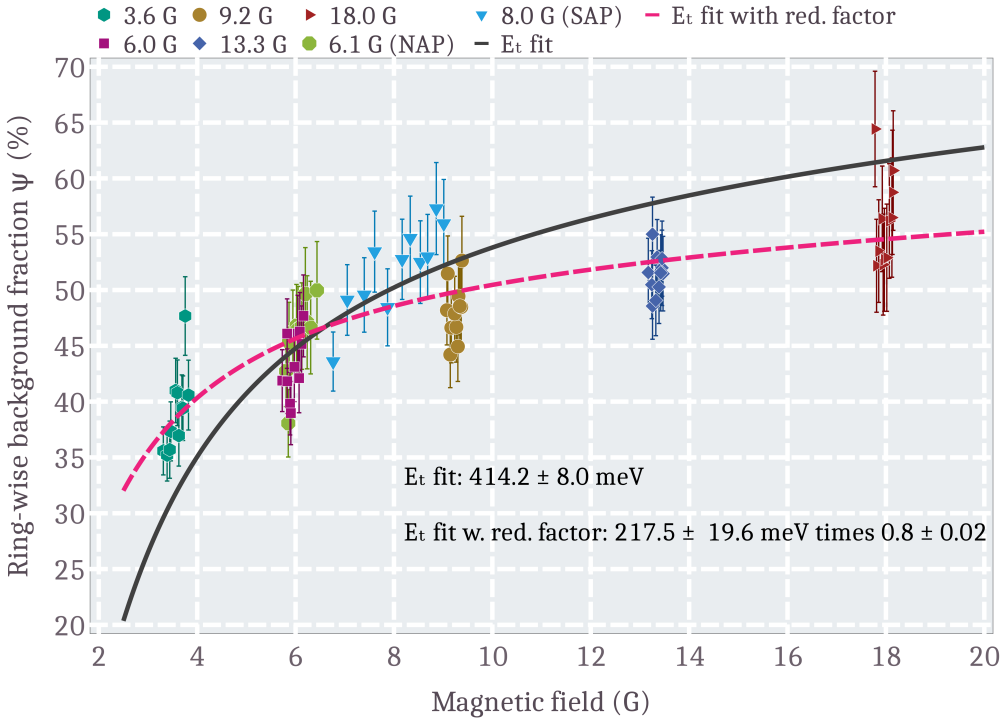

Figure 6.20.: Fit of the transverse energy scale E_t on the ring-wise background fraction Ψ for the pTEF measurement data, taken at $U_{\text{ret}} = 18.6\,\text{keV}$. The fit function is given in eq. 6.15, which corresponds to the solid black line. Additionally, the fit is performed with an additional reducing factor according $\Psi^* = c \cdot \widetilde{\Psi}$ (pink dashed line) to take possibly unconsidered systematics into account.

magnetic fields, underlining the necessity of the pre-factor c. The results of the fits are as follows

$$\text{single scale}: \; E_t = 414.16 \pm 8.01\ \text{meV} \qquad \frac{\chi^2}{\text{ndof}} = 2.687\,, \tag{6.16}$$

$$\text{with pre} - \text{factor}: \; E_t = 217.46 \pm 19.56\ \text{meV}$$

$$c = 0.801 \pm 0.017 \qquad \frac{\chi^2}{\text{ndof}} = 0.898\,, \tag{6.17}$$

whereby the fit with the global reduction factor c better describes the data since the reduced χ^2 is closer to 1. The comparison of the fit results with and without consideration of scattering is shown in fig. A.17.

The existence of an unaccounted systematic leading to a global reduction to 80 % is speculative, although there are possibilities. The largest concern at the performed measurements is the alignment, especially the alignment of the FPD and pTEF to the guiding magnetic field lines and the planarity of the pTEF with respect to the FPD wafer. Due to the stiffness of the pTEF mounting structure (Fig. 6.10), significant tilting of the pTEF surface normals relative to the wafer surface normals is not expected, but was also not

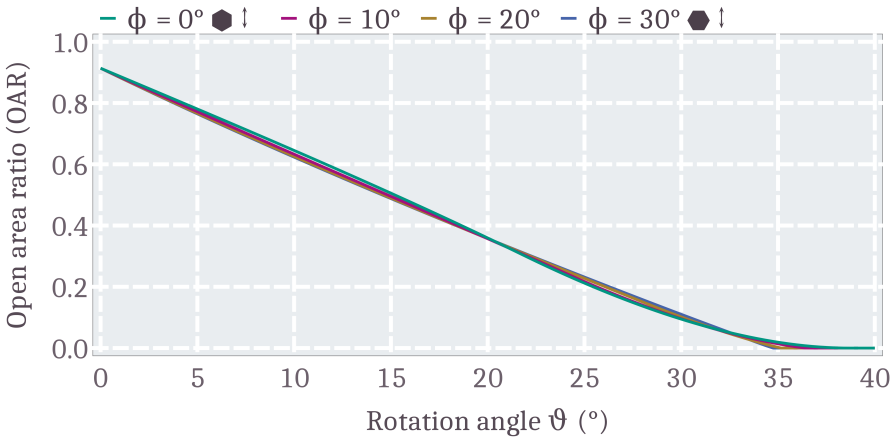

Figure 6.21.: Influence on the OAR by a tilted pTEF relative to the magnetic field. Four cases are demonstrated since the effect of the tilt about the angle ϑ depends on the orientation of the hexagon, which is varied by the azimuthal rotation about ϕ. Data kindly provided by J. Lauer [142].

measured. Therefore, this has an uncertainty on a sub-degree level. Nevertheless, the alignment of the pTEF and FPD relative to the guiding magnetic field remains uncertain, as this quantity can not be measured. Sub-degree tilts of the superconducting coils inside their housings to each other have been measured [78], which does not account for the FPD wafer position inside the beam-tube. The detector section coordinates are regularly measured with a laser camera system, which shows that lateral shifts are only present on the mm-scale which corresponds to small angles on the beamline length of 1.7 m from the main spectrometer exit to the detector. Such misalignment would cause a reduction of the open-area-ratio (OAR) as the direct line-of-sight through the channels gets reduced by the inner channel surface. The influence on the OAR by rotation is shown in fig. 6.21. The remaining open area decreases with the rotation angle ϑ until the inner channel surface shadows it completely. This effect depends slightly on the orientation of the hexagonal channel which is why it is shown for four different cases of azimuthal rotation about the axis parallel to the surface normal around ϕ. To obtain a global reduction to 80 % of the initial OAR, a rotation between 6° and 7° is necessary, depending on the azimuthal orientation. Deviations on the order of a few degrees are not to be expected, as the various effects can conservatively add up to about only 2°, where the open-area is reduced to 94 % of the initial value.

Moreover, defects on the pTEF structure can be taken into account. In fig. 6.22, two pictures of the pTEF, mounted to the fixation ring of the holding structure are shown. In the upper picture, defects on the hexagonal channels can be seen, which directly negatively influence the transmission probability. In addition, the pTEF has a slight curvature while mounted. The maximal height difference from the center to the right side outer edge is about 1 mm which corresponds to tilt angle of $\alpha \leq 1.3°$. This tilt only exists locally and

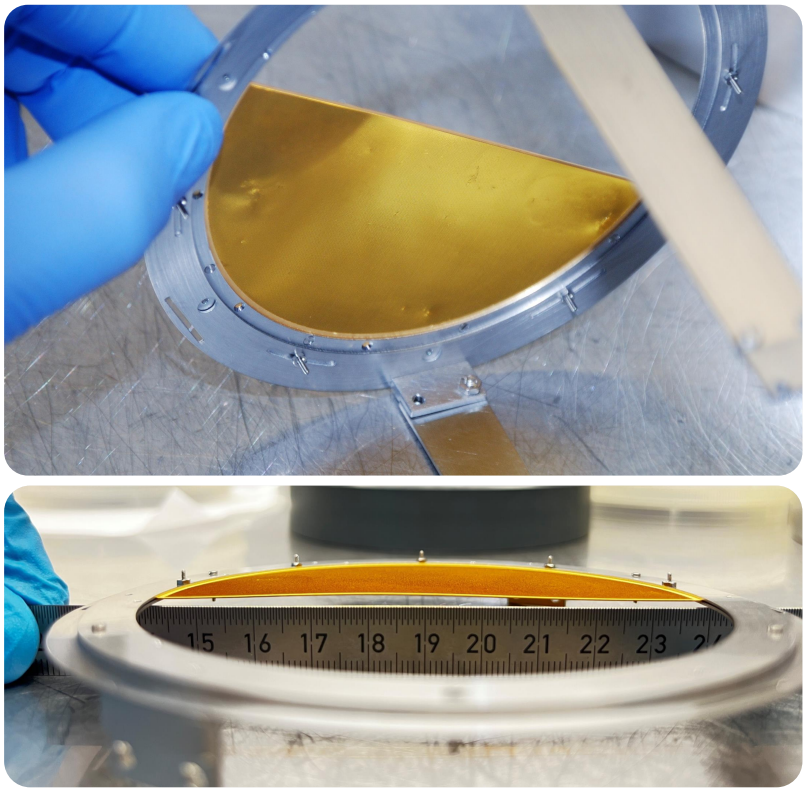

Figure 6.22.: Pictures of the pTEF for describing possible reduction effects. **Top:** Defects on the hexagonal channels can be seen. Three larger areas exist at the edge of the sensitive pTEF area, but also smaller ones occasionally in the center region. **Bottom:** The pTEF is not fully planar mounted to the holding structure. A slight bulge is created, with a maximum height difference of 1 mm from the centre to the edge on the right side.

does not account for the whole filter, through which only a minor effect on the OAR can be deduced.

Nevertheless, various aspects of possible influences on the open-area-ratio or the transmission ability of electrons through the pTEF exist, but can not be accurately quantified. Conservatively, an reduction effect analogous to a tilt of about 1° to 5° can be assumed, which would result in a reduction of the OAR by about 0.9.

Therefore, it can not be concluded, if the transverse energy scale is more likely on the order of 200 meV or 400 meV. Certainly, the initial transverse energy scale is well above the expectation by the Rydberg background model, whereby a value of the transverse energy scale on the order of 10 meV was expected, which also is in accordance with the measurement at 12.0 and 34.1 keV, shown in fig. A.18. Measurements with a pulsed electric dipole field in the main spectrometer had no influence on the background rate, wherefore no significant amount of trapped electrons is derived, based on [96, 97]. Thus, existence of electrons with energies well above the individual spectrometer resolutions, on the order of few eV, which are favourably being trapped, are essentially excluded. Conservatively, a minor part of high energetic electrons below the spectrometer resolution induced by

decay of residual radon can be present, which shifts the transverse energy scale to higher values. However, to compensate the Rydberg background model expectation to energy scales on some hundred meV a large fraction of these had to be present, which is excluded. As a result, other ionisation mechanisms and states of the sputtered atoms have to be taken into account to supply electrons of energies of the observed scale.

6.5. Research on active transverse energy filters

The simulation work on transverse energy filters is being performed parallel to the pTEF investigations regarding active transverse energy filters as replacement of the current FPD which would improve the signal-to-background ratio. The research activities on active transverse energy filters (aTEF) focus on two different approaches on development of a novel detector system based on electron filtering as described in sec. 6.2. In contrast to the pTEF, the electrons with high polar angles are intended to be detected, while background electrons with small polar angles surpass the filter unhindered. On the one hand, research and development of micro-structured silicon wafers is performed which would replace the current wafer, maintaining the present detector electronics at the experiment. On the other hand, micro-scaled scintillators are under development in which the signal electrons produce light which will be collected and the scintillation photons counted with single-photon-avalanche-diodes (SPAD).

Micro-structured silicon wafers

First ideas of aTEFs were based on commercial microchannel-plates (MCP). Here, electrons that hit inside the channels produce secondary electrons which are accelerated, through which an electron avalanche emerges. However, such devices can not be used in strong magnetic fields, such as those present in the KATRIN experiment. The simplest, but also most challenging way to produce an aTEF detector is to micro-structure Si-PIN diodes, such as those already used as a detector at KATRIN, as the current readout electronics of the detector could continue to be used. Etching hexagonal channels into thin silicon wafers is part of the research of collaborators of the University of Münster. The process is based

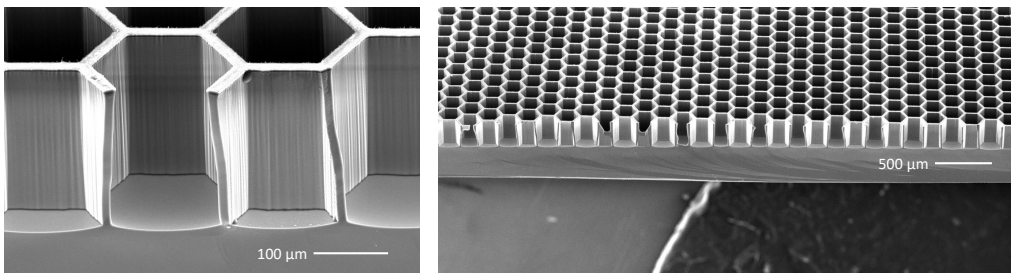

Figure 6.23.: Electron microscope image of a micro-scale cryo-etched silicon wafer. Etching is executed by inductively coupled plasma reactive-ion etching (ICP-RIE). The achieved etch-depth is 225 µm with a hexagon side length of 100 µm and a wall thickness of 10 µm [143].

on photo-lithography to produce a mask of the structure on the wafer and subsequent cryo-etching with reactive ions. The manufacturing result of this procedure is shown in fig. 6.23, an electron microscope image of a cryo-etched Si-PIN diode with a depth of 225 µm, hexagon side length of 100 µm, and a wall thickness of 10 µm. The efficiency of the signal-to-background enhancement depends on the channel depth provided, which is still under development in order to reach depths up to 400 µm, which is challenging in terms of the precision of the walls along the channels. First proof-of-principle measurements with etched Si-PIN diodes have been performed at the Münster Nanofabrication facility, and research is ongoing with respect to the material and detection properties of such novel detectors [143–145].

3D-printing of micro-scaled scintillators

Another approach to using micro-structured units as a novel detector with filtering of electrons according to their transverse energy or polar angle are scintillators in combination of photon detectors [146]. As of now, quadratic structures of plastic scintillators are under development, and first non-scintillating plastic micro-structures have been fabricated. Microscope images of the first 4 times 4 grid structures are shown in fig. 6.24. The plastic structures are manufactured by collaborators of the Institute of Applied Physics (APH) at KIT. They use a novel ultra-precise 3D printer from the company nanoscribe [147], which is based on 2-photon polymerisation, which is also known as direct laser writing [148], making it possible to produce structures with high precision on sub-micrometer scale.

Electrons of high transverse energy interact with the scintillator producing photons which are confined by internal reflections and transported through the material. Depending on their angle to the surface reflection or transmission occurs, according the Fresnel equations [149]. This also includes loss of photons which is tolerable as many photons are produced per incident electron, typically on the order of 10 γ/keV for commercial plastic scintillators [150]. Decoupling of the photons out of the material is then primarily taking place at the top and the bottom of the grid structure.

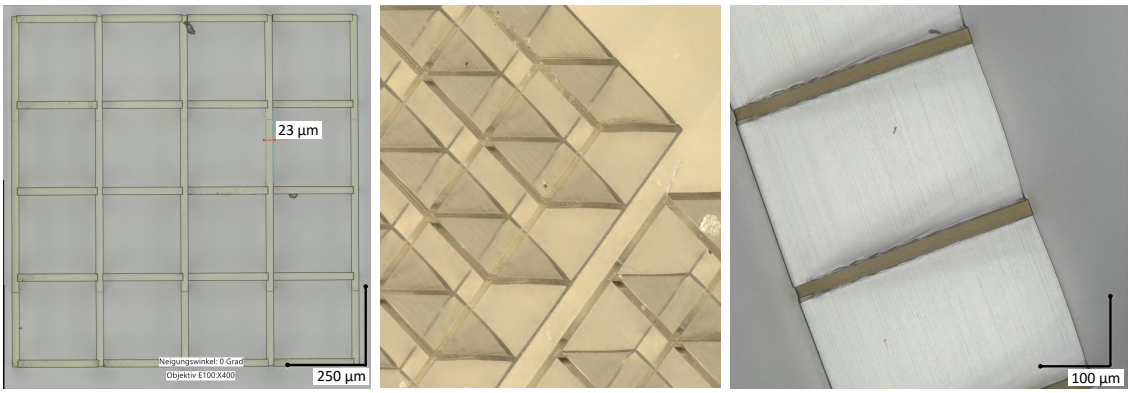

Figure 6.24.: Microscope images of a 3D printed plastic micro-structure by 2-photon polymerisation. The edge length of the quadratic channels is 250 µm with a wall thickness of 25 µm.

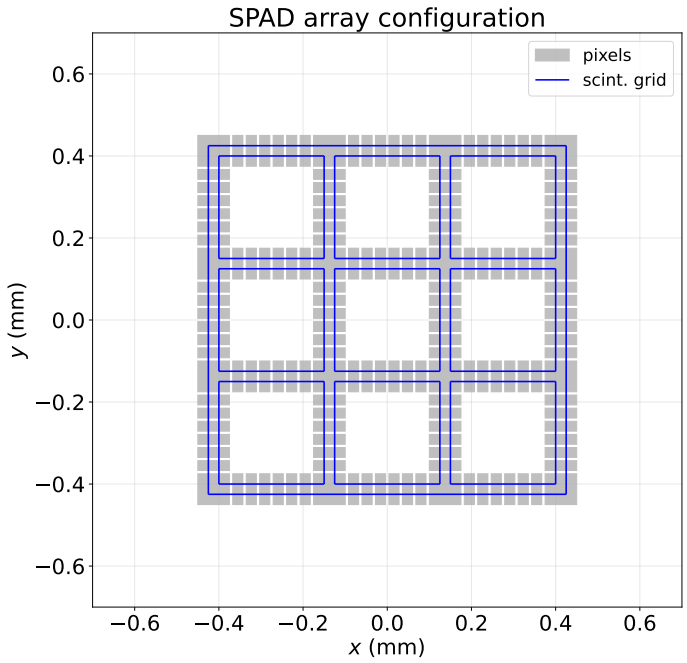

Figure 6.25.: Sketch of 3x3 structure grid of pixelised SPAD array. The blue line represents the position of the plastic scintillator grid on top of the SPADs [142].

At the bottom, an complementary metal-oxide-semiconductor (CMOS) based single photon avalanche diodes (SPAD) array is planned to be used to count the scintillation photons [146, 151]. Such types of detectors are manufactured at the Fraunhofer Institute for Microelectronic Circuits and Systems in research collaboration with the University of Heidelberg. The individual SPADs have a size on the micrometer scale and will be operated in Geiger-mode, which means that photon signals are binary. When a photon arrives at the SPAD, the cell is triggered. With the help of gates and summation specialised readout architectures, smart trigger by groups of pixel are possible. In fig. 6.25, the status of the grid-based CMOS SPAD arrays is shown. Since the photons are dominantly leaving the scintillators at the top and bottom, the SPAD cells can be arranged localised underneath the micro-structure (blue line). A first prototype of such a CMOS SPAD array detector is planned to be manufactured in 2022, with which dedicated studies regarding collection and detection efficiency will be performed. The current design considerations are based on Geant4 simulations, for which further details can be found in [142].

A first test facility with a CMOS based SPAD detector and commercial plastic scintillators is in use at the Institute for Astroparticle Physics (IAP) at KIT Campus North to investigate the properties of this detection system.

7. Developments on the Rydberg background model

From the pTEF measurement campaign, a higher than expected initial kinetic energy scale of the background electrons is observed. The initial kinetic electron energies were expected to be well below 100 meV by the Rydberg model [8, 9, 96]. The ionisation of highly excited hydrogen Rydberg atoms via black-body-radiation (BBR) leads to a mean energy of about 22 meV (see fig. 4.18). Under the assumption of isotropic emission in the sensitive main spectrometer volume the mean transverse energy is obtained to

$$\overline{E}_{\mathrm{t,Ryd}} = \overline{E}_{i,\mathrm{Ryd}} \cdot \overline{\sin^2(\theta_{\mathrm{i,iso}})} \simeq 14.5\,\mathrm{meV}\,. \tag{7.1}$$

A simulated initial energy distribution resulting from the ionisation of Rydberg atoms by BBR is shown in fig. 7.1 together with the initial polar angle θ_i distribution with respect to the magnetic field lines and the squared sinus of θ_i. The squared sinus distribution has a mean value of 0.667, but a significant portion is above 0.9.

However, the transverse energy scale fit on the pTEF measurement data show best compatibility with initial transverse energies in the range of 200 meV to 420 meV, depending on the trueness of the introduced reduction factor. Such transverse energy scales correspond to initial kinetic electron energies in the range of 300 meV to 630 meV which strongly disagree the expectation of the Rydberg background model. Since only the mean transverse energy could be derived, a combination of mechanisms providing very low and higher electron energies can be present, forming a broad energy distribution that complements the Rydberg background electrons. The generation mechanisms of electrons

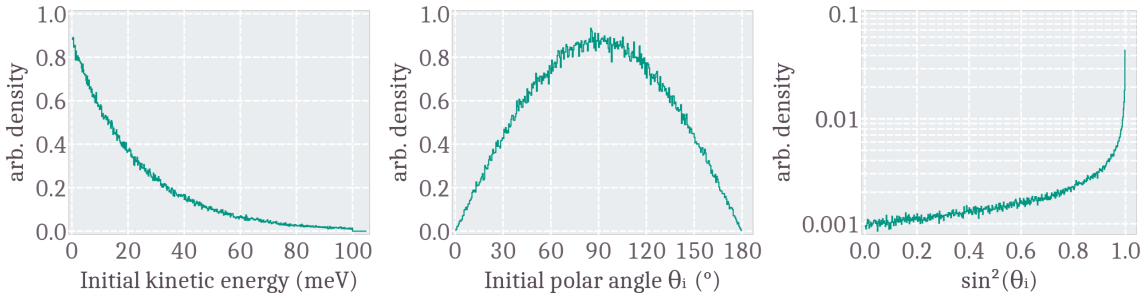

Figure 7.1.: Left: Initial kinetic energy E_i of electrons released by ionisation of Rydberg atoms by BBR. **Center:** Initial polar angle θ_i to the magnetic field distribution for isotropic emission in the sensitive main spectrometer flux tube volume. **Right:** Distribution of the squared sinus of the initial polar angle θ_i which has a mean of 0.667.

within the main spectrometer with energies in the derived range are puzzling, so it is in concordance with the various dependencies of the background rate, for example inner electrode potential. A major contribution of residual radon that would generate secondary eV-electrons is refuted. Furthermore, detailed simulations of the interaction of Rydberg atoms with photons of the black-body-radiation by stimulated transition and ionisation show a remarkably good agreement between measurement and simulation with respect to the sensitive flux tube volumes, the radial background distribution on the FPD, the vessel temperature and the inner electrode potential [9], which is why additional mechanisms must resemble this.

The natural extension of the Rydberg model which deals with hydrogen Rydberg atoms is the consideration of other atomic species. As known from the SRIM simulations all atoms of the main spectrometer stainless steel composition are transferred into the volume by sputtering. Oxygen is the most abundant sputtered species, which certainly depends on the surface composition model. However, this underlines the observation of the background rate reduction by baking the main spectrometer up to 200° [8, 9]. Here, a reduction of only 40 % was achieved which can not be explained by the dependence on surface adsorbed atoms such as hydrogen since these have been effectively released from the surface. Rydberg states of atoms other than hydrogen can be easily taken into account. If their excitation is high, the excited electron is bound to the remaining ionic core of charge +1. The contributions of the other electrons which are close to the nucleus are not seen due to the far distance, especially for states of high angular quantum number l, this results in a circular orbit around the remaining ion which acts as a heavier proton [135]. However, such Rydberg atoms are not able to provide higher electron energies after ionisation. The ionisation by BBR photons delivers the small amount of energy that is necessary to overcome the ionisation threshold which is independent of the atom or threshold energy, generating low energy electrons in the known regime well below 100 meV.

Nevertheless, the consideration of atoms other than hydrogen opens various properties of the involved atoms as they provide more than one electron. In particular, oxygen is an interesting candidate due to its electronic structure which is $1s^2 2s^2 2p^4$, providing a ground state triplet with the term symbol ${}^3P_{2,1,0}$. Term symbols are defined as

$$ {}^{2S+1}L_J \,, \tag{7.2} $$

with the total orbital angular momentum $L = |\sum m_l|$, the total spin $S = |\sum m_s|$ and total angular momentum J for LS-coupling. Only not completely filled subshells contribute to the calculation of L and S, specifically the $2p$ subshell for oxygen since it contains four electrons. The total orbital angular momentum is express by capitals for which holds $L = 1, 2, 3, 4, 5, \ldots = S, P, D, F, G, \ldots$.

The electronic configuration of ground state oxygen ${}^3P_2$ and the first low lying excited states are shown fig. 7.2. The three boxes for the $2p$ subshell represent the three orbitals with $m_l = (+1, 0, -1)$, leading to $L = 1$ for the ground state configuration, which can be filled with up to six electrons under consideration of the Pauli exclusion principle for the spin orientations. The first excited states of oxygen, ${}^1D_2$ and ${}^1S_0$ with excitation energies of 1.94 eV and 4.19 eV [152], respectively, are special as these states are metastable [153].

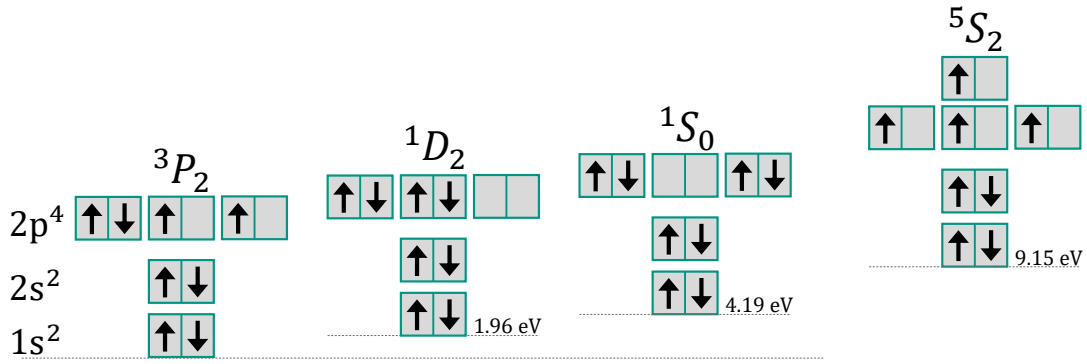

Figure 7.2.: Electronic configuration of lowest states of atomic oxygen. **Outer left:** Ground state configuration of $^3P_2$. **Center:** First and second lowest excited states above the ground state triplet with term symbols $^1D_2$ and $^1S_0$. **Outer right:** First Rydberg state with one electron excited to the 3*s* orbital to the configuration $1s^2 2s^2 2p^3 (^4S^\circ_{3/2}) 3s$.

De-excitation is forbidden by direct electric dipole interaction but possible via electric quadrupole or magnetic dipole transitions which are suppressed. The corresponding lifetimes of these states are $\tau = 108.9\,\mathrm{s}$ ($^1D_2$) and $\tau = 0.7\,\mathrm{s}$ ($^1S_0$) [153, 154]. Further excitation leads to the lowest Rydberg state $1s^2 2s^2 2p^3 (^4S^\circ_{3/2}) 3s$ with a level energy of 9.15 eV [152]. All spins of the outer electrons are aligned so that the total spin amounts to $S = 2$ but $L = |\sum m_l| = 0$ as every orbital is filled once, which leads to the term symbol $^5S_2$. Here, transitions to lower-lying states are also only possible via second-order transitions by spin-orbit interactions with the ^3P ground state, resulting in an enhanced lifetime of $\tau \approx 180\,\mu\mathrm{s}$ [155]. Frequently, the electronic configuration of the remaining ion is mentioned, which is $^4S^\circ_{3/2}$ in the case of oxygen. However, there exist further configurations of the remaining ion in ^2D and ^2P states which have higher ionisation thresholds, 3.3 eV and 5.0 eV respectively, than the ^4S state. This fact leads to another feature of interest when considering oxygen. Since the ionisation thresholds of the ^2D and ^2P states are significantly larger than the threshold of the ^4S state, autoionisation can occur.

Autoionisation of atomic oxygen states is observed after dissociation of oxygen molecules with light [156, 157]. Fragment atoms are also produced in excited states of the remaining ions of states ^2D and ^2P which can be labeled as double excited states with excitation of the remaining ion core. Formation of these excited fragments leads to the dissociation and double ionisation of the primary molecule according to

$$O_2 + h\nu \rightarrow O^* + O^* \rightarrow \underbrace{O^+ + \mathrm{e}^-}_{\text{fast}} + O^* \rightarrow O^+ + \mathrm{e}^- + \underbrace{O^+ + \mathrm{e}^-}_{\text{slow}} . \tag{7.3}$$

Especially in [157], a fast and slow electron signal was observed that was associated with core- (fast) and valence-excitations (slow). The lifetime of the valence-excitation is assumed to be on the order of µs [159], which is emphasised by forbidden transitions in

Table 7.1.: Energies and assignments of atomic autoionising states [158]. Roman letters refer to peak labels in fig. 7.3. Primes and double primes refer to the (^2D) and (^2P) core, respectively. Reused with permission from [157] Copyright (2022) by the American Physical Society.

Peak	Electron kinetic energy (eV)	Assignment
a	0.420	$3p'(^1P,\ ^3D)$
b	0.495	$3p'(^3F)$
b'	0.510	$3s''(^3P)$
c'	0.754	$3s''(^1P)$
c	0.850	$3p'(^1D)$
d	1.567	$4s'(^3D)$
e	1.672	$3d'(^3P)$
f	1.790	$3d'(^1P)$
g	2.001	$3p'$
h	2.464	$4d', 4f'$
i	2.770	$5d'$

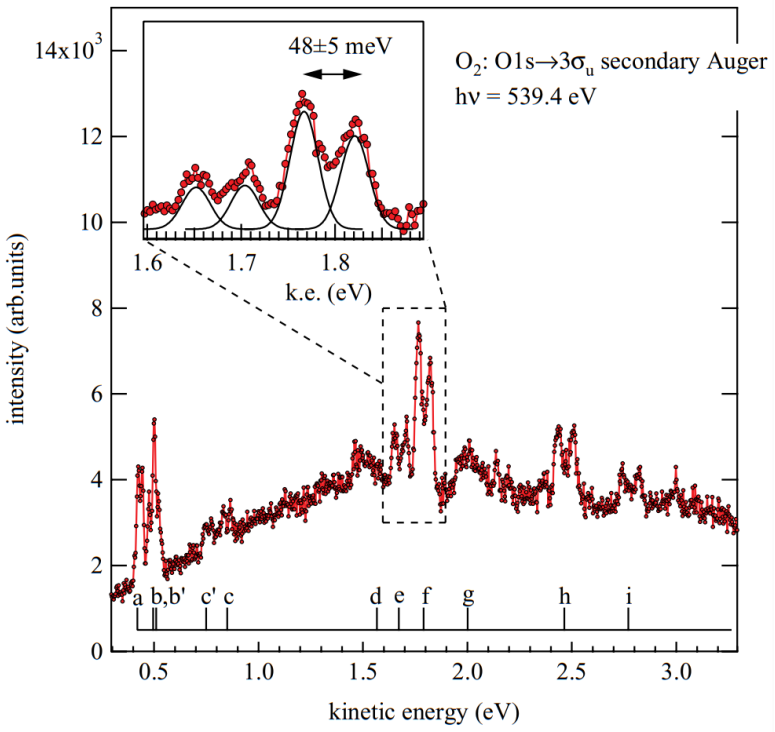

Figure 7.3.: Autoionisation spectrum measured in kinetic-energy range from 0 eV to 3.5 eV. There exist double peaks due to Doppler splitting at observed lines. Peak amplitudes are convoluted with a continuous background shape. Reprinted figure with permission from [157] Copyright (2022) by the American Physical Society.

the scope of *LS*-coupling [160]. The autoionisation electron spectrum, obtained by double ionisation and dissociation of molecular oxygen by 539.4 eV photons is shown in fig. 7.3 with the highlighted peak energies in tab. 7.1.

Several transitions have been observed in the energy range from 0.42 eV up to 2.77 eV which are superimposed with the shake-off continuum [157]. However, these autoionising states and the corresponding electrons have also been observed by interactions with photon energies of approximately 50 eV [156], revealing that the generation of electrons by autoionisation above 1 eV depends on the initial photon energy.

The formation of autoionising states of oxygen can not be exclusively achieved by photons, but also by scattering with other atoms, for example helium atoms [161], also providing electrons of the energies, given in tab. 7.1, measured by Penning ionisation electron spectroscopy. Penning ionisation describes the ionisation of reactants at scattering interactions of atoms or molecules Y_n, whereby the initial excited atoms X^* that are involved transfer their excitation energy according to

$$X^* + Y_n \rightarrow \begin{cases} X + Y_n^+ + \mathrm{e}^- \\ X + Y_n^* \end{cases} \tag{7.4}$$

to either ionise or excite the atoms Y ($n = 1$) or molecules ($n > 1$) [130]. This process of energy transfer is important in the model extension on how the excited states are formed inside the KATRIN main spectrometer. Formerly, resonant neutralisation of hydrogen atoms close the the metallic surface was considered [9, 112] but during sputtering processes, many atoms on the timescale of one decay are released. An example lateral position distribution is shown in fig. 7.4b with a cluster size of 43 atoms and a mean inter-atomic

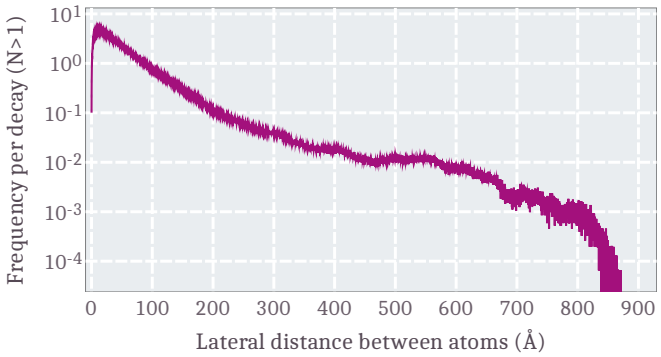

(a) Inter-atomic distances.

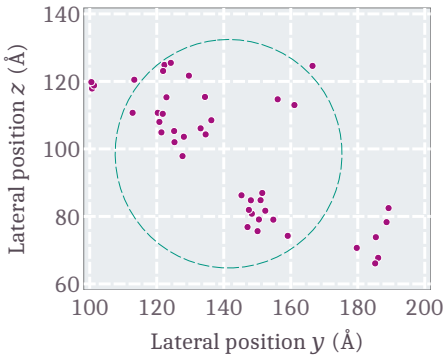

(b) One decay positions.

Figure 7.4.: Inter-atomic distance sputtering of atoms from the main spectrometer surface. **(a):** Distribution of the distance between sputtered atoms on the surface derived from the SRIM simulations (sec. 4.5.3). The distance is collected from each atom to every other atom from the α-decays with at least two sputtered atoms (N>1). **(b):** Example of lateral positions distribution of sputtered atoms on the surface. Here, 43 atoms were sputtered with a mean distance to each other of 37 Å. The size of an excited hydrogen atom to $n = 8$ is highlighted as a green dashed line, according eq. 4.7.

distance of 37 Å, whereas clusters of up to 200 atoms are possible (fig. 4.16). Additionally, the geometric size of a hydrogen Rydberg state is shown with a principle quantum number $n = 8$ that provides a orbital radius of 33.9 Å. The atoms are distributed on a surface of approximately 63 nm^2 with the closest proximity in the range of few angstrom. The inter-atomic distance of the generation positions of all simulated sputtered atoms of the ^{210}Po-decay is shown in fig. 7.4a, whereat most of the atoms have distances below 200 Å to each other with a maximum at approximately 10 Å.

The orbital radius of excited atoms largely exceeds the inter-atomic distances, as it scales with n^2, overlapping electron clouds of atoms are therefore highly probable which result in various scattering interactions within the atomised particles that leave the main spectrometer surface in sputtering processes. Under these considerations and the presence of excited atoms, numerous interactions such as autoionisation, Penning ionisations and excitations, and electron-atom interactions close to the spectrometer surface take place. This leads to several electron generations near the surface, but also to various excited states leaving the surface into the main spectrometer volume. The existence of clustered electron events from the inner main spectrometer surface with cluster sizes up to 50 electrons on a timescale of $\delta t < 200$ µs have been observed in measurements [8]. What was surprising here was the extent of the mapped area to the detector from which the electrons were measured. It was on the order of 0.25 m^2, which can only be explained by short-lived states propagating into the volume and releasing the electrons at a greater distance from the inner spectrometer surface.

However, electron generation at or in the proximity of the inner main spectrometer surface is not of relevance in standard operation at KATRIN. Autoionising states, even with enhanced lifetime, decay on timescales shorter than necessary to provide the measured electron rate in the center of the main spectrometer volume. Certainly, excited states of the high energy part of the sputtered atoms with velocities above 100 km s^{-1} (see fig. A.4) could potentially reach the inner regions of the flux tube, but their appearance probability is only 7 % which makes this scenario worth mentioning, but rather unlikely.

As a result, further mechanism than fast autoionising states have to be considered. Both neutral double Rydberg states and excited anions which exceed the ionisation threshold have to be discussed. In contrary to the fast autoionising states where the remaining ionic core is excited, double Rydberg states deal with two valence electrons excited to higher lying states with $n > 3$, which are also called planetary atoms [162]. Such states can be described by the Hamiltonian of a two-electron atom (or ion) by

$$H = \frac{p_1^2 + p_2^2}{2} - \frac{Z}{r_1} - \frac{Z}{r_2} + \frac{1}{r_{12}} + V_{nc}(r_1) + V_{nc}(r_2) \tag{7.5}$$

in atomic units with the potentials V_{nc} that account for non-Coulombic perturbations [163] and the positions of the electrons r_1 and r_2, as well as their distance to each other r_{12}. Neglecting the potentials V_{nc}, the non-relativistic Hamiltonian of an helium atom is obtained for $Z = 2$ [131, 135, 164], which can be used for the description of these states. Of particular interest are states with $r_1 > r_2$ which is given when both excited electrons are in a state of high angular quantum number l, or $n_2 << n_1$. The orbital radius increases with n^2, as expressed in eq. 4.7, while the orbital motion becomes circular around the remaining ionic core for increasing angular quantum number l. Their autoionisation rate

highly depends on the combined excitation states of the outer electrons, which can be thought as the overlap of electron clouds. Both electrons orbit around the remaining ion in areas of certain residence probability. In the case of a planetary atom, both electrons are highly excited $n_i >> 1$, through which their radiative lifetime is large, as it scales with n^3. Additionally, high angular quantum numbers l_i are assumed, so their orbits are circular and no overlap of their radial residence probability is present, which minimises the interaction between the electrons $V(r_{12})$. The square of the overlap integral can be expressed as

$$\langle \nu l | \nu' l \rangle^2 = \frac{4\nu\nu' \sin^2(\pi(\nu' - \nu))}{\pi^2(\nu'^2 - \nu^2)^2} \tag{7.6}$$

with the quantum defect adjusted quantum number $\nu = n - \delta$ in a quantum defect theory [131]. It is obvious that the overlap integral varies periodically by the squared sine function which is maximal for similar ν_i so does the transition (autoionisation) rate. The transition of autoionising double excited states strongly depends on the inner excited electron with quantum number n_2 since the number of decay channels into the continuum increases proportional to n^2.

In some cases, however, the states of the outer electrons lead to destructive interference due to the spin-orbit interaction between highly excited Rydberg electrons and the residual ionic core. This had been observed in barium [165] and helium [164] atoms, and was theoretically described by semi-classical celestial mechanics by Percival [162]. This destructive interference causes the transition rate Γ to almost disappear, and therefore to outmost enhanced lifetimes of the double excited states up to the order of seconds [162, 164] or stable configurations [166].

The electron energy range in these autoionisation process of doubly excited Rydberg atoms is similar to the one discussed for oxygen. Kinetic energies over the range of few meV to eV are possible which occur as peaks, depending on the electronic structure of the double excited atom [167]. In the same manner, the existence of excited anions can be suggested to be able to ionise by interactions with BBR photons, such as photodetachment processes observed for H^- anions [168] which also deliver electron energies from several hundred meV to eV. In particular, the existence of hydrogen anions at the KATRIN experiment is experimentally proven since negative ions produce an explicit peak in the energy spectrum on the FPD well below the electron peak due ions loosing more energy in the dead layer of the silicon wafer. The formation of H^- anions has showed an inner electrode potential offset dependence [8, 169].

Conclusively, the current Rydberg background model [9, 96], which deals with the sputtering of hydrogen atoms in highly excited states so that ionisation by black-body-radiation photons of meV energy is possible, has to be extended as observation with a passive transverse energy filter showed that the energy spectrum strongly differs from the Rydberg background model prediction of less meV electron starting kinetic energies. Possible generation mechanisms of background electrons over the range of several hundred meV up to eV are discussed which are feasible explanation of the observation for which atomic species other than hydrogen had to be considered. Of relevance are metastable double excited Rydberg states with excitation energies above the ionisation threshold of the corresponding ion. Due to destructive interference of interaction channels of the

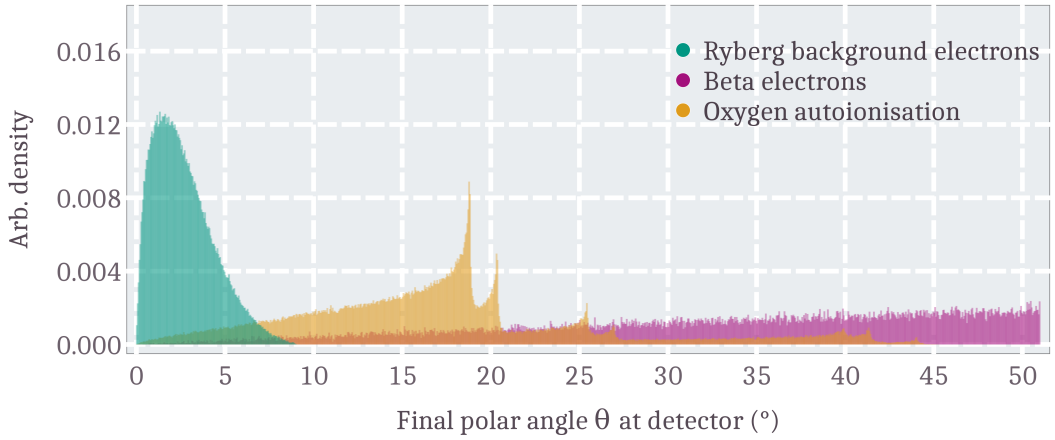

Figure 7.5.: Final polar angle distribution of Rydberg background, tritium beta electrons and electrons from autoionisation of oxygen for the 5 G symmetric magnetic field setting at 18.6 keV retarding potential. Electron energies and relative occurrence according to [156] fig. 2 with the labels A1-A7 and A10.

participating electrons and the remaining ionic core, enhanced lifetimes of these states, up to several seconds, are possible which are able to explain the observed radial background distribution in the KATRIN main spectrometer. Furthermore, autoionising states of short lifetime are presumed to be primarily observed in the outer range of the magnetic flux tube in proximity to the inner main spectrometer vessel surface. However, the velocity of the sputtered atoms can also be excessively high above 100 km s^{-1}, through which electrons of short-lived autoionising states are generated in center-regions. In these processes, the kinetic energy of the resulting electrons are on the order of several hundred meV up to eV, comparable to the autoionisation spectrum of oxygen, as shown in fig. 7.3. These energies lead to enlarged final polar angles at the FPD, thus a reduced background fraction behind the passive transverse energy filter. The final polar angle distribution of electrons, resulting from autoionisation of oxygen is shown in fig. 7.5 according the kinetic energies and relative occurrence from [156]. The distribution of the initial kinetic energy has a mean of $\overline{E}_i = 0.76$ eV.

The novel KATRIN background model contains the former Rydberg background model, as it was very successfully describing the radial background rate and other dependencies in simulations [9], but is extended by further electron generation mechanisms. These result in higher kinetic energy in accordance with the pTEF measurement results under comprehension of Radon-induced background, which would lead to trapped electrons not observed in such quantities. The observed higher mean transverse energy can be explained by the combination of classical Rydberg background electrons and electrons from autoionisation processes of doubly excited multi-electron atoms such as oxygen.

8. Conclusion and outlook

The KATRIN experiment is a very suitable device to investigate the absolute effective electron neutrino mass by ultra-precise spectroscopy of beta electrons from tritium decays. It provides the best upper limit on the neutrino mass with $m_\nu < 0.8\,\mathrm{eV/c^2}$ (90 % C.L.) and aims to reach a final sensitivity of $0.2\,\mathrm{eV/c^2}$ [4]. This limit was reached with the data from the first neutrino mass measurement campaigns KNM1 and KNM2, which corresponds to about 50 measurement days, at reduced source luminosity. The goal is a complete measurement period of 1000 days. Of major importance to fulfill the design neutrino mass sensitivity is the reduction of systematic error contributions. Systematics that arise from background processes dominantly influence the sensitivity on the squared neutrino mass with up to $0.29\,\mathrm{eV^2}$ within one campaign which is unacceptable.

An elevated background level of about 150 mcps, 15 times higher than anticipated limits the statistical sensitivity. In addition, three different contributions by background events were encountered: a retarding potential variation on the background rate, the non-Poisson overdispersion of the measured background electrons within one scan-step, and the scan-step-duration-dependent background, originating from the inter-spectrometer Penning trap. Within the scope of the measurement campaigns KNM2 to KNM5 each of these could be efficiently reduced to a combined level of $0.01\,\mathrm{eV^2}$ error contribution on the squared neutrino mass. The background level, as well as the contribution by residual radon which leads to a non-Poisson broadening of the measured background rate, was reduced or completely removed by changing the MAC-E filter electromagnetic field configuration from NAP (nominal analysing plane) to SAP (shifted analysing plane). Herewith, the maximum potential and the minimum magnetic field are shifted towards the detector through which the sensitive flux tube volume decreases, providing a reduced background rate by a factor of two with no non-Poisson overdispersion but maintaining the transmission conditions of the MAC-E filter. In addition to the eliminated non-Poisson broadening, the scan-step-duration-dependent background source, which was detected during KNM4 and formed in the inter-spectrometer Penning trap, could also be eliminated by grounding the pre-spectrometer. The influence of the high electron flux as a background source, which then enters the main spectrometer and possibly ionises residual gas, is not a concern in the SAP configuration because the sensitive flux tube is further away from the entrance of the main spectrometer. Lastly, the increasing background rate with increasing retarding potential remains the only background-related systematic contribution. This was improved by dedicated background slope measurements in the SAP configuration to $0.01\,\mathrm{eV^2}$. This contribution can be further improved by additional background measurement time.

In order to be able to improve the background level by appropriate countermeasures, knowledge of the mechanism of electron generation is essential. The current Rydberg background model [9], which describes this generation mechanism by the ionisation of

highly excited hydrogen Rydberg atoms by black-body-radiation (BBR) nicely validates the measured data with respect to the radial, temperature, and inner electrode potential dependency. Thereby, the highly excited atoms are generated by sputtering processes from the inner spectrometer surface due to 1 kBq of radioactive decays of ^{210}Pb which accumulated during the construction of the inner electrode system by decays of natural occurring ^{222}Rn.

Former dedicated background measurements [77, 96] indicate that the background electrons are generated with higher initial kinetic energy than expected from the ionisation of Rydberg atoms by BBR. The derived energy scale is on the order of several hundred meV, whereas the expectation is at 22 meV. To further investigate the background from the main spectrometer volume with respect to the initial kinetic energy of the electrons, a novel device was introduced into the KATRIN beamline. The passive transverse energy filter (pTEF) is a gold plate equipped with micro-scale hexagonal channels and acts as a geometrical boundary to electrons in the high magnetic field in front of the detector. Electrons with high initial kinetic energy possess larger transverse energies which then impact on the filter and are not detected with the focal-plane detector (FPD), whereas electrons with small transverse energy (small initial kinetic energy) are transmitted and detected. With the use of the pTEF in front of the FPD, the Rydberg background model can be probed since meV-electrons should be transmitted efficiently with the geometry used. The only model assumptions are the adiabatic motion of the electrons, thus, conservation of the magnetic moment of the cyclotron motion μ and the background density profile in the sensitive flux tube volume. This can be approximated by the distance to the inner main spectrometer surface from which the atoms originate at the sputtering process. The authenticity of the former measurements was limited by special electromagnetic field calculations and models describing the measured data. This problem was solved by measurements with the pTEF.

The observation of higher than anticipated initial kinetic electron energies of the background electrons was confirmed with the pTEF measurement data. By successively changing parameters that influence the final polar angle distribution and thus the transmission probability through the filter, such as the magnetic field and the electric potential, the mean transverse energy scale was derived. Since the background rate reduction behind the pTEF is measured, only the mean value of the initial energy distribution is accessible which is determined to be in the range from 300 meV to 630 meV, depending on the consideration of unidentified systematics. This result contradicts the initial electron energy scale of the current Rydberg background model by at least a factor of 13, so extensions to the background generation mechanism were made which describe all detected characteristics. Firstly, atoms other than hydrogen are considered, which is a rather obvious extension since hydrogen accounts for only a part of the sputtered atoms gathered with SRIM simulations. This opens up the possibility of double excitations of atoms and autoionising states whose resulting background electrons are not dependent on the low energy of the BBR photons and therefore are able to provide higher initial kinetic energy in the required range. During sputtering from the inner main spectrometer surface many atoms are released at single α-decays of ^{210}Po, which in particular lead to many interactions such as excitation and Penning ionisation processes in the proximity of the surface. This explains the large electron cluster sizes observed in measurements [8].

Presumably oxygen plays a key role in the consideration of double excited autoionising states as metastable states of enhanced lifetime exists due to electronic core excitations which are forbidden to de-excite by electric dipole transitions. Electrons, following autoionisation of oxygen have been observed in experiments [156–158] in the range from 420 meV to energies above 2 eV which certainly can explain the pTEF observation, depending on their relative appearance. However, autoionisation is a fast process and would not entirely match the observed radial background distribution, especially in the center of the magnetic flux tube for which lifetimes on the order of µs are necessary which would only account for the high energy part of the sputtered atoms with velocities above 100 km s^{-1}. Apart from this, double excitation can also produce long-lived states called double Rydberg states or planetary atoms [162]. These are characterised by two valence electrons in excited states far apart from each other. This is possible through excitations to states with an additionally high angular quantum number $l \lesssim n$, where the radial probability is located at the associated Larmor radius and the orbit around the remaining ion core is circular. If the principal quantum numbers n_1 and n_2 are high and different, no overlap of their corresponding electron cloud (radial probability) exists which results in significantly enhanced lifetimes up to seconds since the interactions of the electrons with each other or the remaining ionic core are diminished. The presence of such states in combination with the Rydberg background model and fast autoionising states is capable of explaining the observed radial background distribution in the KATRIN experiment and, at the same time provides higher electron energies after ionisation in accordance with the transverse energy scale derived at the pTEF measurements.

In the near future further measurements with passive transverse energy filters are planned, during the upcoming campaign in winter 2022 a new pTEF with two different hexagonal channel geometries will be used. With smaller channel dimensions, the total share of the classical Rydberg background in the total background rate can be extracted, while additionally larger channels are used as a cross reference to this observation with respect to unidentified systematic contributions. Furthermore, the measurements will provide more information since investigation with beta electrons from the tritium source whose final polar angle distribution is well known, will be performed. In parallel to the investigations on the background with passive transverse energy filters, research activities on active transverse energy filters will continue. It is planned to perform light yield investigations on self-made plastic scintillators in combination with single-photon-avalanche-diodes (SPADs) which could be used as a novel detection system at KATRIN, reducing the background rate by their geometry and advanced signal triggers.

Bibliography

[1] W. Pauli. *Offener Brief an die Gruppe der Radioaktiven bei der Gauvereins-Tagung zu Tübingen.* Zürich: Physikalisches Institut der Eidg. Technischen Hochschule, 1930.

[2] Class for Physics of the Royal Swedish Academy of Sciences. "Scientifc Background on the Nobel Prize in Physics 2015 NEUTRINO OSCILLATIONS". In: (2015). URL: https://www.nobelprize.org/uploads/2017/09/advanced-physicsprize2015.pdf.

[3] M. Aker et. al. "The design, construction, and commissioning of the KATRIN experiment". In: *Journal of Instrumentation* 16.08 (Aug. 2021), T08015. DOI: 10.1088/1748-0221/16/08/t08015.

[4] The KATRIN Collaboration. "Direct neutrino-mass measurement with sub-electronvolt sensitivity". In: *Nat. Phys* 18 (2022), pp. 160–166. DOI: https://doi.org/10.1038/s41567-021-01463-1.

[5] C.W. Reich and Balraj Singh. "Nuclear Data Sheets for A = 163". In: *Nuclear Data Sheets* 111.5 (2010), pp. 1211–1469. ISSN: 0090-3752. DOI: https://doi.org/10.1016/j.nds.2010.04.001. URL: https://www.sciencedirect.com/science/article/pii/S0090375210000451.

[6] Mikhail M. Ivanov, Marko Simonovi ć, and Matias Zaldarriaga. "Cosmological parameters and neutrino masses from the final *Planck* and full-shape BOSS data". In: *Phys. Rev. D* 101 (8 2020), p. 083504. DOI: 10.1103/PhysRevD.101.083504. URL: https://link.aps.org/doi/10.1103/PhysRevD.101.083504.

[7] M. Agostini et al. "Probing Majorana neutrinos with double-β decay". In: *Science* 365.6460 (2019), pp. 1445–1448. DOI: 10.1126/science.aav8613. URL: https://www.science.org/doi/abs/10.1126/science.aav8613.

[8] Fabian Harms. "Characterization and Minimization of Background Processes in the KATRIN Main Spectrometer". PhD thesis. Karlsruher Institut für Technologie (KIT), 2015. DOI: 10.5445/IR/1000050027. URL: http://nbn-resolving.org/urn:nbn:de:swb:90-500274.

[9] Nikolaus Rainer-Maria Trost. "Modeling and measurement of Rydberg-State mediated Background at the KATRIN Main Spectrometer". PhD thesis. Karlsruher Institut für Technologie (KIT), 2019. DOI: 10.5445/IR/1000090450.

[10] E. Fermi. "Versuch einer Theorie der β-Strahlen. I". In: *Zeitschrift für Physik* 88.3-4 (1934), pp. 161–177. ISSN: 1434-6001. DOI: 10.1007/BF01351864.

[11] J. Chadwick. "Intensitätsverteilung im magnetischen Spektrum von β - Strahlen von Radium B+C". In: *Verhandlungen der Deutschen Physikalischen Gesellschaft* 16 (1914), pp. 383–391.

[12] Charles Drummond Ellis, W. A. Wooster, and Ernest Rutherford. "The average energy of disintegration of radium E". In: *Proceedings of the Royal Society of London. Series A, Containing Papers of a Mathematical and Physical Character* 117.776 (1927), pp. 109–123. DOI: 10.1098/rspa.1927.0168.

[13] C. L. Cowan et al. "Detection of the Free Neutrino: a Confirmation". In: *Science (New York, N.Y.)* 124.3212 (1956), pp. 103–104. ISSN: 0036-8075. DOI: 10.1126/science.124.3212.103.

[14] G. Danby et al. "Observation of High-Energy Neutrino Reactions and the Existence of Two Kinds of Neutrinos". In: *Physical review letters* 9.1 (1962), pp. 36–44. ISSN: 0031-9007. DOI: 10.1103/PhysRevLett.9.36.

[15] P. A. Zyla et al. "Review of Particle Physics". In: *PTEP* 2020.8 (2020), p. 083C01. DOI: 10.1093/ptep/ptaa104.

[16] K. Kodama et al. "Observation of tau neutrino interactions". In: *Physics Letters B* 504.3 (2001), pp. 218–224. ISSN: 03702693. DOI: 10.1016/S0370-2693(01)00307-0.

[17] CERN ATLAS Experiment. *Atlas-Standard-Model-2*. 2018. URL: https://atlas.cern/discover/physics.

[18] Robert Oerter. *The theory of almost everything: The standard model, the unsung triumph of modern physics*. New York: Plume, 2014. ISBN: 978-1-101-12674-5.

[19] C. S. Wu et al. "Experimental Test of Parity Conservation in Beta Decay". In: *Physical Review* 105 (1957), pp. 1413–1414. DOI: 10.1103/PhysRev.105.1413.

[20] M. Goldhaber, L. Grodzins, and A. W. Sunyar. "Helicity of Neutrinos". In: *Phys. Rev.* 109 (3 Feb. 1958), pp. 1015–1017. DOI: 10.1103/PhysRev.109.1015.

[21] C. N. Yang and R. L. Mills. "Conservation of Isotopic Spin and Isotopic Gauge Invariance". In: *Phys. Rev.* 96 (1 Oct. 1954), pp. 191–195. DOI: 10.1103/PhysRev.96.191. URL: https://link.aps.org/doi/10.1103/PhysRev.96.191.

[22] Samoil Bilenky. *Introduction to the Physics of Massive and Mixed Neutrinos*. Lecture notes in physics 817. Springer Heidelberg Dordrecht London New York, 2010. DOI: 10.1007/978-3-642-14043-3.

[23] Steven Weinberg. "A Model of Leptons". In: *Phys. Rev. Lett.* 19 (Nov. 1967), pp. 1264–1266. DOI: 10.1103/PhysRevLett.19.1264. URL: https://link.aps.org/doi/10.1103/PhysRevLett.19.1264.

[24] Jeffrey Goldstone, Abdus Salam, and Steven Weinberg. "Broken Symmetries". In: *Phys. Rev.* 127 (3 1962), pp. 965–970. DOI: 10.1103/PhysRev.127.965. URL: https://link.aps.org/doi/10.1103/PhysRev.127.965.

[25] P. W. Higgs. "Broken symmetries, massless particles and gauge fields". In: *Physics Letters* 12.2 (1964), pp. 132–133. ISSN: 0031-9163. DOI: doi.org/10.1016/0031-9163(64)91136-9.

[26] The Borexino Collaboration. "Comprehensive measurement of pp-chain solar neutrinos". In: *Nature* 562 (2018), pp. 505–510. DOI: https://doi.org/10.1038/s41586-018-0624-y.

[27] R. Davis. “A review of the homestake solar neutrino experiment”. In: *Progress in Particle and Nuclear Physics* 32 (1994), pp. 13–32. ISSN: 01466410. DOI: 10.1016/0146-6410(94)90004-3.

[28] K. S. Hirata et al. “Real-time, directional measurement of B8 solar neutrinos in the Kamiokande II detector”. In: *Physical Review D* 44.8 (1991), pp. 2241–2260. ISSN: 0556-2821. DOI: 10.1103/PhysRevD.44.2241.

[29] J. et. al. Hosaka. “Solar neutrino measurements in Super-Kamiokande-I”. In: *Phys. Rev. D* 73 (11 2006), p. 112001. DOI: 10.1103/PhysRevD.73.112001. URL: https://link.aps.org/doi/10.1103/PhysRevD.73.112001.

[30] Q. R. Ahmad et al. “Direct Evidence for Neutrino Flavor Transformation from Neutral-Current Interactions in the Sudbury Neutrino Observatory”. In: *Phys. Rev. Lett.* 89 (2002), p. 011301. DOI: 10.1103/PhysRevLett.89.011301.

[31] Y. Fukuda et al. “Evidence for oscillation of atmospheric neutrinos”. In: *Phys. Rev. Lett.* 81 (1998), pp. 1562–1567. DOI: 10.1103/PhysRevLett.81.1562.

[32] K. Zuber. *Neutrino Physics*. Series in High Energy Physics, Cosmology and Gravitation. CRC Press, 2020. ISBN: 9781351764575.

[33] Ziro Maki, Masami Nakagawa, and Shoichi Sakata. “Remarks on the Unified Model of Elementary Particles”. In: *Progress of Theoretical Physics* 28.5 (Nov. 1962), pp. 870–880. ISSN: 0033-068X. DOI: 10.1143/PTP.28.870. eprint: https://academic.oup.com/ptp/article-pdf/28/5/870/5258750/28-5-870.pdf. URL: https://doi.org/10.1143/PTP.28.870.

[34] K. Abe et al. “Constraint on the matter–antimatter symmetry-violating phase in neutrino oscillations”. In: *Nature* 580.7803 (2020). [Erratum: Nature 583, E16 (2020)], pp. 339–344. DOI: 10.1038/s41586-020-2177-0. arXiv: 1910.03887 [hep-ex].

[35] D. Adey et al. “Measurement of the Electron Antineutrino Oscillation with 1958 Days of Operation at Daya Bay”. In: *Phys. Rev. Lett.* 121.24 (2018), p. 241805. DOI: 10.1103/PhysRevLett.121.241805. arXiv: 1809.02261 [hep-ex].

[36] G. Bak et al. “Measurement of Reactor Antineutrino Oscillation Amplitude and Frequency at RENO”. In: *Phys. Rev. Lett.* 121.20 (2018), p. 201801. DOI: 10.1103/PhysRevLett.121.201801. arXiv: 1806.00248 [hep-ex].

[37] T. Abrahão et al. “Search for Signatures of Sterile Neutrinos with Double Chooz”. In: *Eur. Phys. J. C* 81 (2021), p. 775. DOI: 10.1140/epjc/s10052-021-09459-0.

[38] A. Gando et al. “Reactor On-Off Antineutrino Measurement with KamLAND”. In: *Phys. Rev. D* 88.3 (2013), p. 033001. DOI: 10.1103/PhysRevD.88.033001. arXiv: 1303.4667 [hep-ex].

[39] M. A. Acero et al. “First Measurement of Neutrino Oscillation Parameters using Neutrinos and Antineutrinos by NOvA”. In: *Phys. Rev. Lett.* 123.15 (2019), p. 151803. DOI: 10.1103/PhysRevLett.123.151803. arXiv: 1906.04907 [hep-ex].

[40] B. Aharmim et al. “Combined Analysis of all Three Phases of Solar Neutrino Data from the Sudbury Neutrino Observatory”. In: *Phys. Rev. C* 88 (2013), p. 025501. DOI: 10.1103/PhysRevC.88.025501. arXiv: 1109.0763 [nucl-ex].

[41] M. Jiang et al. "Atmospheric Neutrino Oscillation Analysis with Improved Event Reconstruction in Super-Kamiokande IV". In: *PTEP* 2019.5 (2019), 053F01. DOI: 10.1093/ptep/ptz015. arXiv: 1901.03230 [hep-ex].

[42] NuFit. "v5.1: Three-neutrino fit based on data available in October 2021". In: (). URL: www.nu-fit.org.

[43] M. Maltoni et al. I. Esteban M. Gonzalez-Garcia. "The fate of hints: updated global analysis of three-flavor neutrino oscillations". In: *J. High Energ. Phys.* 178 (2020). DOI: 10.1007/JHEP09(2020)178.

[44] L. Wolfenstein. "Neutrino oscillations in matter". In: *Physical Review D* 17.9 (1978), pp. 2369–2374. ISSN: 0556-2821. DOI: 10.1103/PhysRevD.17.2369.

[45] Lutz Schimpf. "Characterisation of energy loss processes of 18.6 keV electrons inside the windowless tritium source of KATRIN". PhD thesis. Karlsruher Institut für Technologie (KIT), 2021. URL: https://publikationen.bibliothek.kit.edu/1000131810.

[46] Rabindra N. Mohapatra and Goran Senjanovi ć. "Neutrino Mass and Spontaneous Parity Nonconservation". In: *Phys. Rev. Lett.* 44 (14 1980), pp. 912–915. DOI: 10.1103/PhysRevLett.44.912.

[47] Rabindra N. Mohapatra and Goran Senjanovi ć. "Neutrino masses and mixings in gauge models with spontaneous parity violation". In: *Phys. Rev. D* 23 (1 1981), pp. 165–180. DOI: 10.1103/PhysRevD.23.165.

[48] N. Aghanim, Y. Akrami, and M. Ashdown et. al. "Planck 2018 results". In: *Astronomy & Astrophysics* 641 (2020), A6. DOI: 10.1051/0004-6361/201833910. URL: https://doi.org/10.1051%2F0004-6361%2F201833910.

[49] Adam G. Riess et al. "A 3% SOLUTION: DETERMINATION OF THE HUBBLE CONSTANT WITH THEHUBBLE SPACE TELESCOPEAND WIDE FIELD CAMERA 3". In: *The Astrophysical Journal* 730.2 (2011), p. 119. DOI: 10.1088/0004-637x/730/2/119. URL: https://doi.org/10.1088%2F0004-637x%2F730%2F2%2F119.

[50] David Parkinson et al. "The WiggleZ Dark Energy Survey: Final data release and cosmological results". In: *Physical Review D* 86.10 (2012). DOI: 10.1103/physrevd.86.103518. URL: https://doi.org/10.1103%2Fphysrevd.86.103518.

[51] Signe Riemer-Sørensen, David Parkinson, and Tamara M. Davis. "Combining Planck data with large scale structure information gives a strong neutrino mass constraint". In: *Phys. Rev. D* 89.10 (2014). DOI: 10.1103/physrevd.89.103505. URL: https://doi.org/10.1103%2Fphysrevd.89.103505.

[52] K. S. Hirata et al. "Observation in the Kamiokande-II detector of the neutrino burst from supernova SN1987A". In: *Phys. Rev. D* 38 (2 1988), pp. 448–458. DOI: 10.1103/PhysRevD.38.448. URL: https://link.aps.org/doi/10.1103/PhysRevD.38.448.

[53] Thomas J. Loredo and Donald Q. Lamb. "Bayesian analysis of neutrinos observed from supernova SN 1987A". In: *Physical Review D* 65.6 (2002). DOI: 10.1103/physrevd.65.063002. URL: https://doi.org/10.1103%2Fphysrevd.65.063002.

[54] S. R. Elliott, A. A. Hahn, and M. K. Moe. “Direct evidence for two-neutrino double-beta decay in ^{82}Se”. In: *Phys. Rev. Lett.* 59 (18 1987), pp. 2020–2023. DOI: 10.1103/PhysRevLett.59.2020. URL: https://link.aps.org/doi/10.1103/PhysRevLett.59.2020.

[55] VLADIMIR I TRETYAK and YURI G ZDESENKO. “TABLES OF DOUBLE BETA DECAY DATA—AN UPDATE”. In: *Atomic Data and Nuclear Data Tables* 80.1 (2002), pp. 83–116. ISSN: 0092-640X. DOI: https://doi.org/10.1006/adnd.2001.0873. URL: https://www.sciencedirect.com/science/article/pii/S0092640X01908733.

[56] XENON Collaboration*. “Observation of two-neutrino double electron capture in 124Xe with XENON1T”. In: *Nature* 568.7753 (Apr. 2019), pp. 532–535. DOI: 10.1038/s41586-019-1124-4. URL: https://doi.org/10.1038/s41586-019-1124-4.

[57] S. I. et al. Alvis. “Search for neutrinoless double-β decay in ^{76}Ge with 26 kg yr of exposure from the Majorana Demonstrator”. In: *Phys. Rev. C* 100 (2 2019), p. 025501. DOI: 10.1103/PhysRevC.100.025501. URL: https://link.aps.org/doi/10.1103/PhysRevC.100.025501.

[58] G. Anton et al. “Search for Neutrinoless Double-β Decay with the Complete EXO-200 Dataset”. In: *Phys. Rev. Lett.* 123 (16 2019), p. 161802. DOI: 10.1103/PhysRevLett.123.161802. URL: https://link.aps.org/doi/10.1103/PhysRevLett.123.161802.

[59] Junpei Shirai and for the KamLAND-Zen Collaboration. “Results and future plans for the KamLAND-Zen experiment”. In: *Journal of Physics: Conference Series* 888 (2017), p. 012031. DOI: 10.1088/1742-6596/888/1/012031. URL: https://doi.org/10.1088/1742-6596/888/1/012031.

[60] A.S. Barabash et al. R. Arnold C. Augier. “Detailed studies of 100Mo two-neutrino double beta decay in NEMO-3”. In: *Eur. Phys. J. C* 79.440 (2019). DOI: https://doi.org/10.1140/epjc/s10052-019-6948-4.

[61] M. Kleesiek et al. “-Decay spectrum, response function and statistical model for neutrino mass measurements with the KATRIN experiment”. In: *The European physical journal / C* 79.3 (2019). 51.03.01; LK 01, Article: 2014. ISSN: 1434-6044, 1434-6052. DOI: 10.1140/epjc/s10052-019-6686-7.

[62] K. Chrysalidis et al. L. Gastaldo K. Blaum. “The electron capture in 163Ho experiment – ECHo”. In: *Eur. Phys. J. Spec. Top.* 226 (2017), pp. 1623–1694.

[63] M. Balata et al. A. Nucciotti B. Alpert. “Status of the HOLMES Experiment to Directly Measure the Neutrino Mass”. In: *J Low Temp Phys* 193 (2018), pp. 1137–1145. DOI: https://doi.org/10.1007/s10909-018-2025-x.

[64] Rastislav Dvornický et al. “Absolute mass of neutrinos and the first unique forbidden β decay of ^{187}Re”. In: *Phys. Rev. C* 83 (4 Apr. 2011), p. 045502. DOI: 10.1103/PhysRevC.83.045502. URL: https://link.aps.org/doi/10.1103/PhysRevC.83.045502.

[65] M Sisti et al. "New limits from the Milano neutrino mass experiment with thermal microcalorimeters". In: *Nuclear Instruments and Methods in Physics Research Section A: Accelerators, Spectrometers, Detectors and Associated Equipment* 520.1 (2004). Proceedings of the 10th International Workshop on Low Temperature Detectors, pp. 125–131. ISSN: 0168-9002. DOI: https://doi.org/10.1016/j.nima.2003.11.273. URL: https://www.sciencedirect.com/science/article/pii/S0168900203031814.

[66] M.S. Basunia. "Nuclear Data Sheets for A = 187". In: *Nuclear Data Sheets* 110.5 (2009), pp. 999–1238. ISSN: 0090-3752. DOI: https://doi.org/10.1016/j.nds.2009.04.001. URL: https://www.sciencedirect.com/science/article/pii/S0090375209000301.

[67] J.E. Purcell and C.G. Sheu. "Nuclear Data Sheets for A = 3". In: *Nuclear Data Sheets* 130 (2015), pp. 1–20. ISSN: 0090-3752. DOI: https://doi.org/10.1016/j.nds.2015.11.001. URL: https://www.sciencedirect.com/science/article/pii/S0090375215000551.

[68] Project 8 Collaboration. *The Project 8 Neutrino Mass Experiment*. 2022. DOI: 10.48550/ARXIV.2203.07349. URL: https://arxiv.org/abs/2203.07349.

[69] J. Angrik et al. *KATRIN Design Report 2004*. FZKA–7090. Forschungszentrum Karlsruhe, 2005.

[70] F. Friedel et al. "Time-dependent simulation of the flow reduction of D2 and T2 in the KATRIN experiment". In: *Vacuum* 159 (2019), pp. 161–172. ISSN: 0042-207X. DOI: https://doi.org/10.1016/j.vacuum.2018.10.002. URL: https://www.sciencedirect.com/science/article/pii/S0042207X18313873.

[71] J. Behrens et al. "A pulsed, mono-energetic and angular-selective UV photo-electron source for the commissioning of the KATRIN experiment". In: *The European Physical Journal C* 77.6 (2017), p. 410. DOI: 10.1140/epjc/s10052-017-4972-9. URL: https://doi.org/10.1140/epjc/s10052-017-4972-9.

[72] Fabian Ruben Friedel. "Ion and plasma systematics during the first KATRIN neutrino mass measurements". PhD thesis. Karlsruher Institut für Technologie (KIT), 2020. 226 pp. DOI: 10.5445/IR/1000126837.

[73] J. F. Amsbaugh et al. "Focal-plane detector system for the KATRIN experiment". In: *Nucl. Inst. Meth. A* 778 (2015), p. 40. DOI: 10.1016/j.nima.2014.12.116.

[74] M.-M. Bé et al. *Table of Radionuclides*. Vol. 5. Monographie BIPM-5. Bureau International des Poids et Mesures, 2010. ISBN: 92-822-2234-8. URL: http://www.bipm.org/utils/common/pdf/monographieRI/Monographie_BIPM-5_Tables_Vol5.pdf.

[75] Daniel Furse et al. "Kassiopeia: a modern, extensible C++ particle tracking package". In: *New Journal of Physics* 19.5 (2017), p. 053012. DOI: 10.1088/1367-2630/aa6950. URL: http://stacks.iop.org/1367-2630/19/i=5/a=053012.

[76] A. Lokhov, B. Bieringer, and G. Drexlin et al. "Background reduction at the KATRIN experiment by the shifted analysing plane configuration". In: *Eur. Phys. J. C* 82.258 (2022). DOI: https://doi.org/10.1140/epjc/s10052-022-10220-4.

[77] Stephan Dyba. “Background reduction by the inner wire electrode and set-up of the condensed krypton source at the neutrino mass experiment KATRIN”. PhD thesis. Westfälische Wilhelms-Universität Münster, 2019. URL: https://repositorium.uni-muenster.de/document/miami/4a73b204-96e6-4922-9d88-a640cd4ad191/diss_dyba.pdf.

[78] Fabian Block. “Determination of Electromagnetic Fields ans Tritium Column Density for Neutrino Mass Analysis with KATRIN”. PhD thesis. Karlsruher Institut für Technologie (KIT), 2021.

[79] M. Aker et al. “Analysis methods for the first KATRIN neutrino-mass measurement”. In: *Phys. Rev. D* 104 (1 2021), p. 012005. DOI: 10.1103/PhysRevD.104.012005.

[80] Jonas Kellerer. “Simulation of the KATRIN Source Plasma using Monte Carlo and Particle in Cell Methods”. PhD thesis. Karlsruher Institut für Technologie (KIT), 2022. DOI: 10.5445/IR/1000143868.

[81] Moritz Benedikt Machatschek. “A Phenomenological Theory of KATRIN Source Potential Systematics and its Application in Krypton-83m Calibration Measurements”. PhD thesis. Karlsruher Institut für Technologie (KIT), 2021. DOI: 10.5445/IR/1000132391.

[82] Florian Fränkle. *Background Report.* 42nd KATRIN Collaboration Meeting, Mar. 8, 2022. URL: https://indico.scc.kit.edu/event/2530/ (visited on 04/13/2022).

[83] Luke Kippenbrock. “Investigation of Background from the Inter-Spectrometer Penning Trap and Secondary Electron Emission in the KATRIN experiment”. PhD thesis. University of Washington, 2019. URL: https://digital.lib.washington.edu/researchworks/handle/1773/43737.

[84] Susanne Mertens. “Study of Background Processes in the Electrostatic Spectrometers of the KATRIN experiment”. PhD thesis. Karlsruher Institut für Technologie (KIT), 2012. DOI: 10.5445/IR/1000027058. URL: http://nbn-resolving.org/urn:nbn:de:swb:90-270589.

[85] Dominic Hinz. *Ionisation mechanisms of Pb-206 induced Rydberg atoms.* Master thesis. 2018. URL: https://www.katrin.kit.edu/publikationen/mth-hinz.pdf.

[86] M. A. Furman and M. T. F. Pivi. “Probabilistic model for the simulation of secondary electron emission”. In: *Phys. Rev. ST Accel. Beams* 5 (12 Dec. 2002), p. 124404. DOI: 10.1103/PhysRevSTAB.5.124404.

[87] F.M. Fränkle et al. “Penning discharge in the KATRIN pre-spectrometer”. In: *Journal of Instrumentation* 9.7 (2014), P07028. DOI: 10.1088/1748-0221/9/07/P07028.

[88] M. Aker et al. “Suppression of Penning discharges between the KATRIN spectrometers”. In: *Eur. Phys. J. C* 80 (Sept. 2020), p. 821. ISSN: 1434-6052. DOI: 10.1140/epjc/s10052-020-8278-y.

[89] M.-M. Bé et al. *Table of Radionuclides.* Vol. 2. Monographie BIPM-5. Bureau International des Poids et Mesures, 2004. ISBN: 92-822-2207-1. URL: http://www.bipm.org/utils/common/pdf/monographieRI/Monographie_BIPM-5_Tables_Vol2.pdf.

[90] M.-M. Bé et al. *Table of Radionuclides*. Vol. 6. Monographie BIPM-5. Bureau International des Poids et Mesures, 2011. ISBN: 92-822-2242-3. URL: http://www.bipm.org/utils/common/pdf/monographieRI/Monographie_BIPM-5_Tables_Vol6.pdf.

[91] M.-M. Bé et al. *Table of Radionuclides*. Vol. 4. Monographie BIPM-5. Bureau International des Poids et Mesures, 2008. ISBN: 92-822-2230-6. URL: http://www.bipm.org/utils/common/pdf/monographieRI/Monographie_BIPM-5_Tables_Vol4.pdf.

[92] Stefan Görhardt. "Background Reduction Methods and Vacuum Technology at the KATRIN Spectrometers". PhD thesis. Karlsruher Institut für Technologie (KIT), 2014. DOI: 10.5445/IR/1000038050. URL: http://nbn-resolving.org/urn:nbn:de:swb:90-380506.

[93] J. Wolf and F. Harms. "Simulation and measurement of the suppression of radon induced background in the KATRIN experiment". In: *AIP Conference Proceedings* 1921.1 (2018), p. 060001. DOI: 10.1063/1.5018997. URL: https://aip.scitation.org/doi/abs/10.1063/1.5018997.

[94] Arthur Kähm. "Untersuchung von Untergrundprozessen durch gespeicherte Elektronen bei KATRIN". Master thesis. Karlsruher Institut für Technologie (KIT), 2020. URL: https://www.katrin.kit.edu/publikationen/Masterarbeit-ArthurKaehm.pdf.

[95] Nancy Wandkowsky. "Study of background and transmission properties of the KATRIN spectrometers". PhD thesis. Karlsruher Institut für Technologie (KIT), 2013. DOI: 10.5445/IR/1000036631. URL: http://nbn-resolving.org/urn:nbn:de:swb:90-366316.

[96] Anna Schaller. "Characterization and mitigation of the background in KATRIN". PhD thesis. Technische Universität München, 2020. URL: http://mediatum.ub.tum.de/doc/1553598/1553598.pdf.

[97] Daniel F. R. Hilk. "Electric field simulations and electric dipole investigations at the KATRIN main spectrometer". PhD thesis. Karlsruher Institut für Technologie (KIT), 2016. DOI: 10.5445/IR/1000065869. URL: http://nbn-resolving.org/urn:nbn:de:swb:90-658697.

[98] Woo-Jeong Baek. "Investigation of background processes of ions and Rydberg atoms in the KATRIN spectrometers". Master thesis. Karlsruher Institut für Technologie (KIT), 2017. URL: https://www.katrin.kit.edu/publikationen/mth-baek.pdf.

[99] F.M. Fränkle et al. "KATRIN background due to surface radioimpurities". In: *Astroparticle Physics* 138 (2022), p. 102686. ISSN: 0927-6505. DOI: https://doi.org/10.1016/j.astropartphys.2022.102686. URL: https://www.sciencedirect.com/science/article/pii/S0927650522000020.

[100] Bundesamt für Strahlenschutz. *Radon im Freien in Deutschland*. 2021. URL: https://www.bfs.de/DE/themen/ion/umwelt/radon/karten/freiluft.html.

[101] MAN DWE GmbH. *DESIGN REPORT: UHV Main spectrometer for KATRIN at Forschungszentrum Karlsruhe*. 30.06.2005.

[102] N. Wandkowsky et al. “Modeling of electron emission processes accompanying radon-iα/i-decays within electrostatic spectrometers”. In: *New Journal of Physics* 15.8 (Aug. 2013), p. 083040. DOI: 10.1088/1367-2630/15/8/083040. URL: https://doi.org/10.1088/1367-2630/15/8/083040.

[103] James F. Ziegler. “SRIM-2003”. In: *Nucl. Instr. Meth. B* 219-220 (2004), pp. 1027–1036. DOI: 10.1016/j.nimb.2004.01.208.

[104] J. P. Biersack and W. Eckstein. “Sputtering studies with the Monte Carlo Program TRIM.SP”. In: *Applied Physics A* 34.2 (1984), pp. 73–94. ISSN: 1432-0630. DOI: 10.1007/BF00614759.

[105] A. Osipowicz. *SRIM Simulations on alpha recoil nuclei in the main spectrometer*. Karlsruhe: 32nd KATRIN Collaboration Meeting, 7.03.2016.

[106] Shuo-Jen Lee and Jian-Jang Lai. “The effects of electropolishing (EP) process parameters on corrosion resistance of 316L stainless steel”. In: *Journal of Materials Processing Technology* 140.1-3 (2003), pp. 206–210. ISSN: 09240136. DOI: 10.1016/S0924-0136(03)00785-4.

[107] S. Trigwell and G. Selvaduray. *Effect of Surface Treatment on the Surface Characteristics of AISI 316L Stainless Steel*. Ed. by NASA Kennedy Space Center. 2005.

[108] P. J. Núñez et al. “Characterization of Surface Finish of Electropolished Stainless Steel AISI 316L with Varying Electrolyte Concentrations”. In: *Procedia Engineering* 63 (2013), pp. 771–778. ISSN: 18777058. DOI: 10.1016/j.proeng.2013.08.255.

[109] Krzysztof Rokosz et al. “XPS depth profiling analysis of passive surface layers formed on austenitic AISI 304L and AISI 316L SS after high-current-density electropolishing”. In: *Surface and Coatings Technology* 276 (2015), pp. 516–520. ISSN: 02578972. DOI: 10.1016/j.surfcoat.2015.06.022.

[110] R. Behrisch and W. Eckstein. *Sputtering by Particle Bombardment: Experiments and Computer Calculations from Treshold to MeV Energies*. Vol. 110. Topics in Applied Physics. Berlin, Heidelberg: Springer Berlin Heidelberg, 2007. ISBN: 978-3-540-44500-5. DOI: 10.1007/978-3-540-44502-9.

[111] Steven Dzioba, Orlando Auciello, and Roger Kelly. “On the kinetic energies of sputtered excited particles, I. Atoms sputtered from Li, LiF, and NaCl”. In: *Radiation Effects* 45.3-4 (1980), pp. 235–245. ISSN: 0033-7579. DOI: 10.1080/00337578008208435.

[112] Ryoichi Kawai and Yoshi-Hiko Ohtsuki. “Resonant neutralization of ions scattered from surfaces with an intermediate velocity”. In: *Nuclear Instruments and Methods in Physics Research Section B: Beam Interactions with Materials and Atoms* 13.1-3 (1986), pp. 605–608. ISSN: 0168583X. DOI: 10.1016/0168-583X(86)90575-6.

[113] Peter Sigmund. “Theory of Sputtering. I. Sputtering Yield of Amorphous and Polycrystalline Targets”. In: *Physical Review* 184.2 (1969), pp. 383–416. ISSN: 0031-899X. DOI: 10.1103/PhysRev.184.383.

[114] Roger Kelly. “On the origin of sputtered excited atoms”. In: *Nuclear Instruments and Methods in Physics Research* 194.1-3 (1982), pp. 583–588. ISSN: 01675087. DOI: 10.1016/0029-554X(82)90585-7.

[115] H. M. Urbassek. “Sputtering of molecules”. In: *Nuclear Instruments and Methods in Physics Research Section B: Beam Interactions with Materials and Atoms* 18.1-6 (1986), pp. 587–595. ISSN: 0168583X. DOI: 10.1016/S0168-583X(86)80093-3.

[116] Roger Kelly. “Statistical model for the formation of excited atoms in the sputtering process”. In: *Physical Review B* 25.2 (1982), pp. 700–712. ISSN: 0163-1829. DOI: 10.1103/PhysRevB.25.700.

[117] G. Falcone, D. Matragrano, and A. Oliva. “Energy distribution of sputtered excited atoms”. In: *Lettere al Nuovo Cimento (1971-1985)* 35.16 (1982), pp. 465–468. ISSN: 1827-613X. DOI: 10.1007/BF02817286.

[118] O. Auciello. “Determination of excited sputtered atoms kinetic energy as a contribution to the understanding of the excitation phenomenon in the sputtering process”. In: *Nuclear Instruments and Methods in Physics Research* 194.1-3 (1982), pp. 549–553. ISSN: 01675087. DOI: 10.1016/0029-554X(82)90579-1.

[119] G. Betz. “Electronic excitation in sputtered atoms and the oxygen effect”. In: *Nuclear Instruments and Methods in Physics Research Section B: Beam Interactions with Materials and Atoms* 27.1 (1987), pp. 104–118. ISSN: 0168583X. DOI: 10.1016/0168-583X(87)90011-5.

[120] M. A. Cazalilla et al. “Theory of Auger neutralization and deexcitation of slow ions at metal surfaces”. In: *Physical Review B* 58.20 (1998), pp. 13991–14006. ISSN: 0163-1829. DOI: 10.1103/PhysRevB.58.13991.

[121] M. W. Thompson. “II. The energy spectrum of ejected atoms during the high energy sputtering of gold”. In: *Philosophical Magazine* 18.152 (1968), pp. 377–414. ISSN: 0031-8086. DOI: 10.1080/14786436808227358.

[122] M. W. Thompson, B. W. Farmery, and P. A. Newson. “I. A mechanical spectrometer for analysing the energy distribution of sputtered atoms of copper or gold”. In: *Philosophical Magazine* 18.152 (1968), pp. 361–376. ISSN: 0031-8086. DOI: 10.1080/14786436808227357.

[123] B. W. Farmery and M. W. Thompson. “III. Energy spectra for copper”. In: *Philosophical Magazine* 18.152 (1968), pp. 415–424. ISSN: 0031-8086. DOI: 10.1080/14786436808227359.

[124] J. Bohdansky. “Important sputtering yield data for tokamaks: A comparison of measurements and estimates”. In: *Journal of Nuclear Materials* 93-94 (1980), pp. 44–60. ISSN: 00223115. DOI: 10.1016/0022-3115(80)90302-5.

[125] Guido Drexlin. “Refined Rydberg background model: the key role of autoionization”. In: *42nd KATRIN Collaboration Meeting* (2022). URL: https://indico.scc.kit.edu/event/2530/contributions/9953/attachments/4909/7401/Refinded_Rydberg_BG_model.pdf.

[126] A. Wucher et al. “Detection of sputtered metastable atoms by autoionization”. In: *Physical Review A* 49.3 (1994), pp. 2188–2190. ISSN: 1050-2947. DOI: 10.1103/PhysRevA.49.2188.

[127] V. G. Drobnich, V. A. Mastyugin, and S. S. Pop. "Investigation of angular and energy distributions of excited sputtered and scattered particles by using a Doppler method". In: *Nuclear Instruments and Methods in Physics Research Section B: Beam Interactions with Materials and Atoms* 58.3-4 (1991), pp. 443–447. ISSN: 0168583X. DOI: 10.1016/0168-583X(91)95883-F.

[128] R. Taranko and E. Taranko. "Resonant electron transfer in ion/atom–metal surface interactions within generalized Anderson–Newns model". In: *Vacuum* 54.1-4 (1999), pp. 161–165. ISSN: 0042207X. DOI: 10.1016/S0042-207X(98)00453-9.

[129] J. Los and J.J.C Geerlings. "Charge exchange in atom-surface collisions". In: *Physics Reports* 190.3 (1990), pp. 133–190. ISSN: 03701573. DOI: 10.1016/0370-1573(90)90104-A.

[130] M. J. Shaw. "Penning ionization". In: *Contemporary Physics* 15.5 (1974), pp. 445–464. ISSN: 0010-7514. DOI: 10.1080/00107517408210804.

[131] T. F. Gallagher. "Doubly excited states". In: *Journal of the Optical Society of America B* 4.5 (1987), p. 794. ISSN: 0740-3224. DOI: 10.1364/JOSAB.4.000794.

[132] Ingolf V. Hertel and Claus-Peter Schulz. *Atoms, Molecules and Optical Physics 1*. Berlin, Heidelberg: Springer Berlin Heidelberg, 2015. ISBN: 978-3-642-54321-0. DOI: 10.1007/978-3-642-54322-7.

[133] Gordon Drake, ed. *Springer Handbook of Atomic, Molecular, and Optical Physics*. New York, NY: Springer Science+Business Media Inc, 2006. ISBN: 0-387-20802-X. DOI: 10.1007/978-0-387-26308-3. URL: http://site.ebrary.com/lib/alltitles/docDetail.action?docID=10228967.

[134] Gerhard Kramm and Nicole Mölders. *Planck's blackbody radiation law: Presentation in different domains and determination of the related dimensional constants*. 2009. DOI: 10.48550/ARXIV.0901.1863. URL: https://arxiv.org/abs/0901.1863.

[135] Thomas F. Gallagher. *Rydberg Atoms*. Cambridge: Cambridge University Press, 1994. ISBN: 9780511524530. DOI: 10.1017/CBO9780511524530.

[136] F. Harms. *Characerization and Minimization of Background Processes in the KATRIN Main Spectrometer: PhD thesis*. Karlsruhe Institute of Technology KIT, 2015.

[137] N. Trost. *Background generation due to stored electrons at the KATRIN main spectrometer: Diploma thesis*. Karlsruhe Institute of Technology KIT, 2013.

[138] Microworks GmbH. URL: https://www.microworks.de/.

[139] Raphael Ostertag. "Investigation of Plasma Effects in the KATRIN Source with ^{83m}Kr". Master thesis. Karlsruher Institut für Technologie (KIT), 2020. URL: https://www.katrin.kit.edu/downloads/mth_ostertag.pdf.

[140] Anton Huber. "Analysis of first KATRIN data and searches for keV-scale sterile neutrinos". PhD thesis. Karlsruher Institut für Technologie (KIT), 2020. URL: https://primo.bibliothek.kit.edu/permalink/f/4jne3t/KITSRCE1000128344.

[141] H. Niedrig. "Physical background of electron backscattering". In: *Scanning* 1.1 (1978), pp. 17–34. DOI: https://doi.org/10.1002/sca.4950010103.

[142] Joscha Lauer. "Application Cases of Transverse Energy Filters in the KATRIN Experiment". Master thesis. Karlsruher Institut für Technologie (KIT), 2022.

[143] K. Gauda et al. *An active transverse energy filter to differentiate low energy particles with large pitch angles in a strong magnetic field.* 2022. DOI: 10.48550/ARXIV.2203.06085.

[144] Kevin Gauda. *Update on aTEF fabrication in Münster.* 41st KATRIN Collaboration Meeting, Oct. 7, 2021. URL: https://indico.scc.kit.edu/event/2476/ (visited on 06/06/2022).

[145] Kevin Gauda. *Si-aTEF: status and consideration in view of pTEF-results.* 42nd KATRIN Collaboration Meeting, Mar. 11, 2022. URL: https://indico.scc.kit.edu/event/2530 (visited on 06/06/2022).

[146] Guido Drexlin. *Scintillating aTEF.* 41st KATRIN Collaboration Meeting, Oct. 7, 2021. URL: https://indico.scc.kit.edu/event/2476/ (visited on 06/06/2022).

[147] Nanoscribe GmbH Co. KG. URL: https://www.nanoscribe.com/de/.

[148] Joachim Fischer and Martin Wegener. "Three-dimensional optical laser lithography beyond the diffraction limit". In: *Laser & Photonics Reviews* 7.1 (2013), pp. 22–44. DOI: https://doi.org/10.1002/lpor.201100046. URL: https://onlinelibrary.wiley.com/doi/abs/10.1002/lpor.201100046.

[149] Frank Träger, ed. *Springer Handbook of Lasers and Optics.* Springer New York, 2007. DOI: 10.1007/978-0-387-30420-5. URL: https://doi.org/10.1007%2F978-0-387-30420-5.

[150] Saint-Gobain Crystals. *BC-400,BC-404,BC-408,BC-412,BC-416 Premium Plastic Scintillators.* 2022. URL: https://www.crystals.saint-gobain.com/files/1691/download (visited on 06/07/2022).

[151] Peter Fischer. *CMOS SPAD Sensor Chip for the Readout of Scintillating Fibers.* 16th Vienna Conference on Instrumentation, 2022. URL: https://indico.cern.ch/event/1044975/contributions/4663697/.

[152] A. Kramida et al. NIST Atomic Spectra Database (ver. 5.9), [Online]. Available: https://physics.nist.gov/asd [2022, June 9]. National Institute of Standards and Technology, Gaithersburg, MD. 2021.

[153] R. H. Garstang. " Energy Levels and Transition Probabilities in P2 and P4 Configurations ". In: *Monthly Notices of the Royal Astronomical Society* 111.1 (Feb. 1951), pp. 115–124. ISSN: 0035-8711. DOI: 10.1093/mnras/111.1.115. eprint: https://academic.oup.com/mnras/article-pdf/111/1/115/8077475/mnras111-0115.pdf. URL: https://doi.org/10.1093/mnras/111.1.115.

[154] A. Omholt and L. Harang. "Measurements of the mean lifetime of the metastable 1S-state of the oxygen atom in the upper atmosphere during auroral displays". In: *Journal of Atmospheric and Terrestrial Physics* 7 (1955), pp. 247–253. ISSN: 0021-9169. DOI: https://doi.org/10.1016/0021-9169(55)90129-X. URL: https://www.sciencedirect.com/science/article/pii/002191695590129X.

[155] Charles E. Johnson. “Lifetime of the $2p^3 3s^5S$ Metastable State of Oxygen”. In: *Phys. Rev. A* 5 (6 June 1972), pp. 2688–2689. DOI: 10.1103/PhysRevA.5.2688. URL: https://link.aps.org/doi/10.1103/PhysRevA.5.2688.

[156] R. Feifel, J. H. D. Eland, and D. Edvardsson. “Valence double ionization of O2 at photon energies below and above the molecular double ionization threshold”. In: *The Journal of Chemical Physics* 122.14 (2005), p. 144308. ISSN: 0009-2614. DOI: 10.1063/1.1872836.

[157] Renaud Guillemin, Marc Simon, and Eiji Shigemasa. “Doppler effect in fragment autoionization following core-to-valence excitation in O_2”. In: *Physical Review A* 82.5 (2010). ISSN: 1050-2947. DOI: 10.1103/PhysRevA.82.051401.

[158] A. A. Wills, A. A. Cafolla, and J. Comer. “The production of autoionizing states of atomic oxygen by the photodissociation of O_2”. In: *Journal of Physics B: Atomic, Molecular and Optical Physics* 24.18 (1991), p. 3989. ISSN: 0953-4075. URL: http://stacks.iop.org/0953-4075/24/i=18/a=013.

[159] Y Hikosaka et al. “Competition between autoionization and dissociation in the $[O_2^+(B\ ^2\Sigma_g^-)]$nl and $[O_2^+(c\ ^4\Sigma_u^-)]$nl Rydberg states investigated by photon-induced dissociation to neutral fragments”. In: *Journal of Physics B: Atomic, Molecular and Optical Physics* 36.21 (Oct. 2003), pp. 4311–4326. DOI: 10.1088/0953-4075/36/21/010. URL: https://doi.org/10.1088/0953-4075/36/21/010.

[160] James A.R. Samson and V. E. Petrosky. “Partially autoionizing states of atomic oxygen”. In: *Journal of Electron Spectroscopy and Related Phenomena* 3.6 (1974), pp. 461–465. ISSN: 03682048. DOI: 10.1016/0368-2048(74)80033-2.

[161] V. Čermák and J. Šrámek. “Electron spectroscopy of autoionizing states of oxygen atoms”. In: *Journal of Electron Spectroscopy and Related Phenomena* 2.1 (1973), pp. 97–100. ISSN: 03682048. DOI: 10.1016/0368-2048(73)80051-9.

[162] I. C. Percival. “Planetary atoms”. In: *Proc. R. Soc. Lond. A.* 353 (1977), pp. 289–297.

[163] K.-D. Heber et al. “Long-range interactions in planetary three-body Coulomb systems”. In: *Physical Review A* 56.2 (1997), pp. 1255–1267. ISSN: 1050-2947. DOI: 10.1103/PhysRevA.56.1255.

[164] A. Burgers and D. Wintgen. “Inhibited autoionization of planetary atom states”. In: *Journal of Physics B: Atomic, Molecular and Optical Physics* 27.8 (1994), pp. L131–L135. ISSN: 0953-4075. DOI: 10.1088/0953-4075/27/8/001.

[165] J. Neukammer et al. “Autoionization Inhibited by Internal Interferences”. In: *Phys. Rev. Lett.* 55 (19 Nov. 1985), pp. 1979–1982. DOI: 10.1103/PhysRevLett.55.1979. URL: https://link.aps.org/doi/10.1103/PhysRevLett.55.1979.

[166] K. Richter and D. Wintgen. “Stable planetary atom configurations”. In: *Phys. Rev. Lett.* 65 (15 Oct. 1990), pp. 1965–1965. DOI: 10.1103/PhysRevLett.65.1965. URL: https://link.aps.org/doi/10.1103/PhysRevLett.65.1965.

[167] M. Seng et al. “Electron Spectroscopy of Planetary Atoms”. In: *Phys. Rev. Lett.* 74 (17 Apr. 1995), pp. 3344–3347. DOI: 10.1103/PhysRevLett.74.3344. URL: https://link.aps.org/doi/10.1103/PhysRevLett.74.3344.

[168] Rainer Reichle, Hanspeter Helm, and Igor Yu. Kiyan. "Photodetachment of H^- in a Strong Infrared Laser Field". In: *Phys. Rev. Lett.* 87 (24 Nov. 2001), p. 243001. DOI: 10.1103/PhysRevLett.87.243001. URL: https://link.aps.org/doi/10.1103/PhysRevLett.87.243001.

[169] Johannes S. Schwarz. "The Detector System of the KATRIN Experiment - Implementation and First Measurements with the Spectrometer". PhD thesis. Karlsruher Institut für Technologie (KIT), 2014. DOI: 10.5445/IR/1000042772. URL: http://nbn-resolving.org/urn:nbn:de:swb:90-427724.

[170] ThaLibster. *Decay chain of Uranium-238: Adapted and remixed from source code by User: BatesIsBack*. 2017. URL: https://commons.wikimedia.org/wiki/File:Decay_Chain_of_Uranium-238.svg.

[171] DIN German Institute for Standardization. "Flat products made of steels for pressure purposes - Part 7: Stainless steels; German version EN 10028-7:2016; ICS 77.140.30". In: (2016). DOI: https://dx.doi.org/10.31030/2398417.

List of Figures

1.1. Outline of a continuous energy spectrum of β-electrons . . . 3
1.2. Standard model of particle physics . . . 5

2.1. Solar neutrino spectrum . . . 9
2.2. Electron neutrino oscillation . . . 12
2.3. Hierarchy of neutrino masses . . . 13
2.4. $0\nu\beta\beta$: Binding energy and Feynman diagram . . . 16

3.1. KATRIN beamline overview . . . 23
3.2. Inner loop system of the WGTS . . . 24
3.3. Technical overview of the DPS and CPS . . . 25
3.4. Monitoring devices: BIXS and FBM . . . 26
3.5. The MAC-E filter principle . . . 28
3.6. Technical overview of the detector system and FPD pixel map of energy resolution . . . 30
3.7. Nominal analysing plane (NAP) configuration of the main spectrometer . 31
3.8. Shifted analysing plane (SAP) configuration of the main spectrometer . . 33
3.9. Model spectrum for different neutrino masses with measurement time distribution (MTD) . . . 34
3.10. Systematic breakdowns for the neutrino mass campaigns KNM1 - KNM5 36

4.1. Overview of various background processes at the KATRIN spectrometers 37
4.2. Electric and magnetic shielding of low energy electrons from the vessel ($U_{vessel} < -18\,000\,V$) and inner electrode ($U_{IE} = U_{vessel} - 200\,V$) surface . 38
4.3. Intrinsic detector background rate as a function of the measured energy 40
4.4. Ratio of detector background rate with and without veto-cuts and FPD pixel map distribution of the intrinsic detector background . . . 40
4.5. Electromagnetic field condition in the inter-spectrometer region . . . 41
4.6. Background rate and desorption time of ^{219}Rn as a function of the baffle temperature . . . 43
4.7. Motion of magnetically trapped electron in the main spectrometer field . 44
4.8. Radial background rate as FPD pixel map and ring-wise representation . 45
4.9. Inner electrode offset potential dependence on the background rate . . . 46
4.10. Decay scheme and energy distribution of ^{210}Pb decay . . . 47
4.11. ^{210}Pb decay investigation for KNM5 data . . . 48
4.12. ^{218}Po implantation depth and lateral positions profile . . . 51
4.13. Evolution of the implantation depth of consecutive α-decays of ^{222}Rn . . 52
4.14. Illustration of sputtering from the inner main spectrometer surface . . . 53

4.15. Energy-dependent sputter yield of ^{210}Po decay inside the main spectrometer vessel surface . . . 55
4.16. Multiplicity spectra of the sputtered atoms . . . 56
4.17. BBR spectrum with hydrogen Rydberg atoms binding energies . . . 57
4.18. Electron energy spectrum by BBR photo-ionisation of Rydberg atoms . . . 58

5.1. Monte Carlo data set of a broadened electron counts distribution . . . 62
5.2. Background rate evolution over time of the measurement campaign KNM2 64
5.3. Subrun-wise events distribution of the KNM2 data set and Monte Carlo simulation to the non-Poisson broadening of a time-dependent background level . . . 65
5.4. Estimate on the non-Poisson broadening for SAP and NAP configuration by different modelled radon activities in the main spectrometer volume . 66
5.5. Dedicated background slope measurement in the SAP configuration . . . 69
5.6. Investigation on the scan-step-duration-dependent background during KNM4|B . . . 70
5.7. Squared neutrino mass sensitivities of the different background related systematics . . . 72

6.1. Travel distance and time of flight of sputtered atoms from the inner MS surface . . . 76
6.2. Simulation of final polar angles for different kinetic starting energies in a 5 G symmetric magnetic field configuration . . . 78
6.3. Polar angle distribution of Rydberg background and tritium beta electrons at the detector . . . 79
6.4. Sketch of transverse energy filter principle . . . 79
6.5. Geometry of micro-structured honeycomb plate . . . 80
6.6. Rydberg background and beta electrons filter efficiency for different side lengths . . . 81
6.7. Photo and optical microscope image of the passive transverse energy filter (pTEF) . . . 82
6.8. Electron microscope images of the fabricated pTEF . . . 83
6.9. Simulated transmission probability of 18.6 keV electrons through the micro-structured pTEF . . . 84
6.10. Dedicated holding structure of the pTEF, mounted on FPD wafer flange . 85
6.11. Magnetic flux tube envelopes of the settings used at the pTEF measurement campaign. . . . 86
6.12. Ring-wise position generation and starting magnetic field strengths of electrons in the SAP configuration . . . 87
6.13. Observable background fraction Ψ of simulated electrons from the individual ring-wise sensitive flux tube volumes for different kinetic starting energies E_i . . . 88
6.14. Measured background fractions for various electromagnetic field configurations . . . 90

6.15. Pixel selection map and exemplary energy histogram of a measurement at 18.6 keV . . . 91
6.16. Background rate as a function of pixel number of data taken during KNM5 92
6.17. Relative rate difference of pTEF to FPD pixel selection for SAP and NAP configuration as a function of the analysing plane flux tube radius 92
6.18. Simulated transmission probability of electrons through pTEF with consideration of backscattering . . . 93
6.19. Relative change on the transmission probability from backscattering effects 94
6.20. Fit of the transverse energy scale E_t for the pTEF measurement data, taken at $U_{\mathrm{ret}} = 18.6\,\mathrm{keV}$ . . . 96
6.21. Influence on the OAR by a tilted pTEF relative to the magnetic field . . . 97
6.22. Pictures of the pTEF for describing possible reduction effects 98
6.23. Electron microscope image of a micro-scale cryo-etched silicon wafer . . 99
6.24. Microscope images of a 3D printed plastic micro-structure 100
6.25. Sketch of 3 times 3 structure grid of pixelised SPAD array 101

7.1. Energy, polar angle and squared sinus of polar angle distribution 103
7.2. Electronic configuration of lowest states of atomic oxygen 105
7.3. Autoionisation spectrum of atomic oxygen 106
7.4. Inter-atomic distance sputtering of atoms from the main spectrometer surface . . . 107
7.5. Final polar angle distribution of Rydberg background, tritium beta electrons and electrons from autoionisation of oxygen . . . 110

A.1. Radial background distribution of different flux tube volumes 141
A.2. Energy spectrum of electrons, released at ^{210}Pb decays with linear scale . 142
A.3. Decay chain of ^{238}U with its daughter atoms ^{222}Rn and ^{210}Pb, final decay to stable ^{206}Pb [170]. . . . 143
A.4. Velocity-dependent sputtering yield of the relevant ^{210}Po decay 145
A.5. Angular-dependent sputtering yield of the relevant ^{210}Po decay 145
A.6. Poisson and Gauss distributions for different mean values 147
A.7. Observable non-Poisson fractions as a function of the measurement time 147
A.8. Inter-arrival time spectrum of secondary electrons induced by Radon decays on the FPD . . . 148
A.9. Radon-induced electron arrivals per decay - cluster size 149
A.10. Ring-wise closest distance to MS wall for SAP configuration 150
A.11. Radial background distribution on the FPD, obtained during KNM3|B and KNM5 . . . 151
A.12. Probability densities along the beamline axis z for the individual FPD rings for the 5.0 G configuration . . . 152
A.13. Probability densities along the beamline axis z for the individual FPD rings for the SAP configuration . . . 152
A.14. Electron transmission probability through pTEF for different energies . . 153
A.15. Flux tube radius at the detector section 153

A.16. Parameter evolution of k_i, describing the energy and magnetic-field-dependent transmission change due to backscattering 154
A.17. Comparison of the transverse energy scale fit with and without consideration of scattering effects 155
A.18. Fit of transverse energy scale E_t for the measurements at 12.0 keV and 34.1 keV 156

List of Tables

4.1. Expected and fit energies E_T of the conversion electrons at ^{210}Pb decays and the fit peak width σ_T in KNM5 data. 49

4.2. Chemical composition of the stainless steel and its passive layer for the simulation with SRIM, given in %. Compounds that are only present in traces or that do not characterise the steel properties are neglected. . . . 50

4.3. Sputtering yields Y, mode energy E_{mode}, mode velocity v_{mode} and surface binding energies E_{bind} of the sputtered atoms from the inner main spectrometer surface. 52275 ^{210}Po decays have been simulated, accordingly the fraction of 52.3 % of initial radon decays. Manganese and molybdenum are not shown as their sputtering yield is smaller than 10^{-2}. 54

5.1. Parameters extracted from KNM measurement campaigns KNM2-KNM5. T_{meas} is the total time of the campaign spent in the background region above E_0, whereas T_{subrun} describes the mean time spent per individual retarding potential in the background region within one scan. The data are fit with a linear function $f(x) = a \cdot t + b$ with slope a and constant b. Here, t_0 is set to the begin of the individual campaigns. Furthermore, the non-Poisson fraction Σ_{np} is given. 63

5.2. Retarding potential slopes fit parameters from KNM measurement campaigns KNM2-KNM5. A linear fit is performed providing a slope over retarding potential a and a rate offset b and the corresponding uncertainties $\sigma_{a,b}$. ΔU denotes the potential range of which the background data are taken and fitted. 68

5.3. Combined scan-step-dependent background slope of the individual campaigns KNM2-KNM5. The derived slope parameter a and its uncertainty σ_a. The total measurement time T_{total} which is used for the analysis and the duration of the longest subrun T_{long} of the dataset is given. 71

6.1. Result of transverse energy scale fits, according eq. 6.12 for initial energies of 100 meV to 900 meV. The energy range ΔE_i of the initial kinetic electron energy and mean energy $\bar{E}_i$ of the simulation data is given. The fit results e_i, their corresponding uncertainty σ_e, and the derived mean initial kinetic energy $\epsilon_{\text{fit}} = {}^{e_i}/_{0.667}$ from the fit result are shown. 89

7.1. Energies and assignments of atomic autoionising states [158]. Roman letters refer to peak labels in fig. 7.3. Primes and double primes refer to the (^2D) and (^2P) core, respectively. Reused with permission from [157] Copyright (2022) by the American Physical Society. 106

A.1. Ring-wise parameters of NAP configuration at $U_{\mathrm{HV}} = -18600V$. The used values for the field calculations with Kassiopeia are given in 8. Given is the downstream volume V_{ds}, the maximal radius r_{ana}, the minimum magnetic field B_{ana}, and the minimum potential U_{ana} at the analysing plane, as well as the longitudinal position z in KATRIN global coordinates of the AP. The Z-position is given in mm with a precision of 0.5 mm. 135
A.2. Ring-wise parameters of SAP configuration at $U_{\mathrm{HV}} = -18600V$. The used values for the field calculations with Kassiopeia are given in 8. Given is the downstream volume V_{ds}, the maximal radius r_{ana}, the minimum magnetic field B_{ana}, and the minimum potential U_{ana} at the analysing plane, as well as the longitudinal position z in KATRIN global coordinates of the AP. Further, the energy resolution ΔE is given for $B_{\mathrm{max}} = 4.2\,\mathrm{T}$, $E = E_0 = 18575\mathrm{eV}$, and $B_{\mathrm{min}} = B_{\mathrm{ana}}$, according eq. 3.2. 138
A.3. ^{210}Pb decay transitions and their probability [91]. If $\beta(17\,\mathrm{keV})$ occurs, the γ transition probability is 100 %. The total appearance probability of an L-shell conversion electron is $P_{\mathrm{ec_L}} = 0.58 \cdot 0.802 \cdot 100\,\% = 46.5\,\%$. 142
A.4. Decay chain of ^{222}Rn with the corresponding α and β^- decay modes, see fig. A.3. The decay energy Q is given in MeV from [91] and the energy of the recoil atom E_{recoil} is calculated according eq. 4.3, given in keV. The half-life of the radioactive reactants is given in years (y), days (d), minutes (m), or seconds (s), correspondingly from [91]. 144
A.5. Chemical composition of the KATRIN main spectrometer stainless steel 1.4429, values are given in % (neglecting the traces of P, S and Si) [101, 171]. 144
A.6. Measurement configuration and region of interest ROIs applied at the measurement campaigns KNM2-KNM5. 146
A.7. Fit parameters c_{1-4} and their uncertainty of the electron transmission probability of eq. 6.8 at 18.6 keV, shown in fig. 6.9. 153
A.8. Ring-wise mean initial magnetic field strengths, determined by the geometric mean of B_i at the generated electron starting positions. 154
A.9. Fit parameters for the evolution of the parameters k_i in fig. A.16, fitted with a second-order polynomial $p(e) = p_1 \cdot e^2 + p_2 \cdot e + p_3$. 155

Appendix

NAP configuration table

Table A.1.: Ring-wise parameters of NAP configuration at $U_{\mathrm{HV}} = -18600V$. The used values for the field calculations with Kassiopeia are given in 8. Given is the downstream volume V_{ds}, the maximal radius r_{ana}, the minimum magnetic field B_{ana}, and the minimum potential U_{ana} at the analysing plane, as well as the longitudinal position z in KATRIN global coordinates of the AP. The Z-position is given in mm with a precision of 0.5 mm.

Ring no.	Pixels	V_{ds} (m^3)	r_{ana} (m)	B_{ana} (G)	U_{ana} (V)	z (mm)
0	0-3	4.52	0.45	6.50	-18599.8	2.6
1	4-15	13.64	0.89	6.50	-18599.8	2.9
2	16-27	13.78	1.18	6.50	-18599.8	2.1
3	28-39	13.89	1.41	6.49	-18599.8	2.6
4	40-51	14.05	1.61	6.49	-18599.8	2.6
5	52-63	14.15	1.79	6.49	-18599.8	3.0
6	64-75	14.32	1.95	6.48	-18599.8	3.8
7	76-87	14.46	2.1	6.48	-18599.8	3.1
8	88-99	14.61	2.24	6.48	-18599.8	2.9
9	100-111	14.74	2.37	6.48	-18599.9	3.1
10	112-123	14.88	2.49	6.48	-18599.9	3.9
11	124-135	15.10	2.61	6.47	-18599.9	3.2
12	136-147	15.16	2.72	6.47	-18599.9	3.1

Code snippets of the NAP configuration simulations

This code snippets declare the used values for the determination of the electromagnetic fields simulated with Kassiopeia [75]. The values for the superconducting magnets are:

```
<external_define name="rs_solenoid1_current" value="{0.0}"/>
<external_define name="rs_solenoid2_current" value="{0.0}"/>
<external_define name="rs_solenoid3_current" value="{0.0}"/>
<external_define name="rs_solenoid_booster_current" value="{0.0}"/>
<external_define name="rs_EGun_solenoid_current" value="{0.0}"/>
<external_define name="rs_magnetic_dipole1_current" value="{0.0}" />
<external_define name="rs_magnetic_dipole2_current" value="{0.0}" />
<external_define name="rscm_current" value="{57.0}"/>
<external_define name="wgts_current_M1M4M5" value="{216.9}"/>
<external_define name="dps1r_dipole_x_current" value="{0.0}" />
<external_define name="dps1r_dipole_y_current" value="{0.0}" />
<external_define name="wgts_current_M2M3" value="{216.2}"/>
<external_define name="wgts_current_M6M7" value="{146.2}"/>
<external_define name="dps1f_dipole_x_current" value="{0.0}" />
<external_define name="dps1f_dipole_y_current" value="{0.0}" />
<external_define name="dps_coil_1_current" value="{56.8}"/>
<external_define name="dps_coil_2_current" value="{56.7}"/>
<external_define name="dps_coil_3_current" value="{56.7}"/>
<external_define name="dps_coil_4_current" value="{56.7}"/>
<external_define name="dps_coil_5_current" value="{56.9}"/>
<external_define name="cps_coil_current" value="{140.0}"/>
<external_define name="ps_1_current" value="{109.5}"/>
<external_define name="ps_2_current" value="{108.8}"/>
<external_define name="pinch_magnet_current" value="{60.9}"/>
<external_define name="detector_magnet_current" value="{39.3}"/>
```

The values for the eLFCS coils are:

```
<external_define name="emcs_use_realistic_model" value="0"/>
<external_define name="elfcs_1_current" value="50.8"/>
<external_define name="elfcs_2_current" value="0.0"/>
<external_define name="elfcs_3_current" value="44.6"/>
<external_define name="elfcs_4_current" value="{79.5*(8.0/14.0)}"/>
<external_define name="elfcs_5_current" value="{43.0*(8.0/14.0)}"/>
<external_define name="elfcs_6_current" value="{64.8*(8.0/14.0)}"/>
```

```
<external_define name="elfcs_7_current" value="{25.7*(8.0/14.0)}"/>
<external_define name="elfcs_8_current" value="52.8"/>
<external_define name="elfcs_9_current" value="34.9"/>
<external_define name="elfcs_10_current" value="38.7"/>
<external_define name="elfcs_11_current" value="9.2"/>
<external_define name="elfcs_12_current" value="35.9"/>
<external_define name="elfcs_13_current" value="92.7"/>
<external_define name="elfcs_14_current" value="13.2"/>
<external_define name="elfcs_15_current" value="0.0"/>
<external_define name="elfcs_16_current" value="0.0"/>
<external_define name="elfcs_17_current" value="0.0"/>
<external_define name="elfcs_18_current" value="0.0"/>
<external_define name="elfcs_19_current" value="0.0"/>
<external_define name="elfcs_20_current" value="0.0"/>
```

The parameters of the high voltage configuration are:

```
<external_define name="ground_potential" value="0."/>
<external_define name="hull_potential" value="-18400"/>
<external_define name="ie_common_potential" value="-200.0"/>
<external_define name="ap_offset_potential" value="0."/>
<external_define name="steep_cone_additional_offset" value="0."/>
<external_define name="fpd_pae_voltage" value="0."/>
<external_define name="upstream_full_metal_cone_offset" value="40."/>
<external_define name="upstream_steep_cone_offset" value="40."/>
<external_define name="upstream_small_flat_cone_offset" value="0."/>
<external_define name="upstream_middle_flat_cone_offset" value="0."/>
<external_define name="upstream_large_flat_cone_offset" value="0."/>
<external_define name="central_cylinder_offset" value="0."/>
<external_define name="downstream_large_flat_cone_offset" value="0."/>
<external_define name="downstream_middle_flat_cone_offset" value="0."/>
<external_define name="downstream_small_flat_cone_offset" value="0."/>
<external_define name="downstream_steep_cone_offset" value="40."/>
<external_define name="downstream_full_metal_cone_offset" value="40."/>
```

SAP configuration table

Table A.2.: Ring-wise parameters of SAP configuration at $U_{\mathrm{HV}} = -18600V$. The used values for the field calculations with Kassiopeia are given in 8. Given is the downstream volume V_{ds}, the maximal radius r_{ana}, the minimum magnetic field B_{ana}, and the minimum potential U_{ana} at the analysing plane, as well as the longitudinal position z in KATRIN global coordinates of the AP. Further, the energy resolution ΔE is given for $B_{\mathrm{max}} = 4.2\,\mathrm{T}$, $E = E_0 = 18575\mathrm{eV}$, and $B_{\mathrm{min}} = B_{\mathrm{ana}}$, according eq. 3.2.

Ring no.	Pixels	V_{ds} (m^3)	r_{ana} (m)	B_{ana} (G)	U_{ana} (V)	z (m)	ΔE (eV)
0	0-3	1.69	0.38	6.41	-18593.5	5.21	2.84
1	4-15	5.03	0.76	6.34	-18593.7	5.29	2.81
2	16-27	4.99	1.01	6.23	-18593.9	5.41	2.77
3	28-39	4.94	1.20	6.11	-18594.2	5.53	2.71
4	40-51	4.90	1.37	5.99	-18594.4	5.66	2.66
5	52-63	4.87	1.52	5.86	-18594.7	5.78	2.60
6	64-75	4.84	1.66	5.72	-18594.9	5.90	2.54
7	76-87	4.83	1.78	5.57	-18595.2	6.01	2.47
8	88-99	4.83	1.90	5.41	-18595.6	6.13	2.39
9	100-111	4.82	2.01	5.22	-18595.9	6.24	2.31
10	112-123	4.84	2.11	5.02	-18596.3	6.36	2.22
11	124-135	4.87	2.21	4.80	-18596.7	6.47	2.12
12	136-147	4.92	2.31	4.56	-18597.1	6.59	2.01

Code snippets of the SAP configuration simulations

This code snippets declare the used values for the determination of the electromagnetic fields simulated with Kassiopeia [75].

The values for the superconducting magnets are:

```
<external_define name="rs_solenoid1_current" value="{0.0}"/>
<external_define name="rs_solenoid2_current" value="{0.0}"/>
<external_define name="rs_solenoid3_current" value="{0.0}"/>
<external_define name="rs_solenoid_booster_current" value="{0.0}"/>
<external_define name="rs_EGun_solenoid_current" value="{0.0}"/>
<external_define name="rs_magnetic_dipole1_current" value="{0.0}" />
<external_define name="rs_magnetic_dipole2_current" value="{0.0}" />
<external_define name="rscm_current" value="{57.0}"/>
<external_define name="wgts_current_M1M4M5" value="{216.9}"/>
<external_define name="dps1r_dipole_x_current" value="{0.0}" />
<external_define name="dps1r_dipole_y_current" value="{0.0}" />
<external_define name="wgts_current_M2M3" value="{216.2}"/>
<external_define name="wgts_current_M6M7" value="{146.2}"/>
<external_define name="dps1f_dipole_x_current" value="{0.0}" />
<external_define name="dps1f_dipole_y_current" value="{0.0}" />
<external_define name="dps_coil_1_current" value="{56.8}"/>
<external_define name="dps_coil_2_current" value="{56.7}"/>
<external_define name="dps_coil_3_current" value="{56.7}"/>
<external_define name="dps_coil_4_current" value="{56.7}"/>
<external_define name="dps_coil_5_current" value="{56.9}"/>
<external_define name="cps_coil_current" value="{140.0}"/>
<external_define name="ps_1_current" value="{109.5}"/>
<external_define name="ps_2_current" value="{108.8}"/>
<external_define name="pinch_magnet_current" value="{60.9}"/>
<external_define name="detector_magnet_current" value="{39.3}"/>
```

The values for the eLFCS coils are:

```
<external_define name="emcs_use_realistic_model" value="0"/>
<external_define name="elfcs_1_current" value="120"/>
<external_define name="elfcs_2_current" value="-4"/>
<external_define name="elfcs_3_current" value="116"/>
<external_define name="elfcs_4_current" value="70"/>
<external_define name="elfcs_5_current" value="70"/>
```

```
<external_define name="elfcs_6_current" value="70"/>
<external_define name="elfcs_7_current" value="70"/>
<external_define name="elfcs_8_current" value="110"/>
<external_define name="elfcs_9_current" value="110"/>
<external_define name="elfcs_10_current" value="110"/>
<external_define name="elfcs_11_current" value="-60"/>
<external_define name="elfcs_12_current" value="-28"/>
<external_define name="elfcs_13_current" value="58"/>
<external_define name="elfcs_14_current" value="5"/>
<external_define name="elfcs_15_current" value="120"/>
<external_define name="elfcs_16_current" value="120"/>
<external_define name="elfcs_17_current" value="-120"/>
<external_define name="elfcs_18_current" value="-119"/>
<external_define name="elfcs_19_current" value="-120"/>
<external_define name="elfcs_20_current" value="-120"/>
```

The parameters of the high voltage configuration are:

```
<external_define name="hull_potential" value="-18395.0"/>
<external_define name="ie_common_potential" value="-205.0"/>
<external_define name="ap_offset_potential" value="0."/>
<external_define name="steep_cone_additional_offset" value="0."/>
<external_define name="fpd_pae_voltage" value="0."/>
<external_define name="upstream_full_metal_cone_offset" value="125"/>
<external_define name="upstream_steep_cone_offset" value="125"/>
<external_define name="upstream_small_flat_cone_offset" value="25."/>
<external_define name="upstream_middle_flat_cone_offset" value="25."/>
<external_define name="upstream_large_flat_cone_offset" value="25."/>
<external_define name="central_cylinder_offset" value="10."/>
<external_define name="downstream_large_flat_cone_offset" value="2."/>
<external_define name="downstream_middle_flat_cone_offset" value="0."/>
<external_define name="downstream_small_flat_cone_offset" value="2."/>
<external_define name="downstream_steep_cone_offset" value="45."/>
<external_define name="downstream_full_metal_cone_offset" value="105."/>
```

Background dependencies

Radial profile

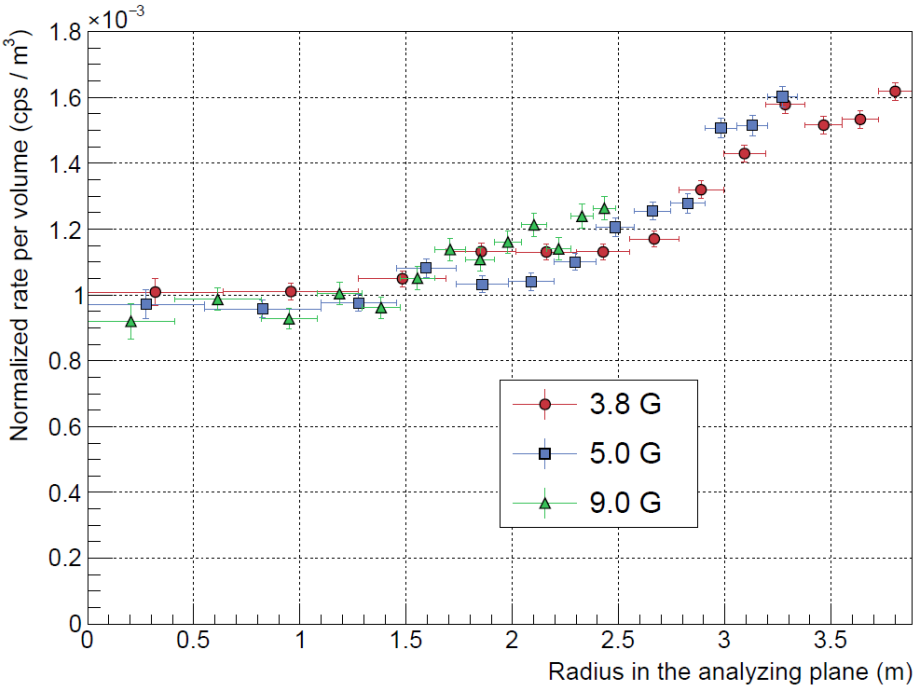

(a) Volume normalised radial background rate.

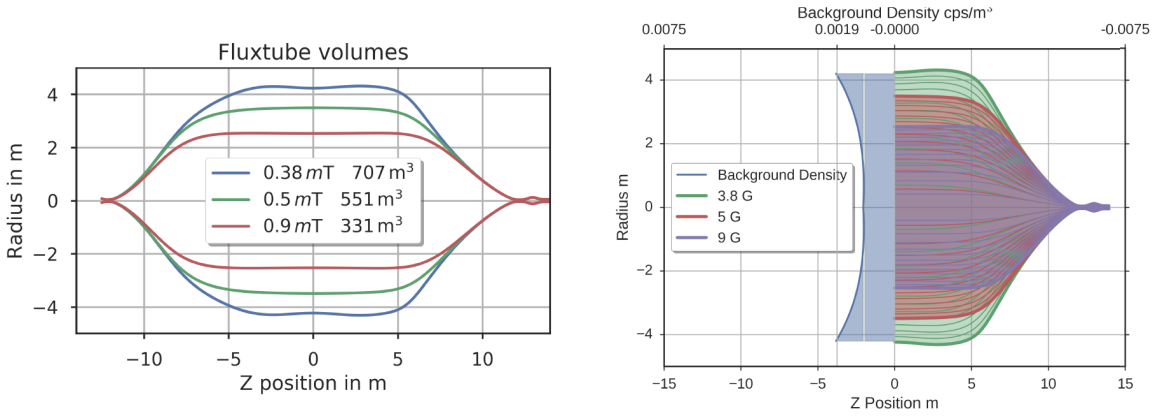

(b) Flux tube volumes and background density.

Figure A.1.: (a): Radial background distribution for different symmetric magnetic field settings with varying volume and flux tube radii [8]. **(b):** Left: Magnetic flux tubes for different magnetic field strengths and their enclosing volumes. Right: Sensitive flux tube volumes with the radial background density mapped on the detector [9].

^{210}Pb decay

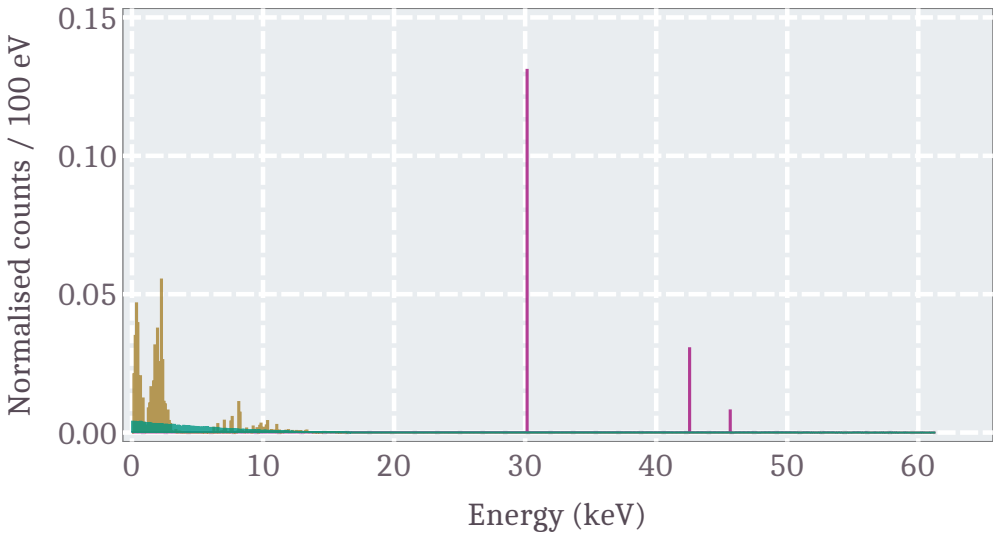

Figure A.2.: Energy spectrum of electrons, released at ^{210}Pb decays with linear scale. 10^6 decays have been simulated which result in a total of 1867360 electrons.

Table A.3.: ^{210}Pb decay transitions and their probability [91]. If β(17 keV) occurs, the γ transition probability is 100 %. The total appearance probability of an L-shell conversion electron is $P_{\mathrm{ec_L}} = 0.58 \cdot 0.802 \cdot 100\,\% = 46.5\,\%$.

	Energy (keV)	Probability (%)
β	17.0	80.2
β	63.5	19.8
γ	46.54	80.2
$\mathrm{ec_L}$	30.152	58.0
$\mathrm{ec_M}$	42.540	13.7
$\mathrm{ec_N}$	45.601	3.5
$\mathrm{e_{Auger}}$	<10.7	36.0

^{238}U decay chain with daughters ^{222}Rn and ^{210}Pb

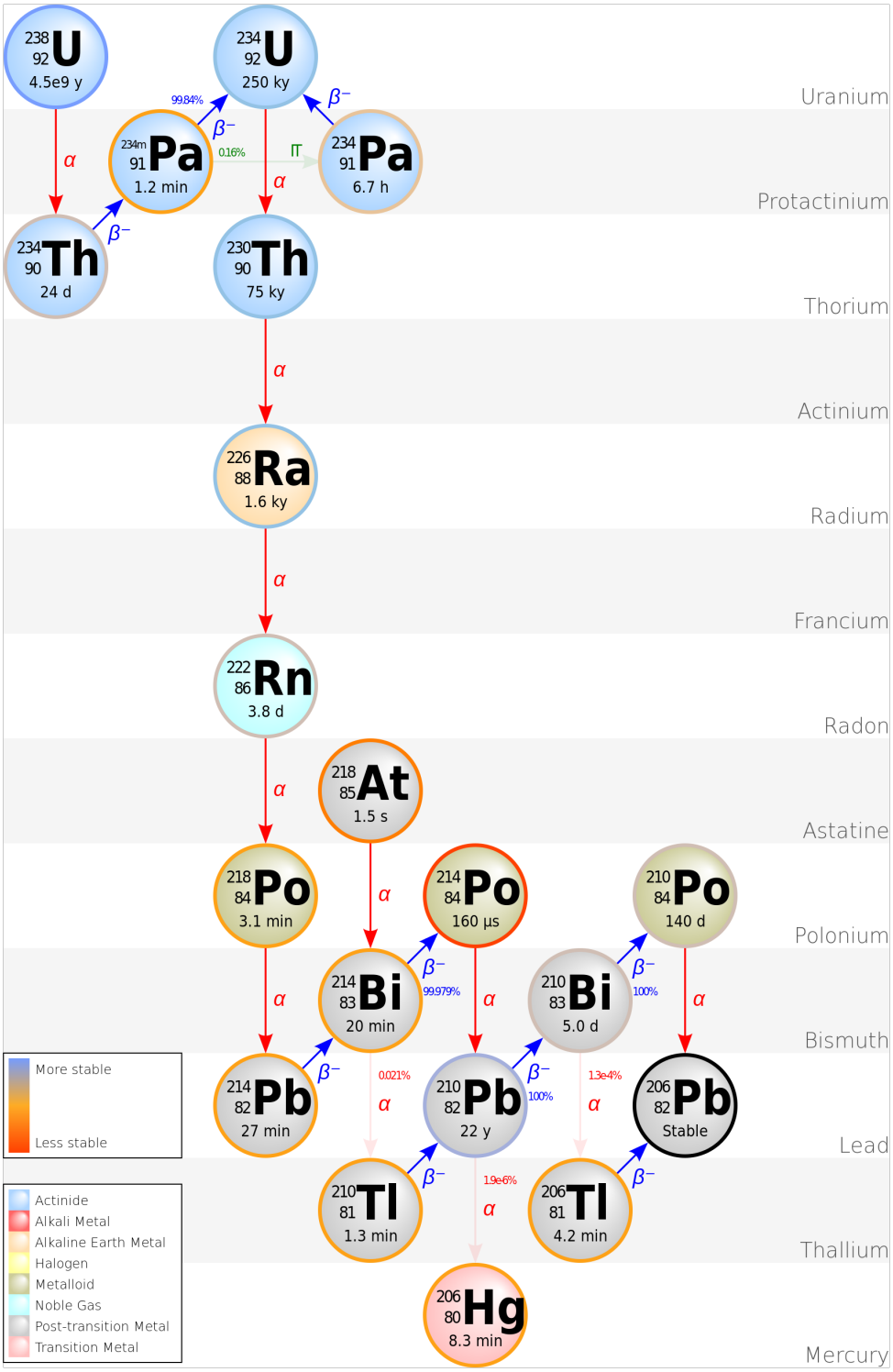

Figure A.3.: Decay chain of ^{238}U with its daughter atoms ^{222}Rn and ^{210}Pb, final decay to stable ^{206}Pb [170].

Decay chain and recoil atom energies of ^{222}Rn

Table A.4.: Decay chain of ^{222}Rn with the corresponding α and β^- decay modes, see fig. A.3. The decay energy Q is given in MeV from [91] and the energy of the recoil atom E_{recoil} is calculated according eq. 4.3, given in keV. The half-life of the radioactive reactants is given in years (y), days (d), minutes (m), or seconds (s), correspondingly from [91].

Reactant	Product	Mode	Q (MeV)	E_{recoil} (keV)	$T_{1/2}$
^{222}Rn	^{218}Po	α	5.5903	100.726	3.2332(8) d
^{218}Po	^{214}Pb	α	6.1147	112.196	3.071(22) m
^{214}Pb	^{214}Bi	β^-	1.019	2.61×10^{-3}	26.916(44) m
^{214}Bi	^{214}Po	β^-	3.270	8.38×10^{-3}	19.8(1) m
^{214}Po	^{210}Pb	α	7.8335	146.420	162.30(12) µs
^{210}Pb	^{210}Bi	β^-	0.0635	1.7×10^{-4}	22.23(12) y
^{210}Bi	^{210}Po	β^-	1.1612	3.03×10^{-3}	5.011(5) d
^{210}Po	^{206}Pb	α	5.4075	102.9991	138.3763(17) d

Main spectrometer stainless steel composition

Table A.5.: Chemical composition of the KATRIN main spectrometer stainless steel 1.4429, values are given in % (neglecting the traces of P, S and Si) [101, 171].

C	Mn	N	Cr	Mo	Ni	Fe
≤ 0.03	≤ 2	0.17 ± 0.05	17.5 ± 1.0	2.75 ± 0.25	12.5 ± 1.5	balance

SRIM simulations

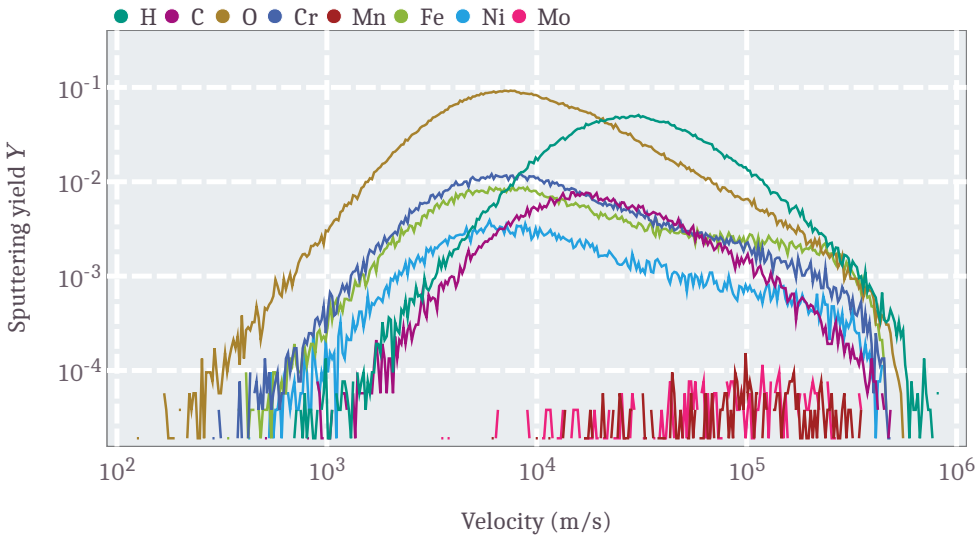

Figure A.4.: Velocity-dependent sputtering yield of the relevant ^{210}Po decay with the additional sputtering on the opposite side by transmitted recoils.

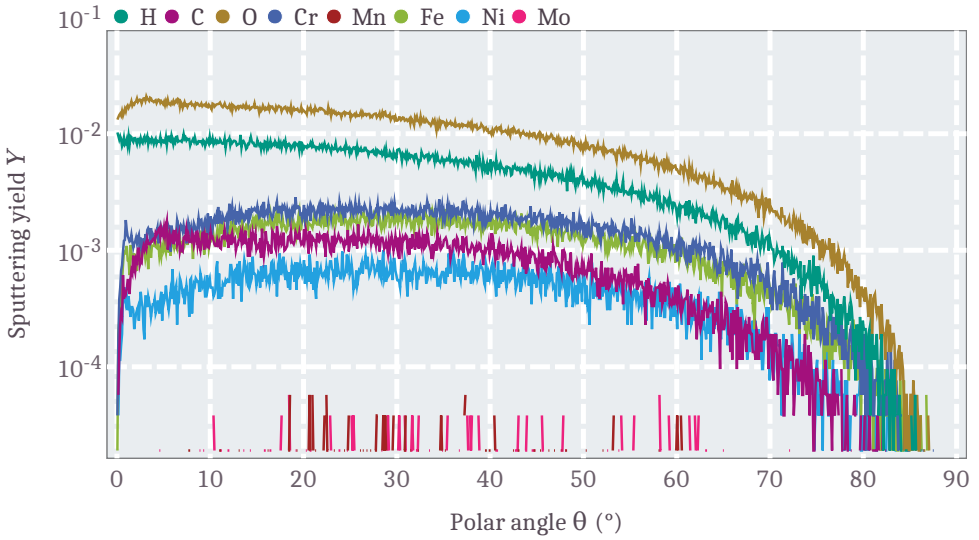

Figure A.5.: Angular-dependent sputtering yield of the relevant ^{210}Po decay with the additional sputtering on the opposite side by transmitted recoils. The polar angles to the surface normal follow a cosine distribution [9].

Table A.6.: Measurement configuration and region of interest ROIs applied at the measurement campaigns KNM2-KNM5.

KNM2	14 - 32 keV	NAP (6.3 G)
KNM3-A	22 - 34 keV	SAP
KNM3-B	22 - 34 keV	NAP (6.3 G)
KNM4 all	22 - 34 keV	SAP
KNM5	22 - 34 keV	SAP

KNM ROIs and pixel-cuts

Applied pixel-cuts at the KNM measurements, the named pixels with its numbering ranging from 0 to 147 have been excluded from the analysis:

- KNM2: 97, 98, 110, 111, 121, 122 (large noise), 100 (shadowed by FBM), 112, 113, 123, 124, 125, 126, 127, 128, 129, 130, 134, 135, 136, 137, 138, 139, 140, 141, 142, 143, 144, 145, 146, 147 (alignment)
- KNM3-KNM5: 100 (FBM), 99, 112, 113, 123, 124, 125, 126, 127, 128, 129, 130, 135, 136, 137, 138, 139, 140, 141, 142, 145, 146, 147 (alignment)

Non-Poisson fraction Σ_{np}

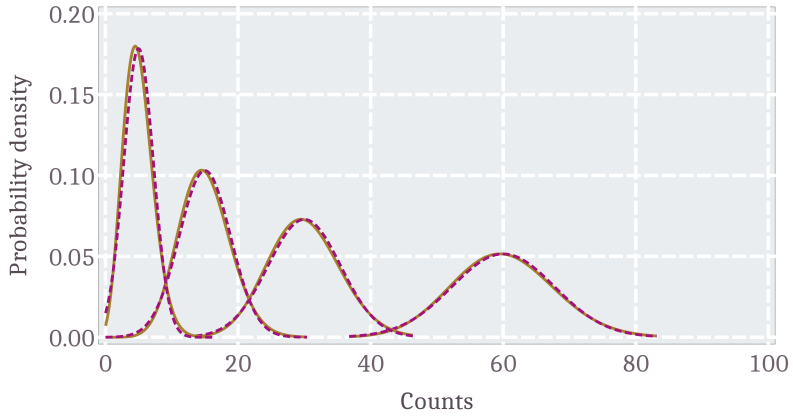

Figure A.6.: Poisson and Gauss distributions for different mean values $\mu_i = 5, 15, 30, 60$ and the standard deviations $\sigma_i = \sqrt{\mu_i}$ for the Gauss distributions. For high enough μ the Poisson equals the Gauss distribution.

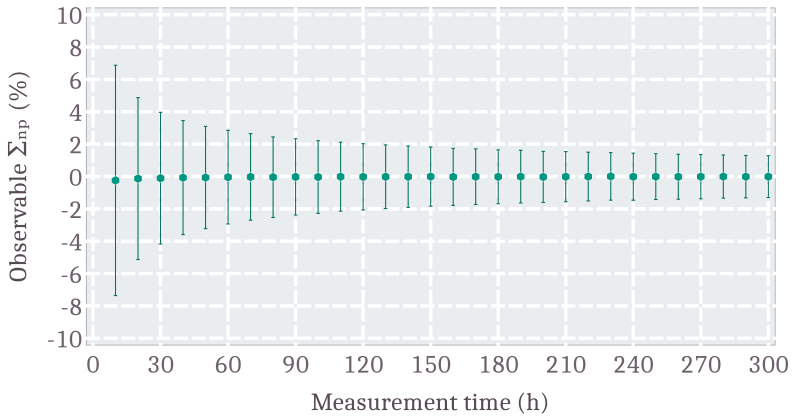

Figure A.7.: Observable non-Poisson fractions as a function of the measurement time. For given measurement times ranging from 10 h to 300 h, the observable non-Poisson fraction was extracted by 50k trials at each measurement time by the mean and standard deviation of the resulting distribution of fractions. The uncertainty on Σ_{np} follows a $x^{-1/2}$ distribution. At 60h, $\sigma_\Sigma = 2.9\,\%$ which means that in 68.2 % of all observations an absolute fraction smaller than 2.9 % (positive or negative) is measured, or larger for 31.8 %, although the real value is zero.

Radon-induced electron inter-arrival times

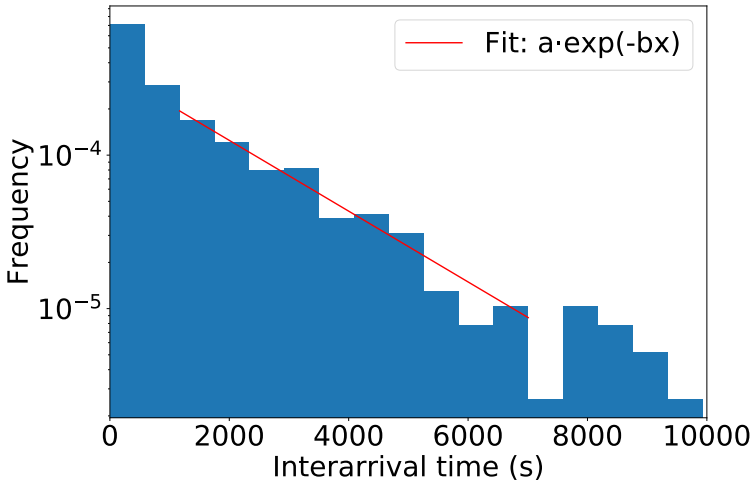

Figure A.8.: Inter-arrival time spectrum of background electrons, induced by Radon decays on the FPD. The pressure at this simulation was set to $p = 4{\times}10^{-11}$ mbar, but only 1500 decays have been simulated, as such simulations are time-consuming. An exponential fit is made which shows that the arrival times are also nearly Poisson distributed but in reality arrivals of secondary electrons of different primary electrons as source arrive at the detector since the inter-arrival times are up to several thousands of seconds.

Radon-induced electron cluster sizes for NAP and SAP

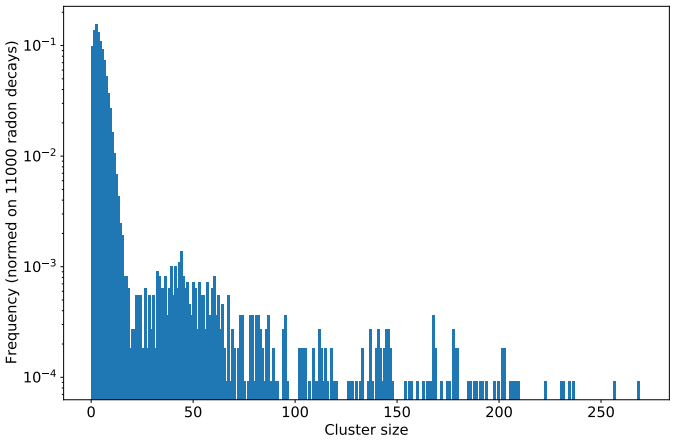

(a) NAP.

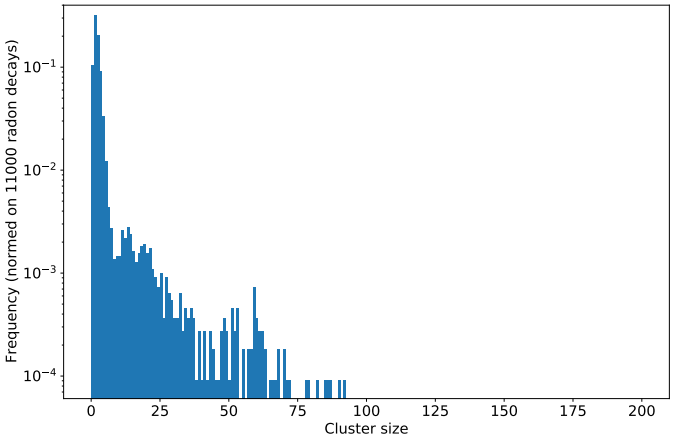

(b) SAP.

Figure A.9.: Cluster sizes of Radon-induced electrons for NAP and SAP configuration. The cluster size is the amount of electrons, arriving at the detector for one radon decay, which releases several electrons per decay, which further produce secondary electrons by residual gas ionisation. **(a):** Simulation result for the NAP configuration, cluster sizes up to 260 electrons are observed with a mean of 6.8 electrons of this distribution. **(b):** Result for the SAP configuration, cluster sizes up to 90 are observed with a mean of 2.3 electrons.

Closest distance to MS Wall - SAP

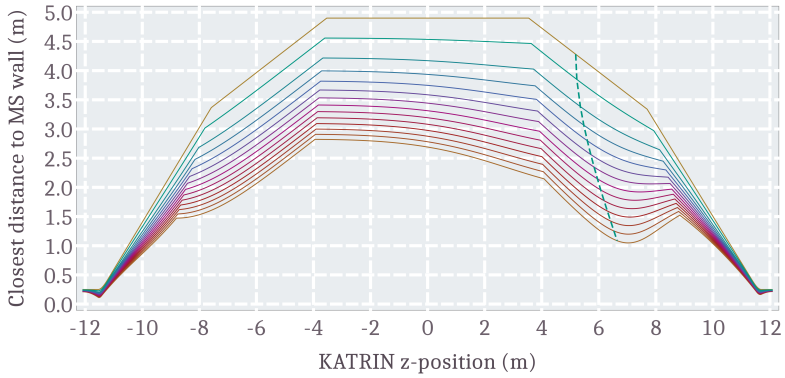

Figure A.10.: Ring-wise closest distance to MS wall for SAP configuration

Radial background distribution KNM3|B and KNM5

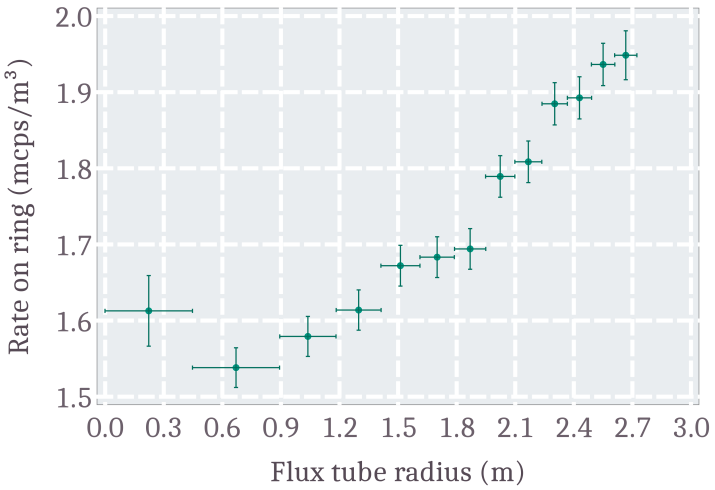

(a) KNM3|B.

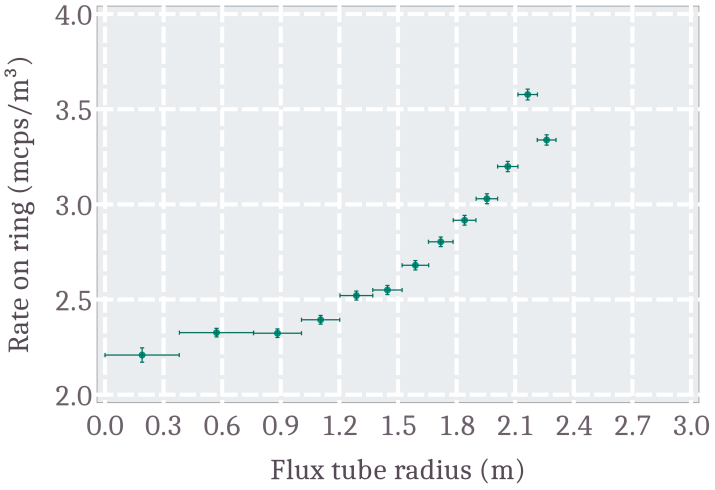

(b) KNM5.

Figure A.11.: Radial background distribution on the FPD, obtained during KNM3|B (NAP) and KNM5 (SAP). No pixel cut was applied as the background is not that affected compared to the beta electrons with respect to the global misalignment. The rate is normalised to the volume mapped on the individual detector rings as a function of the flux tube radius in the corresponding analysing plane.

Final polar angle electron simulation

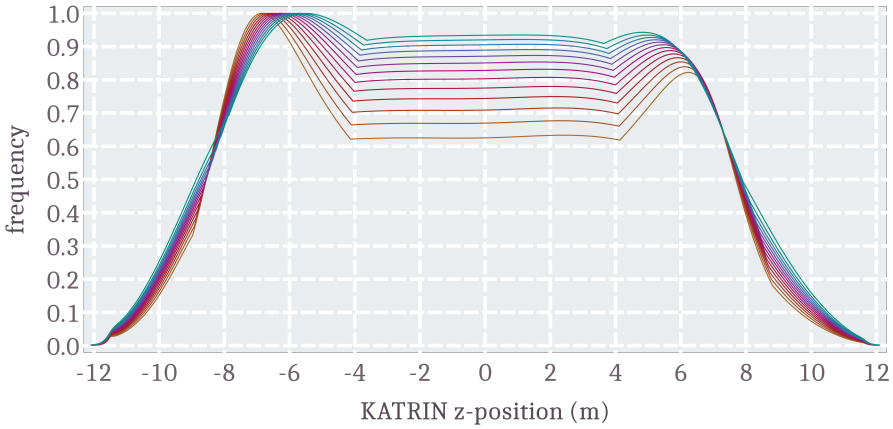

Figure A.12.: Probability densities along the beamline axis z for the individual FPD rings for the 5.0 G configuration. All probabilities are normalised to a maximum value of 1. It is distributed most homogeneous for inner FPD pixels (green line) and the effect of the closer distance to the wall is more pronounced for outer detector rings (light brown line).

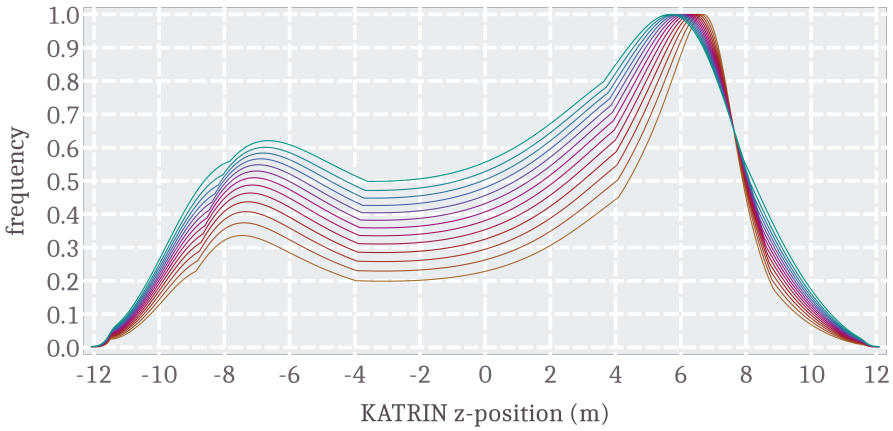

Figure A.13.: Probability densities along the beamline axis z for the individual FPD rings of the SAP configuration. All probabilities are normalised to a maximum value of 1. It is distributed most homogeneous for inner FPD pixels (green line) and the effect of the closer distance to the wall is more pronounced for outer detector rings (light brown line).

Table A.7.: Fit parameters c_{1-4} and their uncertainty of the electron transmission probability of eq. 6.8 at 18.6 keV, shown in fig. 6.9.

Parameter	value	uncertainty
c_1	−1.2889	0.005 22
c_2	90.1438	0.094 63
c_3	56.0010	1.050 48
c_4	15.8852	1.075 54

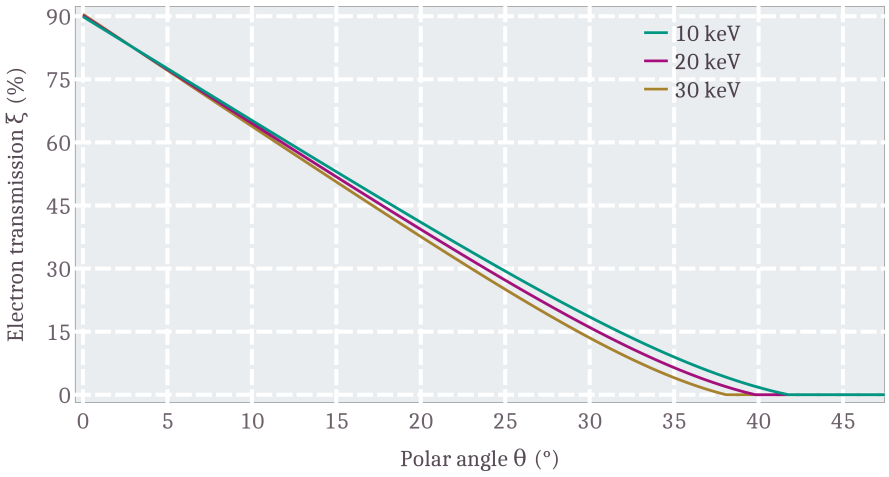

Figure A.14.: Electron transmission probability through pTEF for different energies of 10, 20, and 30 keV.

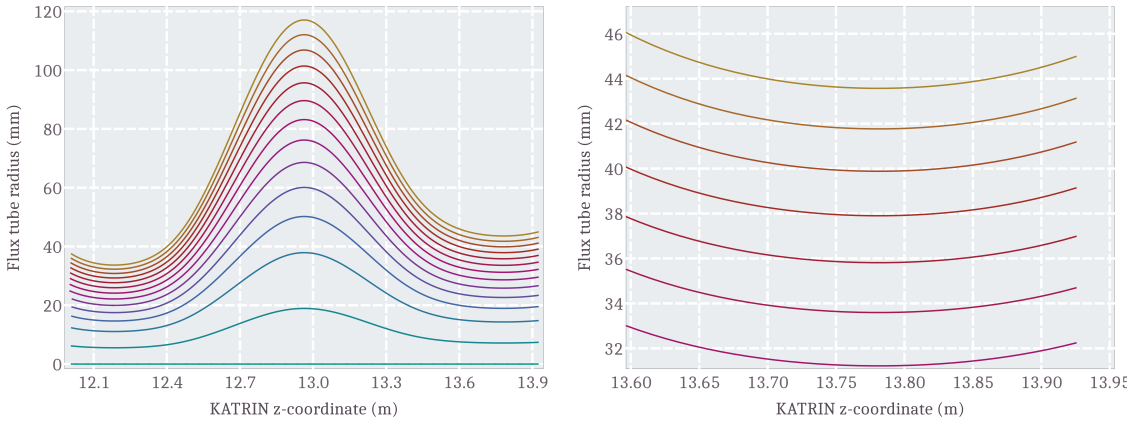

(a) Detector section flux tube.

(b) Local flux tube.

Figure A.15.: Flux tube radius at the full detector section and around the FPD wafer and the pTEF position at $z = 13.783\,75$ m.

Table A.8.: Ring-wise mean initial magnetic field strengths, determined by the geometric mean of B_i at the generated electron starting positions.

FPD ring	2.7 G	5.0 G	5.0 G sym.	8.0 G	12.0 G	17.0 G	SAP
1	3.86	6.15	6.42	9.43	13.49	18.19	9.25
2	3.84	6.12	6.31	9.34	13.42	18.15	9.06
3	3.76	6.1	6.32	9.31	13.47	18.13	8.86
4	3.73	6.06	6.27	9.32	13.51	18.07	8.78
5	3.68	6.03	6.18	9.35	13.39	18.01	8.57
6	3.64	5.99	6.16	9.23	13.37	18.02	8.38
7	3.59	6.0	6.06	9.24	13.35	18.0	8.17
8	3.54	5.92	6.02	9.26	13.36	17.89	7.89
9	3.49	5.9	5.98	9.23	13.33	17.99	7.64
10	3.43	5.82	5.91	9.17	13.31	17.85	7.31
11	3.37	5.78	5.85	9.14	13.33	17.79	7.03
12	3.32	5.77	5.79	9.08	13.21	17.8	6.68
13	3.25	5.69	5.71	9.03	13.19	17.63	6.37

Backscattering effects at the pTEF measurement configurations

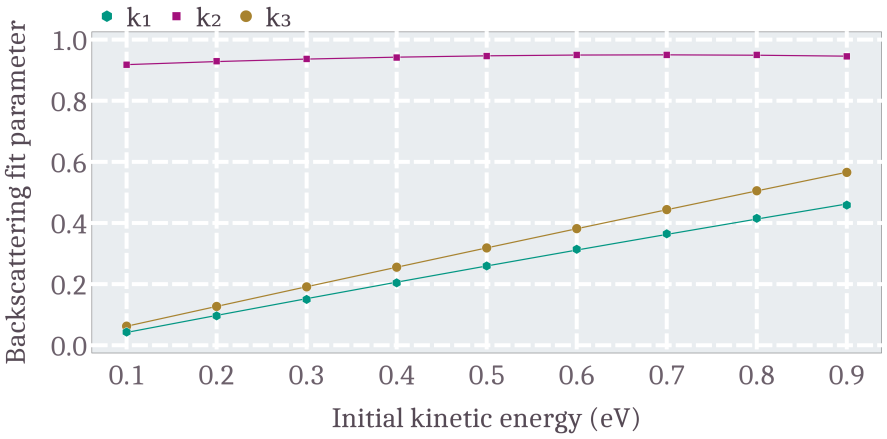

Figure A.16.: Parameter evolution of k_i, describing the energy and magnetic-field-dependent transmission change due to backscattering. The individual derived parameters k_i are fitted with second-order polynomials to describe the backscattering effect on the transmission probability η as a function of the initial kinetic energy of the electrons which are used in eq. 6.14, through which the change as a function of the magnetic field is obtained.

Table A.9.: Fit parameters for the evolution of the parameters k_i in fig. A.16, fitted with a second-order polynomial $p(e) = p_1 \cdot e^2 + p_2 \cdot e + p_3$.

	k_1	k_2	k_3
p_1	-0.0458	-0.09360	-0.0276
p_2	0.5711	0.1282	0.6574
p_3	-0.0147	0.9063	-0.0032

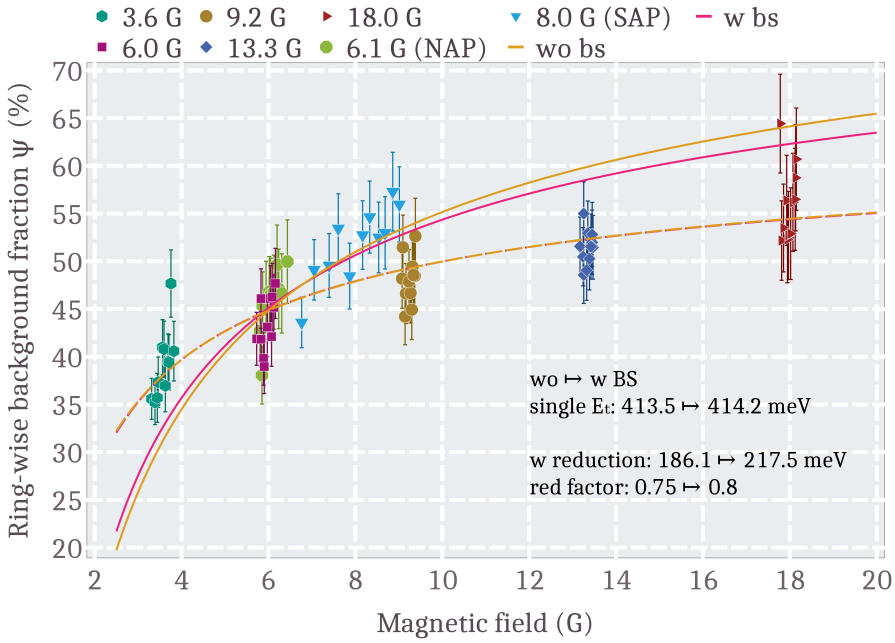

Figure A.17.: Comparison of the transverse energy scale fit with and without consideration of scattering effects. The single fit on the transverse energy scale E_t is not influenced by the consideration of backscattering (bs), although the reduced χ^2 improves from 3.59 to 2.67. However, at the fit with a global reduction factor, the transverse energy scale increases, so does the reduction factor, which is equal to less reduction. The reduced χ^2 remains at 0.898.

Transverse energy scale fit at 12.0 keV and 34.1 keV retarding potential

At 12.0 keV a lower transverse energy is obtained in addition to a stronger reduction. This is caused by an increased background fraction at the 2.7G measurement. This may arise by the better spectrometer resolution as higher energetic electrons are more efficiently being trapped and do not reach the detector. Therefore this part of the electron energy spectrum misses and the transmission is enhances as only a lower energetic part is being detected. Or scattering enhances the low magnetic field part more drastic. The reduced χ^2 are

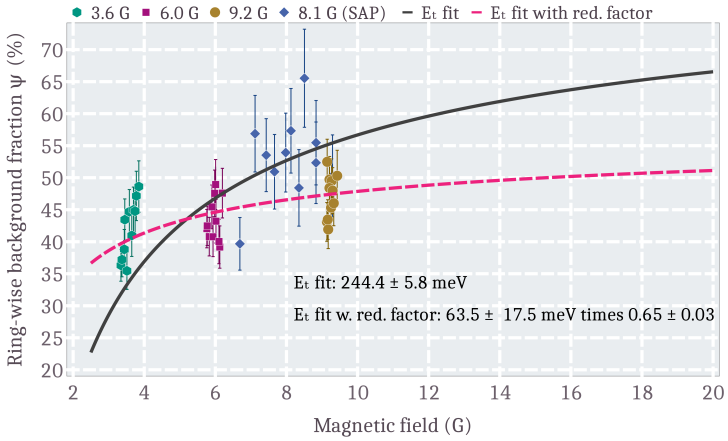

(a) 12.0 keV.

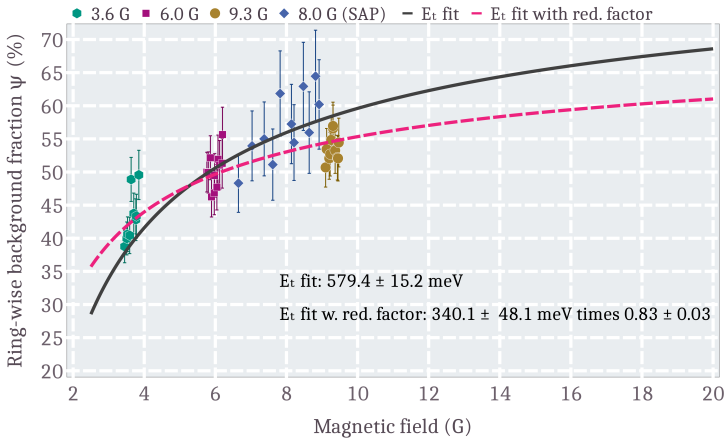

(b) 34.1 keV.

Figure A.18.: Fit of transverse energy scale E_t for the measurements at 12.0 keV and 34.1 keV without consideration of scattering.

worse with 4.29 for the single E_t fit and 1.42 with the reduction factor. At 34.1 keV larger background fractions are obtained, which is expected by the final polar angle dependence on the final energy. However, larger transverse energies are fitted to the data, but with a smaller reduction. Both reduced χ^2 are rather good with 1.41 of the single E_t fit and 0.69 for the fit with reduction. Also here, the higher energy scale may arise from the background electron energy dependence of the spectrometer resolution. However, no significant amount of trapped electrons have been observed at dedicated measurements. Both measurements are less reliable as the magnetic field range is reduced compared to the measurement at 18.6 keV. In both cases, no scattering is considered as the measurements are less reliable, certainly the effect of scattering is different to the case of 18.6 keV as the polar angle distribution is different.

Acknowledgment

Hiermit möchte ich all denen danken, die mich im Laufe meines Lebens und während meiner Promotion begleitet haben. Das Gelingen dieser Arbeit war zum Teil auch euer Verdienst. Auch wenn ich nicht alle namentlich nennen kann, möchte ich mich im Besonderen bedanken bei:

- Prof. Dr. Guido Drexlin, der mich schon vor einiger Zeit mit seiner Theorie zum Rydberg-Untergrund im KATRIN Hauptspektrometer begeisterte. Die Feinheiten des Untergrundmodells haben wir öfters in fruchtbaren Gesprächen diskutiert. Ebenso bedanke ich mich für die Möglichkeit dieser Promotion herzlichst, ebenfalls bei meinem Korreferenten Prof. Dr. Ralph Engel.
- Meinen geschätzten Kolleg:innen des IAP für die ausgezeichnete Atmosphäre.
- Ich möchte insbesondere Leonard Köllenberger & Dr. Stephanie Hickford danken für ihre offenen Ohren bezüglich Fragen von Analysetechniken, aber auch für die gemeinsame Zeit neben der Arbeit.
- Weiterer Dank geht an Dr. Ferenc Glück, Dr. Jan Behrens und Joscha Lauer für die Unterstützung bei Simulationen und Problemen mit Kassiopeia, die maßgeblich zum Erfolg dieser Arbeit beitrugen.
- Ausdrücklicher Dank geht an die Techniker Alexander Verbeek, Alan Kumb und Hendrik Weingardt für die tatkräftige Unterstützung bei Arbeiten am Monitorspektrometer und die erfrischenden Gespräche, die nicht zwingend etwas mit der Arbeit zu tun hatten.
- Desweiteren geht außerordentlicher Dank an meine Familie und Freunde. Ich danke meinen Eltern Jürgen & Daniela und meinem Bruder Benedict. Ebenso möchte ich mich bei meinen Großeltern, Großonkel und meiner Großtante bedanken sowie bei meiner Schwiegerfamilie. Ohne euer Zutun würde es diese Arbeit vielleicht nicht geben, denn ihr wisst jeden noch so trostlosen Tag mit Quatsch und Tratsch zu einem tollen zu machen.
- Auf meine Freunde Achim & Sandra, Kathrin, Julia & Frederik, Philip & Anja sowie Andreas und noch weitere (die Liste würde lang werden) konnte ich mich immer verlassen - vielen lieben Dank!

Das Beste kommt bekanntlich zum Schluss: Meine größte Dankbarkeit gebührt meiner Frau Lisa. Falls notwendig hälst du mir den Rücken frei in allen Lagen, so auch während dieser Arbeit. Du hast mir geholfen, mich auf diese zu fokussieren und mich dabei stets motiviert und aufgemuntert, falls es mal nicht so lief. Dich an meiner Seite zu haben ist Gold wert, dich lass ich nicht mehr los ♡.